

**US Army Corps
of Engineers**

Waterways Experiment
Station

Technical Report SERDP-98-10
September 1998

Strategic Environmental Research and Development Program

Multisensor Methods for Buried Unexploded Ordnance Detection, Discrimination, and Identification

*by Dwain K. Butler, Ernesto R. Cespedes, Cary B. Cox, WES
Paul J. Wolfe, Wright State University*

19981005 161



Approved For Public Release; Distribution Is Unlimited

DEMO COPY - NOT FOR DISTRIBUTION 4



Prepared for Headquarters, U.S. Army Corps of Engineers

The contents of this report are not to be used for advertising, publication, or promotional purposes. Citation of trade names does not constitute an official endorsement or approval of the use of such commercial products.

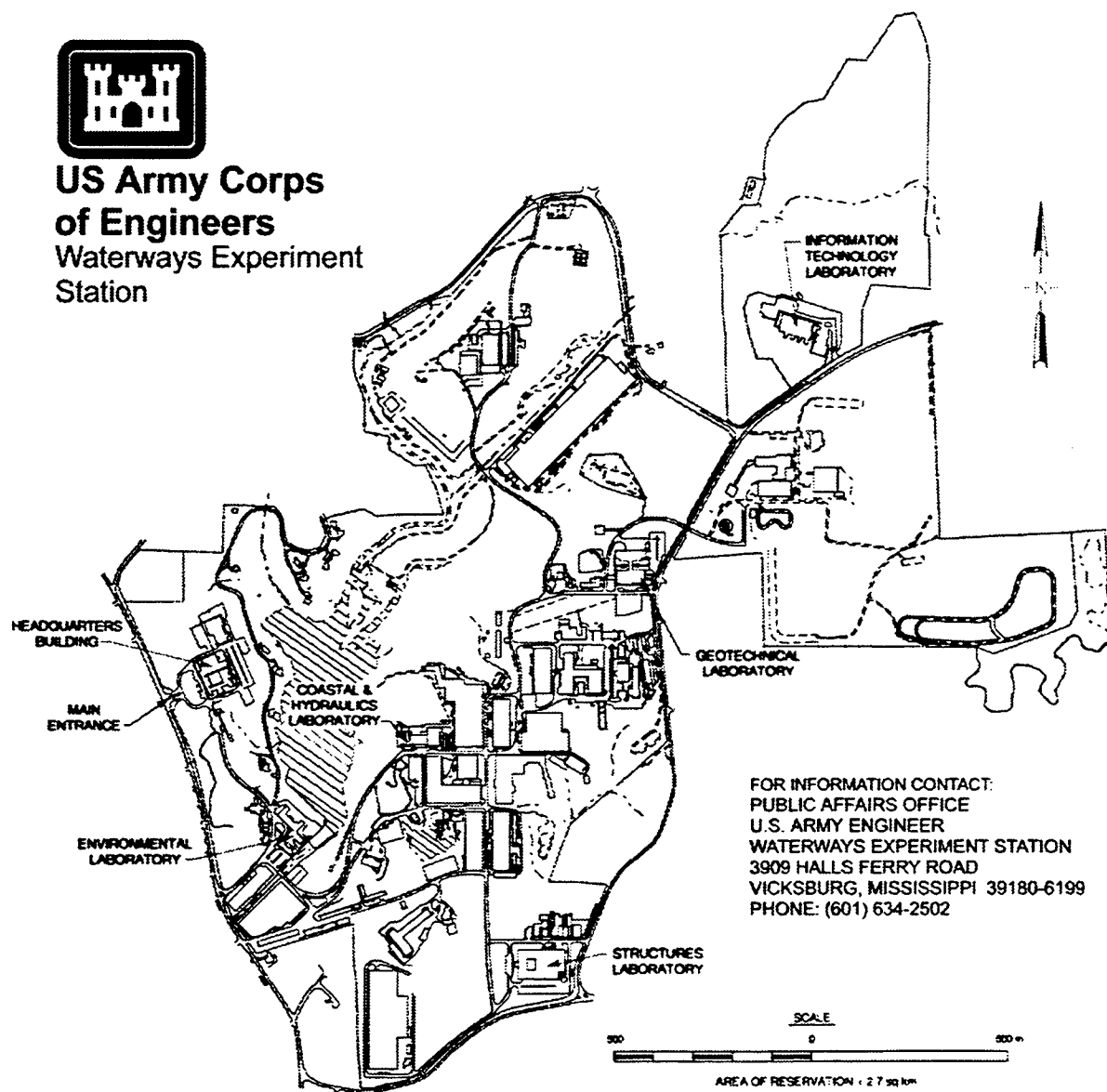
The findings of this report are not to be construed as an official Department of the Army position, unless so designated by other authorized documents.



PRINTED ON RECYCLED PAPER



**US Army Corps
of Engineers**
Waterways Experiment
Station



FOR INFORMATION CONTACT:
PUBLIC AFFAIRS OFFICE
U.S. ARMY ENGINEER
WATERWAYS EXPERIMENT STATION
3909 HALLS FERRY ROAD
VICKSBURG, MISSISSIPPI 39180-6199
PHONE: (601) 634-2502

Waterways Experiment Station Cataloging-in-Publication Data

Multisensor methods for buried unexploded ordnance detection, discrimination, and identification / by Dwain K. Butler ... [et al.] ; prepared for Strategic Environmental Research and Development Program. 181 p. : ill. ; 28 cm. — (Technical report ; SERDP-98-10)
Includes bibliographic references.

1. Ordnance — Detection. 2. Military weapons — Detection. 3. Explosives, Military — Detection. 4. Mines (Military explosives) — Detection. I. Butler, Dwain K. II. United States. Army. Corps of Engineers. III. U.S. Army Engineer Waterways Experiment Station. IV. Strategic Environmental Research and Development Program (U.S.) V. Series: Technical report (U.S. Army Engineer Waterways Experiment Station) ; SERDP-98-10.

TA7 W34 no.SERDP-98-10

Contents

Preface	v
1—Introduction	1
Background	1
UXO Detection, Discrimination, and Identification: Status	2
UXO Detection, Discrimination, and Identification: Approaches	5
Scope of Report	6
2—Geophysical Methods and Multisensor Interpretation Approaches	7
Geophysical Methods for UXO Detection and Discrimination	7
Multisensor Data Interpretation Approaches for UXO Detection and Discrimination	11
Empirical interpretation procedures for complementary, multi- sensor datasets	11
Analysis and data management tools for multisensor data integration and interpretation	12
Integrated multisensor interpretation	16
Joint inversion	19
3—Data Sources for the Investigation	21
Development of WES Ordnance Signature Datasets	21
Naval Research Laboratory (NRL) Ordnance Signature Library	24
DARPA Background Clutter Program	25
Datasets from MTADS Surveys at the Magnetic Test Range, Twenty-nine Palms, California	27
4—Data Management and Analysis Methods for Detection Enhancement	32
GIS Data Management Examples	32
Image Processing of Multisensor Data for Detection Enhancement	34
5—Synopsis and Examples of Current UXO Detection Analyses	41
Capability	41
Introduction	41
Fits to Twenty-nine Palms MTADS Datasets	42
Simple Model Fits to Magnetic Data from DARPA Site	43
Proposed Multisensor Data Integration Algorithm	48

6—Development of Phenomenological Modeling Capability	52
Magnetic Modeling Program	52
Background	52
Program description and input/output	55
Magnetic modeling program validation	57
Phenomenology studies with magnetic modeling program	59
Electromagnetic Induction Modeling Considerations	63
Background	63
Quasi-empirical TDEM modeling considerations	68
Phenomenological Modeling and Multisensor Data Integration	70
Geophysical parameter space plots (cross-plotting)	70
Manual implementation of proposed multisensor integration algorithm	73
7—Considerations of Emerging Technology for UXO Applications	80
Introduction	80
Multichannel, Multicomponent TDEM System	81
Background	81
Single-component analyses procedures	81
Multicomponent parameter space analyses techniques	87
Multifrequency FDEM System	93
Closure for Two Emerging EMI Technologies	98
8—Summary, Conclusions, and Recommendations	101
Summary and Conclusions	101
Recommendations	102
References	105
Appendix A: WES Ordnance Signature Datasets, Magnetic Profile Measurements	A1
Appendix B: <i>MAGMOD</i> Program Listing	B1
SF 298	

Preface

The work documented in this report was performed during the period June 1996 through December 1997 and was sponsored by the Strategic Environmental Research and Development Program (SERDP). The project "Multisensor Data Fusion for Detection of Unexploded Ordnance" was SERDP project No. 1052, Category 6.2 Applied Research, under the Cleanup Thrust Area. Dr. John Harrison and Mr. Bradley Smith were SERDP Directors during the period of performance of this project.

Co-Principal Investigators for this project were Dr. Dwain K. Butler, Geotechnical Laboratory (GL), and Dr. Ernesto R. Cespedes, Environmental Laboratory (EL), U.S. Army Engineer Waterways Experiment Station (WES), Vicksburg, Mississippi. Dr. Paul Wolfe, Wright State University, Dayton, Ohio, participated in this project during the summer of 1996, while at WES under the U.S. Army Summer Faculty Research and Engineering Program, and subsequently under the Post Summer Faculty Research and Engineering Program. Dr. Cary B. Cox, Information Technology Laboratory, WES, developed the graphical users' interface for the magnetic modeling program. Assistance with various aspects of data processing and graphics presentation were provided by Messrs. Donald E. Yule and Michael K. Sharp, and Dr. Janet E. Simms, WES, and Mr. John C. Morgan, IIT Research Institute, Chicago, IL. Additional collaborators for this project were Mr. Duncan McNeill and Dr. Miro Bosnar, Geonics, Inc., Mississauga, Ontario, Canada, Messrs. Ian MacLeod and Louis Racic, Geosoft, Inc., Toronto, Ontario, Canada, Dr. I. J. Won, Geophex, Ltd., Raleigh, NC, and Messrs. James. R. McDonald and Herbert H. Nelson, Naval Research Laboratory, Washington, DC. Geophysical data used for various aspects of this project were acquired and provided by Parsons Engineering Sciences, Inc., Fairfax, VA, Geophex, Ltd., Raleigh, NC, and Blackhawk-Geometrics, Inc., Golden, CO. This report was prepared by Dr. Butler.

Dr. M. John Cullinane, EL, UXO programs coordinator for WES, provided guidance during this work. General supervision was provided by Dr. William F. Marcuson III, Director, GL, and Dr. John W. Keely, Acting Director, EL.

At the time of publication of this report, Director of WES was Dr. Robert W. Whalin. Commander of WES was COL Robin R. Cababa, EN.

The contents of this report are not to be used for advertising, publication, or promotional purposes. Citation of trade names does not constitute an official endorsement or approval of the use of such commercial products.

1 Introduction

Background

Unexploded Ordnance (UXO) cleanup is the number one priority Army Cleanup Problem requirement and is identified as a major problem throughout the Department of Defense (DoD). The problem is enormous in scope and complexity. In excess of 11 million acres (approximately 44,500 km²) of land are contaminated with UXO. The UXO ranges in size from 20-mm rounds to 2,000-lb bombs. Approximately 50 percent of the UXO is estimated to lie on or very near the surface, while the remaining 50 percent is buried at depths to 6 m or more. Before the UXO-contaminated DoD lands can be cleaned up (remediated), the extent of UXO contamination must be determined; i.e., the surface and buried UXO must be located. To achieve the UXO location requirement, Johnson et al. (1996) define a hierarchical four-stage systems process of UXO sensing, consisting of (1) *prescreening*, (2) *cuing*, (3) *detection*, and (4) *classification*. *Prescreening* is the stage of prioritizing potentially UXO-contaminated lands for follow-on survey based on historic records and subsequent intended land use. Of the lands prioritized for follow-on survey, the *cuing* stage consists of location of regions of UXO fields, within the larger areas, by an expedient large-area coverage approach (likely an airborne survey). It seems logical to combine the *prescreening* and *cuing* stages of Johnson et al. (1996) into a single *screening* stage. In this report, an additional stage of *discrimination* is defined. The term *identification* is also defined and is considered the same as the *classification* stage of Johnson et al. Thus, following the example of Johnson et al, this report considers a four stage UXO location process: *screening*, *detection*, *discrimination*, *identification/classification*.

While surface UXO can be located visually and with remote (airborne) imaging techniques in many cases, the surface area to be surveyed is very large and cluttered with metallic and other cultural debris. In addition, the vegetative covers of the UXO contaminated lands vary greatly as does the surface soil and rock type and texture. Although the surface UXO problem is large and complex, the fact that it can be addressed with remote imaging systems is a major advantage, since such systems can survey large areas rapidly with high resolution. Demonstrations of the U.S. Army Engineer Waterways Experiment Station (WES) Remote Minefields Detection System (REMIDS) airborne system have successfully located and mapped surface UXO (Bennett 1995). Since surface UXO and large concentrations of surface ordnance debris are indicators of the possible presence of buried UXO, airborne imaging survey systems such

as REMIDS, possibly augmented with additional sensors, can make a major contribution to the *screening* stage for location of buried UXO fields.

The second stage in the sensing hierarchy involves the *detection* of buried UXO. General purpose detection of buried UXO requires the application of ground surface geophysical surveys to detect geophysical anomalies caused by the buried UXO. Detection of buried UXO is identified as a major technology shortfall in numerous recent studies and field demonstrations (e.g., Johnson et al. 1996, U.S. Army Environmental Center (USAEC) 1994, Office of the Secretary of Defense (OSD) 1997), and is a considerably more difficult problem than surface UXO mapping. *Discrimination* of anomalies likely caused by ordnance-like targets from “false alarm” anomalies caused by other buried objects (particularly metallic objects) and geologic features is even more difficult.

Past research, development and demonstration efforts to address the buried UXO problem have been disjointed and have concentrated on adaptations of off-the-shelf technology and demonstrations at test sites. The present work is the initial investment by the Strategic Environment Research and Development Program (SERDP) to address technology shortfalls in buried UXO detection and discrimination. On-going and new SERDP efforts will continue the investment in detection and discrimination and initiate study of UXO identification. UXO *identification (classification)* is the final step in UXO sensing, and consists (a) of determining the specific type of ordnance that most likely produces a given ordnance-like anomaly and ultimately (b) of confirming the presence of explosives associated with buried ordnance-like objects. This report documents initial efforts to develop procedures for data integration and interpretation of multisensor (multimethod) datasets for UXO detection and discrimination.

UXO Detection, Discrimination, and Identification: Status

The status of capability for buried UXO detection, discrimination, and identification is summarized as follows: (a) *can detect UXO, within definable limits*; (b) *cannot effectively discriminate UXO anomalies from “false alarm” anomalies*; (c) *cannot identify UXO*. The definable limits for item a refer to combinations of ordnance size and burial depth that result in geophysical anomalies at the surface which can likely be detected relative to site-specific background noise (geologic background and cultural clutter). “False alarm” anomalies are caused by buried ordnance debris, other metallic objects, gravel and cobbles, soil heterogeneities, tree roots, and other natural and cultural features. Without significant discrimination capability, large numbers of false alarms that must be verified (dug up) are the dominant cost and time drivers for UXO site cleanup (remediation).

The results of recent field demonstrations, such as the Jefferson Proving Ground (JPG) Technology Demonstrations (USAEC 1994, 1995, 1996, 1997; Altshuler et al. 1995), exhibit buried ordnance detection probabilities exceeding 90 percent by Phase III (as shown in Tables 1 and 2). However, even with

Table 1 A Synopsis of JPG UXO TD Phase II Results				
(160 UXO Targets Buried for Phase II)				
Demonstrator	Targets Reported	Ordnance Detection Rate (%)	"False Alarms" Per Hectare	No. False Alarms Per Ordnance Item Detection
Geophex	398	71	19.7	3.41
Geometrics	521	83	26.9	3.96
Parsons	602	85	32.5	4.68
Bristol	566	62	38.3	6.97
ADI (Combined)	598	65	34.5	9.35
Coleman	280	29	15.9	9.56
Scintrex	255	50	45.3	10.10
GeoPotentia	168	11	12.0	13.00
Geo-Centers	1,409	72	84.0	20.70
Vallon	1,903	57	225.9	68.00

Table 2 A Synopsis of JPG UXO TD Phase III Results				
Artillery and Mortar Range (Scenario 2) (117 Targets -- 67 Ordnance; 50 Nonordnance)				
Demonstrator	Targets Reported	Ordnance Detection Rate (%)	"False Alarms" Per Hectare	No. False Alarms Per Ordnance Item Detection
NAEVA	202	97	19.0	1.37
Geophex	174	67	21.1	2.20
Geometrics	282	90	38.4	3.00
Ensco	279	70	43.6	4.34
Geo-Centers	486	93	80.7	6.10
ADI	456	85	76.8	6.32
Rockwell	151	21	27.1	9.07
GeoPotential	23	3	4.3	10.00
GRI	1,319	90	258.2	20.15

ordnance detection improving to acceptable rates, the number of false alarms is unacceptably high, i.e., poor discrimination capability. For JPG Phase II, four demonstrators had ordnance detection rates > 70 percent; the number of false alarms for each ordnance item detected, however, ranged from 3.4 to 20.7 for these demonstrators (Table 1). Although JPG Phase III was considerably easier for ordnance detection than Phase II in that the ordnance items were consistently shallower (Figure 1), it is notable that ordnance detection rates improved considerably. Four demonstrators for JPG Phase III *Scenario 2*

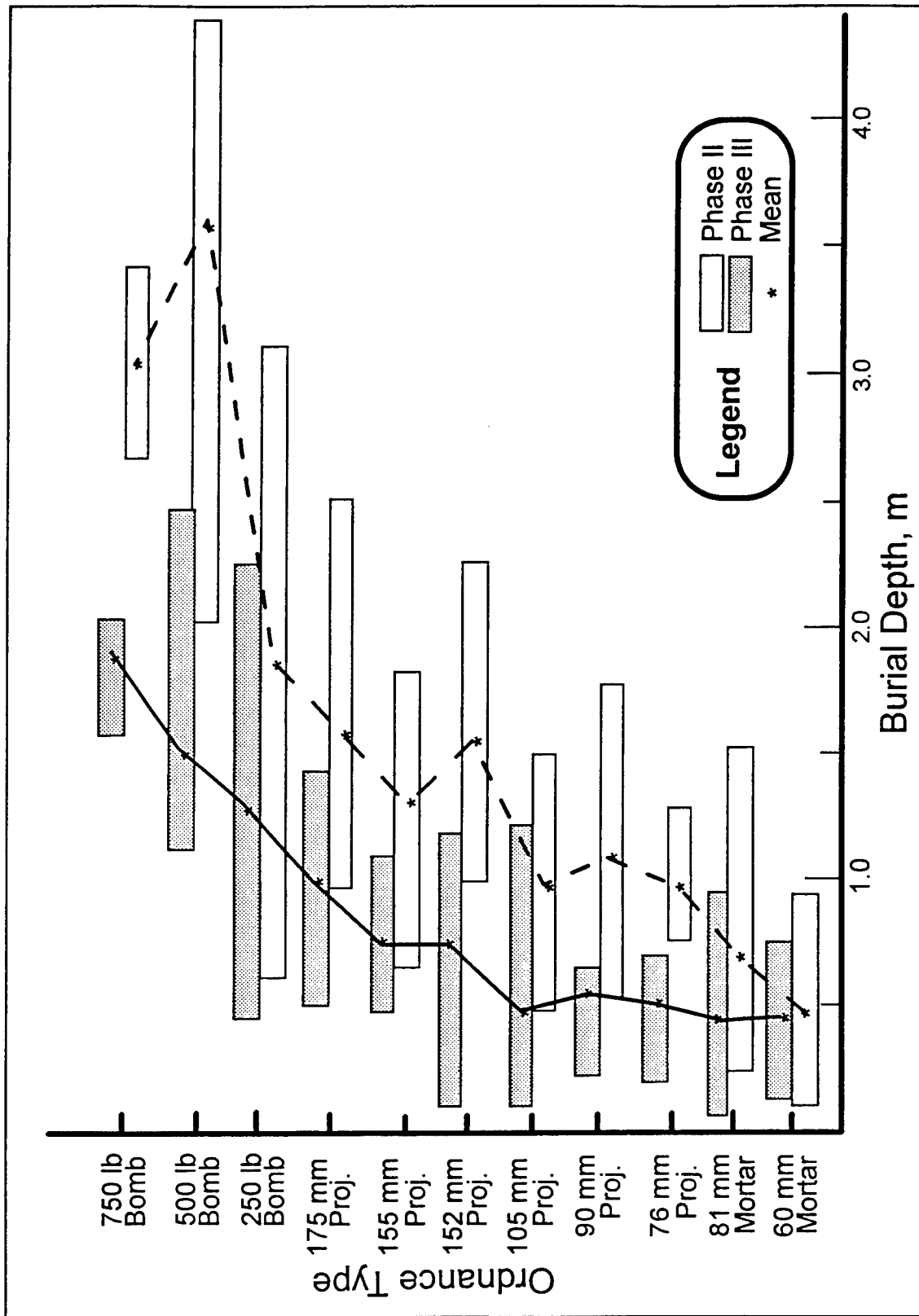


Figure 1. Comparison of ordnance target burial depths for JPG Phases II and III

(Table 2) had ordnance detection rates ≥ 90 percent; but the numbers of false alarms per ordnance item detected ranged from 1.4 to 20.2, still unacceptably high although showing some improvement. The JPG and other field demonstrations exhibit limited capability for ordnance identification or classification (item *c* above). Even classification into broad ordnance categories, such as bombs, projectiles, and mortars, is not reliably possible with current fielded detection systems. Capability for verification of explosive content in *buried* ordnance does not exist.

UXO Detection, Discrimination, and Identification: Approaches

Detection of UXO can be achieved with single or multiple geophysical method (single- or multisensor) approaches. Single-sensor (total field magnetometers or electromagnetic induction systems) approaches have demonstrated probabilities of ordnance detection > 75 percent, however most demonstrators use a multisensor approach. Generally, demonstrators with considerable field experience with geophysical methods and the interpretation of geophysical data exhibit consistently better UXO detection performance in both demonstrations and live site surveys. Geophysicists have long recognized the value of integrated, complementary, multimethod approaches for a variety of subsurface detection and mapping objectives. Complementary geophysical methods measure parameters affected by different physical properties of the subsurface. Detection of UXO requires high-quality data collection efforts with special attention to accurate positioning of measurements. The next requirements for UXO detection consist of a procedure for selection of anomalies and a decision criteria for target declaration. For multisensor datasets, the anomaly selection criterion may be a requirement for coincident anomalies on two (or more) complementary datasets. The final requirement is to interpret the single- or multisensor datasets for information about the target, e.g., map position, estimated depth, and ferrous mass.

There is a general consensus that measurements with *presently fielded single-sensor geophysical systems* do not contain sufficient information to allow discrimination of UXO anomalies from false-alarm anomalies. General-purpose anomaly discrimination requires multisensor data acquisition using two or more complementary geophysical methods or the use of emerging geophysical systems which measure much more information about anomalies in terms of time variation effects, frequency variation effects, or spatial gradients of fields. The emerging geophysical systems can be described as multichannel, multifrequency, and/or multicomponent. Indeed a multicomponent measurement system can be considered a multisensor system, even if the same physical parameter is measured along different spatial directions. The most important step for UXO discrimination is multisensor data integration and interpretation (sometimes called "data fusion"). A key requirement for successful multisensor discrimination is the development of innovative discrimination algorithms. The different approaches to and levels of sophistication of data integration and interpretation are discussed in Chapter 2.

Identification or classification of UXO anomalies as specific ordnance types requires the development of new and innovative geophysical technology. A

possible approach may be the detection of characteristic acoustic or electromagnetic resonance responses that allow identification; this approach will most likely be applicable to localized interrogation of the subsurface beneath previously detected anomalies. More challenging will be the definitive verification of explosive content in the target. Explosive detection will require that the ordnance be either extremely shallow or that a sensor probe be placed in close proximity to a previously detected target identified as likely UXO. Possible sensor approaches for explosives detection include neutron activation, neutron backscatter, or soil gas analyses. *For convenience, the acronym UXO is often used rather loosely in this report to refer to an ordnance item, whether inert or truly an unexploded ordnance (UXO). All of the ordnance items at test sites referenced in Chapter 3 ("Data Sources for the Investigation") are inert.*

Scope of Report

Chapter 2 briefly surveys the geophysical methods commonly utilized for UXO detection and discrimination, discusses the fundamental physics and phenomenology concepts, and surveys the approaches to multisensor integration and interpretation. Sources of data for this investigation are described in Chapter 3. Analysis methods for data management and detection enhancement are discussed in Chapter 4, and a synopsis of current UXO detection capability is presented in Chapter 5. Chapter 6 describes efforts to develop fundamental phenomenological modeling capability for UXO. Chapter 7 presents the results of investigations of UXO detection and discrimination utilizing emerging geophysical technology, and conclusions and recommendations are outlined in Chapter 8.

2 Geophysical Methods and Multisensor Interpretation Approaches

Geophysical Methods for UXO Detection and Discrimination

For completeness, a brief overview follows of the geophysical methods, concepts, and applications rationale for buried UXO detection and discrimination. Currently, most *live site* UXO detection surveys utilize total field magnetic and/or electromagnetic (EM) induction methods. Often the magnetic surveys include measurement of the total field vertical gradient. Demonstrations at *test sites* have included ground penetrating radar surveys, various emerging electromagnetic induction systems, various emerging magnetic systems, and airborne surveys. Generally, ground penetrating radar (GPR) surveys for UXO detection have been unsuccessful due to inappropriate site conditions (high EM attenuation and/or high background clutter) for application of radar, inappropriate selection of radar system parameters, inexperienced personnel, or a combination of these factors. Airborne surveys for detection of buried UXO (say > 10 cm deep) have been spectacularly unsuccessful; evidence from the JPG demonstrations failed to indicate any detection capability for airborne systems (Altshuler et al. 1995, USAEC 1996). Additional geophysical methods proposed for application to UXO detection and discrimination include microgravimetry and acoustic/seismic systems.

Geophysical methods interrogate or probe the physical properties of subsurface materials and specifically detect the presence of contrasts in physical properties of subsurface materials. The geophysical techniques are classified in Figure 2 based on the nature of the “energy source” for the method and on the nature of the physical phenomenon that is exploited. The potential fields methods, for example, are generally passive and involve measurement of natural or preexisting potential fields, e.g., the earth’s gravitational and magnetic fields. Practical application of the potential fields methods detect anomalies in the fields caused by “localized” contrasts in physical properties of subsurface materials (e.g., density contrast for the gravity method). EM methods are both active and passive; although methods applicable to UXO detection are active, in that an EM transmitter is part of the system.

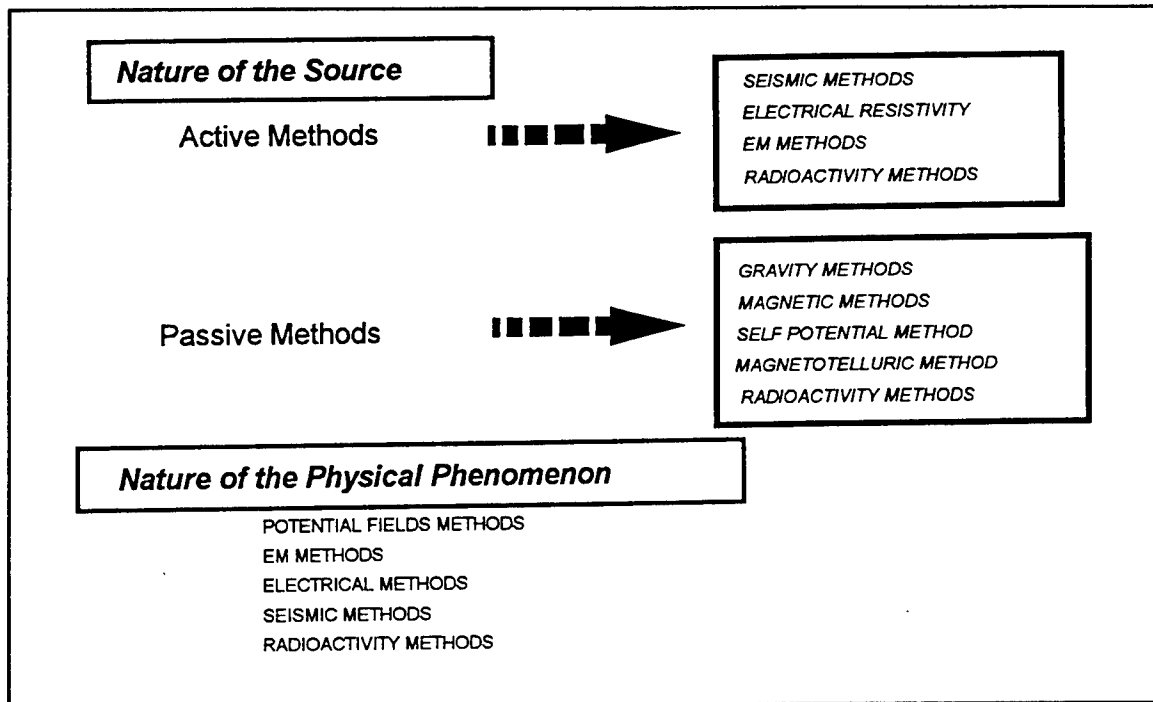


Figure 2. Classifications of geophysical methods

Measurements during geophysical surveys are generally in basic units, e.g., distance, time, voltage, current, magnetic field strength, or meter units. The process of converting measured quantities to interpreted parameters, in terms of a subsurface model, an image of the subsurface, or surface maps of individual parameters, is illustrated in Figure 3. Proceeding from the calculated parameters to the interpretation stage requires some form of modeling and an understanding of fundamental concepts and phenomenology. While it may be possible to produce surface anomaly maps directly after the measurement or calculated parameters stages, it is not possible to achieve a rigorous multi-method interpretation without fundamental phenomenological understanding of the methods. A synopsis of the major geophysical methods, concepts (key principle), measured quantities, the key physical parameters, and the interpreted parameters is shown in Figure 4. Finally, the tabulation below lists the geophysical methods likely to be encountered in UXO detection and discrimination efforts and gives abbreviations which will be used subsequently in this report:

Geophysical Methods and Abbreviations	
I. EMI – Electromagnetic Induction Methods	
FDEM – Frequency domain EMI; quadrature and in-phase component measurement; single-frequency; multifrequency; multicomponent	
TDEM – Time domain EMI; transient decay signatures; single-channel (gate); multichannel; multicomponent	
II. Magnetic Methods	
TFM – Total field magnetic	
TFG – Total field vertical magnetic gradient	
III. GPR – Ground Penetrating Radar	
Pulse (time domain), CW (frequency domain), chirp, etc., systems	
IV. Microgravity Methods	
V. Seismic or Acoustic Methods	

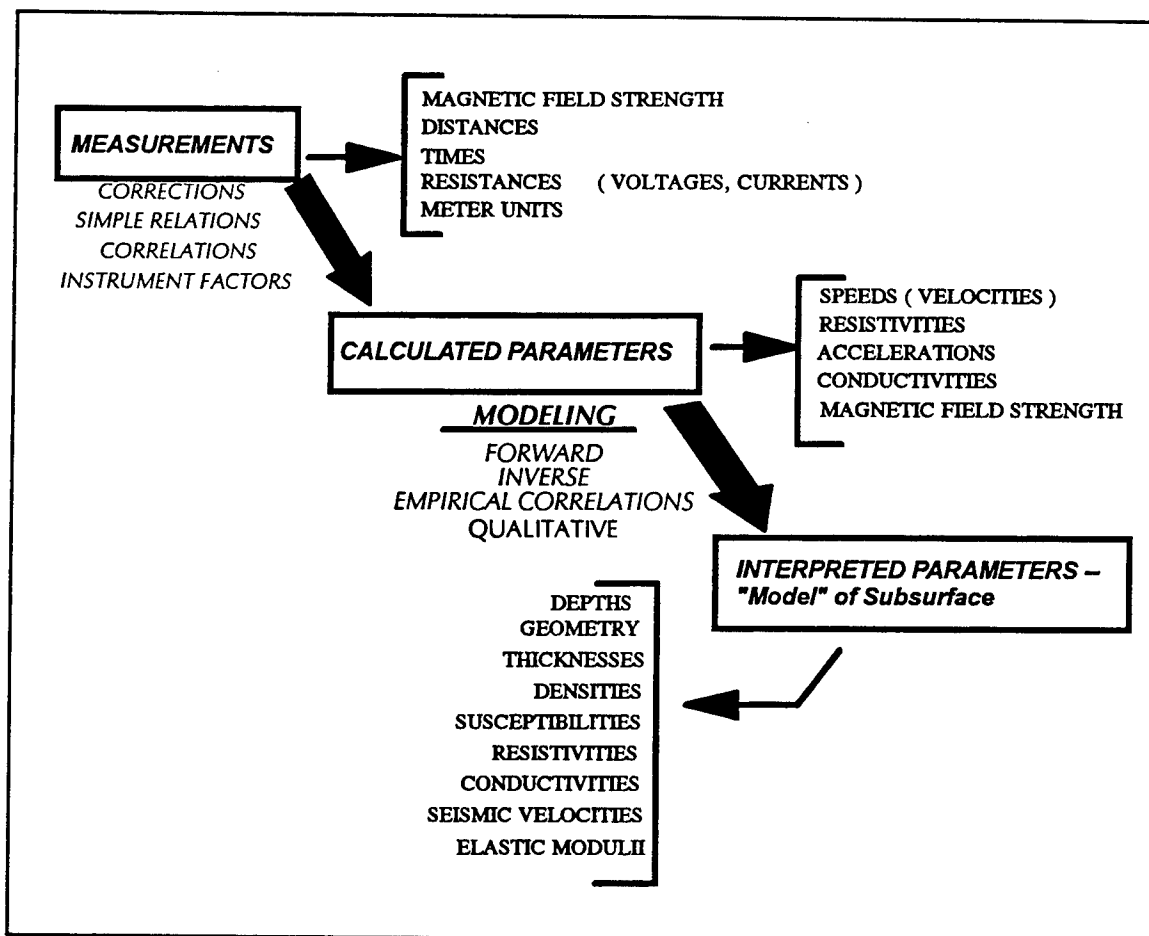


Figure 3. Concept of geophysical measurements and their transformation to interpreted parameters

Surveys including two or more of the methods discussed above are multi-method or multisensor surveys or approaches to characterization of the subsurface. Characterization includes detection and discrimination as defined for UXO. The methods from the tabulation above (main categories) or from Figure 4 are termed complementary methods, when the methods respond to different key physical properties or sets of properties. In this sense, a survey with magnetic and EMI methods would be a multisensor, complementary methods survey. However, a survey with FDEM and TDEM methods would be multisensor but not a complementary methods survey (Butler 1986, Butler and Fitterman 1986). Also, a survey with a multiaxis TDEM system is considered multisensor but does not constitute complementary measurements.

METHOD	PRINCIPLE	MEASUREMENT	KEY PHYSICAL PROPERTY	INTERPRETED PARAMETERS
MAGNETIC	DETECTION OF VARIATIONS IN THE EARTH'S MAGNETIC FIELD CAUSED BY LOCAL VARIATIONS IN MAGNETIC PROPERTIES OF SUBSURFACE MATERIALS	MAGNETIC FIELD STRENGTH	MAGNETIC SUSCEPTIBILITY	DEPTH, GEOMETRY AND MAGNETIC SUSCEPTIBILITY OF LOCALIZED SUBSURFACE FEATURE
GRAVITY	DETECTION OF VARIATIONS IN THE GRAVITATIONAL FIELD OF THE EARTH CAUSED BY ANOMALOUS MASSES	RELATIVE DISPLACEMENTS OF MASS ON A BEAM	DENSITY	DEPTH, GEOMETRY, AND DENSITY OF LOCALIZED SUBSURFACE FEATURE
ELECTROMAGNETIC INDUCTION	SECONDARY MAGNETIC FIELDS ARE PRODUCED BY INDUCED CURRENTS IN SUBSURFACE CONDUCTORS (Transient and CW Sources)	MAGNETIC FIELD STRENGTHS, VOLTAGES, TIMES, DISTANCES	ELECTRICAL RESISTIVITY, MAGNETIC SUSCEPTIBILITY, DIELECTRIC PERMITTIVITY	DEPTH, THICKNESSES, GEOMETRY, CONDUCTIVITIES
GROUND PENETRATING RADAR	EM WAVES PROPOGATE THRU GEOLOGIC MEDIA WITH SPEEDS DEPENDENT ON EM PROPERTIES OF MEDIA, AND REFLECT AND REFRACT AT INTERFACES BETWEEN DIFFERENT MEDIA	DISTANCES, TIMES AND AMPLITUDES	ELECTRICAL RESISTIVITY, MAGNETIC SUSCEPTIBILITY, DIELECTRIC PERMITTIVITY	EM SPEEDS, DEPTHS, THICKNESSES, GEOMETRY
ELECTRICAL RESISTIVITY	ELECTRICAL CURRENT FLOW THRU GEOLOGICAL MEDIA CONTROLLED BY PROPERTIES OF THE MEDIA – SOIL/ROCK TYPE, POROSITY AND PORE FLUID TYPE/CONTENT	CURRENTS, VOLTAGES AND DISTANCES	ELECTRICAL RESISTIVITY	DEPTHS, THICKNESSES, ELECTRICAL RESISTIVITIES, POROSITY
SEISMIC	SEISMIC OR ELASTIC WAVES PROPOGATE THROUGH MEDIA WITH SPEEDS DEPENDENT ON MECHANICAL PROPERTIES AND REFLECT AND REFRACT AT INTERFACES	DISTANCES, TIMES AND AMPLITUDES	COMPRESSIONAL- AND SHEAR-WAVE SEISMIC VELOCITIES (DENSITY, ELASTIC MODULI)	DEPTHS, LAYER VELOCITIES, GEOMETRY / STRUCTURE, ELASTIC MODULI

Figure 4. Geophysical methods, measurements, and interpreted parameters.

Multisensor Data Interpretation Approaches for UXO Detection and Discrimination

Classically or traditionally, geophysicists have achieved multisensor (multi-method) data interpretation in an ad hoc, empirical manner, which relied extensively on knowledge of phenomenologies and experience. The data from each survey method are interpreted individually and then integrated with each other and with any available geological ground truth to form an interpreted model of the subsurface (e.g., Butler et al. 1996). Various types of analysis and data management tools have been developed to aid the interpretation process. The formal interpretation of a given dataset is known as geophysical inversion, where an earth model is deduced directly from data. In its most rigorous form, geophysical inversion produces a best-fit model to the data in a statistical sense. Frequently geophysical inversion proceeds from the assumption of an initial model; the physical properties and dimensions of the model are adjusted to achieve a best-fit to the data (Parker 1994, Meju 1994, Butler et al. 1982). It is after the point of achieving an interpretation of the individual datasets that integrated interpretation has traditionally started. Procedures and capabilities for achieving true, formal joint inversion of multisensor datasets are rapidly emerging (e.g., Sandberg 1990, Dobroka et al. 1991, Lavelly and Grimm 1997). The following sections survey the approaches to multisensor data interpretation, proceeding from the empirical approach to true joint inversion.

Empirical interpretation procedures for complementary, multisensor datasets

The ad hoc, empirical approach to multisensor interpretation relies on considerable knowledge of the phenomenologies of the geophysical methods and experience of the interpreter. Geophysical survey programs are conducted with specific objectives, e.g., groundwater exploration, cavity detection, UXO detection, etc. The geophysical methods used for the programs are selected with knowledge of the physical nature of the subsurface targets (e.g., saturated porous media, air- or water- or clay-filled cavity, localized metallic, conductive object), the expected depth or depth range, the anticipated target size and geometry, and the nature of the geologic material above and/or surrounding the target. Data from each survey method are interpreted using well-established approaches (Telford, Geldart, and Sheriff 1990, Burger 1992, Headquarters, U. S. Army Corps of Engineers (HQUSACE) 1995). Empirical relationships, "rules-of-thumb," and past experience with similar problems then guide the multimethod interpretation process, such as Ohm's law, Archie's relationships, porous media density model, Wylie's time average equation for seismic velocity in porous media, simple dipole magnetic field model, and tabulations of seismic velocity, electrical resistivity, magnetic susceptibility, and dielectric permittivity of geologic materials (see for example, Sheriff 1991 and Carmichael 1989, for definitions and discussions of these concepts).

A common problem in geophysics is to interpret soil and/or rock type and condition for a given layer in a layered model of the subsurface. Seismic refraction and electrical resistivity survey results are commonly interpreted in the form of a layered model. Using the empirical tools discussed previously, a qualitative interpretation of the soil and rock type and condition can be inferred

from joint consideration of the seismic compression wave velocity and the electrical resistivity. The basic concepts of qualitative geologic interpretation are illustrated in Figure 5, although real geologic conditions may differ from the indications in the figure.

Another illustration of the empirical approach to integrated interpretation of geophysical survey data, and one more closely related to UXO detection (i.e., localized anomalies) and discrimination, is the problem of cavity detection (Butler 1994). Subsurface cavities can be manmade (tunnels and mines) and natural (caves, caverns, and fissures in karst areas). The cavities can be air-, clay-, or water-filled, and tunnels can be lined and contain metal. Common features on the weathered surface of limestones in karst areas are limestone pinnacles and clay-filled grikes (areas between two pinnacles or dissolution features in top of rock; Franklin et al. 1981). Figure 6 contains examples of qualitative interpretation of localized anomalies in a karst region geophysical site characterization (Butler 1983). An important concept of geophysical interpretations is that frequently there are ambiguities or uncertainties. Often the ambiguity may be significantly reduced by consideration of additional sources of information. However, there will always be some degree of fundamental or inherent ambiguity in geophysical interpretations, and only when direct investigation of the subsurface is conducted, can ambiguity be totally removed (Butler et al. 1996, Simms and Butler 1992, Simms, Butler, and Powers 1995).

Finally, Figure 7 illustrates the procedure for qualitative interpretation of UXO-like, localized anomalies in geophysical survey results. As with the previous example, there is ambiguity in the interpretation of UXO-like anomalies. Spatial properties of the anomalies (e.g., spatial wavelength) are used to estimate depths and infer geometries and orientations. With experience, the geophysicist (or data analyst) can become proficient at discriminating UXO anomalies from false-alarm anomalies, but it is a slow and painstaking process. And even with an experienced interpreter, ambiguity (false alarms) cannot be eliminated.

Analysis and data management tools for multisensor data integration and interpretation

Analysis and data management tools are key links between field acquisition of large datasets and integrated multisensor interpretation. Approaches vary from custom-designed analysis and data management software, developed to support specific sensor systems or platforms (e.g., McDonald and Robertson 1996), to the use of commercially available software, where the field data are reformatted as necessitated by software input requirements. Modern graphics software are invaluable for visualizing geophysical survey data over areas. Line contour plots/maps, shades of gray maps, full color maps, and shaded relief maps greatly enhance capability for detecting anomalies and data trends. Multisensor datasets, particularly when collected separately or at different times, may not be exactly spatially co-located. For example, EMI and magnetic survey datasets, even if collected at the same survey line spacing, may have different measurement spacings along the lines. Also, the survey lines

Example of Empirical Integration of Complementary Geophysical Datasets

Geologic Interpretation

<u>Seismic Velocity</u>	<u>Electrical Resistivity</u>	<u>Qualitative Interpretation</u>
High	High	Impermeable Rock.
High	Intermediate	Rock. Possible aquifer.
High	Low	Rock. Possible aquifer; probably brackish.
Intermediate	High	Dry, unconsolidated sediments at depth; or weathered or fractured rock.
Intermediate	Intermediate	Possible aquifer in unconsolidated sediments; or weathered Rock.
Intermediate	Low	Clay or aquifer with brackish water.
Low	High	Dry unconsolidated sediments; no clay.
Low	Intermediate	Unconsolidated, wet sediments.
Low	Low	Wet, clayey sediments; or brackish saturated, unconsolidated sediments.

Seismic Velocity -- High (> 3,000 m/s); Low (<1,000 m/s)

Electrical Resistivity -- High (>300 Ohm-m); Low (< 10 Ohm-m)

Figure 5. Empirical integration of complementary geophysical datasets for geologic interpretation

Example of Empirical Integration of Complementary Geophysical Datasets

Geologic Feature Interpretation in Karst Region

<u>Gravity Anomaly</u>	<u>Electrical Resistivity</u>	<u>Magnetic Anomaly</u>	<u>Qualitative Interpretation of Features</u>
↑ Low	Low	High	Clay pocket or grike (at the top of rock) or Clay-filled sinkhole
Low	High	None	Air-filled cavity
Low	Low	High	Clay-filled cavity
High	High	None or relative low	Limestone Pinnacle

↑ Indicates ambiguity. Additional information required,
e.g., spatial characteristics of anomalies.

Figure 6. Empirical integration of complementary geophysical datasets for feature interpretation in karst regions

**Example of Empirical Integration
of Complementary Geophysical Datasets**
Simplistic Assessment UXO-Like, Localized Anomaly

<u>EMI Anomaly</u>	<u>Magnetic Anomaly</u>	<u>Qualitative Interpretation of Features</u>
None	None	No UXO present or UXO buried too deep to be detected in presence of site noise
High	None	Conductive feature, possibly non-ferrous metallic object
None	High	Ferrous metal object, buried too deep for EMI detection
High	High; High/Low*	Ferrous metal object; possibly UXO
Long, linear-trending anomalies (Highs and Lows)		Likely cultural in origin
Large-area, irregular shaped anomaly features (highs and lows)		Likely geologic in origin

*** Generally, closely spaced high/low pair, with low sometimes not apparent.**

Figure 7. Empirical integration of complementary geophysical datasets for UXO-like, localized anomalies

themselves may deviate somewhat between sensor types. Many types of integrated multisensor interpretation procedures work best or most efficiently with co-located multisensor data. A common procedure for achieving spatially co-located datasets is to fit the original datasets with individual "best-fitting" surfaces and then sample the surfaces at regularly spaced grid points. The subject of gridding is beyond the scope of this report; however, it is important to carefully consider the gridding procedure and its possible effects on trends and anomalies in the datasets (e.g., Gallagher 1989, Scollar et al. 1990, MacLeod and Dobush 1990, Bhattacharyya 1969). Modern graphics software can readily process large data volumes, fit the data with user-selectable surfaces (inverse distance weighting, minimum curvature, kriging, polynomial regression, etc.), and produce a regular grid of "data" values from the surface fits (e.g., Golden Software 1995, Geosoft 1996). In this manner, maps of the survey results for each sensor survey can be produced from gridded values that are co-located. The co-located multisensor datasets are then ready for integrated processing and interpretation. Often each sensor dataset may be individually processed in some way (e.g., background subtraction, image processing, various kinds of filtering operations, etc.) prior to integrated processing and interpretation. Some of the graphics software packages (e.g., Geosoft 1996) have relational links between the different sensor datasets and allow direct transition to simple types of integrated multisensor dataset analyses.

Geographic information systems (GISs) are ideal tools for management of multisensor datasets and all additional site information (e.g., topography, vegetation, surface clutter, etc.). Each sensor dataset and each additional type of site information are entered as separate map-planes in the GIS. Importantly, all of the map-planes are georeferenced. Most GIS's allow for input of any type of information with corresponding position tags (locations). Also, most GIS's allow for the procedures discussed in the preceding paragraph, i.e., can fit the sensor datasets with best-fitting surfaces and sample at regular grid points, to produce co-located multisensor datasets. A GIS includes relational database capabilities, so that one or more georeferenced map-planes can be queried to produce derived map-planes. For example, a typical query relevant to UXO detection and discrimination applications might include a derived map showing all locations where a geophysical anomaly (e.g., magnetic or EMI) is coincident in location with a mapped surface metallic object. Another example of a typical query is to produce a derived map showing locations (or areas) where coincident geophysical anomalies occur on two or more map planes (e.g., coincident magnetic and EMI anomalies). Often a derived map, such as described in the previous example, will be the final product of an integrated multisensor interpretation effort. Derived maps may also be functional combinations of two or more map-planes (sum, difference, or more complicated relationship). A GIS may also have linked or embedded expert systems or neural network classifiers (Burrough 1986, Millhouse et al. 1996).

Integrated multisensor interpretation

A common approach to multisensor interpretation is the use of forward modeling and comparison to measurements. For each geophysical method, forward modeling depends on postulating a model of the subsurface and then utilizing a physics-based empirical, analytical, or numerical approach for computing the predicted response of the postulated model. The forward modeling

can be manually or automatically iterated to achieve a fit or match of model prediction to measured data (a process known as geophysical inversion). Often the forward modeling software will compute a goodness of fit value (e.g., root-mean-square (rms) error) to the measured data, and automated inversion seeks to minimize a goodness of fit measure (Parker 1994, Meju 1994, Butler et al. 1982). Integrated interpretation occurs when the forward modeling procedure includes *inter*-method iteration as well as *intra*-method iteration or constraints.

For the most common suite of geophysical methods used for UXO detection surveys, TFM and TDEM, the following tabulation indicates some of the parameters involved in models for analytical or numerical forward modeling or as initial models for inverse modeling:

Magnetic Model	TDEM Model
Geometry (e.g., sphere or prolate spheroid)	Geometry (e.g., sphere, cylinder or prolate spheroid)
Length, Diameter	Length, Diameter
Depth	Depth
Inclination, Azimuth	Inclination, Azimuth
Magnetic Permeability of UXO	Electrical Conductivity of UXO
Magnetic Permeability of Soil/Rock	Electrical Conductivity of Soil/Rock
Earth's Magnetic Field Magnitude	EM Transmitter Dipole Moment
Earth's Field Inclination and Declination	Receiver Time Gate (or Gates)

Many of these parameters are known for particular cases and will be fixed (constant) for the forward modeling and manual iteration cycles. Geometrical considerations for these two models are illustrated in Figure 8, where the geometry for the magnetic and electromagnetic sources and for the UXO are shown. As discussed previously, the magnetic method is passive, using the earth's magnetic field as the source, and the resulting, induced anomalous magnetic field (superimposed on the inducing earth's field) is static. The EM methods are active and the resulting, induced anomalous electromagnetic field is time-varying, with frequency content (FDEM) or time decay characteristics (TDEM) dependent on the EM source characteristics. Since the electrical conductivity and magnetic permeability of UXO targets are generally much larger than surrounding geologic materials, the induced background responses from surrounding geologic materials are much smaller than the superimposed, anomalous responses from the UXO.

The most common approach to integrated multisensor interpretation involves feature and parameter extraction. Features or parameters are determined from analyses or inversions of measurements and then either used in parameter cross plots or for sequential input to other analyses or inversions (Bell and Barrow 1997). For example, if a localized anomaly is detected at approximately the same apparent location with both TFM and TDEM surveys, the feature causing the anomalies is both magnetically permeable and

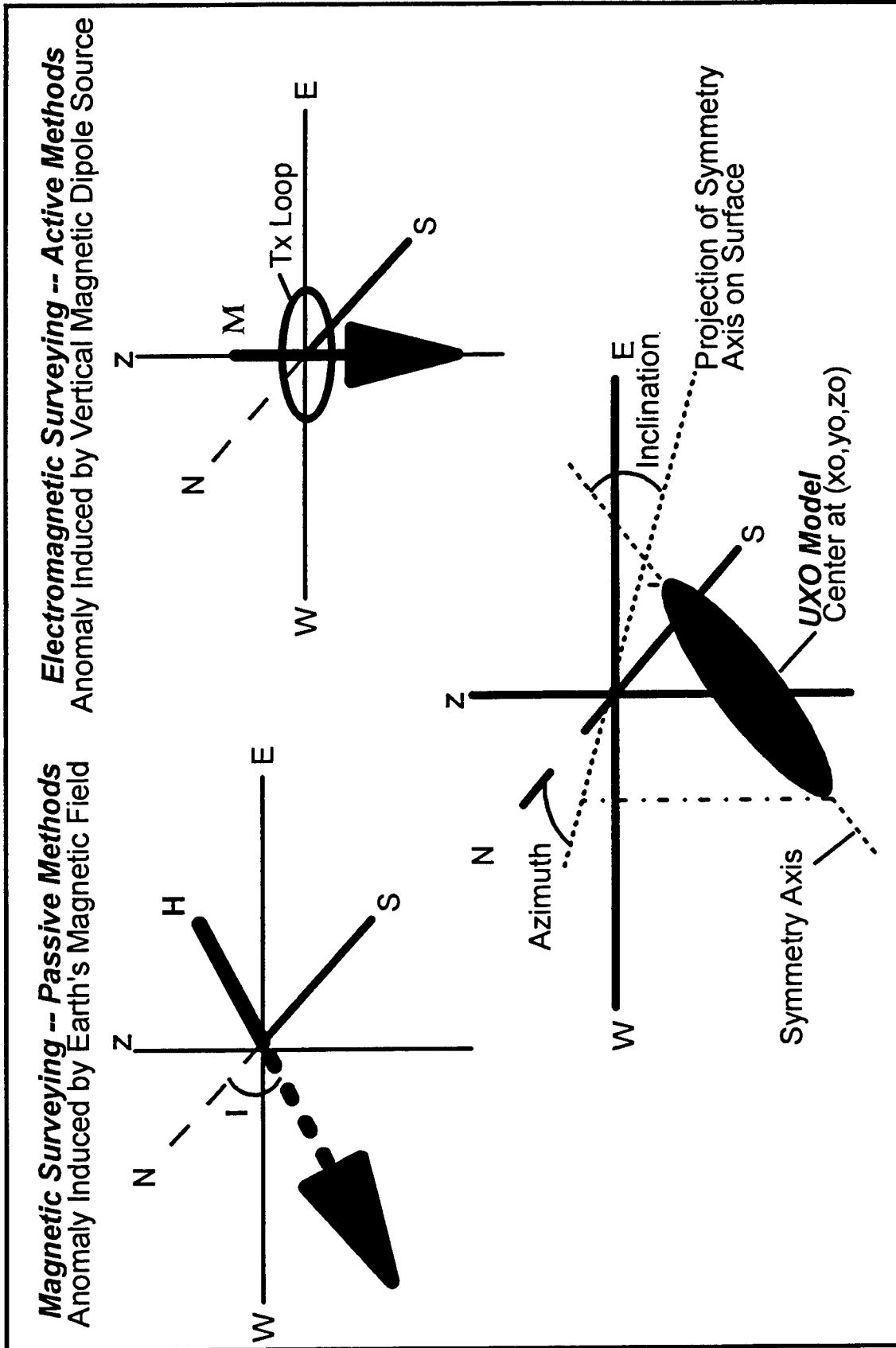


Figure 8. Geometrical considerations for UXO magnetic and electromagnetic anomaly response modeling

electrically conductive relative to the surrounding geologic materials and is potentially UXO. An integrated interpretation could consist of (a) determining the depth to the conductive objective from analysis of TDEM measurements and then (b) inputting the depth as a fixed or constrained model parameter during inversion of the magnetic data. The previous form of integrated interpretation can be considered a sequential inversion process or simplified joint inversion; a proposed algorithm for accomplishing sequential inversion of magnetic and TDEM data is presented later in this report (including an example). A hypothetical example of a parameter cross plot is shown in Figure 9, interpreted object mass versus interpreted object volume, from an analyses of coincident, localized gravity and magnetic anomalies, respectively. In principle, a parameter cross-plot could be used for both discrimination and identification. For example, two points in Figure 9, determined from inversion (interpretation) of gravity and magnetic data (asterisks), lie very close to points representing known UXO (solid circles), allowing identification of the buried object as a specific UXO. Another point in Figure 9, determined from inversion of gravity and magnetic data, lies outside the region of mass-volume space corresponding to known UXO, allowing discrimination of the buried object as non-UXO. Examples of various types of parameter cross plots are discussed later in this report.

Joint inversion

Joint inversion is the most rigorous and self-consistent procedure for achieving truly integrated interpretation of multimethod geophysical datasets (Meju 1994, Laveley and Grimm 1997). Rigor and self-consistency do not necessarily imply that joint inversion is the best or most efficient or most accurate approach to integrated interpretation of multisensor datasets for UXO discrimination and identification in all cases. However, the “best-fitting” model resulting from joint inversion of complementary datasets, e.g., TFM and TDEM data, will generally have considerably less ambiguity than single-method inversion or the various forms of integrated interpretation (e.g., sequential inversion) discussed previously. The complementary methods interrogate or “illuminate” the target in distinctly different manners. For UXO targets, intelligent estimates of material property parameters and of the contrast between the UXO and surrounding materials are possible. Also, the properties of the EMI source and the earth’s field are known. Thus, if the joint inversion utilizes a common geometric model for both datasets, e.g., a prolate spheroid, the number of parameters that must be determined in the joint inversion reduces to two intrinsic properties (length and diameter) and three extrinsic properties (depth, inclination, and azimuth). Joint inversion considerably improves the resolution and error of the model solution (Laveley and Grimm 1997), compared to single-method inversion for the same number of model parameters. Joint inversion has been attempted, with varying degrees of success, for gravity and magnetics, seismic and electrical resistivity, seismic and GPR, and electrical resistivity and TDEM. Joint inversion of TFM and TDEM datasets is a well-posed inversion problem; however, forward modeling capability for TDEM for realistic three-dimensional (3-D) UXO geometries (e.g., prolate spheroid) does not currently exist.

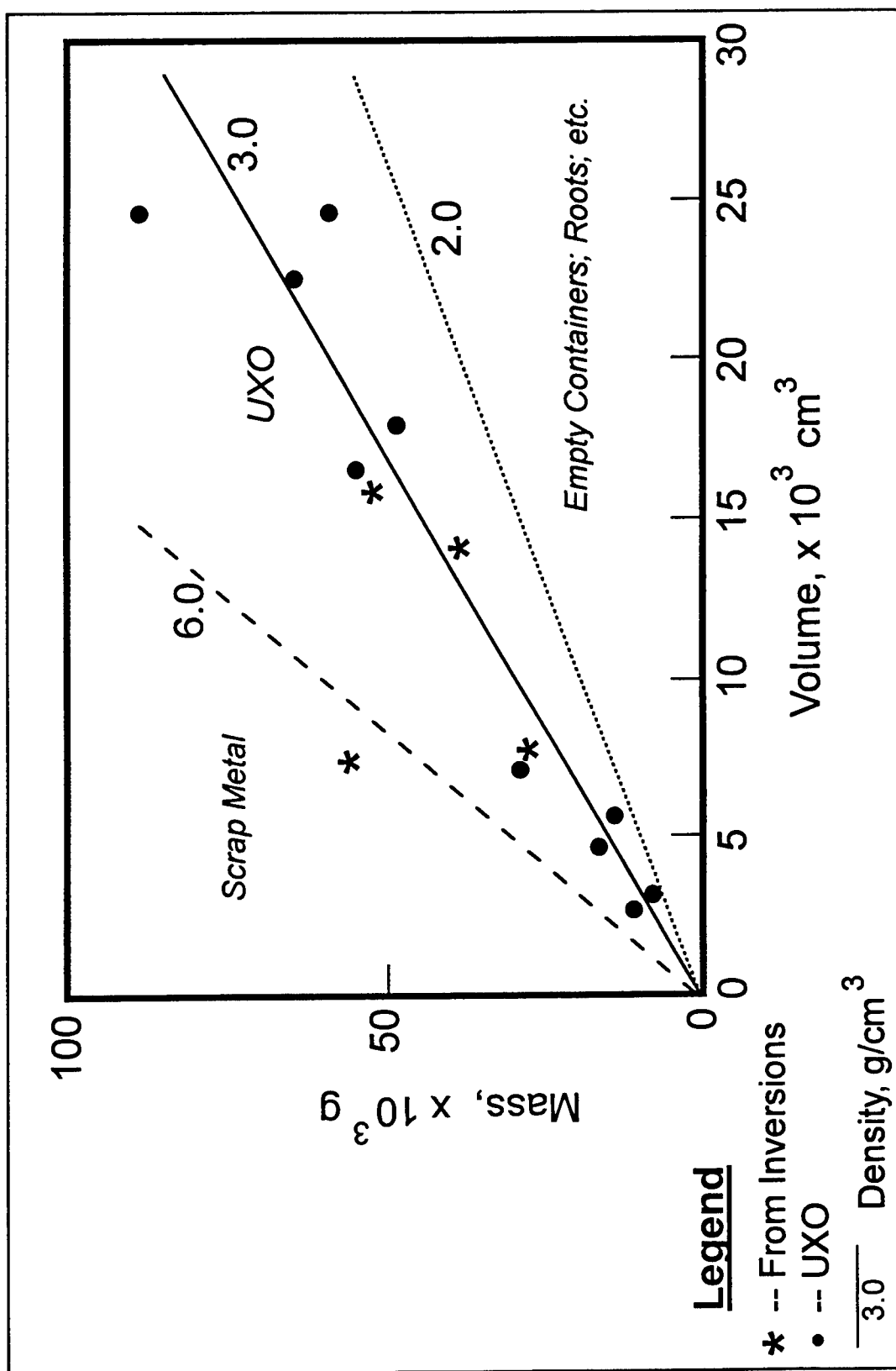


Figure 9. Cross plot of parameters derivable from gravity and magnetic datasets for UXO discrimination and identification

3 Data Sources for the Investigation

Key to the success of efforts to develop multisensor/multimethod interpretation are data signatures from known ordnance targets. There is a sparsity of published multisensor data, acquired over known ordnance targets. Initially this investigation planned to make extensive use of data from the JPG UXO Technology Demonstrations; however, the actual sensor data was not provided to the Government and the baseline ordnance item details were not released by the Government until after the primary period of execution of this investigation. Future data collected at JPG will be provided to the Government and baseline ordnance details will be available following the demonstrations. The JPG Phase III baseline data have now also been released. To remedy the lack of readily available multisensor datasets to support UXO detection, discrimination, and identification research, ordnance signature databases are actively being developed by Department of Defense agencies (Army, Navy, Defense Advanced Research Projects Agency (DARPA), and others), private industry, and universities. The sections below review the available ordnance signature datasets identified at the initiation of this project and efforts undertaken as part of the project to acquire well-controlled magnetic and acoustic ordnance signatures.

Development of WES Ordnance Signature Datasets

Early in this project, the requirement was established for geophysical signature datasets of known ordnance items to validate phenomenological modeling developments. The main thrust of the work was measurement of high-accuracy, high-resolution magnetic signatures of inert ordnance, using a single, stationary magnetometer, to support magnetic modeling capability development. A supplementary thrust was measurement of acoustic signatures over ordnance, to investigate persistent reports of the existence, diagnostic utility, and practical utility of acoustic resonances from ordnance (e.g., Baum 1996). The test facility is located in a wooded area on the campus of Wright State University, Dayton, Ohio. Ordnance items in the measurement study were: 60-mm mortar rounds, 81-mm mortar rounds, 90-mm artillery shells, 105-mm artillery shells and 155-mm artillery shells.

For the magnetic signature studies each ordnance item is placed in an orientable holder made of wood with non-magnetic metal fasteners. The center of the holder is orientable about a horizontal axis to allow positioning at any inclination. The holder is mounted on a turntable that allows orientation at any azimuthal angle relative to magnetic north. The site is a wooded area of campus; a preliminary magnetic survey determined the absence of magnetic anomalies. After the holder assembly is positioned and leveled, but before an ordnance item is placed in the holder, magnetic readings are taken along the track which holds the magnetometer. This gives background profiles that show the field to be very uniform.

For the initial set of magnetic measurements, the magnetometer sensor is moved in 10-cm increments along a track that is oriented north-south and is adjusted to hold the sensor 1.2 m above the center of the ordnance, except for the 60-mm mortar round for which a smaller height is used. Measurements are acquired with a proton precession magnetometer. Three readings are averaged at each position. A base station is established away from the zone of influence of the ordnance and readings are taken there at least once an hour. These readings are used to remove the effects of time-variation of the earth's field from the measured data.

In the initial series of TFM measurements, the 90-mm artillery shell was most extensively studied. For all of the items, the datasets include magnetic profiles measured along a profile across their center, with measurements at 10-cm spacing along the profile. This was done at the following combinations of inclination angle (relative to horizontal) and azimuthal angle (in degrees):

Inclination 0	Azimuth 0, 45, and 90
Inclination 30	Azimuth 0, 45, and 90
Inclination 60	Azimuth 0 and 90
Inclination 90	Azimuth 0

For the 90-mm artillery shell, the dataset also includes these measurements along north-south profiles offset by 40 cm and 80 cm from the center of the shell. After base station corrections and alignment adjustments, the resulting curves show smooth variation of the magnetic field along each profiles. There are major differences in the magnitude and shape of the profiles with ordnance orientation, such as illustrated in Figure 10 for measurements over a 105-mm artillery projectile. The TFM profiles are well-defined by the 10-cm measurements spacing, and the smooth profile curves indicate high accuracy measurements. Additional results of the ordnance magnetic signature measurements are given in Appendix A.

The acoustic studies are preliminary in nature and seek expression of characteristic acoustic resonances that might allow identification of various ordnance types. The same ordnance items listed above are studied, with two types of measurement approaches. In the first type, a microphone is placed near the item and the output of the microphone is input to a spectrum analyzer. The ordnance are struck with a hard object and the resulting sound spectrum recorded. The 90-mm and 105-mm projectiles produce characteristic resonances at 6.5 kHz and 5.8 kHz, respectively. However, the other three sizes

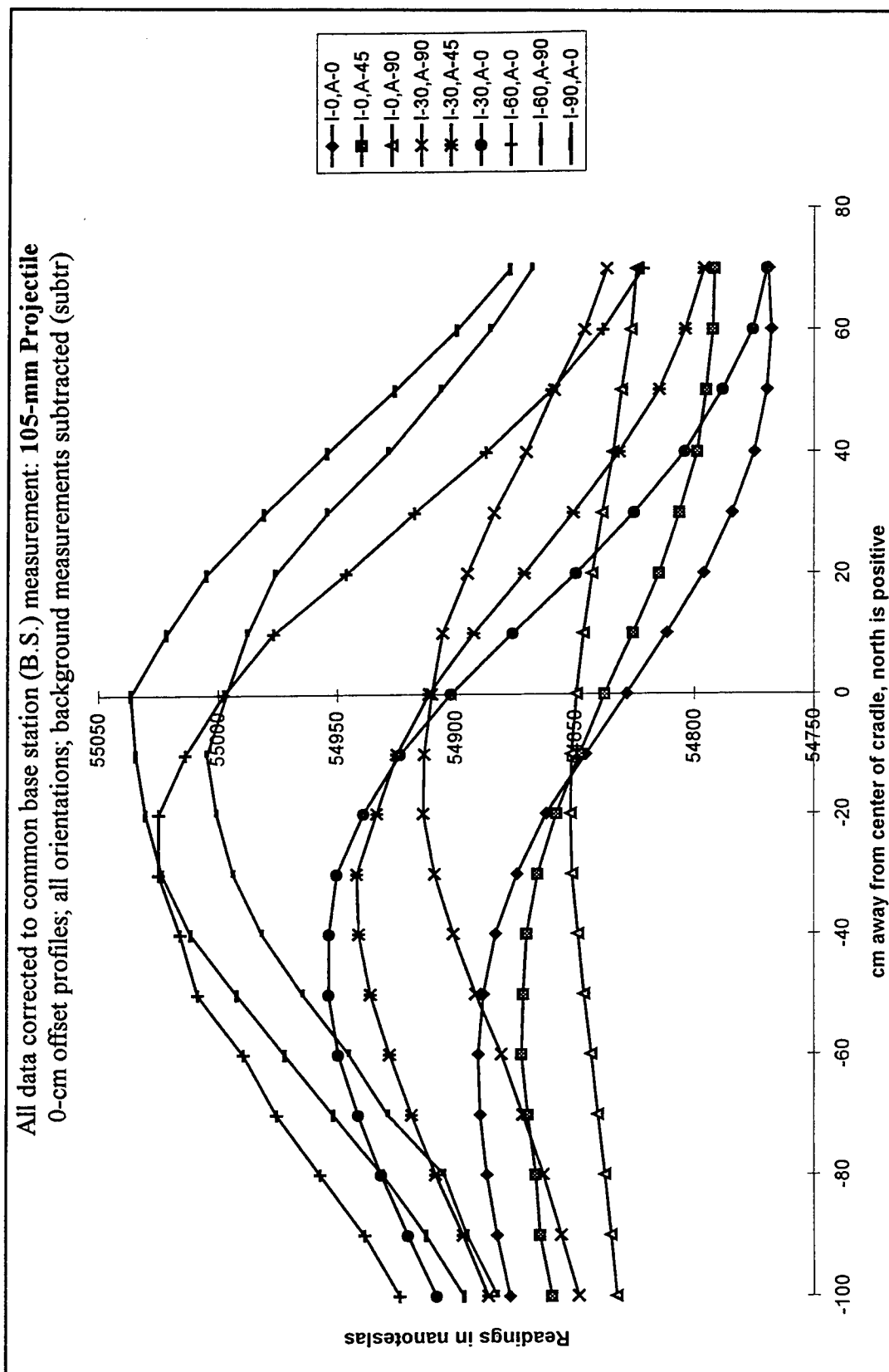


Figure 10. Example from WES ordnance signatures datasets; TFM measurements over center of 105-mm projectile, 1.2 m below sensor, and for nine orientations

do not produce obvious resonances that are strong and consistent between samples and relatively independent of the location of the strike.

For the second type of measurement, an item is placed in a home-made acoustic enclosure. A microphone is attached to the backside of the item and a speaker one meter away is swept through a range of frequencies from 3 kHz to 10 kHz. Again, the strongest, most consistent resonances are at the same frequencies as before for the 90 mm and 105 mm projectiles. Subsequently, the items were covered to various depths in wet and dry sand; with the perhaps intuitive result that the strength of the resonances progressively decrease as more of the item was covered.

Impulsive measurements in a container filled with sand or water likewise indicate that the resonance strengths progressively decrease as the items are more deeply buried. Preliminary and tentative conclusions of the acoustic tests, for the limited suite of ordnance tested, are that two ordnance types have characteristic resonances, but the resonances are too damped on burial to provide a viable identification technique for buried ordnance. A subsequent report will present the acoustic results in detail as well as all measured magnetic signatures.

Naval Research Laboratory (NRL) Ordnance Signature Library

The Multisensor Towed Array Detection System (MTADS) is the culmination of at least a decade of engineering development (McDonald and Robertson 1996). The MTADS has overcome many of the difficulties of multisensor integration on a towed platform. MTADS utilizes separate towed platforms to acquire high-resolution passive magnetic (eight TFM sensors or four TFG sensor sets) and active electromagnetic (three overlapping TDEM sensors) measurements. A differential global positioning system (DGPS) is used for primary navigation in the field. To support modeling and detection and discrimination algorithm development, an ordnance signature library is being developed using MTADS (Nelson, McDonald, and Robertson 1997, Barrow et al. 1997).

For development of the NRL ordnance signature library, MTADS sensors are used to acquire TFM, TFG and TDEM (Geonics EM61) datasets over inert ordnance placed on the surface, in a 1 m deep hole, and in a 7 m deep well. Special jigs hold the ordnance items at predetermined depths and orientations. Tables 3, 4 and 5 summarize the datasets from the signature library that were available from NRL for use in the present investigation. As an example, TFM and TDEM datasets from the NRL signature library for a 105 mm projectile (depth = 0.49 m; inclination = 0; azimuth = 90) are shown in Figure 11. The datasets in Figure 11 are shown as images, i.e., color-filled contour maps. The NRL ordnance library is used for phenomenology modeling validation (primarily TFM modeling) and for parameter cross-plotting investigations.

Table 3 Ordnance Items, Depths and Orientations, for the TFM Data Sets, NRL Ordnance Signatures Library			
Item	Depths	Azimuth	Inclination
20 mm projectile	Surface	0°, 90°	0°
30 mm projectile	Surface	0°, 90°	0°
M42 grenade	Surface, 15 cm	0°, 90°	0°
M46 submunition	Surface, 15 cm	0°, 90°	0°
60 mm mortar	0.25, 0.5 m	45° steps	45° steps
81 mm mortar	0.5, 0.75, 1 m	45° steps	45° steps
105 mm projectile	0.5, 0.75, 1 m	45° steps	45° steps
5-in. rocket	1, 1.5 m	45° steps	45° steps

Table 4 Ordnance Items, Depths and Orientations, for the TFG and EM61 Data Sets, NRL Ordnance Signatures Library					
Item	Gradiometer Survey			EM-61 Survey	
	Depths	Azimuth	Inclination	Depths	Azimuth and Inclination
20 mm projectile	Surface	0°, 90°	0°	Surface	0°, 90°
30 mm projectile	Surface	0°, 90°	0°	Surface	0°, 90°
M42 grenade	Surface, 15 cm	0°, 90°	0°	Surface, 15 cm	0°, 90°
M46 submunition	Surface, 15 cm	0°, 90°	0°	Surface, 15 cm	0°, 90°
60 mm mortar	0.25 m	45° steps	45° steps	0.25, 0.5, 0.75, 1 m	90° steps
81 mm mortar	0.5, 0.75 m	45° steps	45° steps	0.5, 0.75, 1 m	90° steps
105 mm projectile	0.5, 0.75 m	45° steps	45° steps	0.5, 0.75, 1, 1.25 m	90° steps
5-in. rocket	1 m	45° steps	45° steps	0.5, 1, 1.5 m	90° steps
155 mm projectile				1.5, 2 m	90° steps

DARPA Background Clutter Program

In addition to the preceding ordnance signature libraries developed in well-controlled, “laboratory-type” settings, two additional sources of well-controlled, multisensor datasets acquired in settings more “real world” are utilized in the investigation. The DARPA-sponsored Background Clutter Data Collection Experiment was designed to address a void in multisensor data collected specifically to characterize the natural background and manmade clutter at sites where buried UXO and landmines are typically found (George and Altshuler 1997). Within the limited scope of the effort, a variety of geologic settings was accommodated at four test sites at two geographic locations: Fort A. P. Hill, Virginia—two “wet, sand” sites, Firing Point 20 (FP20) and Firing Point 22 (FP22); Fort Carson, Colorado—a “dry, sand” site, Turkey Creek

Table 5
Mass and Dimensions of Ordnance Items, NRL Ordnance Signatures Library

Item	Length (cm)	Diameter (cm)	Mass (kg)
60-mm mortar	35.6	6.0	1.0
81-mm mortar	42	8.1	2.3
2.75-in. rocket	33	7.0	4.1
4.2-in. mortar	45	10.7	8.6
105-mm projectile	39	10.5	9.5
5-in. rocket	49	12.7	20
155-mm projectile	62	15.5	25.4
Mk81 bomb (250 lb)		23.0	56.7
8-in. projectile	78.7	20.3	73.9
Mk82 bomb (500 lb)	156	28.0	113
Mk83 bomb (1000 lb)	191.5	36.6	227

Site, and a “dry, clay” site, Seabee Site. Each test site was a standard 125 m × 100 m with a central 100-m × 100-m background area (Center Square). The only *emplaced* objects in the Center Square were five sets of registration targets, each set consisting of a buried iron sphere and an aluminum plate spaced 4 m apart (an additional aluminum plate was placed on the surface midway between the buried sphere and plate for infrared (IR) data collection). On two sides of the sites, target sidebars were established, containing a variety of buried inert ordnance, inert landmines, and other objects. Inert ordnance targets consist of 60 mm and 81 mm mortars and 105 mm and 152 mm projectiles. The general site layout is shown in Figure 12. Details regarding target locations in the sidebars has not been released, except for the region noted as the Calibration Area in Figure 12 (shaded). Individual target locations and descriptions for the Calibration Area are shown in Figure 13 (George and Altshuler 1997).

Seven contractors obtained high-resolution multisensor data over the test sites. Although data density over the sites varied from one sensor system to another, typical data density is 10 to 20 cm along track, with 25- to 50-cm track spacing. Data acquired by Geophex, Geometrics, and Parsons were provided directly to WES and also to DARPA. All data acquired under the Backgrounds Data Collection Experiment are available on approximately 35 CD-ROM's, that are distributed for DARPA by Walcoff and Associates (George and Altshuler 1997). Although direct correlation of processed data with the baseline target cannot be presented in this report (except for the Calibration Area), the datasets are useful for illustrating target detection in general and for illustrations of data management and of “image processing” to enhance anomalies. The following tabulation briefly summarizes the types of sensor data collected at the test sites:

Sensor/Method	Contractor	Details
Magnetometry	Geometrics	Six Geometrics G-858 cesium vapor magnetometers. Mounted on cart; configured to give high-density total field magnetic and horizontal and vertical magnetic gradient.
	Geophex	Two-element Geometrics G-858 total field magnetometer system.
EMI	Coleman Research Corp	Three-element Geonics EM61 (TDEM) array (1-m Tx/Rx)
	Parsons Engineering Science, Inc.	Custom built, 0.5 m Tx and Rx, Geonics EM61 (TDEM).
		Prototype multichannel, multicomponent EM61-3D, with 1 m Tx and 3-orthogonal axis 0.5 m Rx (TDEM)
	Science Applications International Corp.	Array of eight overlapping Schiebel EMI coils (TDEM).
	Geophex	Prototype Multifrequency FDEM system, operated at 4,050 Hz and 12,270 Hz.
GPR	Coleman Research Corp.	GPR array (2 Tx, 3 Rx). Frequency domain; 2 MHz stepped-frequency over range 100 - 610 MHz. Additional Tx-Rx with 10 MHz stepped-frequency over range 1,000 - 4,000 MHz. Vehicle towed.
	Geocenters, Inc.	"Focused Array Radar" (4 Tx, 4 Rx). Frequency domain, swept frequency over range 700-1,300 MHz.
	Lawrence Livermore National Laboratories	Prototype GPR. Frequency domain over range 5 MHz - 18 GHz, with up to 801 steps. Operated in monostatic, cross-polarized mode.
IR	Geo-Centers, Inc.	Forward-looking system.
	Science Applications International, Inc.	Down-looking system.

Datasets from MTADS Surveys at the Magnetic Test Range, Twenty-nine Palms, California

Another well-controlled, "real world" multisensor dataset source is the MTADS survey results at the Magnetic Test Range (MTR) at Twenty-nine Palms, California (McDonald et al. 1997). The MTR is approximately 220 m \times 150 m (about 8 acres) in size. Table 6 lists the ordnance, number of items, and associated burial depth range of the 70 ordnance items buried at the site (from McDonald et al. 1997). Three complete surveys of the site are available: TFM, TFG, TDEM. For the TFM survey, the sensors were set 0.25 m above the surface, and data are acquired at approximately 0.06 m along track, with 0.25-m track spacing; while for the TFG survey, the sensors were reconfigured with sensor pairs at 0.40 m and 0.95 m above the surface and 0.5-m track spacing. The lower transmit/receive coils of the TDEM array (3 EM61's) were 0.40 m above the surface, and data are acquired approximately 0.15 m along track, with 0.5-m track spacing.

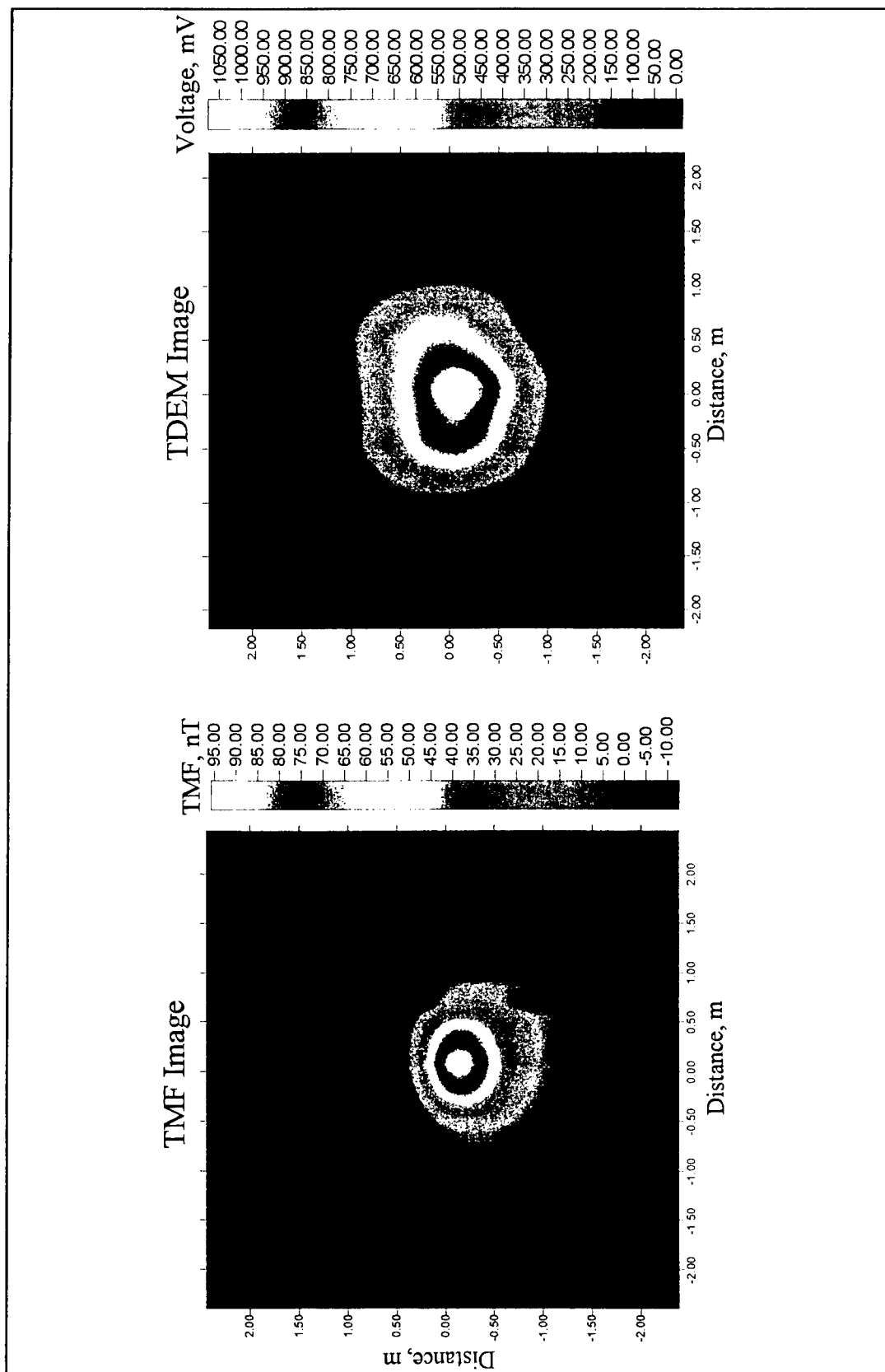


Figure 11. NRL ordnance signature library example; TFM and TDEM data images for 105-mm projectile, depth = 0.49 m, inclination = 0 deg, azimuth = 90 deg

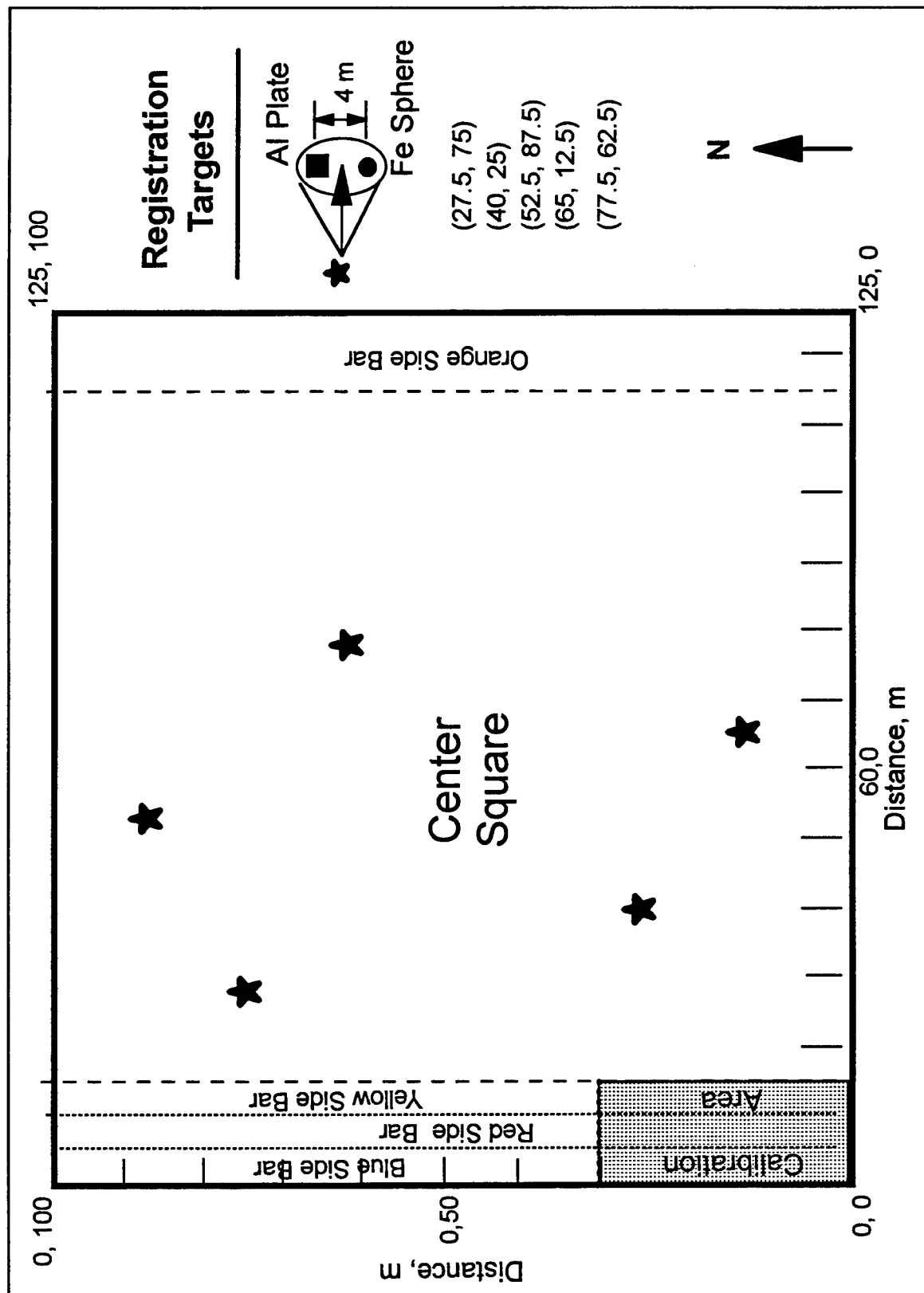


Figure 12. Basic layout of the DARPA 1-hectare sites

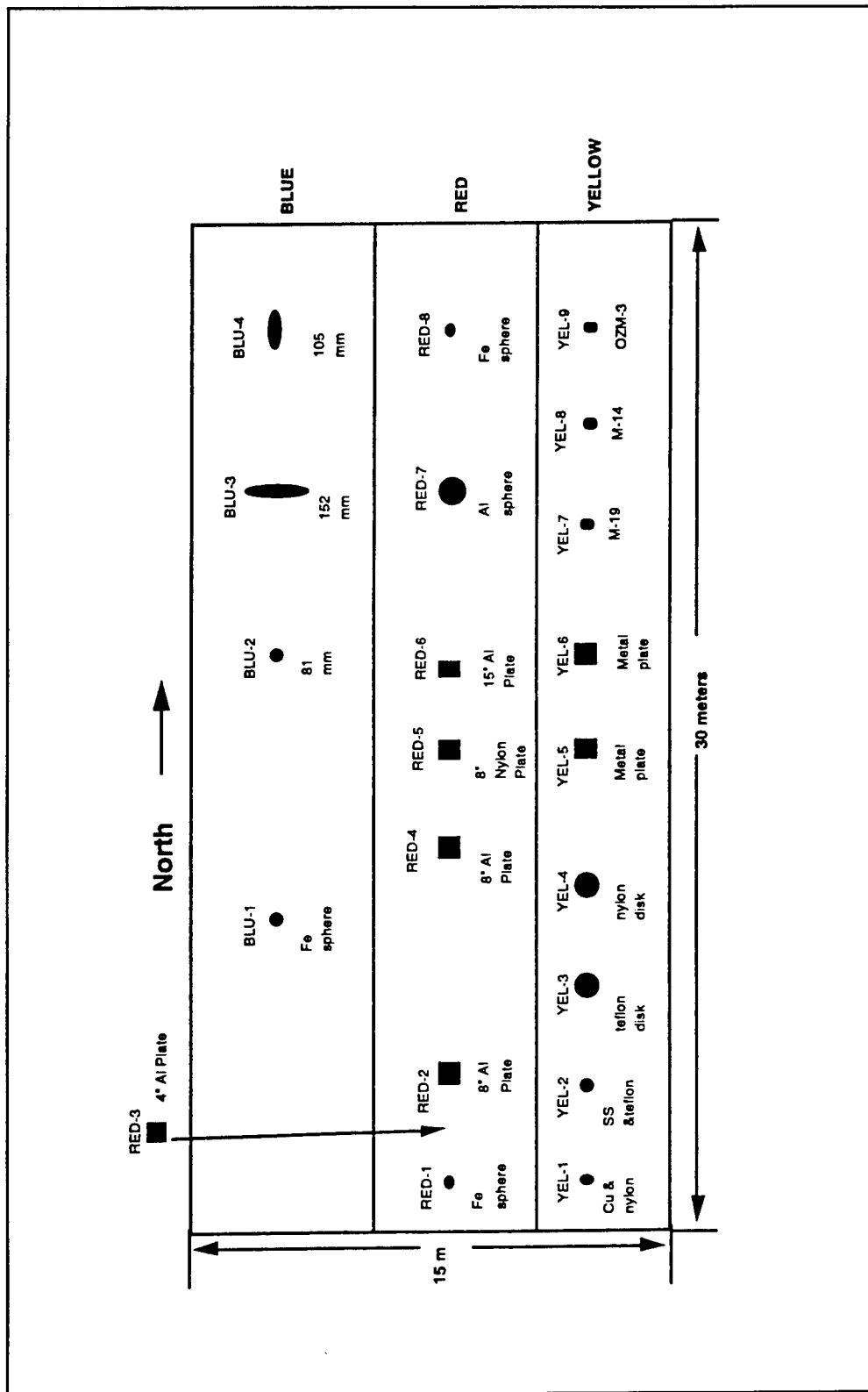


Figure 13. Calibration area layout for the DARPA 1-hectare sites

Table 6 Ordnance Inventory at the Twenty-nine Palms Magnetic Test Range (MTR)		
Ordnance	Number of Items	Range of Depths (m)
60-mm Mortar	10	0.15-0.46
81-mm Mortar	7	0.46-0.76
105-mm Projectile	10	0.46-1.10
155-mm Projectile	10	0.61-1.22
8-in. Projectile	10	1.83-2.74
Mk 81 Bomb	10	1.43-3.11
Mk 82 Bomb	10	1.22-4.42
Mk 117 Bomb	1	3.96
Mk 83 Bomb	1	5.09
Mk 84 Bomb	1	4.88

4 Data Management and Analysis Methods for Detection Enhancement

The importance of data management and analysis tools is emphasized in Chapter 2, and selected examples are presented here using data from the DARPA sites. As mentioned previously, there are three approaches to meeting the data management and analysis requirements for multiple (multisensor) datasets: (1) develop special purpose data acquisition, management and analysis software for a specific system (e.g., McDonald and Robertson 1996); (2) utilize commercially available general purpose graphics software that has some GIS-type functionality, such as simultaneous display of two or more maps and data linkages between the maps (e.g., Geosoft 1996); (3) use a full functioned GIS for data display, mapping, relational links, and analyses.

GIS Data Management Examples

Data for the DARPA Fort Carson sites, including site characterization results and contractor sensor datasets, were input to the ARCVIEW[®] GIS (ESRI 1997). The DARPA site characterization data, acquired prior to any burial activities at the sites, included detailed mapping of topography, vegetation, and surface features (e.g., rocks, animal burrows, metallic objects, fences, etc.), as well as geophysical surveys, soil sampling, and soil classifications and laboratory EM property measurements. The first example, Figure 14, is the topographic map overlying the key site features map for the Turkey Creek Site, Fort Carson. Clicking on a site feature brings up an information box describing all details of the feature. The "x's" indicate surface site features, e.g., rocks or cultural features, and the solid circles in Figure 14 are the locations of the releasable buried targets. The display in Figure 14 is an important benchmark map for correlation with all site characterization geophysical surveys and with contractor geophysical sensor datasets. Topographic features, surface vegetation and roots, rocks, and metallic cultural features can all produce geophysical anomalies which may contribute to the false alarm rate, affecting UXO detection and discrimination. Another example illustrates a

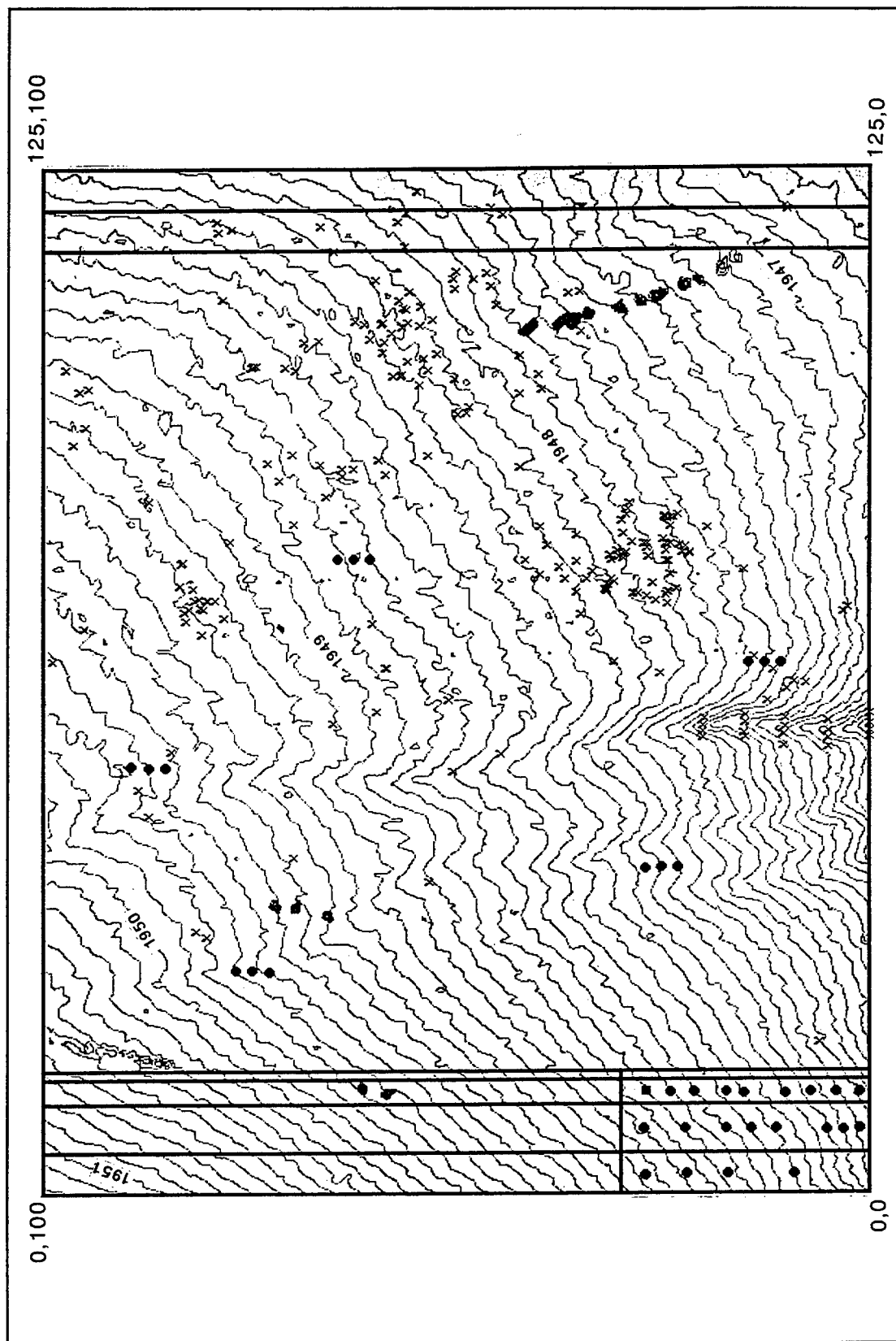


Figure 14. GIS overlay of four maps for the Turkey Creek Site, Fort Carson: basic layout; releasable targets (solid circles); site features (x's); elevation contours (in meters)

simple query of two site characterization maps (TFM and EM31¹) for the Firing Point 20 Site, Fort A. P. Hill: The query computes an average value for the geophysical measurements defining the TFM map and the EM31 (FDEM) map. The query then produces a map, Figure 15, which indicates all areas where *both* the TFM and EM31 measurements are greater than the average values. Two linear features are defined in Figure 15, trending from southwest to northeast at the top of the map. These linear features are prominent on many of the subsequent TFM, TDEM, and FDEM datasets acquired at the site. These features were subsequently verified as caused by buried communications cables. In general the coincident anomaly areas defined in Figure 15 indicate locations where sensor datasets may be more complicated to interpret and are possible sources of false alarms.

The GIS provides a versatile environment for display of sensor “images.” For example, Figure 16 is an image or map of TDEM measurements (EM61, 0.5 m Tx-Rx) for the Turkey Creek Site at Fort Carson. Color values in the map are based on multiples of the standard deviation above or below the mean value for the dataset. The map indicates localized, high-resolution anomalies indicative of known buried metallic objects and some localized anomalies of unknown origin (false alarms). All five of the registration target sets are clearly indicated. It is a simple procedure to enlarge selected areas of the map for more detailed examination of anomalies. The enlarged example in Figure 16 includes two sets of the registration targets, with the anomalies identified with the actual buried objects for one of the sets. The aluminum plate and iron sphere of the registration target sets are spatially separated by 4 m (center to center); the anomalies caused by the targets are well resolved. There are several small magnitude anomalies that could be due to unknown buried metallic objects (note the small spatial extent anomalies just to the right of the lower right registration targets in the enlarged view).

Another useful tool with the GIS is the capability of easily performing data transformations on one or more map layers. The background noise and clutter in Figure 16 is evident and was discussed in the preceding paragraph. A useful technique for suppressing background and clutter is setting a display threshold. Figure 17 is a map of all values in Figure 16 that exceed the mean plus one standard deviation (displayed in red). In the central area, the background and clutter contributing to potential false alarms is virtually eliminated.

Image Processing of Multisensor Data for Detection Enhancement

A commercially available graphics software package that has some GIS functionality, including simultaneous display of multiple co-registered data maps and some relational links between maps, is OASIS montaj (Geosoft

¹ The EM31 is a single frequency (9.6 kHz; Tx-Rx spacing = 3.7 m) EMI system manufactured by Geonics, Inc., Mississauga, Ontario, Canada.

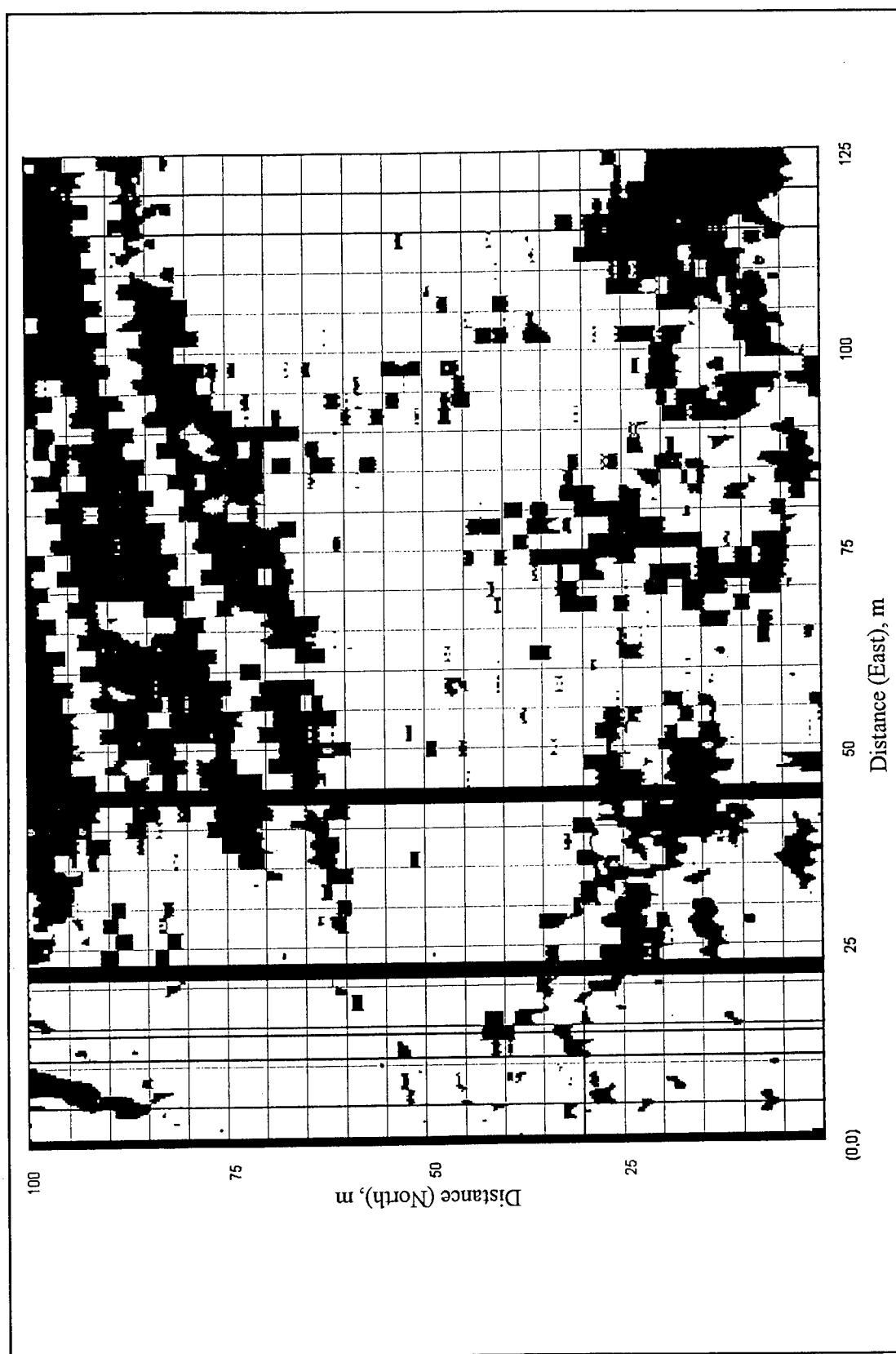


Figure 15. Results of GIS query of WES site characterization data for the Firing Point 22 Site, Fort A.P. Hill. The query computes average values for the TFM and EM31 (conductivity) maps and produces a derived map showing all areas where both TFM and EM31 values are above the averages (in black). Vertical black bars or strips are areas of no data. Distance in meters

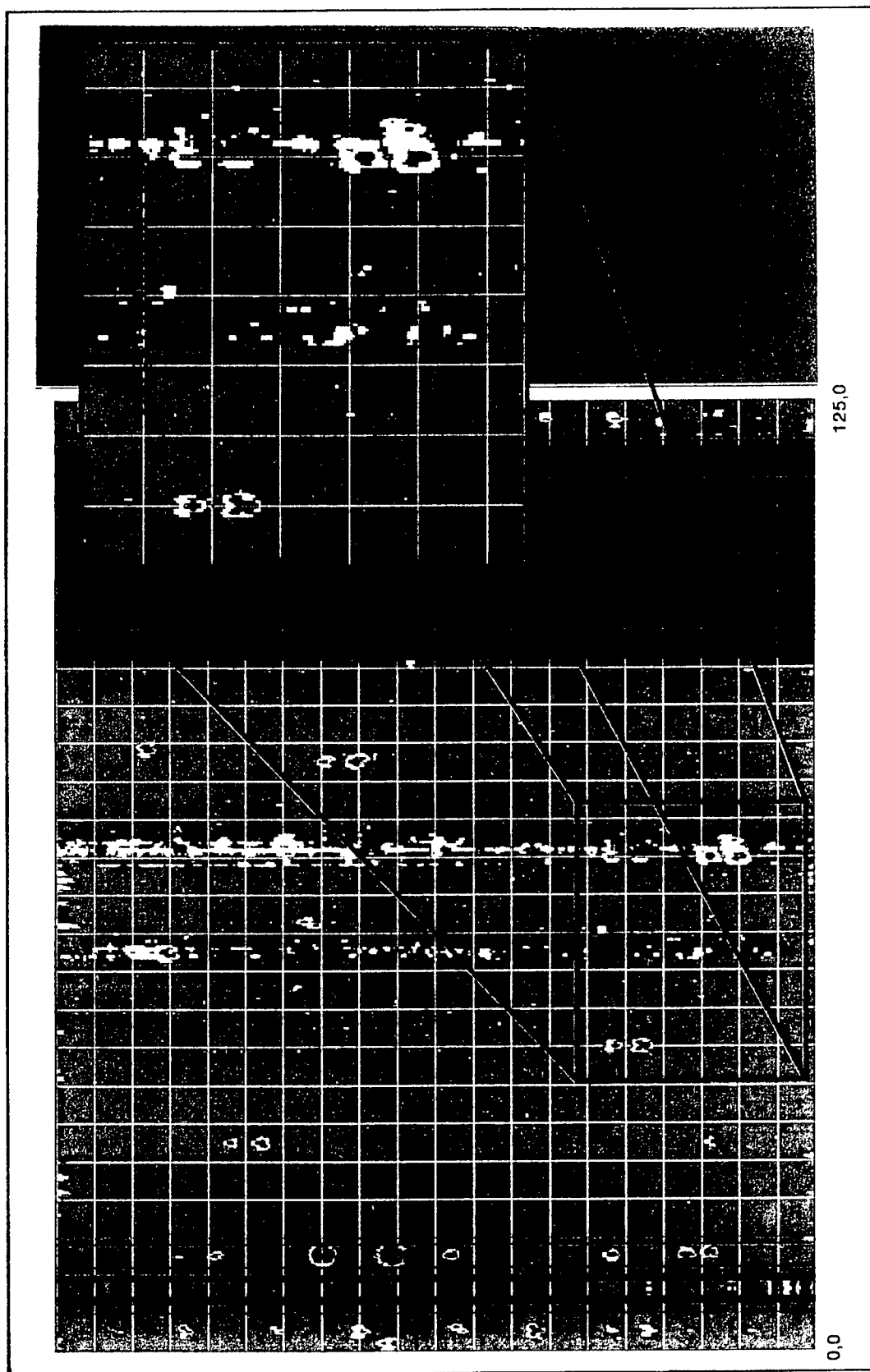


Figure 16. GIS map of EM61 (0.5-m Tx-Rx) for the Turkey Creek Site, Fort Carson. Zoom capability shows close-up of anomalies caused by two of the sets of registration targets in the Center Square. Vertical black bars indicate no data acquired. Grid line spacing -- 5 m x 5 m

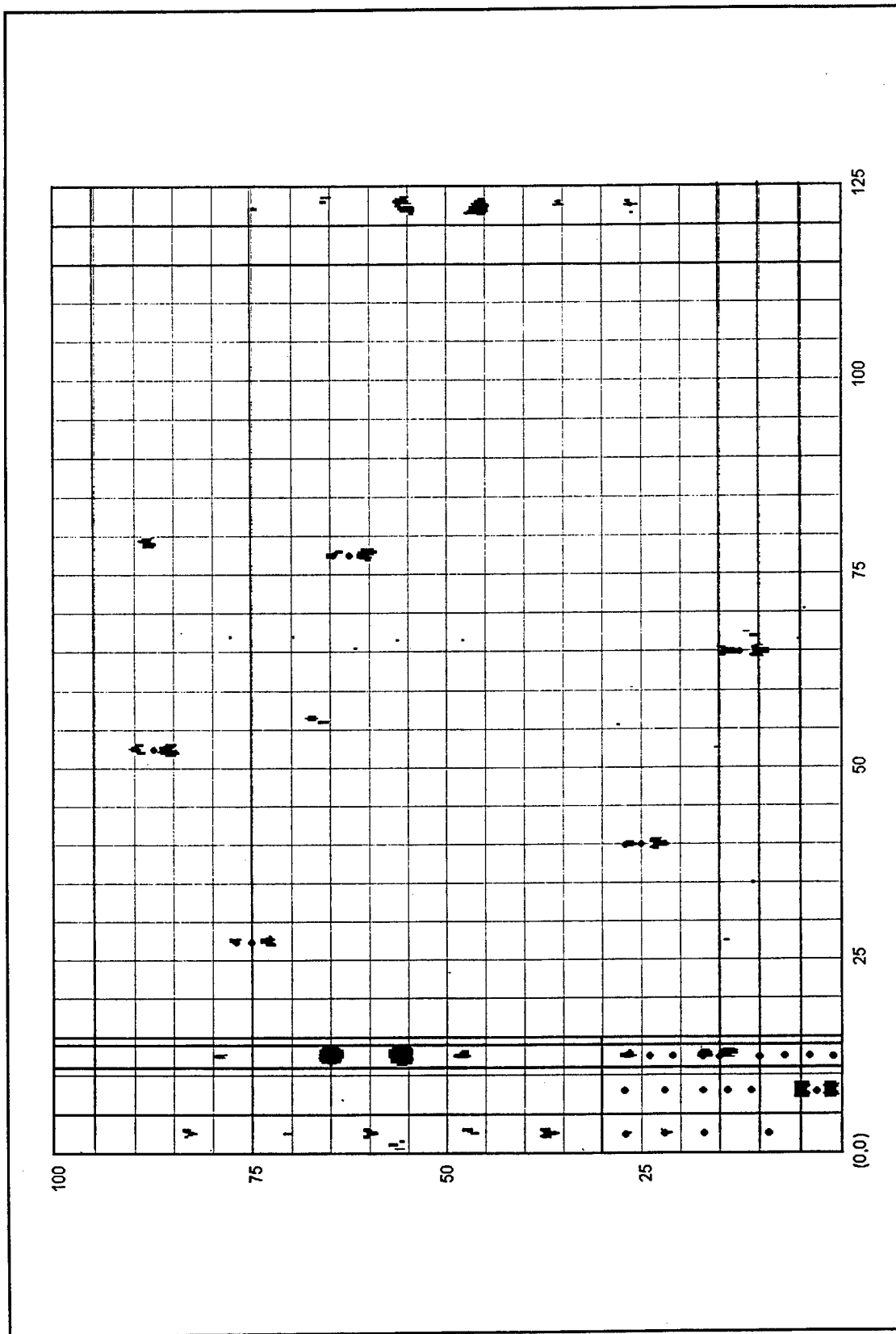


Figure 17. Derived map showing only the areas in Figure 16 where the EM61 (0.5-m Tx-Rx) top coil values exceed the mean plus 1-standard deviation. Distance is in meters; north is to top of figure

1996). Figure 18 is an example of a side-by-side presentation of TFM analytic signal (see Chapter 5 for a definition of the magnetic analytic signal) and TDEM (EM61) image maps for the Firing Point 20 Site, Fort A. P. Hill. The images are a shade of gray version of maps originally in color; a single and different color for each image, with color intensity increasing as data magnitude increases. There is considerable clutter noise in both images; although some small magnetic clutter signals are suppressed in the analytic signal representation. Both of these maps can be treated as images, with pixel size defined by the basic gridding and data acquisition spacings. The original color images were combined to form a color-merged composite or false color image. Figure 19 is the shade of gray version of the color composite image, where increasing brightness (i.e., black to white) indicates increasing intensity of both original color images. For example, a localized "white anomaly" in the composite image is a target or feature with both high magnetic analytic signal magnitude and high EM61 magnitude. Many of the potential false alarm targets in the two original images are suppressed, many localized anomalies representing potential targets of interest are evident and enhanced, and several linear clutter features are well-defined.

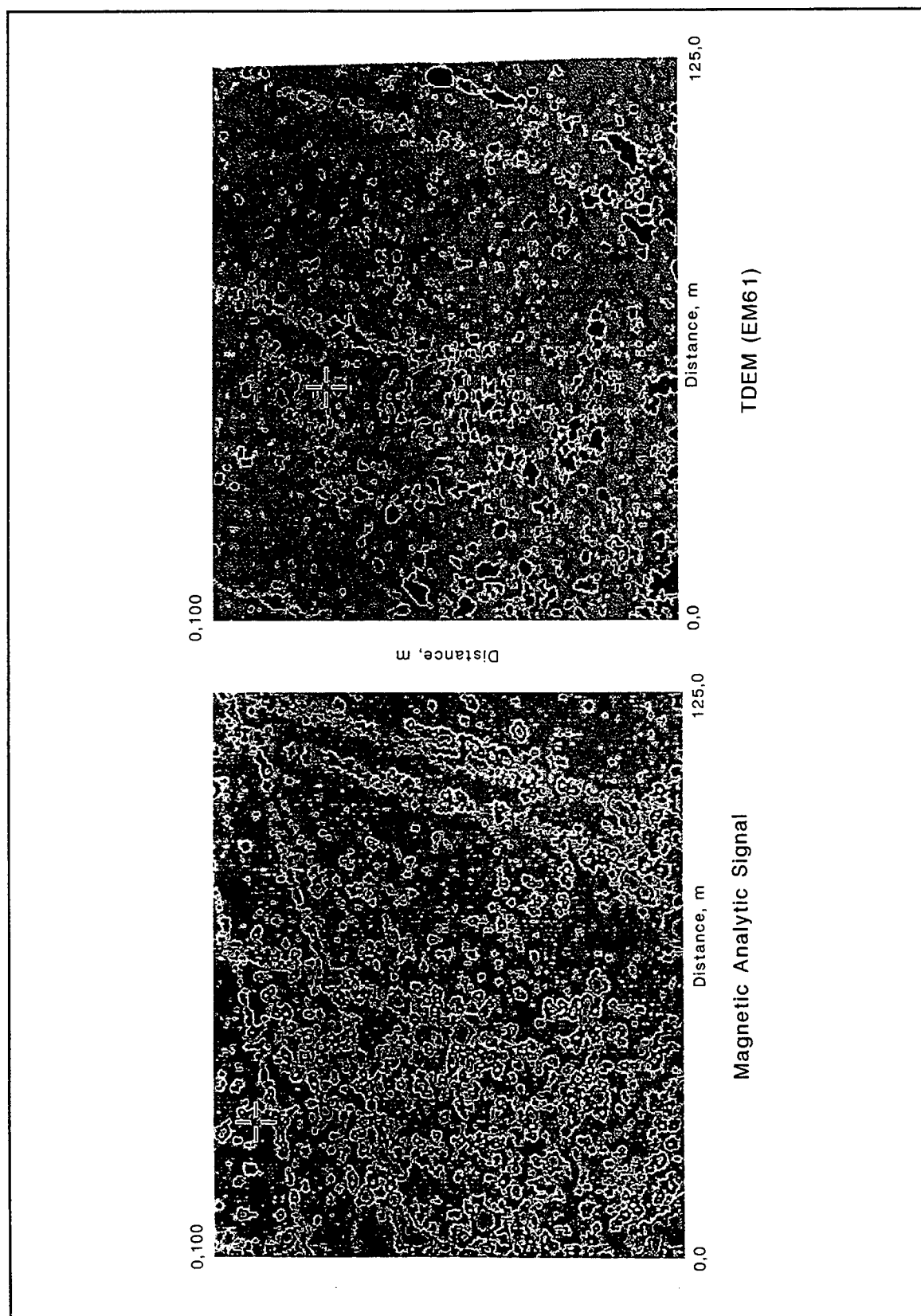


Figure 18. Shade of gray versions of color image maps of magnetic analytic signal and TDEM (EM61) for Firing Point 20, Fort A.P. Hill, Virginia

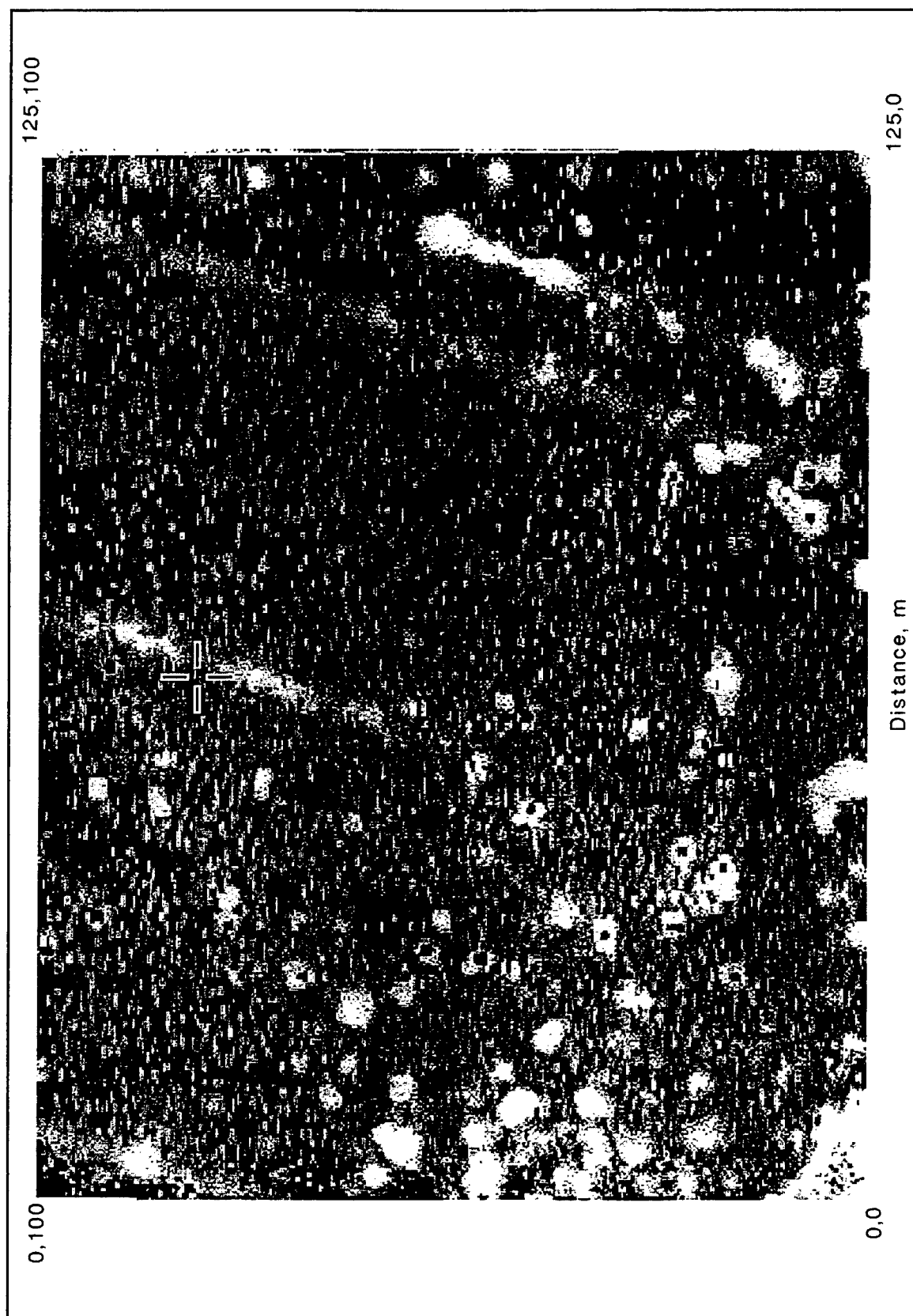


Figure 19. Shade of gray version of color-merged composite image of magnetic analytic signal and TDEM (EM61) images for Firing Point 20, Fort A.P. Hill

5 Synopsis and Examples of Current UXO Detection Analyses Capability

Introduction

While there is predominantly only rudimentary, empirical multisensor (multimethod) integration in fielded UXO detection systems, detection and depth interpretation capability from single-method datasets is actually quite good, particularly for fielded TFM and TDEM systems. The primary problem, as discussed earlier, is that there is not a significant discrimination capability based on single method data. Although there is some automated anomaly selection capability, many of the interpretation approaches require manual (interpreter) anomaly picking or selection (often consisting of “boxing-in” the anomaly). Interpretation of a selected TFM or TDEM anomaly proceeds by applying an empirical or analytical model to the anomaly characteristics. Currently, model based interpretation generally relies on simple geometric models, such as spheres or cylinders. For example, most available TFM interpretation approaches use a simple dipole model (equivalent to a uniformly magnetized sphere) to fit anomaly data. From the simple dipole model TFM anomaly interpretation, the position and depth coordinates and dipole magnetic moment (magnitude and orientation) of a best-fitting magnetic dipole are determined. The best-fitting simple dipole magnetic moment magnitude gives an equivalent sphere size (radius and ferrous mass; e.g., Pennella 1982), which correlates to ordnance diameter (Barrow et al. 1997).

Since the field of a simple magnetic dipole is equivalent to the field of a uniformly magnetized sphere, the earth’s field-induced magnetization for this model (in the absence of remnant magnetization) will be in the direction of the earth’s field. However, the simple dipole model fit to measured data over UXO are frequently not in the direction of the earth’s field, because ordnance items are not uniformly magnetized spheres. The effects of the elongated shape of UXO on induced magnetic moments in the earth’s field are studied by McFee and Das (1990) and Altshuler (1996) using a prolate spheroid model. Barrow et al. (1997) investigate the ambiguities resulting from variations in best-fitting simple dipoles due solely to changes in orientation of the UXO. Barrow et al. also investigate the capability of the prolate spheroid model to *replicate* the variation in best-fitting dipole (magnitude and orientation) as a

function of size and orientation of the UXO. The prolate spheroid model predictions of the variation differ only in small details, likely resulting from slight symmetry breaking along the long axis of real ordnance. Application of the simple magnetic dipole model to interpretation of TFM anomalies achieves good performance for determining position and depth, with typical errors of ± 10 to 20 percent. It cannot be used to determine the size (length and diameter) and orientation (Barrow et al. 1997) uniquely or accurately.

Similarly for the TDEM analysis, a spherical model is often used to estimate depth and size (Barrow et al. 1997). For the EM61 TDEM system, a simple algebraic formula allows depth estimates based on the ratio of an upper to a lower receiver coil signals (Hollyer, Racic, and Butler 1997). The simple dipole model for magnetic interpretation and the sphere model for TDEM interpretation cannot account for effects of ordnance elongation on the induced anomalies. The breakdown of the simple dipole or sphere models for interpreting anomalies becomes most pronounced for objects buried less than (1) the ordnance length in depth for TFM or (2) one to two times the effective transmitter radius for TDEM. A great advantage to the simple model interpretations is computational speed; the interpretations can be accomplished in near-real time. Two examples that illustrate current capabilities and a prototype multisensor integration algorithm are presented below.

Fits to Twentynine Palms MTADS Datasets

As discussed previously, discrimination capability for reduction of false alarms is key to reducing UXO cleanup time and cost. Accurate burial depth estimates for UXO are also extremely important for UXO remediation/cleanup time and cost estimates and for safety considerations during excavation of UXO items. Based on considerable experience at test sites and at live sites, i.e., predictions based on interpretations of geophysical anomalies compared to actual excavation details of the features producing the anomalies, there is an understanding of the accuracy and reliability of simple model predictions. Simple magnetic dipole model fits of ordnance depth and size to TFM data are typically good to ± 10 to 15 percent for location, ± 20 percent for depth, and ± 25 percent for size (e.g., Bell 1997).

The results of the MTADS surveys at Twentynine Palms successfully demonstrated detection capability in a real world setting, with probabilities of detection (*for a joint or "fused" analysis*) ranging from 73 percent for 0.5-m critical radius to 94 percent for 2.0-m critical radius, where a detection occurs when a declared ordnance location is within the specified critical radius of a true ordnance location. The false alarm ratio metric (number of false alarms per ordnance item detected) ranged from 1.9 for individual analyses of magnetic or TDEM anomalies to 3.0 for a joint analysis. Joint analysis of the three MTADS datasets consisted of visual correlation, with selection and deselection based on anomaly coincidence, type, and predicted size and depth considerations. The joint analysis resulted in three additional valid ordnance

target detections (for a 2-m critical radius), raising the probability of detection to 94 percent but significantly increasing the number of false alarms. The joint analysis results here are consistent with the experience at JPG. *Joint analysis as currently practiced* desirably increases the probabilities of detection but also undesirably increases the number of false alarms.

Due to the wide and realistic depth range of ordnance at the Twentynine Palms site, interpreted or fitted depths provide a good assessment of depth estimation capabilities for simple model fits. Comparisons of fitted depth to true depth for some of the ordnance items detected by each of the three MTADS sensor suites are shown in Figure 20. The fitted depths in Figure 20 generally cluster about the dashed, "perfect-fit" line. There are a few outliers in the gradiometer fitted depths, and the TDEM (EM-61) fitted depths deviate considerably for true depths comparable to and less than the transmitter equivalent radius (approximately 0.6 m). Figure 21 contains a comparison of fitted size from the TDEM data versus true caliber (diameter) and against an equivalent sphere radius. For a given ordnance size (caliber or equivalent sphere radius), the mean of the fit sizes correlates well with the true size. However, the spread of TDEM fit sizes varies by factors of typically 2 to 3 for a given true ordnance size. The spread in computed depths and sizes can be partially explained by the fact that the simple spherical model cannot account for variations in ordnance orientation, which can have significant effect on TDEM anomaly signature.

Simple Model Fits to Magnetic Data from DARPA Site

A small window (5 m \times 50 m) of TFM data from the DARPA Seabee Site, Fort Carson, Colorado, is shown in Figure 22. The Fort Carson sites are "quiet" magnetically, so that anomalies from shallow, buried, ferrous objects are pronounced. In Figure 22, five prominent TFM anomalies are indicated (enclosed) by boxes. A commercially available inversion program, MagAID, developed by AETC, Inc., and marketed by Geometrics, Inc. (AETC-Geometrics 1996), fits simple dipole models to measured TFM anomaly signatures. MagAID determines the set of simple magnetic dipole parameters which best fit the measured data by minimizing the Chi-squared statistic between the measured data and model predictions. The program uses a modified gradient search technique through the parameter space (Marquardt 1963; DeProspero and DiMarco 1996). Applying the MagAID analysis procedure to the five selected anomalies in Figure 22 results in the interpreted parameters in Table 7.

Twenty TFM anomalies caused by buried objects (some known objects and some unknown objects) at various locations on the Seabee Site were inverted to obtain simple dipole fit model parameters. While the actual known object identities, locations, and depths cannot be released, the average errors of the

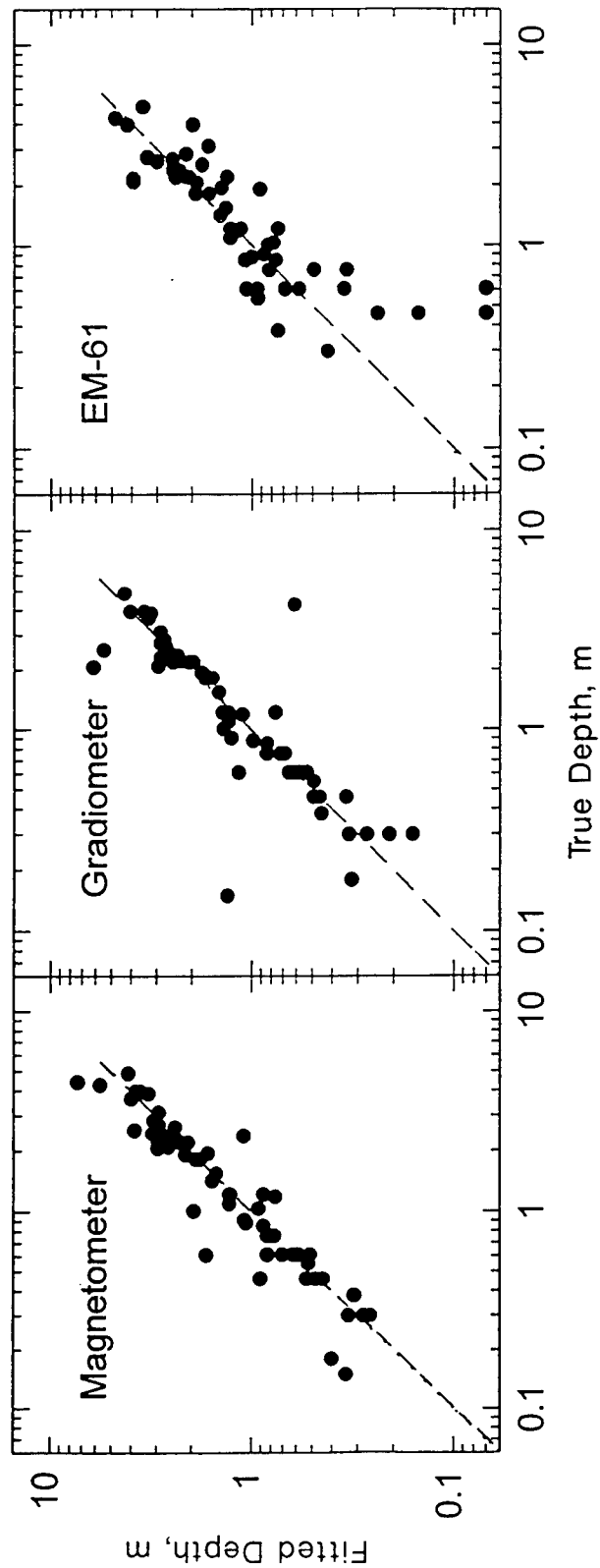


Figure 20. Correlation of fitted depths from analyses of TFM, TFG, and TDEM data to the true depths for buried ordnance items at Twentynine Palms, California (McDonald et al, 1997)

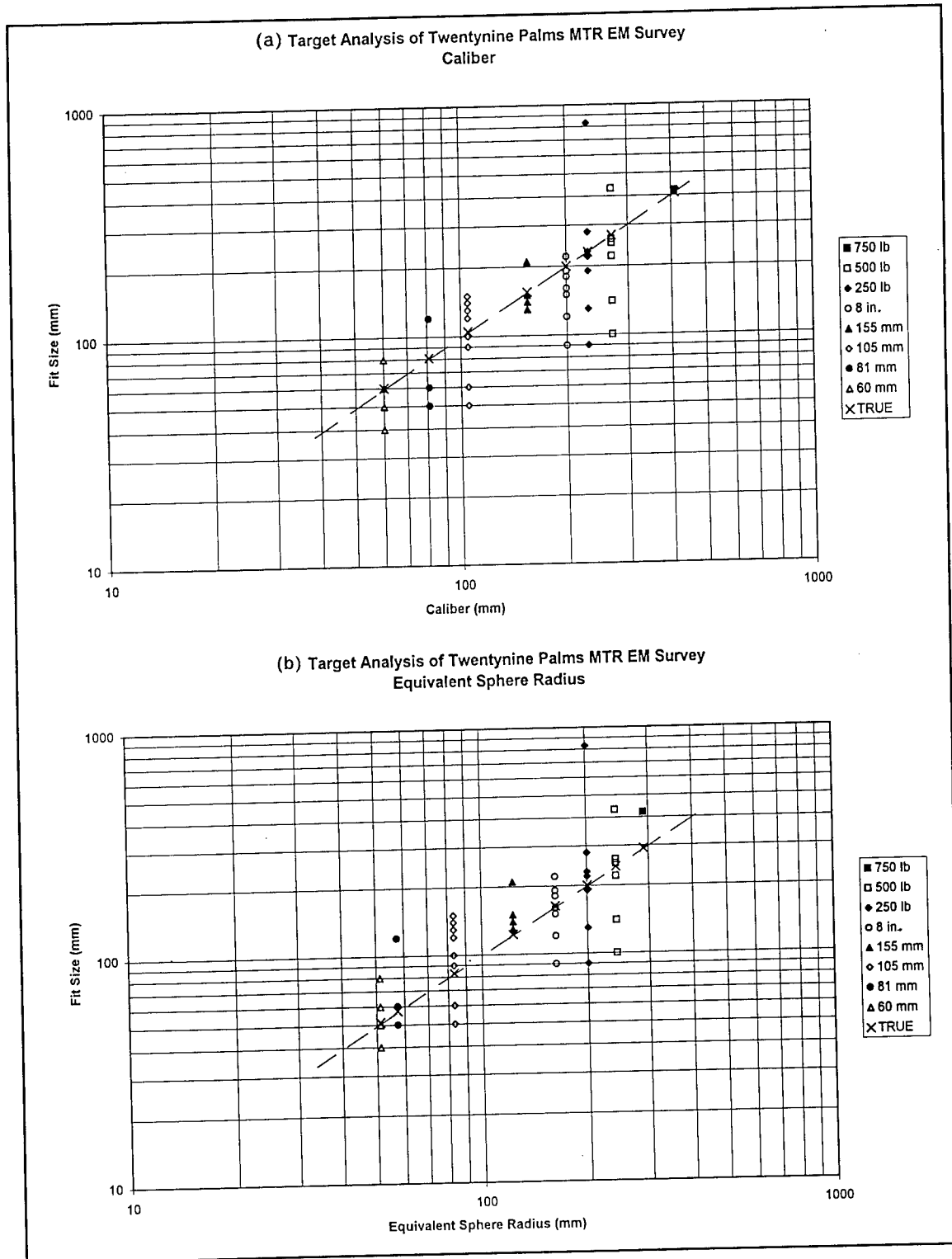


Figure 21. Correlation of fitted size from analyses of the Twentynine Palms TDEM data as a function of (a) caliber (top) and (b) equivalent sphere radius (bottom)

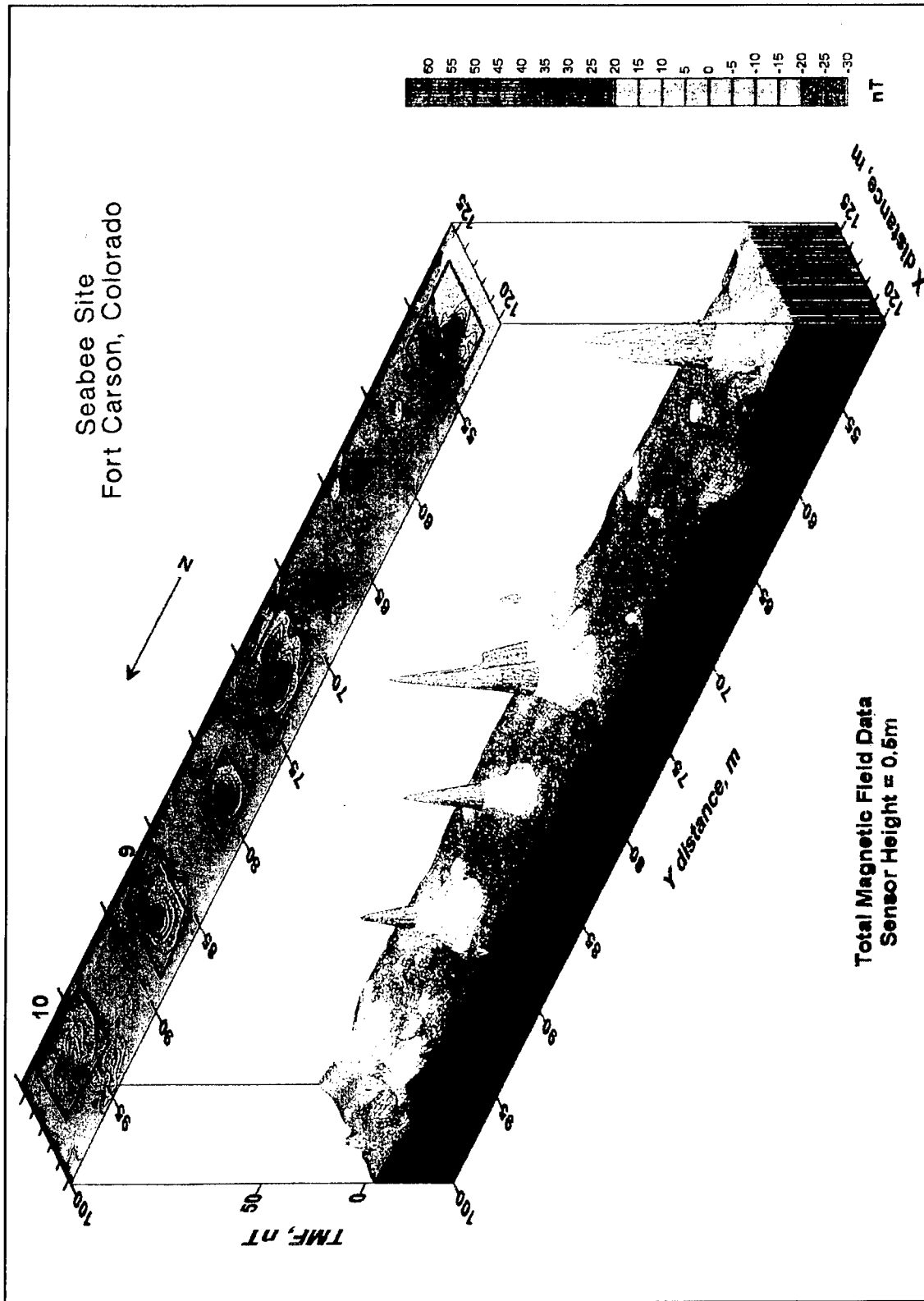


Figure 22. Selected window (5 m x 50 m) of TFM data, Seabee Site, Fort Carson. Five prominent anomalies selected and indicated by the boxed areas

Table 7 Interpretation of TFM Anomalies, Seabee Site, Fort Carson					
Object No.	Interpreted Object Location – X, m	Interpreted Object Location – Y, m	Interpreted Object Depth, m	Interpreted Object Size, mm ¹	Fit Quality (≤1.0)
6	122.1	53.8	0.60	112	0.77
7	122.7	73.9	0.77	127	0.92
8	122.1	80.0	0.43	80	0.99
9	122.8	87.6	0.83	110	0.84
10	123.2	96.4	1.29	120	0.88
¹ The Object Size is the probable ordnance diameter, assuming the object causing the anomaly is ordnance. Optionally the Object Size can be output as the radius of a dipole equivalent sphere.					

twenty interpretations that correspond to known objects gives insight to the inversion capabilities of the program:

Average Location Error – 0.3 m
Average Depth Error (percent of actual) – 45 percent
Average Size Error (percent of actual) – 14 percent

The average location error is approximately the same as the average measurement spacing; the measurement grid is approximately 10 to 20 cm along lines and 25 to 50 cm between lines. The large average depth error of the interpretations, as a percentage of actual depth, is due to the fact that actual depths of buried objects at the DARPA sites are small. There is a strong correlation of computed depths with actual depths.

Conclusions from the error results for the MTADS Twentynine Palms surveys and the error results listed above for the DARPA TFM target fits are consistent with the extensive results from the recently reported MTADS surveys at the Badlands Bombing Range (McDonald et al. 1997). A large number of targets were dug up after TFM and/or TDEM anomaly detection, selection, and interpretation. The average error of target locations (interpreted versus dug target location) was 12 cm, and 95 percent of all targets were located within 29 cm. The predicted versus actual target depths for all dug targets are strongly correlated but show considerable variation, particularly for shallow targets. Similar strong correlation between predicted size and actual size exists, but considerable variation exists also. As in previous examples, multisensor data integration for the MTADS Badlands Bombing Range surveys was accomplished by visually correlating TFM and TDEM anomalies.

Proposed Multisensor Data Integration Algorithm

The examples of multisensor data integration discussed to this point are predominantly empirical, involving side-by-side visualization of datasets and selection of spatially coincident anomalies on two or more datasets, e.g., the MTADS examples and the example in Figure 18. An intermediate stage of multisensor data integration, between the visual correlation procedure and true joint inversion of multiple datasets, is to invert one dataset using selected results from the inversion of, or parameter extraction from, a second dataset; this procedure is termed a sequential or simplified joint inversion process in Chapter 2.

For TFM and TDEM datasets, a proposed, prototype algorithm for integrated interpretation is illustrated in Figure 23. The algorithm assumes that the TFM data is converted into the magnitude of the analytic signal (e.g., Hollyer, Racic, and Butler 1997), as in the example in Figure 18. The magnitude of the analytic signal, equal to the square root of the sum of the squares of the three spatial gradients of the TFM (Roest, Verhoef, and Pilkington 1992), is determined from the TFM data by first applying a convolutional filter to the gridded TFM data to obtain the horizontal gradients and then a fast Fourier transform or a discrete Hilbert transform (Butler 1995) to obtain the vertical gradient (Hollyer, Racic and Butler 1997; Geosoft 1996). The advantage of the TFM analytic signal is that dipolar anomalies are converted to monopolar anomalies centered over the buried object, making automatic peak-picking feasible and more efficient. Coincident peaks selected by the algorithm will be related to ferrous objects, for which the depths are computed by analyses of the TDEM anomaly characteristics (Hollyer, Racic, and Butler 1997).

Interpreted depth (to center of the ferrous object, Z_0) from the TDEM analysis is used as a fixed parameter (constraint) in the inversion of the magnetic analytic signal anomaly. The value of using the TDEM depth to constrain the magnetic inversion is that the fewer the number of “free” parameters in an inversion, the faster the inversion will converge and the more “unique” the inversion result (model) will be. Alternatively, the prototype algorithm can be modified to obtain the horizontal location (X_0 , Y_0) as well as the depth (Z_0) from the TDEM analysis, to further constrain the magnetic analytic signal inversion. Finally, inverting the magnetic analytic signal gives the magnetic moment, which can be correlated to the ferrous mass of the object causing the anomaly. The ferrous mass is then correlated to ferrous masses of known ordnance items to produce a likely UXO type classification (e.g., Pennella 1982). This prototype algorithm (Figure 23) can be implemented with minimal effort in existing data analysis and visualization software packages (e.g., Geosoft 1996).

A modified prototype algorithm, illustrated in Figure 24, analyzes the TFM data directly, using the TDEM-determined location and depth as constraints, and determines a best-fitting prolate spheroid model. A manual implementation example of this modified prototype algorithm is demonstrated in the next chapter. Variations in this proposed approach to joint interpretation are obvious. For example, constraints resulting from interpretation of TFM data

can be applied to inversion of the TDEM data to a final model. Also, the procedure can be iterated to minimize an overall goodness of fit criteria to the measured data, closely approaching a true joint inversion.

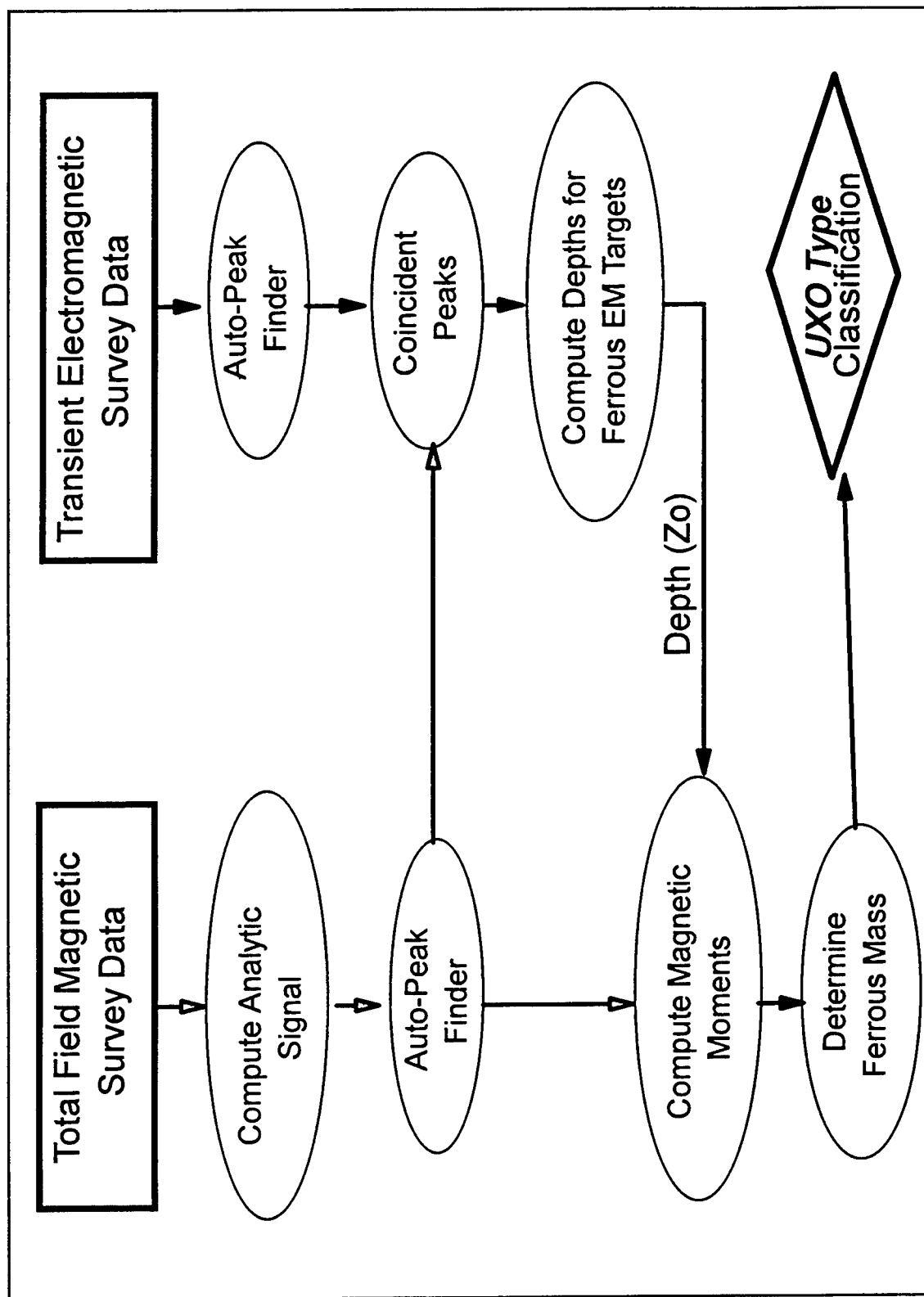


Figure 23. Prototype algorithm for integrated multisensor data processing

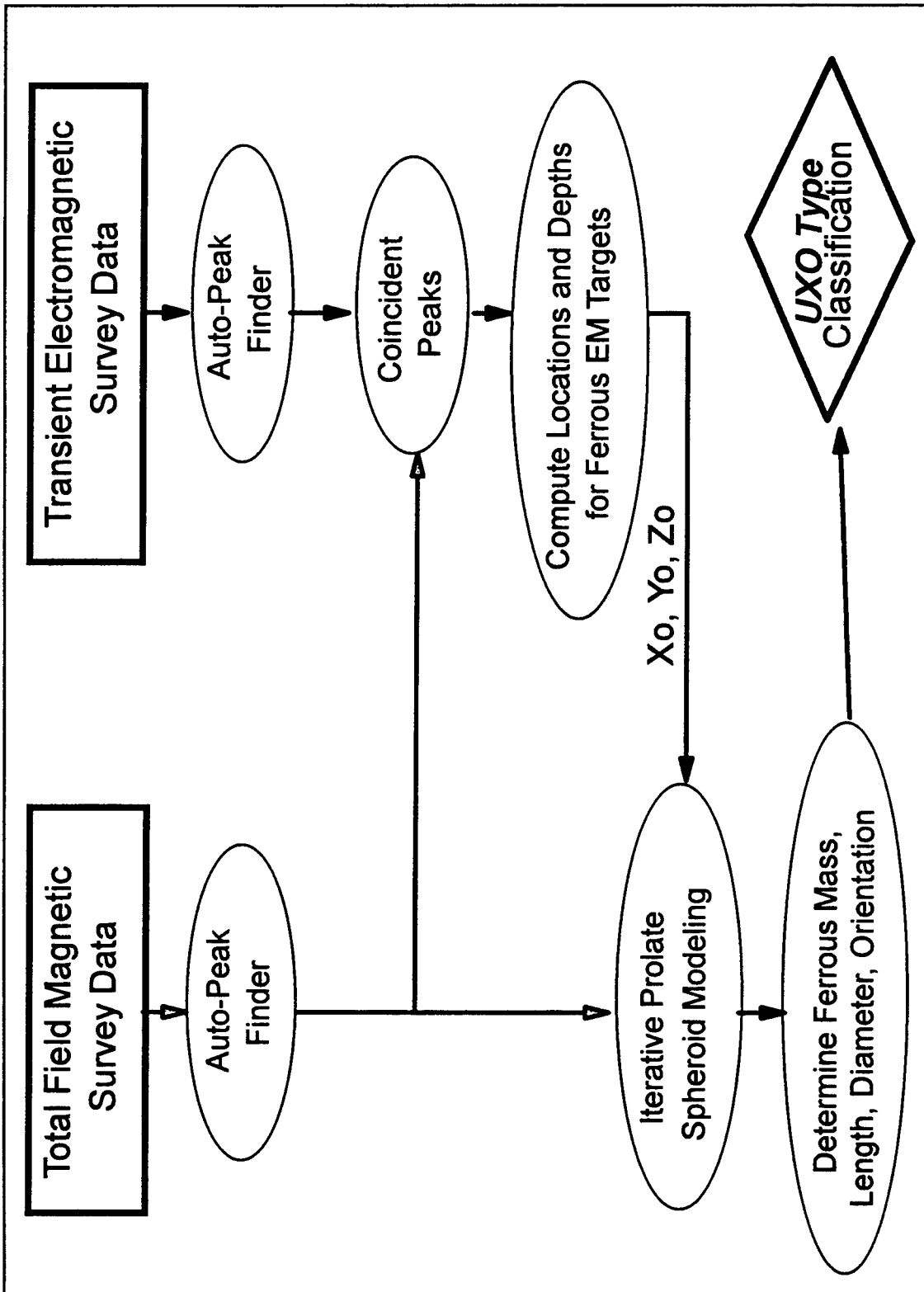


Figure 24. Modified prototype algorithm for integrated multisensor data processing

6 Development of Phenomenological Modeling Capability

The value and role of geophysical signature modeling capabilities are discussed in Chapter 2. A major effort of this study was development of analytical modeling capability for geometries that more closely approximate ordnance than the sphere. Primary weaknesses of the spherical model of ordnance is that the spherical symmetry gives no orientation dependence of the ordnance relative to the inducing field. Also, for magnetic signature modeling, the ordnance is assumed to be a solid ferrous sphere, with the size determined from the ferrous mass and the density of iron or steel, and the sphere cannot reflect demagnetization effects associated with the elongated ordnance geometry. While the geometry of ordnance could be modeled nearly exactly with finite element or other discretized numerical modeling approaches, the computational time and the parameters of the model may not be conducive to inverse modeling. Discretized numerical modeling is valuable for studying phenomenological effects, but the thrust of the current modeling efforts are to develop analytical modeling tools which can be adapted ultimately for automated inverse modeling. Simple geometries which more closely approximate ordnance shapes than the sphere are the prolate spheroid and circular cylinders. Both full-field analytical and multipole expansion solutions for the induced magnetic field of a prolate spheroid (or oblate spheroid) exist; this geometry is exploited in the current TFM modeling capability development. TDEM modeling for geometries other than the sphere is difficult and is not developed to the same extent as TFM modeling capability.

Magnetic Modeling Program

Background

Altshuler (1996) reviews the deficiencies of a spherical model for ordnance and evaluates a prolate spheroid model. A key conclusion of Altshuler from studies of solid versus spherical shell and spheroidal shell models is that it is the outer ferrous volume of the ordnance that is critical to the magnetic signature, not the ferrous mass. The prolate spheroid model is a realistic

representation of the general shape of ordnance and also has the elongated geometry of ordnance that can replicate demagnetization and orientation effects. A prolate spheroid with the length and diameter of an ordnance item is a good approximation to the outer ferrous volume of the ordnance. The induced magnetic field external to a spheroid can be determined by a full field solution (Stratton 1941; Altshuler 1996) or a multipole expansion (McFee and Das 1990). In the multipole expansion, there is no monopole term, and the quadrupole term is zero due to symmetry. Thus, an octapole term is the next higher term after the dipole term; and, since the octapole term falls off as $1/r^5$, there is no practical reason to include anything higher than the octapole term. Altshuler (1996) compares the dipole field (for a spheroid model) with the full field solution and concludes that for measurement distances greater than about two semimajor axes (the length) from the center of volume of the spheroid, the dipole model field prediction is within 10 percent of the full field model prediction. Thus for small distances, the octapole field contribution becomes more significant. Advantages of a multipole solution compared to a full field solution are primarily (a) reduced computational time and (b) ability to separate the prolate spheroid dipole term for comparison with the dipole solution for a sphere; with the primary disadvantage being a possible minor lack of accuracy for very close distances of the model to the signature calculation plane.

The U.S. Army Engineer Waterways Experiment Station (WES) implementation of a multipole expansion magnetic field solution for a spheroid model follows the outline of McFee and Das (1990). Geometry for the magnetic modeling problem is illustrated in Figure 8. There are two obvious coordinate systems for the spheroid model, a body-centered system (x_1, x_2, x_3), with the x_3 axis along the long symmetry axis of the spheroid, and a space-centered system (X_1, X_2, X_3), in which the spheroid center is at (X_0, Y_0, Z_0) as shown in Figure 8. Assuming uniform, parallel magnetization M of the spheroid, the multipole expansion of the secondary induced magnetic induction at a point r in free space is

$$b = b^{(2)} + b^{(8)}, \quad (1)$$

where $b^{(2)}$ is the dipole field component and $b^{(8)}$ is the octapole field component. The dipole field component is given by

$$b^{(2)} = [\mu_0 / (4\pi r^3)] \{ -m^{(2)} + (3/r^2) (r \cdot m^{(2)}) r \}, \quad (2)$$

where μ_0 is the magnetic permeability of free space, $r = |r|$, and $m^{(2)}$ is the dipole moment. The expression for the octapole field $b^{(8)}$ is more complicated, involving a rank three octapole moment tensor. The dipole moment is related to the magnetization by

$$m^{(2)} = MV, \quad (3)$$

where $V = (4/3)\pi ea^3$ is the volume of a spheroid, $e = L / (2a)$ is a shape factor for the spheroid, L is the length of the spheroid, and $2a$ is the spheroid diameter orthogonal to the symmetry axis. This formulation is also valid for a sphere, where $e = 1$ (i.e., $L = 2a$ and a is the radius of the sphere) and $V = (4/3)\pi a^3$ is the volume of a sphere. Also, for the sphere, in the absence of permanent magnetization, M will always be in the direction of the inducing earth's field and the octapole field component $b^{(8)}$ is zero.

For the spheroid, the induced field will not always be in the direction of the earth's inducing field even in the absence of permanent magnetization. Resolving the earth's field \mathbf{b}_0 into components along the body-centered coordinate system (b_{01}, b_{02}, b_{03}), the magnetization in the spheroid can be expressed (Stratton 1941, McFee and Das 1990)

$$\mathbf{M} = (1/\mu_0) \mathbf{F} \cdot \mathbf{b}_0, \quad (4)$$

where the diagonal components F_i , $i = 1, 2, 3$, of the demagnetization tensor \mathbf{F} (the tensor is diagonalized in the body-centered coordinate system) are called the demagnetization factors. Furthermore, for the spheroid, $F_1 = F_2$. The demagnetization factors are functions of the shape factor e and the relative magnetic permeabilities of the spheroid material ($\mu_{r1} = \mu_1 / \mu_0$) and the surrounding medium ($\mu_{r2} = \mu_2 / \mu_0$). For the case of an ordnance item buried in soil, generally $\mu_{r1} \gg \mu_{r2}$ and $\mu_{r2} \approx 1$. Finally, for a sphere, $e = 1$ and $F_1 = F_2 = F_3$. For the spheroid, two cases can be distinguished, the prolate spheroid with $e > 1$ (the case used to model UXO), and the oblate spheroid with $e < 1$ (which might be used to model a ferrous metallic mine). The modeling program checks for the value of e and uses the appropriate expressions for F_i . Also, the program allows for calculation of \mathbf{b} (Equation 1) or just the dipole field component $b^{(2)}$.

Finally, the calculated components in the body-centered coordinate system are rotated into the space or earth-referenced coordinate system

$$\mathbf{B} = \mathbf{A} \cdot \mathbf{b}, \quad (5)$$

where \mathbf{A} is the Euler rotation tensor (e.g., Arfken 1985). *The space coordinate system employed for the solution (and the computer program) is a right-handed system with X positive to the north, Y positive to the west, and Z positive upward. For a buried ordnance item model, the depth to the center of the spheroid is negative. Inclination of the spheroid is relative to the positive Z-axis, and thus an inclination of 90 deg is horizontal. Azimuth of the spheroid is defined as the angle between a vertical plane through the spheroid and the positive X-axis (north), with counterclockwise angles positive. This modeling convention contrasts to the customary definitions of inclination and azimuth used for the validation and phenomenology studies: inclination (I) positive down from horizontal; azimuth (A) positive counterclockwise from north.*

The program allows calculation and plotting of the magnitude of the secondary field \mathbf{B} (Equation 5), the magnitude of the total field $\mathbf{B}_t = \mathbf{B} + \mathbf{B}_0$, the components of the total field $B_{ti} = B_i + B_{0i}$ ($i = 1, 2, 3$) that would be measured by vector magnetometers, and the magnitude of the total magnetic field anomaly, i.e., the value measured by total field magnetometers $|\mathbf{B}_t|$ minus the ambient Earth's field,

$$\Delta B_{TMF} = |\mathbf{B} + \mathbf{B}_0| - B_0 = (B^2 + B_0^2 + 2 \mathbf{B}_0 \cdot \mathbf{B})^{1/2} - B_0, \quad (6)$$

where the Δ indicates an anomaly value. The octapole component contribution to the preceding values calculated by the magnetic modeling program can be "switched off" for plotting just the dipole contribution.

Program description and input/output

The magnetic modeling program is implemented in the MATLAB® (registered Trademark of The MathWorks, Inc., Natick, MA) programming environment to take advantage of the built-in graphics capabilities during the development and validation phases of the capability. The program is initiated by executing the script *magmod*. A graphical user's interface (GUI) simplifies and expedites input, model execution, and specification of graphical output format. Model input parameters and output format are specified on three GUI screens. The complete program listing is at Appendix B.

Main screen. The first screen is the main or master screen that has several "push buttons" for accomplishing the following:

Push Button	Description
<i>Edit Input Parameters</i>	Enters the second screen, for data input specifications
<i>Run Model</i>	Executes the model calculations, with the current input parameters and plot specifications
<i>Edit Plot Instructions</i>	Enters the third screen to specify output plot format, including page orientation, number of plots, types of plots, etc.
<i>Plot Results</i>	Reproduces the specified graphical output on the computer screen
<i>Hard Copy</i>	Produces a hard copy of the output on the specified printer/plotter

In addition, there are three secondary push buttons for specifying a "batch run-plot," to make a movie from the output graphics, and to play the movie. Two fill-in boxes allow specification of a comparison data file and a code for the desired printer or plotter. The comparison data file could be TFM profile measurements acquired over known or unknown anomaly targets with the same distance scale as the calculated profile values. The comparison data profile can be superimposed on the calculated profile; this is a useful feature for program validation or for iterative forward modeling.

Input parameter screen. The input parameter screen consists of a number of fill-in boxes that can be freely edited. To the right side of each fill-in box is a description of the parameter to be entered. Initially there is a check box to indicate metric units (or English units if unchecked). The following tabulation gives the parameter list in the order of appearance on the screen:

<u>Input</u>	<u>Parameter Description</u>
_____	Minimum X- (north) value of grid in m or ft
_____	Maximum X- (north) value of grid in m or ft
_____	Minimum Y- (west) value of grid in m or ft
_____	Maximum Y- (west) value of grid in m or ft
_____	Height of instrument (sensor) above ground in m or ft
_____	Earth's magnetic field in nanoTeslas (nT)
_____	Inclination of earth's field in degrees
<u>*.mat</u>	Output file name
_____	Length of body in m or in.

_____	Diameter of body in m or in.
_____	Relative magnetic permeability of body
_____	Angle of body symmetry axis relative to Z-axis in degrees
_____	Angle of body vertical plane relative to X in degrees, positive counterclockwise (CCW)
_____	X-coordinate (X_0) of body center in m or ft
_____	Y-coordinate (Y_0) of body center in m or ft
_____	Z-component (Z_0) of body center in m or ft (negative for buried objects)

For a given set of anomaly calculations for a list of models, many of the input parameters will remain constant between program runs.

Plot specification screen. The plot screen allows specification of the numerous plot options available. At the top are two check boxes, to specify dipole, octapole, or both components. The Plot Format click box brings up a number of portrait and landscape plot orientation options. The File Name fill-in box is used to specify the output file name (same as specified on the parameter input screen); this box is filled in by default with the most recently completed model calculation result but may be edited to plot other saved output files. As many as six plots or graphs can be specified for a single output page; these are indicated beneath the heading "Data Type." Clicking on any of the six boxes brings up a list of data types which can be plotted, and highlighting a parameter selects it for plotting. The data types which can be plotted are:

<u>Data Type</u>	<u>Plot Type</u>	<u>Cross Values</u>
-- X-component of total magnetic field		
-- Y-component of total magnetic field		
-- Z-component of total magnetic field		
-- Magnitude of the secondary field		
-- Total field anomaly		
-- Vector representation of horizontal components		
-- <i>Representation of spheroidal body</i>		
-- <i>Surface of spheroidal body</i>		
-- <i>Listing of major parameters</i>		

For the data types, except the last three options in the above list, selection brings up a click box under the heading Plot Type.

Clicking a Plot Type box opposite a selected Data Type brings up a list of options for how to plot the data. Various types of plots are possible: 3-D surface representations; contour plots; profile plots (projections). Three-dimensional surface plots are representations of the value of a calculated magnetic value (along a vertical axis) and its variation over the specified ranges of X and Y. The 3-D plots can be color-filled, a shade of gray, shaded relief, or have superimposed contours. Likewise, the contour plots, which are two-dimensional (2-D) can be a shade of gray, have color contour lines, or color-filled contours. An effective display option is to have a 3-D representation plot vertically offset from its 2-D contour plot counterpart. The projection or

profile plot option is a familiar way of visualizing the detailed variation and shape of the anomaly signature along a surface line parallel to the X-axis (north-south) or parallel to the Y-axis (east-west). From one to four profile or projection lines can be plotted on the same graph. When the projection plot type option is selected, a box opens under Cross Values to specify the desired locations of the profile lines. For example, if the Plot Type selection "3 Projections Parallel to X-Axis" is selected, three Y-values must be provided in the Cross Values box, indicating Y-values where the profiles cross the Y-axis. A common procedure, for the above example, is to have the center of the spheroid beneath the point (0,0) and to have one profile cross at $Y = 0$ and the remaining two profiles cross at $Y = -1$ m and $Y = 1$ m. This procedure gives a central profile that generally indicates the maximum signature magnitudes and the spatial wavelength of the signature, and then indicates changes in signature characteristics laterally; the profiles allow rational consideration of along-track and cross-track measurement spacings required to capture the relevant characteristics of the signature for the specific case.

Example. A specific example illustrates most of the input and output features discussed above. Results of a model validation comparison to measurement data from the NRL ordnance signature library is shown in Figure 25. The comparison is for a 105-mm artillery projectile, oriented horizontally and pointing north. The figure consists of four plots corresponding to various Data Type and Plot Type specifications: (a) the upper left display is a shaded relief 3-D TFM anomaly plot vertically above a standard contour plot; (b) the upper right display is a representation of the input spheroidal model; (c) the lower left display is a north-south profile TMF anomaly plot (parallel to the north-south axis and crossing the east-west axis at 0) showing model calculation (solid line) and superimposed measurement results (+); (d) the lower right display is a listing of the program input parameters. Also included in the lower left plot is a legend displaying the profile axis-crossing value, the maximum and minimum TFM values along the profile, and the profile distance between maximum and minimum values.

Magnetic modeling program validation

Validation of the WES magnetic modeling program addresses two considerations, reality checks and correlation or comparison with well-controlled magnetic signature measurements.

a. Reality checks.

- (1) For given input parameters, the calculated anomaly signature must become smaller in magnitude and broader in spatial extent as the depth of the spheroid is increased.
- (2) For a spheroid model, identical results should be obtained for indistinguishable cases with different input parameter values.
- (3) Calculations for pairs of indistinguishable inclinations, e.g., 0 and 180 deg or 90 and 270 deg, must be identical.
- (4) Calculations for pairs of indistinguishable azimuths, e.g., 45 and 225 deg, must be indistinguishable.

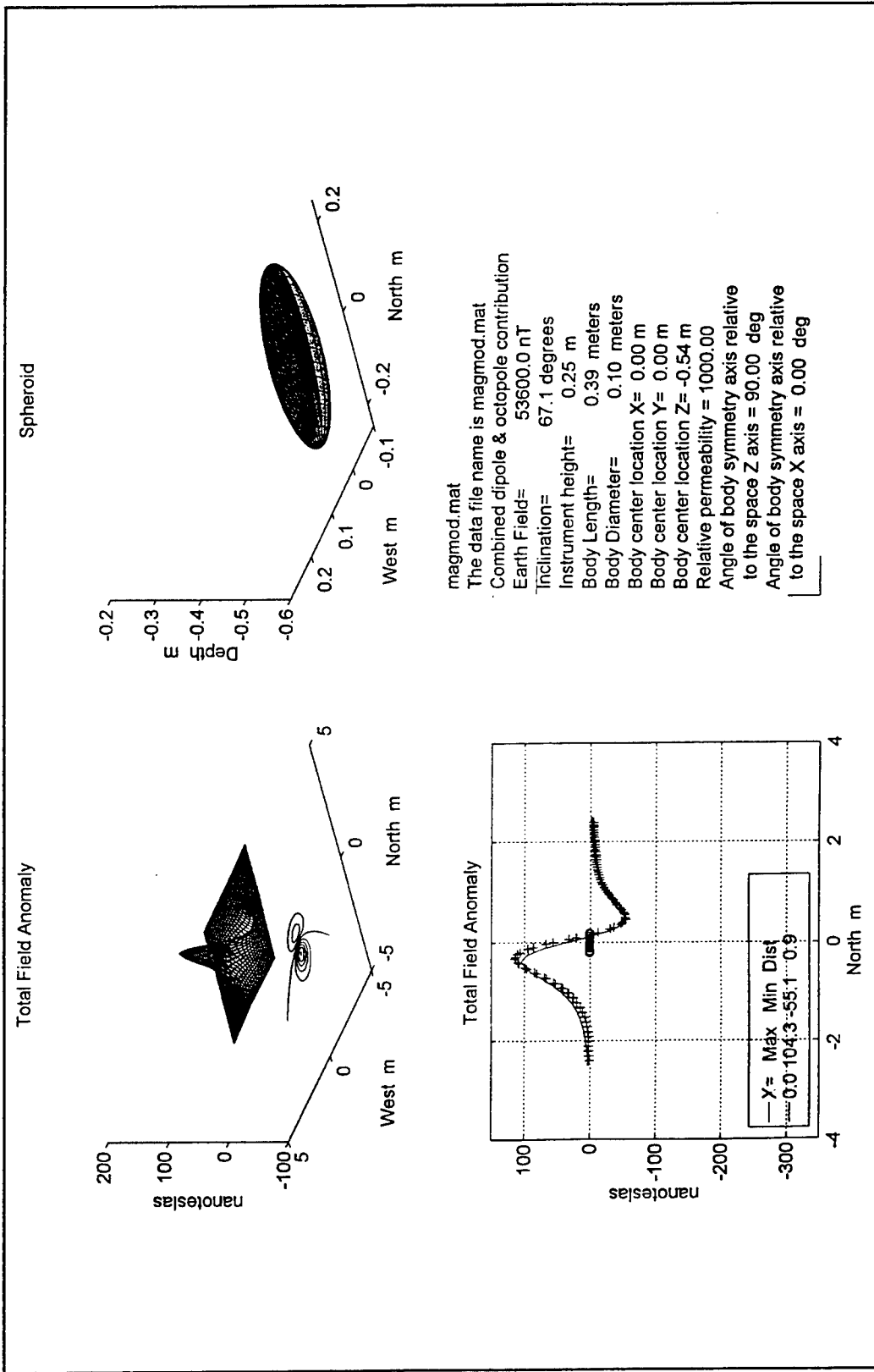


Figure 25. Example output of magnetic modeling program. The total field anomaly profile plot (lower left) includes a validation model calculation (solid line) of a specific case from the NRL ordnance signature library (+): 105-mm artillery projectile oriented horizontally and pointing north

- (5) For a prolate spheroid model, the calculations must show changes as the object is rotated (i.e., the inclination and/or azimuth changes) relative to the Earth's field orientation, reflecting demagnetization effects due to the elongated geometry.
- (6) For the simple case of a sphere (i.e., $L = 2a$ or $e = 1$), the calculated magnetic anomaly should have a simple dipolar shape and should not vary as the input angles are varied.

b. Correlation with well-controlled magnetic signature measurements.

An example of this type of validation is given in Figure 25, where the calculated signature for a spheroidal model of a 105-mm projectile agrees very closely with measured signature data over an inert 105-mm projectile. This type of detailed profile comparison was conducted for numerous cases from the NRL ordnance signature database. Good correlation of calculated signatures with all cases from the signature database is achieved with the specified length and diameter of the ordnance as input parameters for the spheroid, except for the 60- and 81-mm mortars, where the length is modified to reflect the ferrous length and not the total ordnance item length. Detailed comparisons of magnetic modeling program signature calculations with measured signatures from the WES ordnance signatures database are also good and will be presented in a subsequent report.

Another validation example is shown in Figure 26, where color-filled contour maps of calculated signatures (bottom) are compared directly with measured signatures (top) for a 105-mm projectile at five azimuths in the horizontal plane. The agreement between the top and bottom in both specifics and generalities is quite good. Note that the calculated signatures for azimuths of 0 and 180 deg are identical as expected. The measured signatures for the 0- and 180-deg azimuth cases do show some differences, however it is not possible to determine from this one example if the differences are due to the fore/aft asymmetry of the actual ordnance item or is due to noise in the 180-deg azimuth measured case.

Phenomenology studies with magnetic modeling program

After validation, the magnetic modeling program can be used with some confidence for phenomenology studies and for multisensor integration investigations. A valuable use of a magnetic modeling program is to study or predict the detectability of a given ordnance item as a function of depth and orientation and to compare the detectability of different ordnance items. For example, graphs in Figures 27 and 28 compare the maximum positive TFM anomaly for a 155-mm projectile and a 500-lb bomb, respectively, as a function of depth to object center for three inclination and azimuth combinations (*Note the definitions for inclination (I) and azimuth (A) in Figures 27 and 28 used for all validation and phenomenology studies in this report*). With an estimate of site-specific magnetic noise, which includes both time-varying and background "clutter" components (including spatial variability), maximum depths for detection of given ordnance items can be estimated. For example, if the average magnetic noise level at a site is 5 nT and assuming that measurement spacing is adequate to delineate the anomaly signature, then a 10-nT anomaly

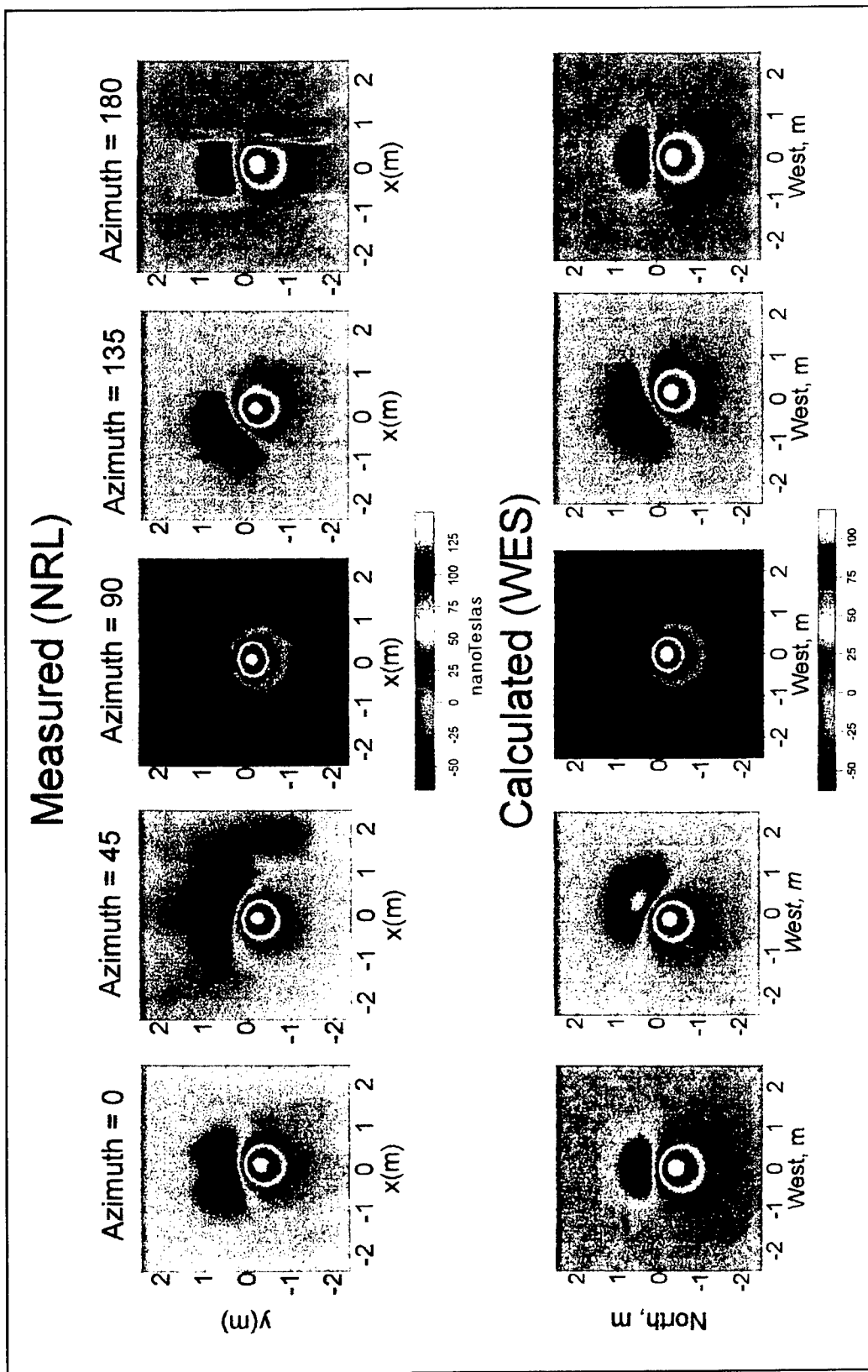
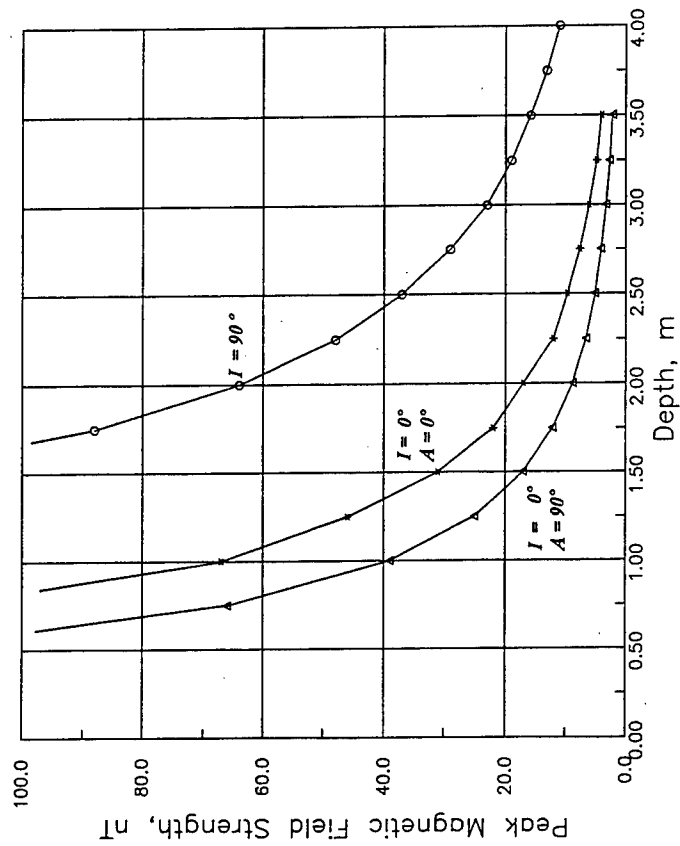


Figure 26. Validation example for measured (top) and calculated (bottom) TFM signatures for 105-mm artillery projectile, oriented horizontally and for azimuths of 0, 45, 90, 135, 180 deg. Depth below surface is 0.5 m and instrument height is 0.25 m

Maximum Positive Magnetic Field Strength Anomaly 155 mm Artillery Projectile Model

Earth's Field -- Inclination = 65; Magnitude = 55,000 nT
 Sensor Height = 0.5 m



Definition of Inclination (I)
 and Azimuth (A) of UXO Model

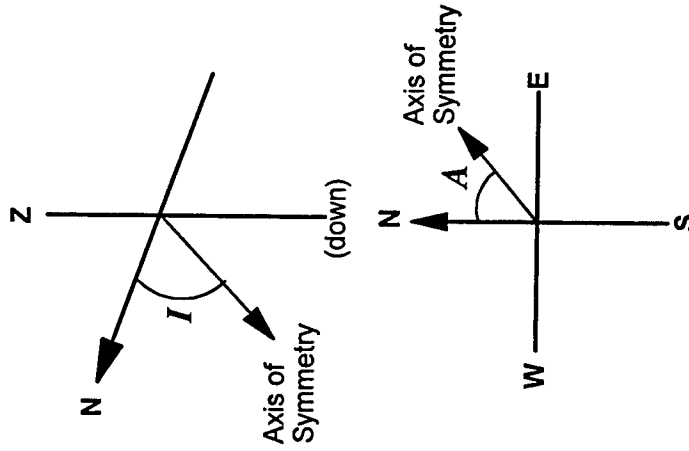
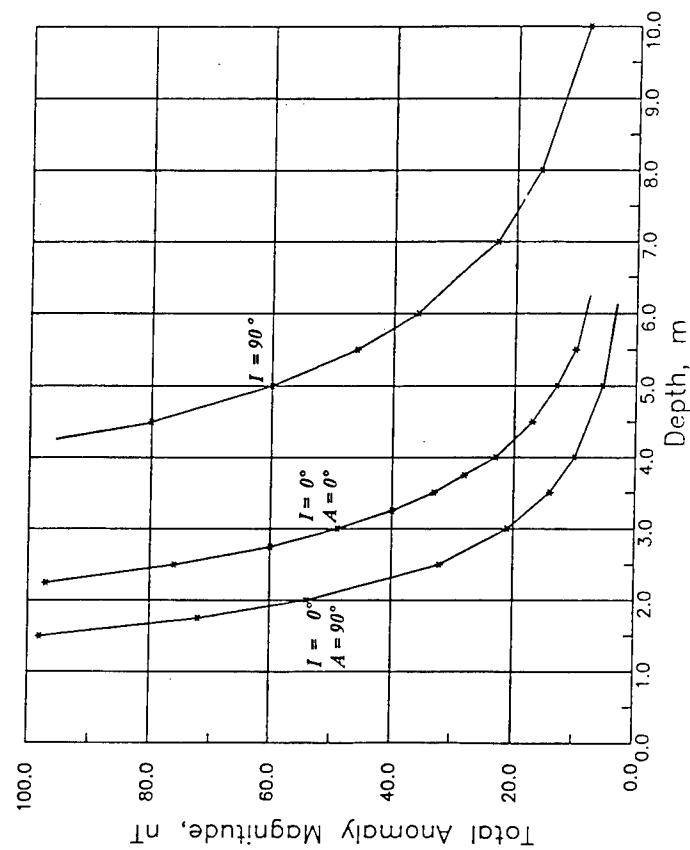


Figure 27. Maximum positive TFM anomaly calculations for 155-mm artillery projectile for three inclination and azimuth orientation combinations

Maximum Positive Magnetic Field Strength Anomaly

500 lb Bomb Model

Earth's Field -- Inclination = 65; Magnitude = 55,000 nT
Sensor Height = 0.5 m



Definition of Inclination (I)
and Azimuth (A) of UXO Model

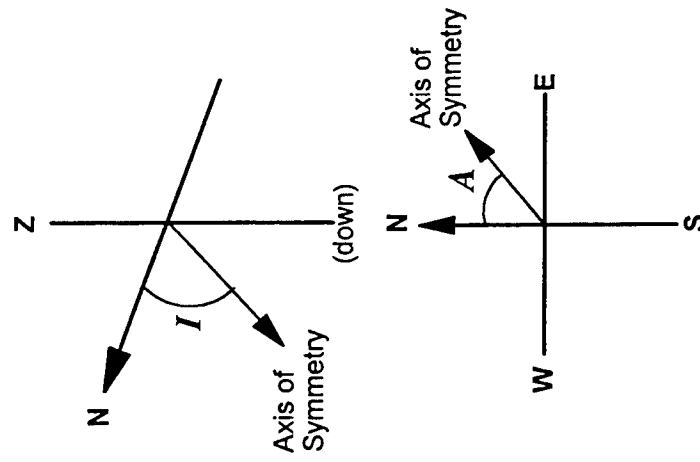


Figure 28. Maximum positive TFM anomaly calculations for 500-lb bomb for three inclination and azimuth orientation combinations

(two times the average noise level) is reliably detectable. Using the 10-nT threshold for detection and Figure 27, a 155-mm projectile is detectable to a depth of approximately 2 m for the worst-case orientation (inclination = 0, *relative to horizontal*, and azimuth = 90 deg) and to a depth of approximately 4 m for the best-case orientation (inclination = 90 deg). Similarly, using the 10-nT threshold and Figure 28, a 500-lb bomb is detectable to a maximum depth of approximately 4 m for the worst-case orientation and to a maximum depth of approximately 9 m for the best-case orientation.

Another example of phenomenology studies is illustrated in Figure 29. This example dramatically illustrates the effects of orientation/demagnetization effects caused by the orientation of the elongated ordnance (155-mm projectile) relative to the earth's magnetic field. For both cases in Figure 29, the inclination of the earth's field is 65 deg, which is typical of the inclination at Fort Carson, CO, and Fort A. P. Hill, VA. In the first case (left), the inclination of the spheroid model (45 deg relative to horizontal) is in the approximate direction of the earth's field, and the TMF anomaly signature is dipolar in appearance with a peak positive magnitude of nearly 240 nT. For the second case (right), the inclination of the spheroid model (-45 deg relative to horizontal) is approximately perpendicular to the Earth's field, and the TFM anomaly signature is monopolar in appearance with a peak positive magnitude of only 110 nT (less than one-half the magnitude of the first case). This example makes it dramatically obvious why a simple magnetic dipole (equivalent sphere) inversion can result in significant errors in ordnance depth and/or size.

Electromagnetic Induction Modeling Considerations

Background

Due to the complexity of general solutions of EMI responses for realistic UXO geometries, this section only briefly reviews work of others and preliminary investigations conducted during the present effort. Rigorous analytical solutions to date are for simple geometries, e.g., layered earth, spheres, plates, and circular cylinders (McNeill and Bosnar 1996, Barrow et al. 1996, Ward and Hohmann 1987). Das et al. (1990) extend consideration to a prolate spheroid but point out that rigorous analytical solutions do not exist for the general case of a conducting, permeable spheroid. Analytical solutions often require numerical evaluation or approximation but do not require problem discretization, as in finite difference, finite element, boundary integral, or hybrid computational techniques. Numerical modeling, involving space, time and/or frequency discretization, complex/realistic geometries, and the full range of physical properties and processes, is notoriously computationally intensive (Hohmann 1987, Laveley 1996); currently this type numerical modeling is reserved for phenomenological studies but is not practical for the repetitive, iterative calculations generally required for geophysical inversion. Thus numerical modeling and even analytical solutions resort to approximations of various types: asymptotic approximations; quasi-static solutions; low-frequency or high-frequency limit solutions for FDEM; early-time or late-time

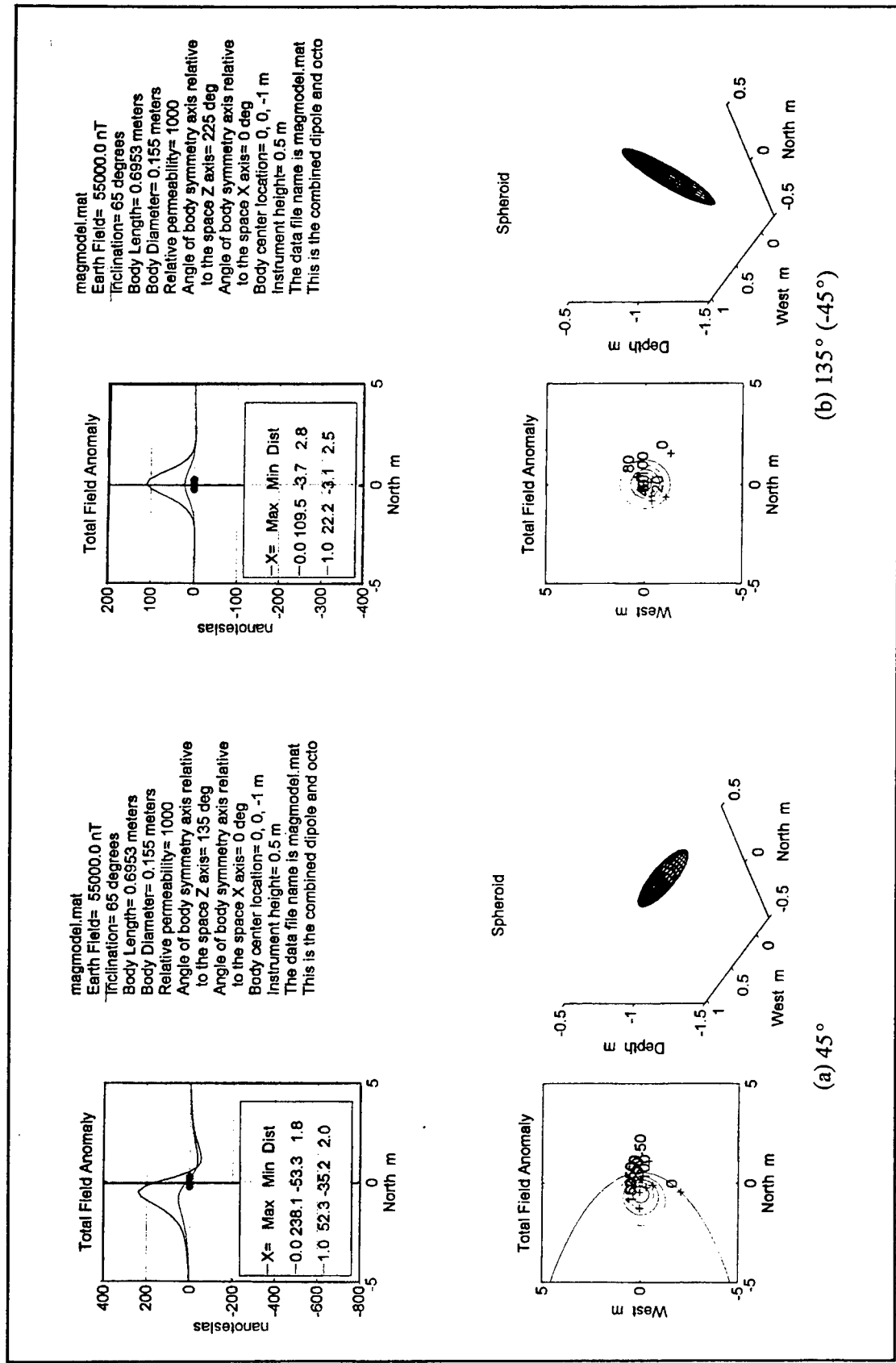


Figure 29. Example of phenomenology study. Magnetic model signature calculation for 155-mm artillery projectile with inclination (a) approximately in the direction of the earth's field inclination and (b) approximately perpendicular to the earth's field

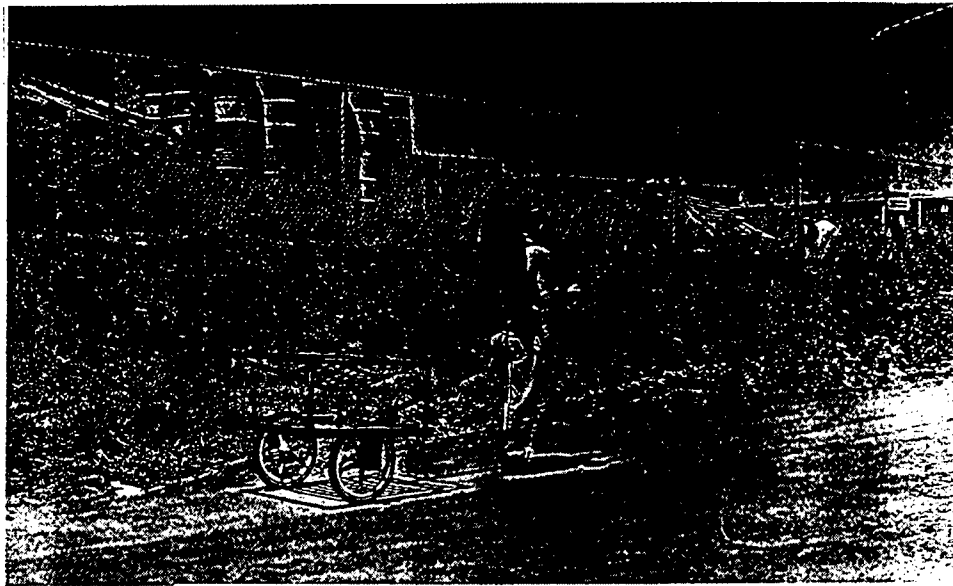
solutions for TDEM. Many of these approximations in time or frequency domains are equivalent for different combinations of physical properties (Wait 1982, Butler and Fitterman 1986, Butler 1986, Ward and Hohmann 1987).

As discussed in Chapter 2, EMI methods, particularly TDEM methods, are used extensively for UXO detection and mapping surveys. An extensively used TDEM system, the Geonics EM61 standard system consists of a 1-m \times 1-m transmitter (Tx) coil and two 1-m \times 1-m receiver (Rx) coils, with one Rx concentric to the Tx and the second Rx offset 0.4 m vertically (Figure 30a). A specialized, nonstandard 0.5-m \times 0.5-m Tx and Rx coil EM61 system was used in the DARPA program. The EM61, like many TDEM systems, operates by rapidly turning off a current in the Tx and detecting transient (decaying) magnetic fields at the Rx's from induced current transients in the subsurface. The physics of the transient induction process and descriptions of general purpose TDEM systems are reviewed by Butler and Fitterman (1986), and the induction process in compact, conductive, permeable metallic objects outlined descriptively by McNeill and Bosnar (1996). A schematic of the transmit, induction, and measurement process is illustrated in Figure 30b-d.

General purpose TDEM systems sample the transient signal with many time-gates or channels, typically 20 to 30. The standard EM61 measures the vertical component of the secondary field and integrates the transient over one time-gate extending from 0.47 to 0.87 ms; the time gate is selected to enhance sensitivity to metallic objects (for the NRL MTADS system described previously, the time-gate is moved closer to the transmit pulse for even higher sensitivity; Nelson, McDonald, and Robertson, 1997). The prototype TDEM system (EM61-3D) used at the DARPA sites records 20 time channels for each of 3 orthogonal Rx coils (the vertical and 2 horizontal components).

A decay curve recorded with the vertical component Rx coil of the prototype EM61-3D system is shown in Figure 31, with the time-gate (window) of the standard EM61 indicated. The decay curve in Figure 31 was recorded over a 20-cm \times 20-cm aluminum plate buried at 5 cm (approximately 45 cm below the Tx) at one of the DARPA sites. The two Rx measurements for the standard EM61 give two integrated magnitude measurements and their difference (or vertical gradient) as a function of position as the system is pulled along the ground surface. Typically, the EM61 data are displayed in map form, and signatures of shallow metallic objects are apparent, allowing accurate location of the positions of the objects. Depth estimates are determined from the spatial wavelengths of the signatures or based on gradient information from the top and bottom Rx's. Current efforts apply empirical adjustments based on measured signatures to spherical model predictions to account for ordnance shape and orientation effects (Barrow et al. 1996 and 1997) with increasing success.

For the limited information acquired with the standard EM61 and typical FDEM systems used for UXO surveys that operate at only one or two frequencies, detection, location, depth estimates, and limited discrimination capability likely represent the maximum capability. Additional capability for discrimination is possible when the EMI data are integrated with other geophysical data (Chapter 2). Another possibility, for increasing discrimination and identification/classification capability, is to obtain more information with the EMI systems. Two enhanced capability prototype EMI systems (first used for UXO applications during the DARPA program) are described in more detail in



a. Photograph of standard EM61.

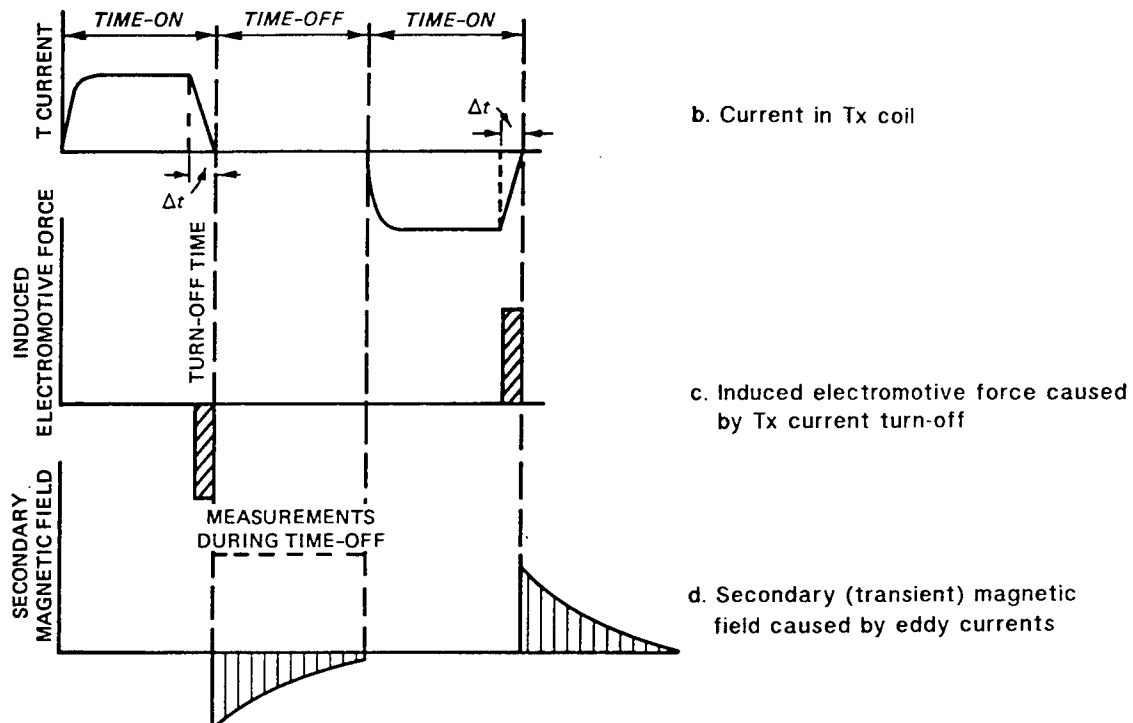


Figure 30. (a) Photograph of the standard EM61; (b-d) schematic of the transient induction and measurement process

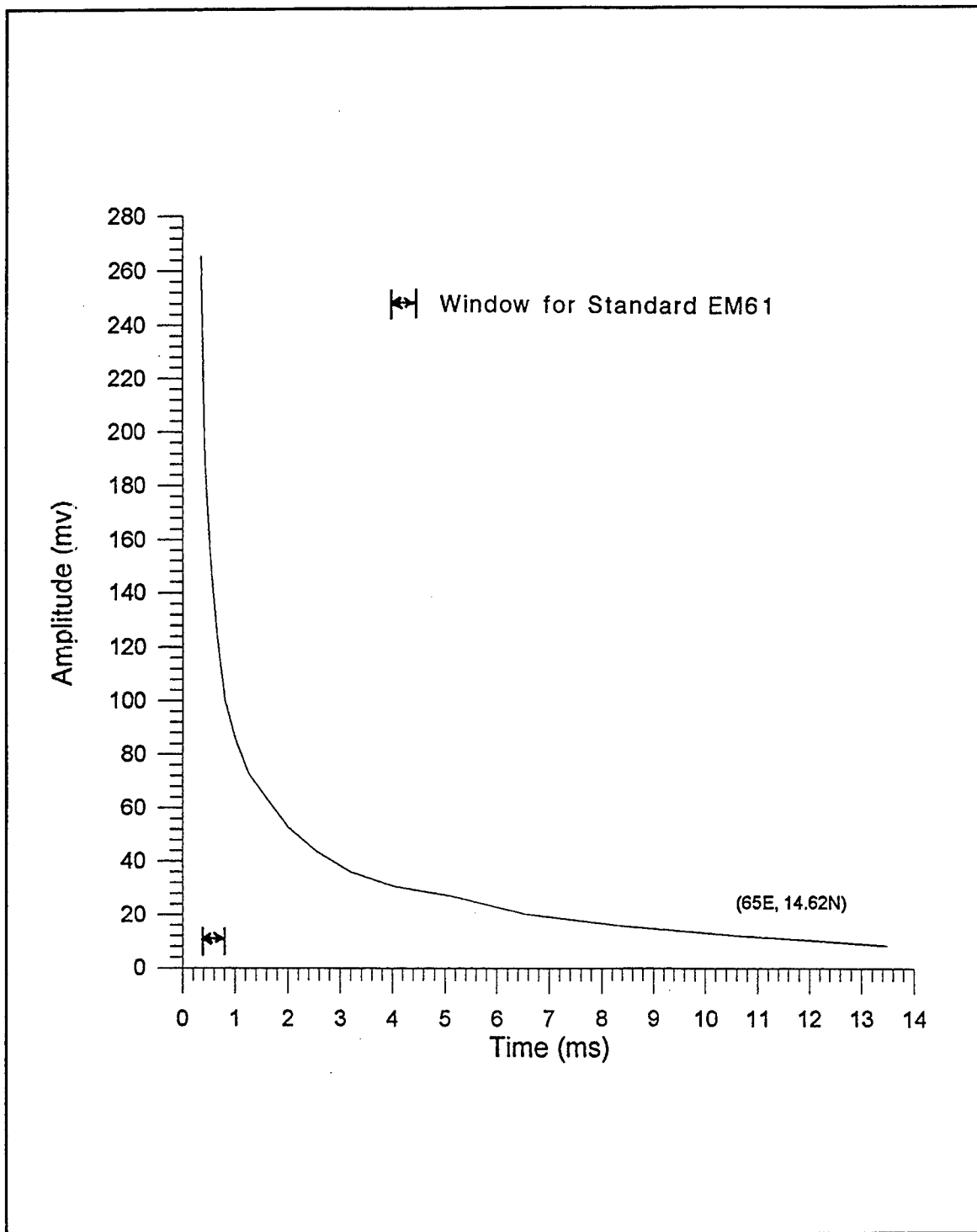


Figure 31. Vertical component decay curve recorded with EM61-3D over an aluminum plate (20 x 20 cm) buried at 5 cm at a DARPA site; time window for standard EM61 is indicated

the next chapter. These enhanced capability systems include a multichannel, multicomponent TDEM system and a multifrequency FDEM system. EMI modeling and analysis capability during the current effort is addressed specifically to the multichannel, multicomponent TDEM system; since it likely has the most general applicability, and then modeling the standard EM61 signatures of ordnance is a special case.

Three techniques for modeling the full time domain EMI response of a compact, conductive, permeable ordnance object are (1) simple model-based approach with empirical adjustments for time response (quasi-empirical approach), (2) complete physics-based analytical time domain solution for well-defined, realistic geometry (e.g., a prolate spheroid), and (3) a discretized, numerical complete solution for actual ordnance geometry. Preliminary investigations of a quasi-empirical approach are presented here. The capability allowed by approach (2) would greatly enhance the feasibility of true joint inversion for multisensor integration and should be aggressively pursued. Recently initiated efforts address approach (3) under a variety of programs; these efforts will significantly advance understanding of TDEM phenomenology and enable parameter studies, although utility of these approaches as tools for data inversion is uncertain.

Quasi-empirical TDEM modeling considerations

McNeill and Bosnar (1996) discuss the response of compact, simple geometry objects to static and transient EM fields. Specifically, they reference spheres, plates (discs), and rods (or cylindrical shells). Also, the contributions of finite electrical conductivity and finite magnetic permeability to the overall EMI response are considered. To model these simple geometry objects, appropriately placed and oriented magnetic dipoles reproduce the key features of the quasi-static spatial signatures. For elongated or flattened objects such as rods and discs, the EMI response is distinctly different depending on the orientation of the object relative to the inducing magnetic field. For the long axis of rods perpendicular to the inducing field or the plane of discs perpendicular to the inducing field, the response of permeable (ferrous material) and nonpermeable objects are similar; when the inducing field is abruptly turned off, a dipolar response due to decaying eddy currents (conductivity response) dominates. For an inducing field parallel to the long axis of rods or parallel to the plane of discs, the eddy current response is small, but a dipolar-like polarization response is induced in permeable objects; for this case the response is virtually zero for nonpermeable objects. For a general orientation of the inducing field, the response of plates and rods can be approximated by orthogonal dipolar responses in the two symmetry directions of the objects. McNeill and Bosnar (1996) present measured time decays of the induced fields in ferrous and non-ferrous spheres, plates, and cylindrical shells and actual ordnance items; and for the cylindrical shells and ordnance items, the responses for the inducing field parallel to and perpendicular to the long axes are given.

McNeill¹ proposes an initial approach for time-domain response of UXO that utilizes orthogonal dipoles, along and perpendicular to the long axis, to represent the total EMI *spatial* response (see also Das et al. 1990). The procedure then modifies the relative contribution of each dipole according to the *measured decay characteristics of specific ordnance items*, determined with the ordnance item parallel to and perpendicular to the primary inducing field of an EM61 Tx. For each calculation location (X,Y), the inducing field (which is assumed uniform at the object position) is resolved into components along the orthogonal dipole orientations, which simulate the azimuth and inclination of the ordnance. Indication of the capability of this approach to replicate general observations of TDEM signatures and spatial signature evolution with time is illustrated in Figure 32 from McNeill¹ (155-mm projectile simulated at depth of 2 m, inclination 45 deg, and azimuth 45 deg). The upper set of contour plots (2-m \times 2-m area) is the root square magnitude of the horizontal field, i.e., $B_h = (B_x^2 + B_y^2)^{1/2}$. Both the horizontal and vertical components indicate the target azimuth (45 deg). The effect of excitation of the perpendicular dipole is noted at early time, which decreases with time. The long axis excitation dominates at late time.

The WES implementation of this quasi-empirical approach to TDEM signature modeling, allows further investigation of the signatures as functions of the depth, orientation parameters, and time evolution. In Figure 33 for example, the early time (0.3 ms) dip response of the model is investigated, for a depth of 2 m and azimuth of 45 deg. The model signatures exhibit an intuitive transition from bi-orthogonally symmetric (symmetric about both the azimuth direction and perpendicular to the azimuth) for a dip of 0 deg, proceeding to axially symmetric about the 45 deg azimuth for a dip of 45 deg, and finally to completely circularly symmetric for a dip of 90 deg. The azimuth response of the model is illustrated in Figure 34, for azimuths of 45 and 90 deg and a dip of 45 deg. As the azimuth is changed, the signature components maintain shape and magnitude, as required. Future plans for this model include efforts to determine rational procedures for including physical size of the object in the model (currently the dipole size parameters are normalized to unity and size only enters in the measured time decay over actual size ordnance) and validating depth and orientation signature dependence by correlation with measured signatures.

Phenomenological Modeling and Multisensor Data Integration

Geophysical parameter space plots

Selected examples of multisensor data presented previously illustrate data integration procedures, and a specific type of analysis in geophysical

¹ Personal Communication, July 1997, J. D. McNeill, Geonics, Limited, Mississauga, Ontario, Canada.

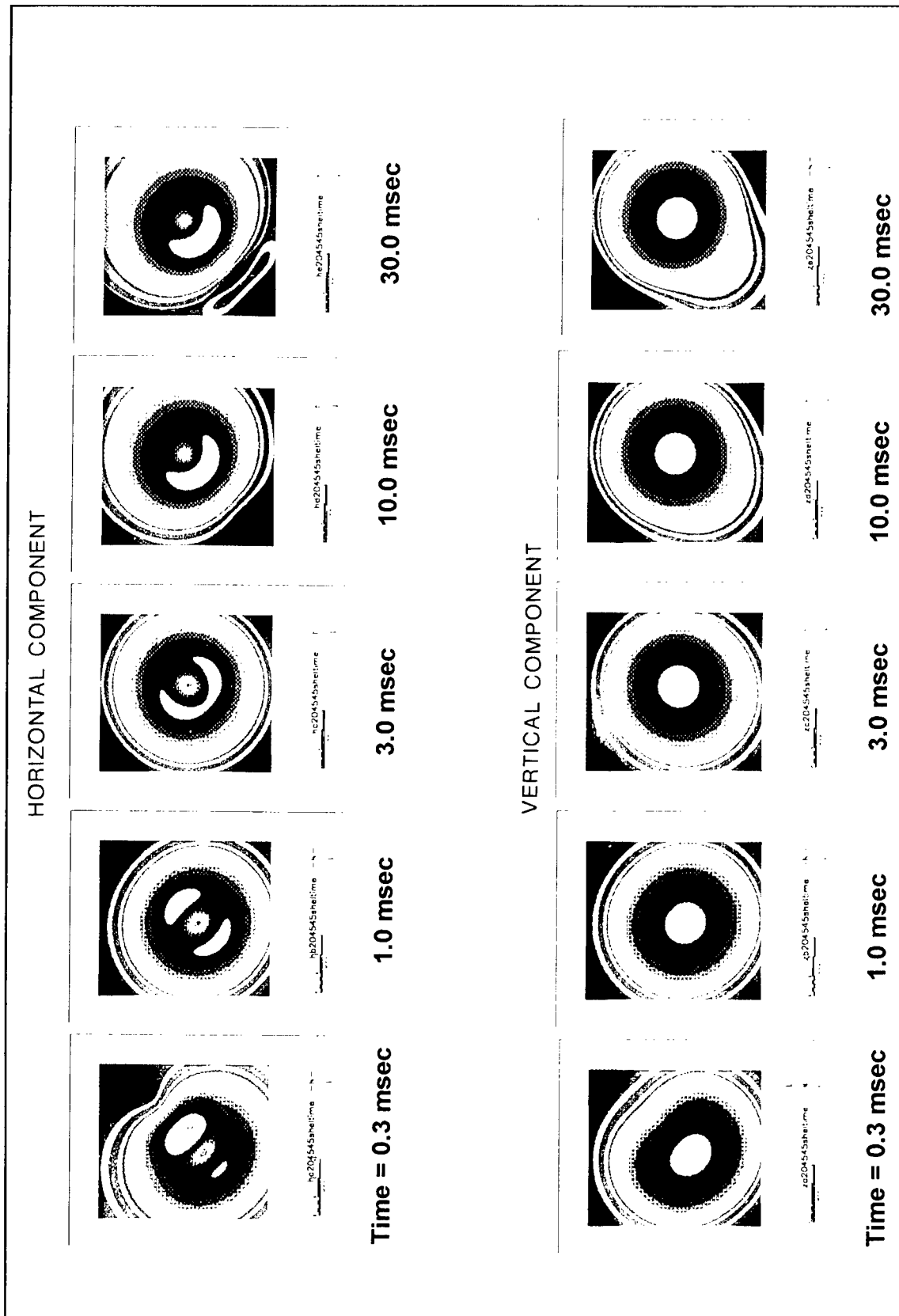


Figure 32. Theoretical calculations of the spatial and time EMI response of a 155-mm ordnance item. Depth = 2 m; Azimuth = 45 deg; Inclination = 45 deg. The top plots are the root mean square of the horizontal components. Each plot area is 2 m x 2 m (McNeill¹)

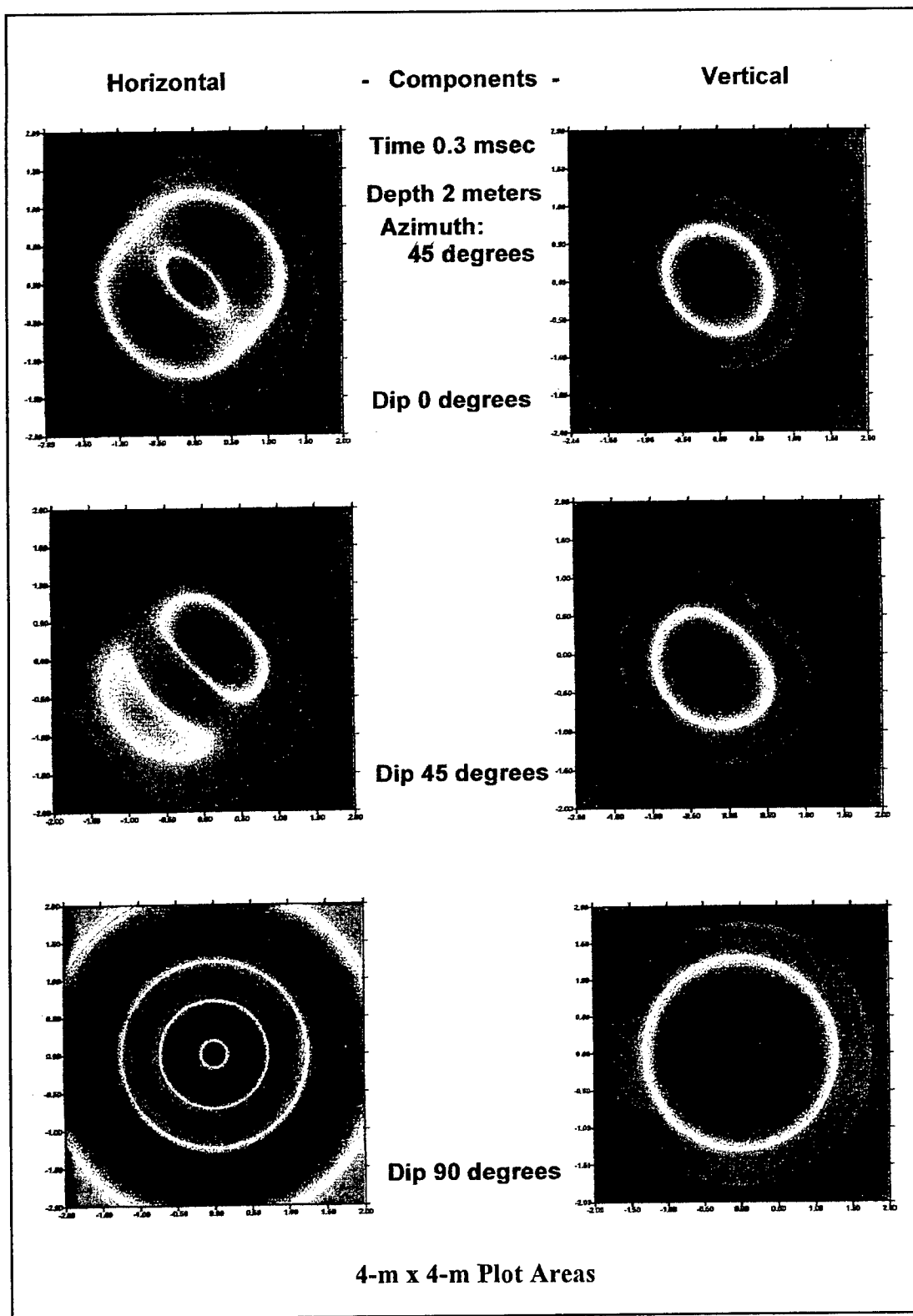


Figure 33. Theoretical early-time (0.3 msec) EMI response for 155-mm projectile model, depth = 2 m, azimuth = 45 deg ; model dip response

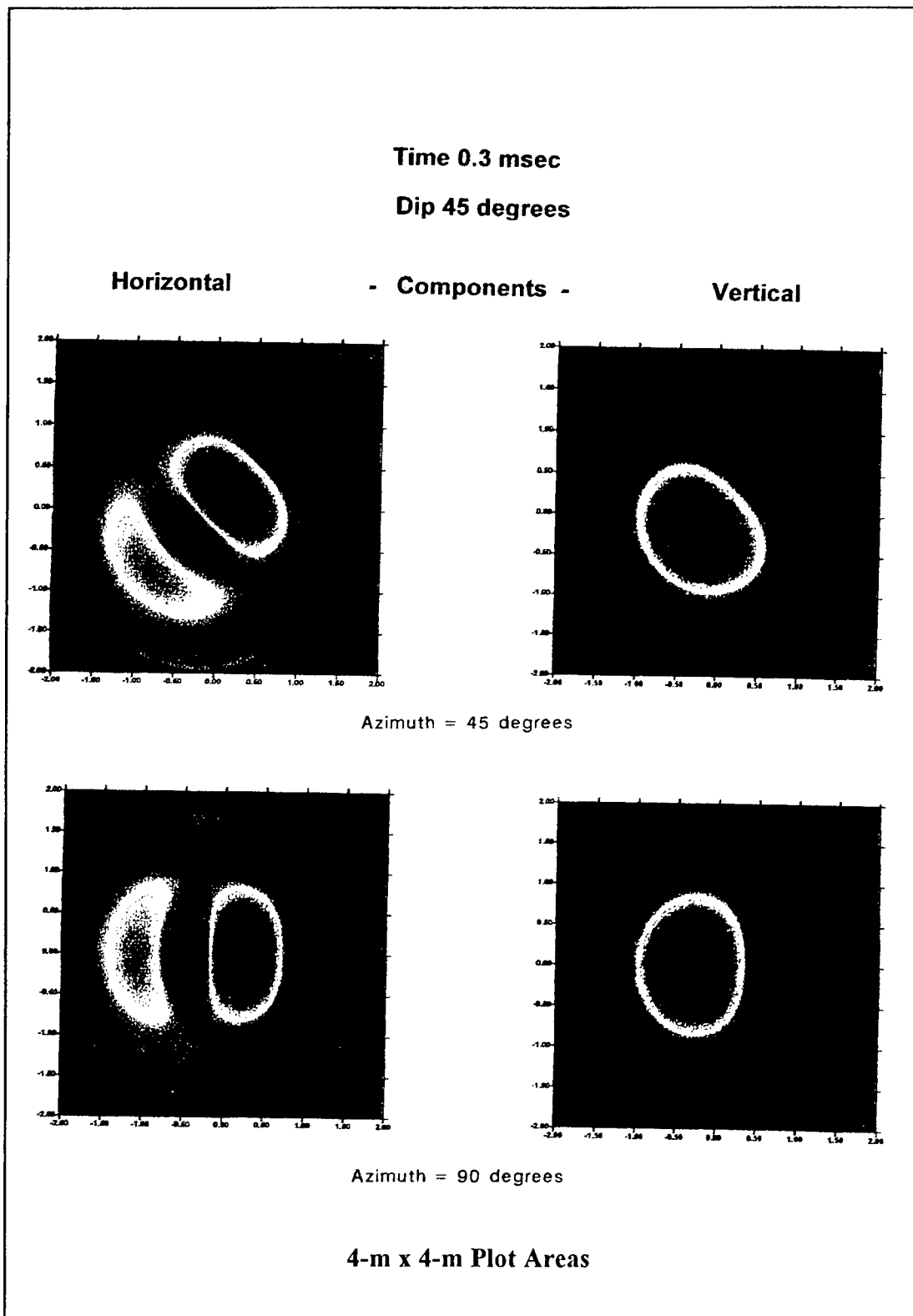


Figure 34. Theoretical early-time (0.3 msec) EMI response for 155-mm projectile model, depth = 2 m, dip (inclination) = 45 deg; model azimuth response

measurement/parameter space now illustrates the importance of developing phenomenological modeling capability. The role of model-based analyses and interpretation of multisensor geophysical data in general is discussed extensively in Chapter 2. An example of TFM and TDEM data from the NRL ordnance signature library in Figure 35 serves to illustrate the key points (4 m \times 4 m area for top plots). The data are for a 105-mm projectile at depth 0.49 m, inclination 0, and azimuth 90 deg. The TFM data in the left plot is the same as one of the cases in Figure 26, used to validate the magnetic modeling program. The TDEM data in Figure 35 is similar and consistent with the TDEM early-time modeling examples in Figures 32 through 34 (except for the obvious difference in ordnance size and inclination). Thus with some advances in understanding and modeling capability for the TDEM case, both of the sensor datasets in Figure 35 can be modeled, allowing a model-based interpretation. The middle plots are principal N-S profile plots across the center of the signature in the top plots. The bottom plot is a measured parameter space plot, which simultaneously portrays (integrates) the amplitude and phase relationships of the two signature profiles. Parameter space plots for four cases are given in Figure 36 for two orientations of the same ordnance item and for two ordnance items with the same orientation; depth is approximately the same for all four cases.

Parameter space plots have diagnostic characteristics, allowing interpretation of the object(s) causing the multisensor anomalies with fewer known parameters and/or assumptions (e.g., Butler 1995). Parameter space analyses techniques are not limited to 2-D spaces, with a 3-D space from three datasets, e.g., TFM, TFG, and TDEM, a common possibility. Also, parameter space plots can be in terms of extracted key parameters, such as the example in Figure 9. In terms of multisensor integration by nonmodel based approaches such as neural networks or "fuzzy logic," the parameter space plot collapses multisensor signature information to a form better adapted to a holistic type analysis. For model-based approaches to multisensor (multimethod) integration, assumption of a common geometry for each dataset allows direct solution for the common model parameters, e.g., length, diameter, depth, inclination, azimuth. The model-based solution proceeds from either (a) a geometrical analysis of the parameter space figure or (b) iterative forward modeling (inverse solution in parameter space). Forward modeling capability for each geophysical method, once validated as discussed previously, allows systematic study of parameter space geometries in a more rigorous and comprehensive manner than relying on measured data alone.

Manual implementation of proposed multisensor integration algorithm

The NRL Twentynine Palms MTADS data afford opportunities for multisensor integration investigations. Figure 37 shows an approximately 36-m \times 36-m area display of TFM, TFG, and TDEM datasets (McDonald et al. 1997). The yellow circles in Figure 37 indicate the location of a group of closely spaced inert 60-mm mortar rounds. To illustrate the role of phenomenological modeling in UXO detection and discrimination, a manually implemented version of the proposed algorithm in Figure 23 is applied to the geophysical

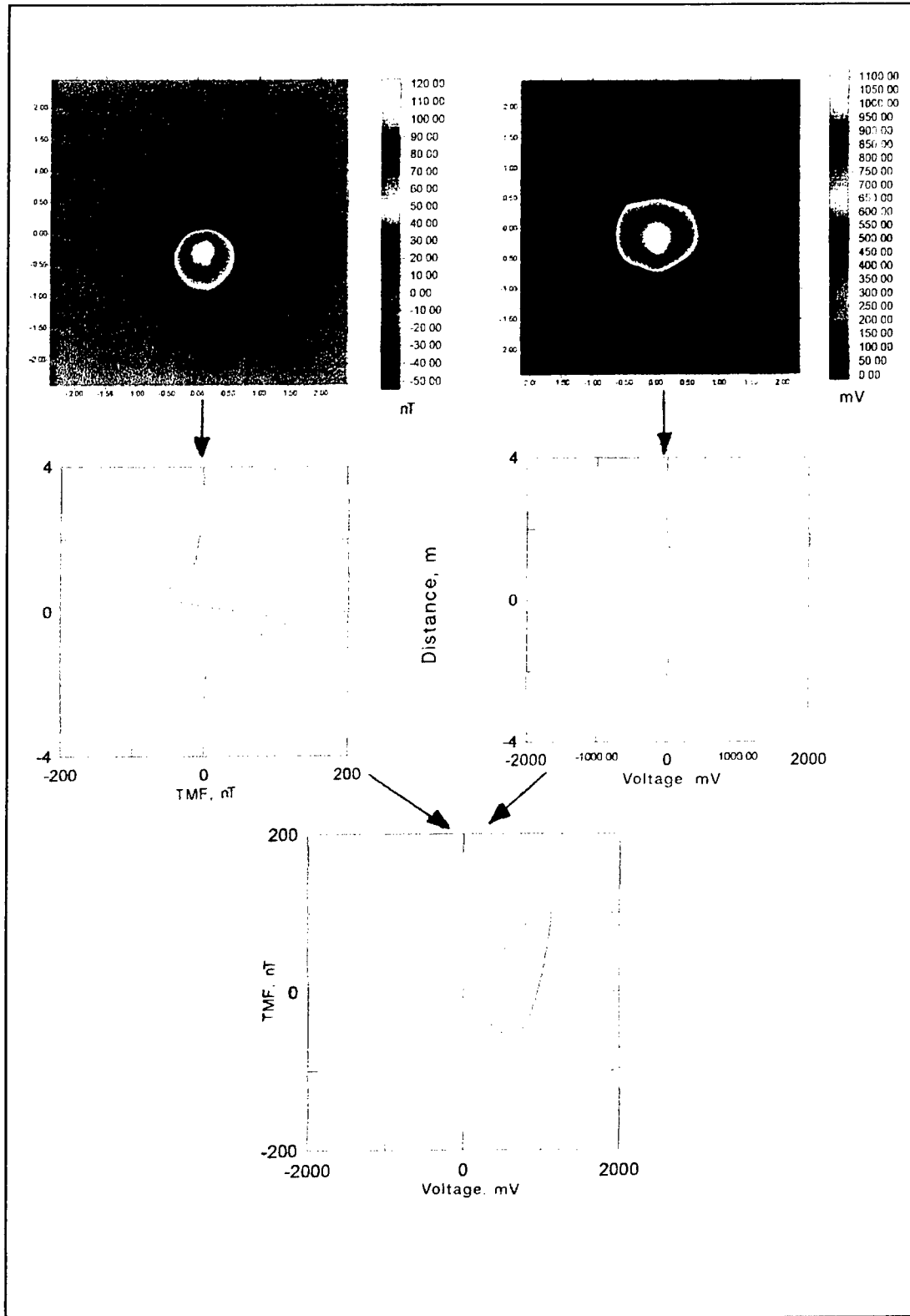


Figure 35. Multisensor datasets from the NRL ordnance signature library, TFM to left and TDEM to right; 105-mm projectile at 0.5 m depth, 0 deg inclination, 0 deg azimuth. Lower graph is geophysical parameter space plot from the principal profiles (center plots) across the ordnance

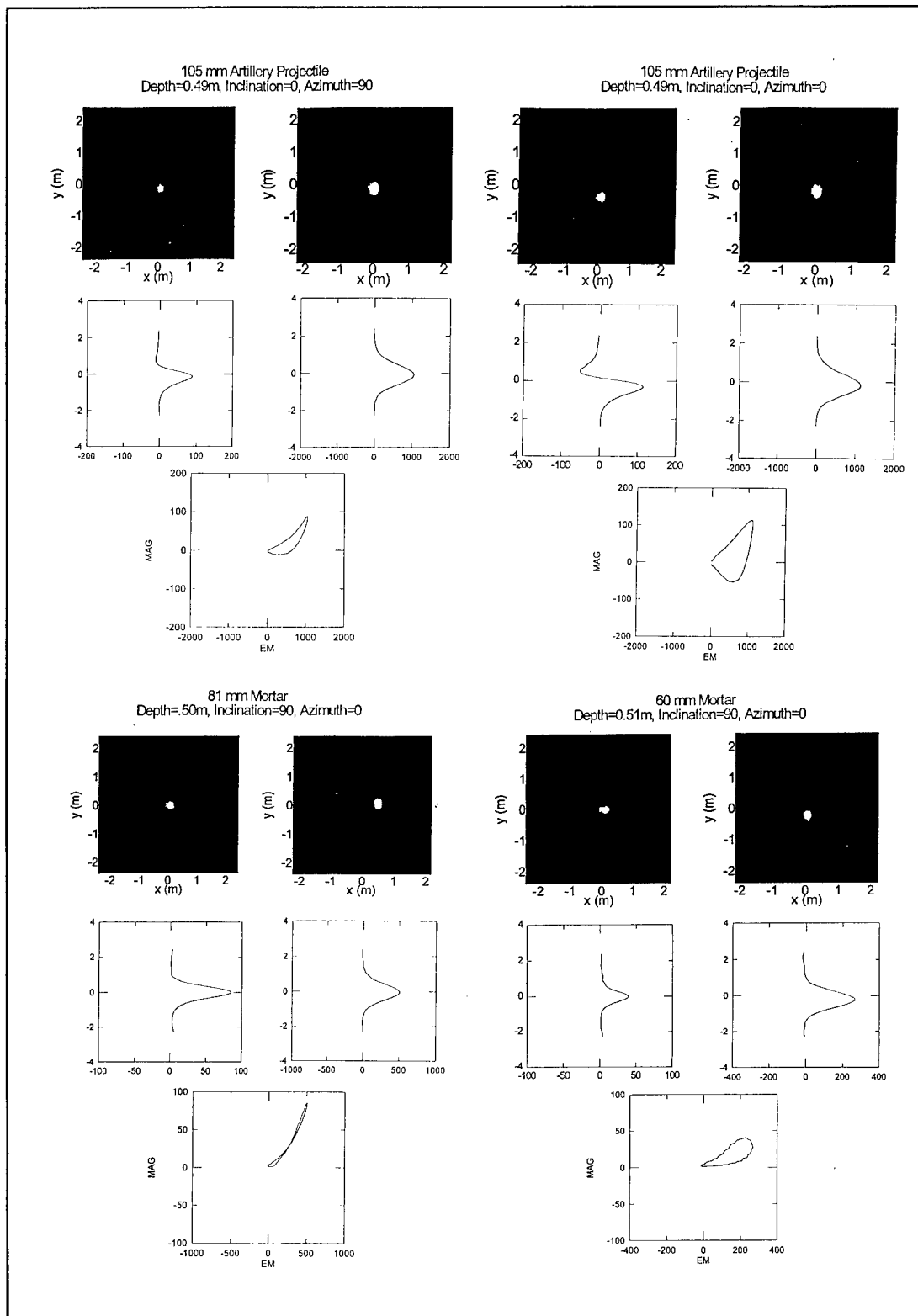


Figure 36. Parameter space plots for TFM and TDEM datasets from NRL ordnance signature library. Top two sets of plots are for 105-mm projectiles with identical depths and inclinations but different azimuths (0 and 90 deg). Bottom two sets of plots for 60-mm (left) and 81-mm (right) mortars with identical depths, azimuths, and inclinations

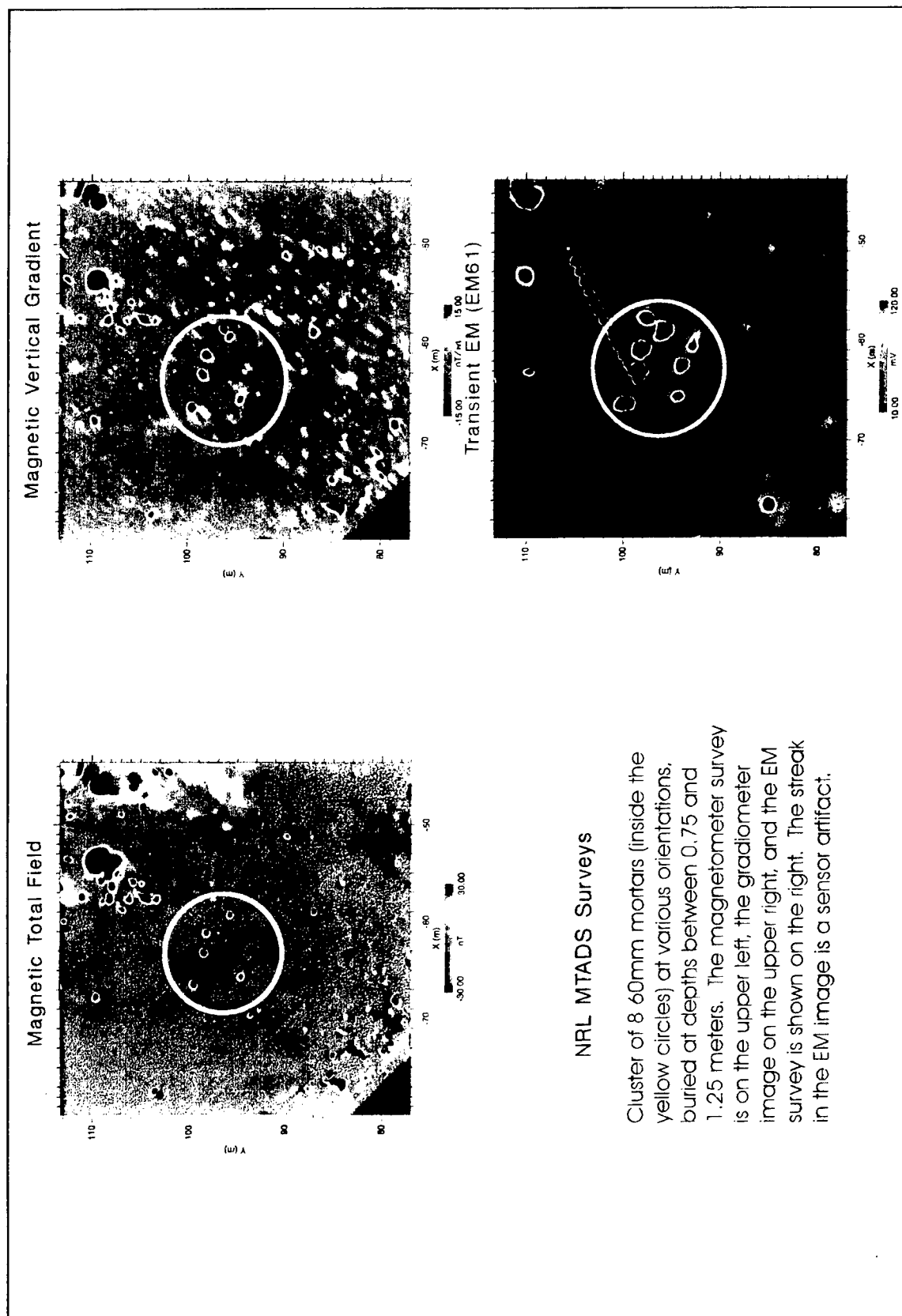


Figure 37. NRL MTADS surveys (TFM, TFG, TDEM) over cluster of eight 60-mm mortars

anomalies caused by the shallow buried 60-mm mortars (Figure 38). All eight anomalies caused by the mortar rounds are shown dramatically in the TDEM data, while two of the eight mortars are barely visible in the TFM and TFG data with the selected plotting thresholds and contour intervals. The TDEM dataset is used to estimate location and depth for the eight anomalies. Locations are estimated at the centers of the TDEM anomalies. Depths are estimated from anomaly magnitudes and spatial wavelengths, knowing that all targets are 60 mm and buried at shallow depths. Orientations for the eight targets are estimated from characteristics of the magnetic anomalies, and for illustrative purposes, all mortars are estimated to lie at an inclination of 0 deg relative to horizontal and to have azimuths of 0, 45, or 90 deg. Using the target estimates and the known Earth's field, *magmod* is used to compute the magnetic signatures of the eight mortars.

To compute the combined/composite total magnetic field of the eight mortars, a MATLAB® script *combine2* is executed. Each case is computed separately using *magmod* and each saved with distinct output file names. The eight output files from *magmod* are input to *combine2*, which computes the composite field. The composite field output from *combine2* is subsequently input to the *magmod* to display the output composite file. After minor manual iterations with *magmod* the composite predicted TFM field is shown in Figure 39. The key details, of the TFM map of the 60-mm mortars in Figure 37, are replicated in Figure 39.

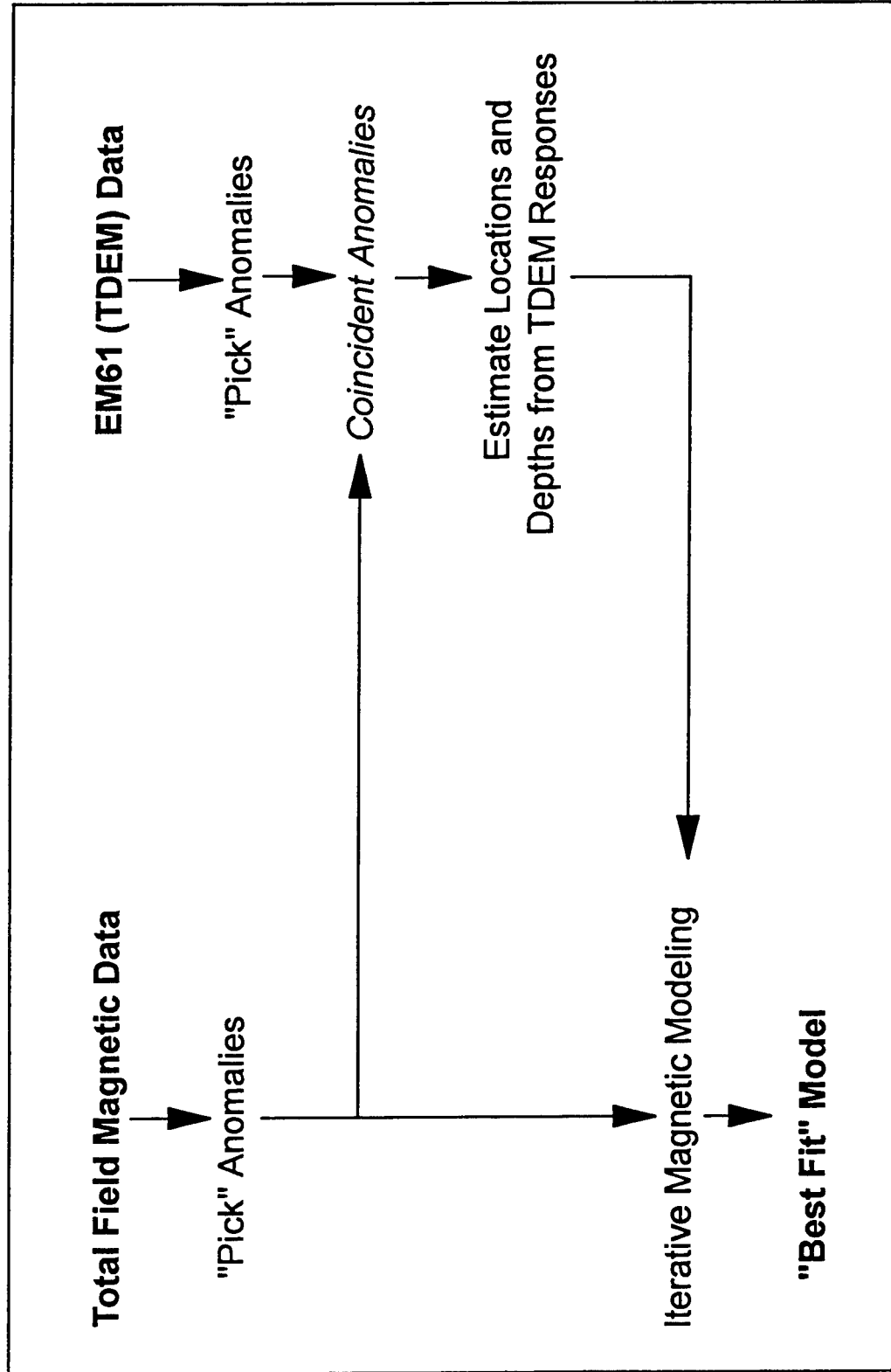


Figure 38. Flow diagram for manual implementation of simplified version of a proposed algorithm for multisensor data integration

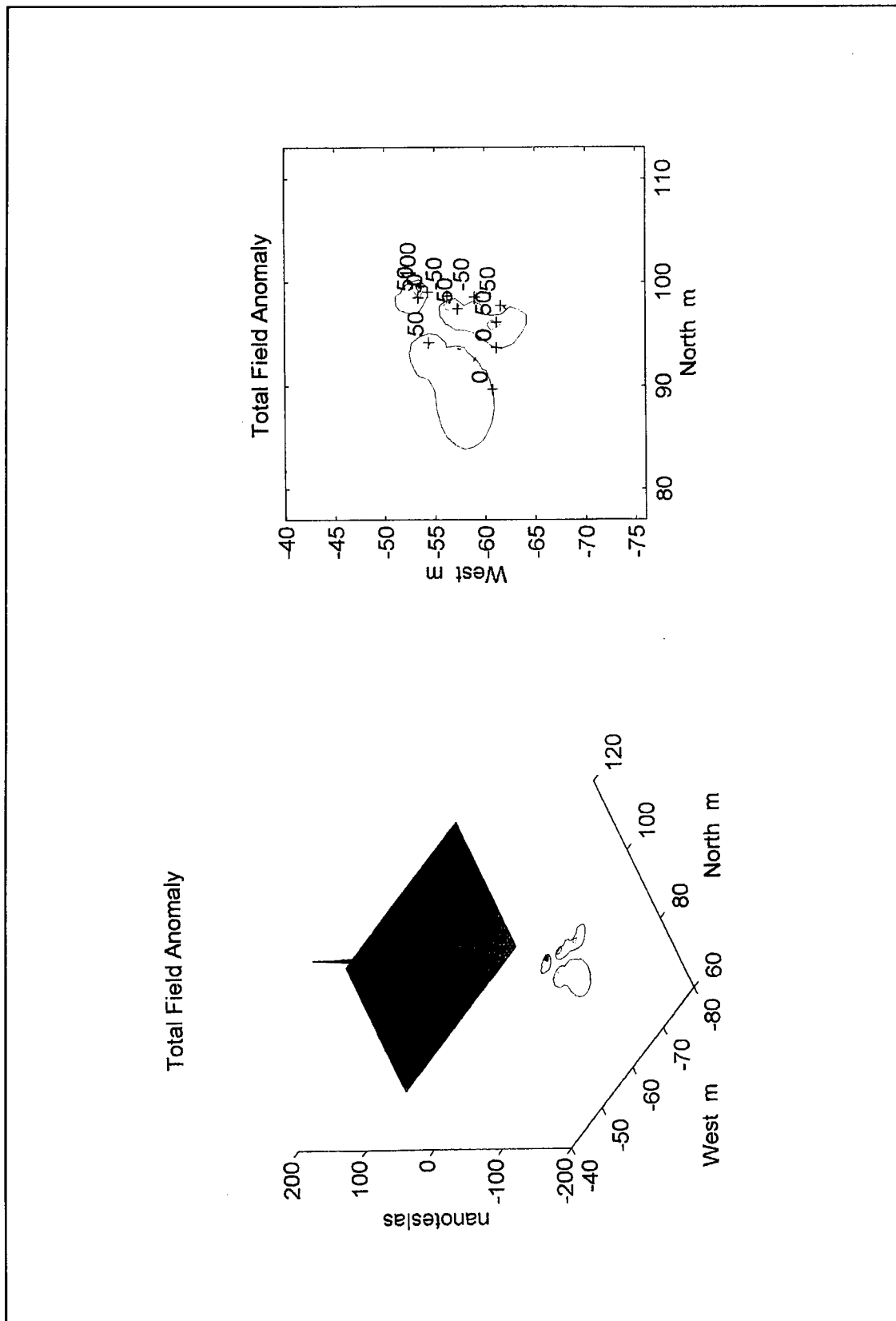


Figure 39. Result of manual implementation of simplified multisensor integration algorithm (Figure 38) to replicate total magnetic field of cluster of eight 60-mm mortars measured by NRL MTADS system at Twentynine Palms. Ordnance locations and depths estimated from TDEM images (Figure 37). Initial orientation estimates from TFM images, then manual iteration of *magmod* to replicate general features of TFM images

7 Considerations of Emerging Technology for UXO Applications

Introduction

The potential importance of innovative, emerging geophysical technologies for advancing UXO discrimination and identification or classification is discussed in Chapters 1 and 2 and is illustrated in this chapter. New and emerging technologies that may allow improved discrimination and ultimately identification of UXO are:

- a. Multichannel, multicomponent TDEM systems.
- b. Multifrequency, multicomponent FDEM systems.
- c. Multicomponent vector magnetometers.
- d. Tensor magnetic gradiometers.
- e. Near real-time, high-resolution microgravimetry.
- f. Acoustic wavefield imaging.

In this chapter, the potential contribution of emerging technologies a and b above is assessed by examples from data acquired at the DARPA sites. The emerging technology TDEM and FDEM systems applied at the DARPA sites were prototype systems; and, as a result of the lessons learned from these first data collection efforts, needed improvements are identified. *Some data, particularly for the prototype TDEM, were noisy and do not represent the ultimate potential of the technology.* In this chapter, selected display and analyses approaches are explored for the data from the prototype systems. In no way is the total potential of the emerging technologies for UXO discrimination and identification assessed or achieved in this report.

Multichannel, Multicomponent TDEM System

Background

A prototype multichannel, multicomponent TDEM system, designated the EM61-3D¹, was used for data acquisition at the four DARPA sites (Parsons Engineering Science, Inc. 1997). The EM61-3D utilizes the standard EM61 Tx coil (1 m × 1 m) with three orthogonal, 0.5-m-diam Rx coils within the Tx, to measure the vertical and two horizontal components of the secondary induced transient field (i.e., a multisensor system). The system uses a standard TDEM receiver electronics package which samples the transient with 20 channels (gates), and records a full set of 60 measurements at each surface location (0.4-s intervals). Figure 40 shows the EM61-D in operation at Fort Carson, Colorado, and gives the times of the 20 gates at each of the two base operating frequencies (repetition rate) of the system. Most of the surveys were conducted at the 7.5-Hz repetition rate and transients (decay curves) from three Tx waveforms were stacked to produce each complete record.

Data acquired with the EM61-3D over one of the 1-hectare DARPA sites results in a very large data volume. The present effort concentrated on ways of looking at small segments of the data volume to assess interpretive procedures for UXO detection, discrimination, and identification. All examples presented below are from surveys at the Seabee and Turkey Creek sites at Fort Carson, Colorado.

Single-component analyses procedures

Single-component maps. One obvious way of examining the data is to produce site maps of individual components for selected time gates. For example, channels (time-gates) 2 to 5 span the standard EM61 window, and channel 3 is approximately in the center of the integrated time-gate recorded by the standard EM61. Anomaly features are observed in the time-gate maps, including registration targets and other known features. There is obviously background response levels due to the geology of the sites, cultural clutter, and a significant level of system noise; this suggests applying a low-cut amplitude threshold to enhance anomalies caused by buried metallic objects (similar to the GIS layer query in Figure 17). For the three components and all time-gates, there will be 60 site maps for each site. With this rich data set, there are considerable possibilities for image processing type analyses for background subtraction and localized anomaly enhancement, change detection as a function of time, and “false-color” type images which combine the three components at selected times.

Three-axis representation of single-component complete decay curves. A second procedure is to examine profiles of the complete time decay for selected profile lines. The three-axis representation in Figure 41 is for the vertical component recorded along segment of a north-south line at the Seabee Site. The

¹ Geonics, Limited, Mississauga, Ontario, Canada.



EM61-3D Time Gate Locations (in ms)

Gate	7.5 Hz, ms			30 Hz, ms		
	Start	Center	Width	Start	Center	Width
1	.320	.353	.065	.320	.328	.256
2	.385	.428	.085	.336	.347	.261
3	.470	.525	.110	.358	.371	.268
4	.580	.648	.135	.385	.402	.274
5	.715	.803	.175	.419	.441	.284
6	.890	1.003	.225	.463	.491	.296
7	1.115	1.258	.285	.519	.554	.311
8	1.400	1.583	.365	.590	.636	.331
9	1.765	1.998	.465	.681	.739	.356
10	2.230	2.525	.590	.798	.871	.388
11	2.820	3.198	.755	.945	1.039	.429
12	3.575	4.055	.960	1.134	1.254	.480
13	4.535	5.148	1.225	1.374	1.527	.546
14	5.760	6.543	1.565	1.680	1.876	.631
15	7.325	8.323	1.995	2.071	2.321	.739
16	9.320	10.590	2.545	2.570	2.888	.876
17	11.870	13.490	3.250	3.206	3.613	1.053
18	15.120	17.190	4.145	4.019	4.537	1.276
19	19.260	21.900	5.285	5.055	5.715	1.561
20	24.550	27.920	6.740	6.376	7.218	1.925
End of 20	31.290			8.061		

Figure 40. Photograph of the EM61-3D in use at Fort Carson, Colorado (top), and listing of the 20 time gates for each of two operating base frequencies (repetition rates) of the system

time axis “comes out of the plane of the figure” and represents approximately 21.9 ms of the decay curve. Noise both spatially and temporally is obvious in the representation, however anomalies caused by known buried items are apparent and two of the known (and openly releasable) ordnance items are indicated. Three facts are evident from examination of numerous raw and spatially and temporally smoothed representations like Figure 41:

- a. Buried metallic objects have higher initial (early-time) TDEM magnitudes than background.
- b. The decay persists with higher magnitudes to later times than background.
- c. The spatial extent of TDEM anomalies along track are greater for ordnance items oriented along track than for items oriented cross track.

Two-axis representation of individual component complete decay curves.

Another technique for displaying the similar information to that in Figure 41 is to view the decay curves in two dimensions as illustrated in Figure 42. In Figure 42 each of the three recorded components is displayed separately in a magnitude versus profile distance plot. At each profile position, a series of vertical dots represents the 20 measurements of magnitude versus time of the decay curve. The background clearly forms a horizontal “noise” band; the noise band is considerably smaller for the y-component (along-track component). Data spikes which extend above or below the noise band are indicated as targets (T), which are very likely buried metallic objects and possible ordnance items. Seven targets are indicated in both the z-component (vertical) and y-component data at the same locations, while three of the same targets are indicated in the z-component data. Note that values can be negative for the x- and y-components, while the values are positive for the z-component.

Characteristics of complete decay curves at single locations. The forms of the z-component decay curve at given surface locations over known objects are illustrated in Figure 31 (an aluminum plate) and in Figure 43 (60-mm and 81-mm mortars, 105-mm and 152-mm projectiles). As suggested by McNeill and Bosnar (1996) and McNeill¹, there is considerable expectation that characteristics of the complete decay curves over metallic objects will provide discrimination capability and possible identification potential for UXO. Several observations supporting the preceding proposition are apparent in Figures 31 and 43 and in many additional decay curves examined during the investigations (many over “bare” ground and buried non-metallic objects):

- a. All of the metallic objects have high initial (early) time magnitudes, and after an initial rapid decay, maintain finite magnitudes for late times.
- b. Nonmetallic objects have low to intermediate initial magnitudes and decay to near-zero magnitudes generally in less than 5 ms.
- c. The decay curve for the aluminum plate decays monotonically to very near-zero magnitude at late times.

¹ Personal Communication, July 1997, J.D. McNeill, Geonics, Limited, Mississauga, Ontario, Canada.

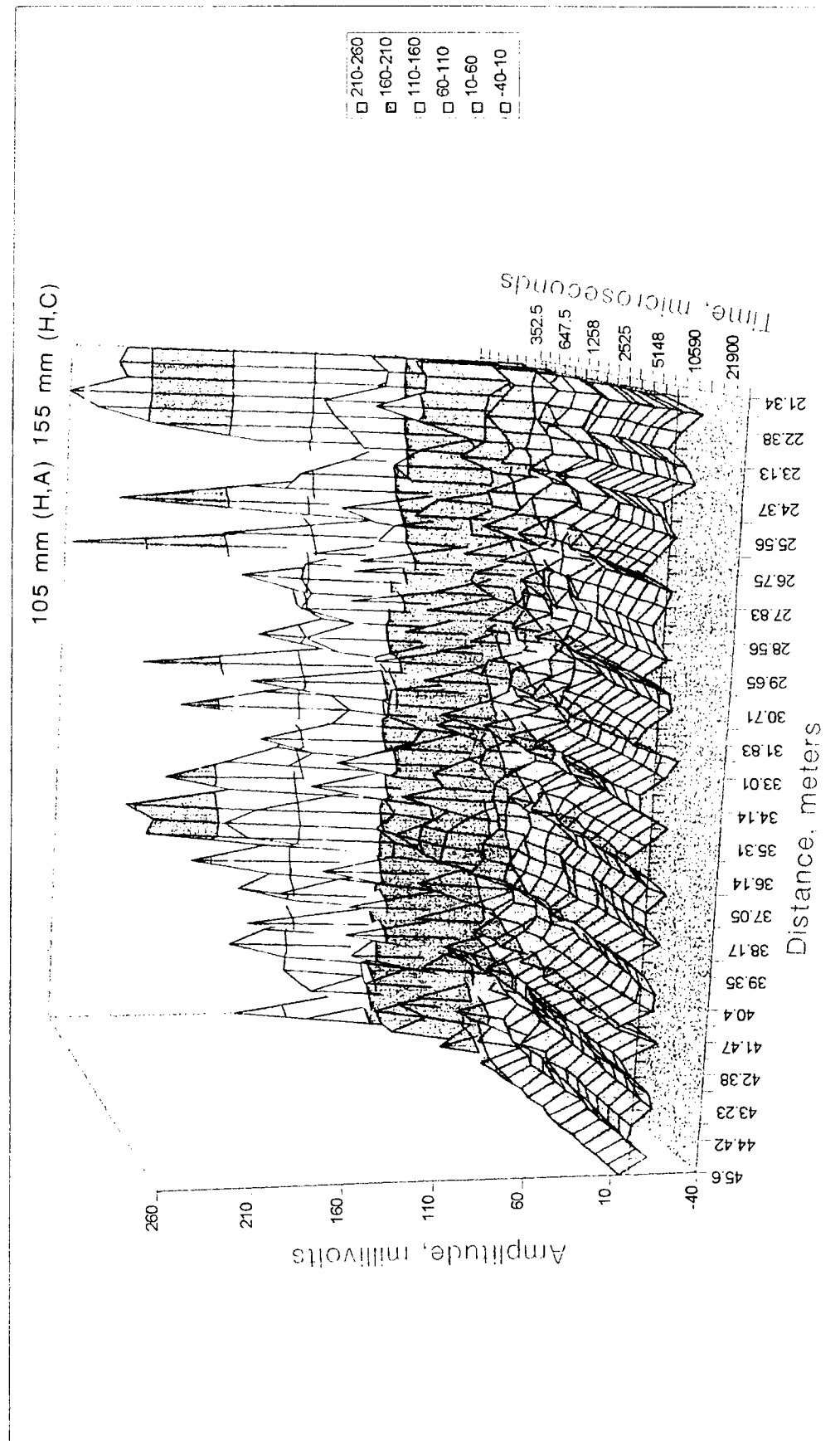


Figure 41. Three-axis portrayal of EM61-3D vertical component raw data from the Seabee Site, Fort Carson, along a N-S line. The designations for the orientations of the two identified ordnance items are: H--horizontal; A--along-track; and C--cross-track

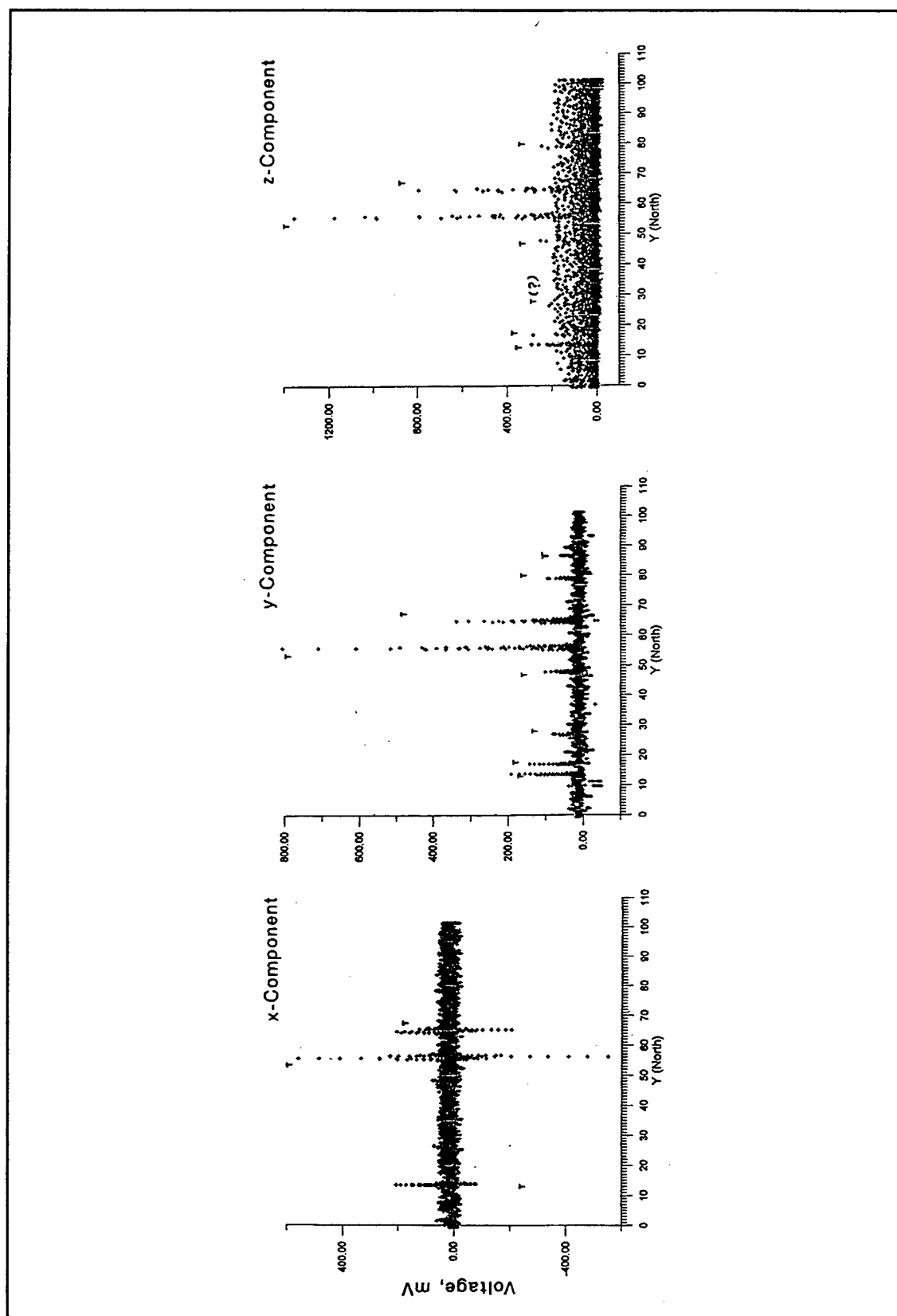


Figure 42. Three-component profile representations of TDEM decay curves at Seabee Site, Fort Carson; 20 decay curve measurements plotted at each profile position. Targets (T) indicated where peaks rise above the "noise" band for each component

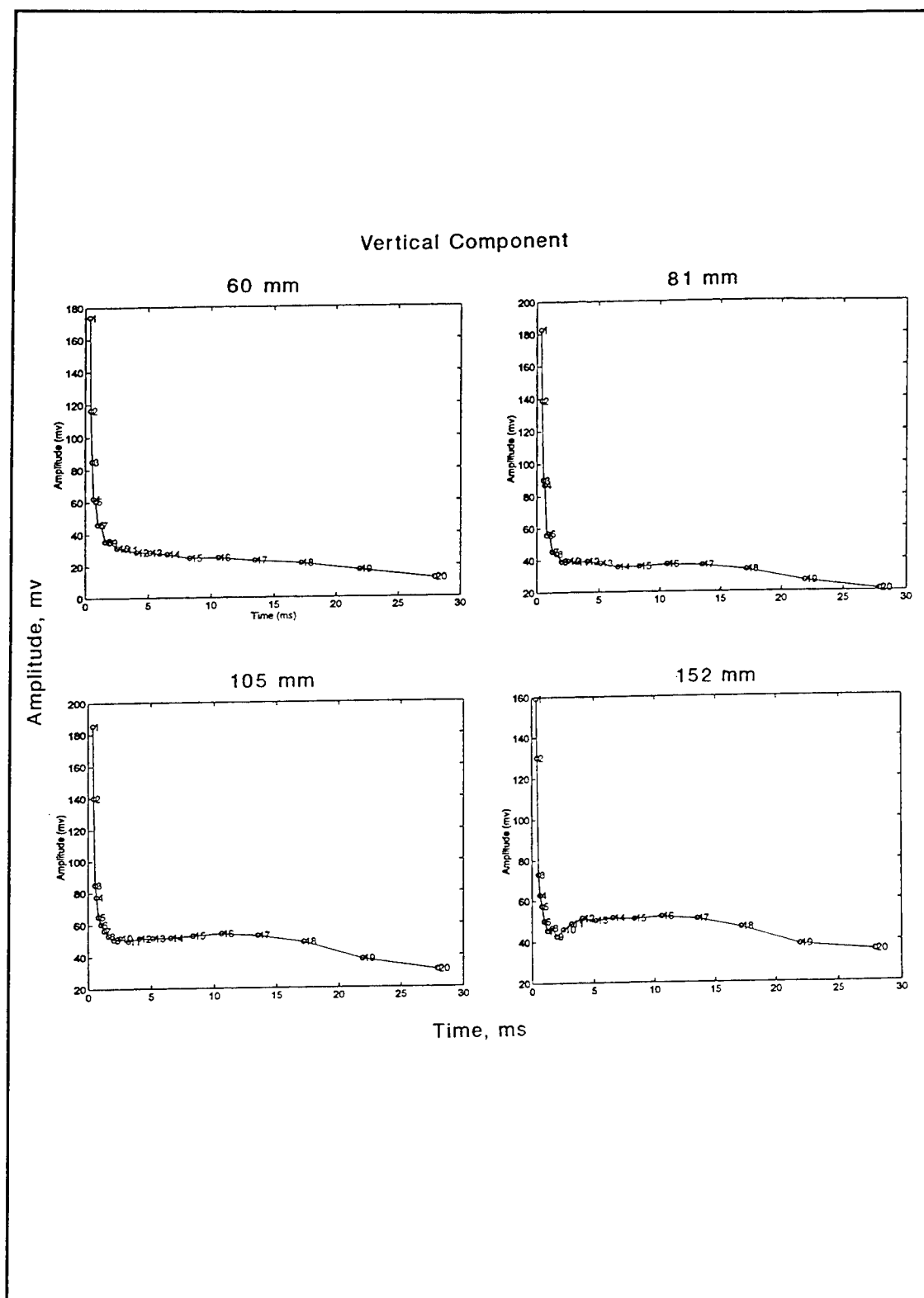


Figure 43. TDEM decay curves (vertical component) over four shallow ordnance items, Seabee Site, Fort Carson

- d. The decay curves for the ordnance items (ferrous) are quite smooth and indicate nonmonotonic decay at intermediate times.
- e. The magnitude at channel (time-gate) 20 increases as size of the ordnance item increases.

The above observations lend considerable support to the potential for discrimination and identification of UXO from observations of complete decay curves for TDEM. McNeill and Bosnar (1996) suggest that the decay curves can be fitted with various forms of decaying exponential functions with two to three fitting parameters, which may be diagnostic for ordnance versus non-ordnance discrimination and of ordnance type.

Single parameter discriminant. Examination of Figures 31 and 43, as well as many other decay curves, suggests that a parameter such as the area under the curves might be an effective discriminant. The area is related to the “energy” induced in subsurface volumes, particularly compact metallic objects. Areas under the decay curves along the same profile line shown in Figure 42 are displayed in profile form in Figure 44. The same seven target (T) locations shown in Figure 42 are indicated in Figure 44 and correlate with dramatic peaks in decay curve areas, with the background areas forming a very narrow “noise” band. Although not examined in detail, the absolute values of areas of x- and y-component decay curves above buried metallic objects apparently will also produce maxima above a background noise band.

Multicomponent parameter space analyses techniques

The individual three-component displays in Figure 42 and considerations of the decay curve areas considerations strongly suggest that some form of multicomponent (multisensor) analysis technique will provide diagnostic tools for UXO identification. Two types of multicomponent parameter space representations are presented and briefly described here: (1) spatial profile figure in three-component space at selected times; (2) decay time figure in three-component space at selected position. The first type multiparameter space representation is a spatial profile crossing an anomaly feature of interest (identified by the techniques discussed above), where each “point” on the figure represents the three-component magnitudes at a given surface location, and the entire figure is for a selected time (i.e., there could be 20 such figures). The second type representation is for a selected surface location and the figure is formed by 20 points, with each point representing the three-component magnitudes at a specific time. Perhaps the greatest difficulty in three-component parameter space analyses as suggested here is to visualize, recognize, and characterize the geometry of the figures formed by the two types of representations. A possible approach to analyzing the geometry is to examine projections of the figures on the three orthogonal component space planes. Another procedure for geometric and time-evolution analyses requires reducing the space to 2-D by combining the two horizontal components into a horizontal magnitude, as was done for Figures 32 through 34.

Spatial profiles in three-component space. Examples of spatial three-component space plots are shown in Figures 45 and 46. Each figure shows

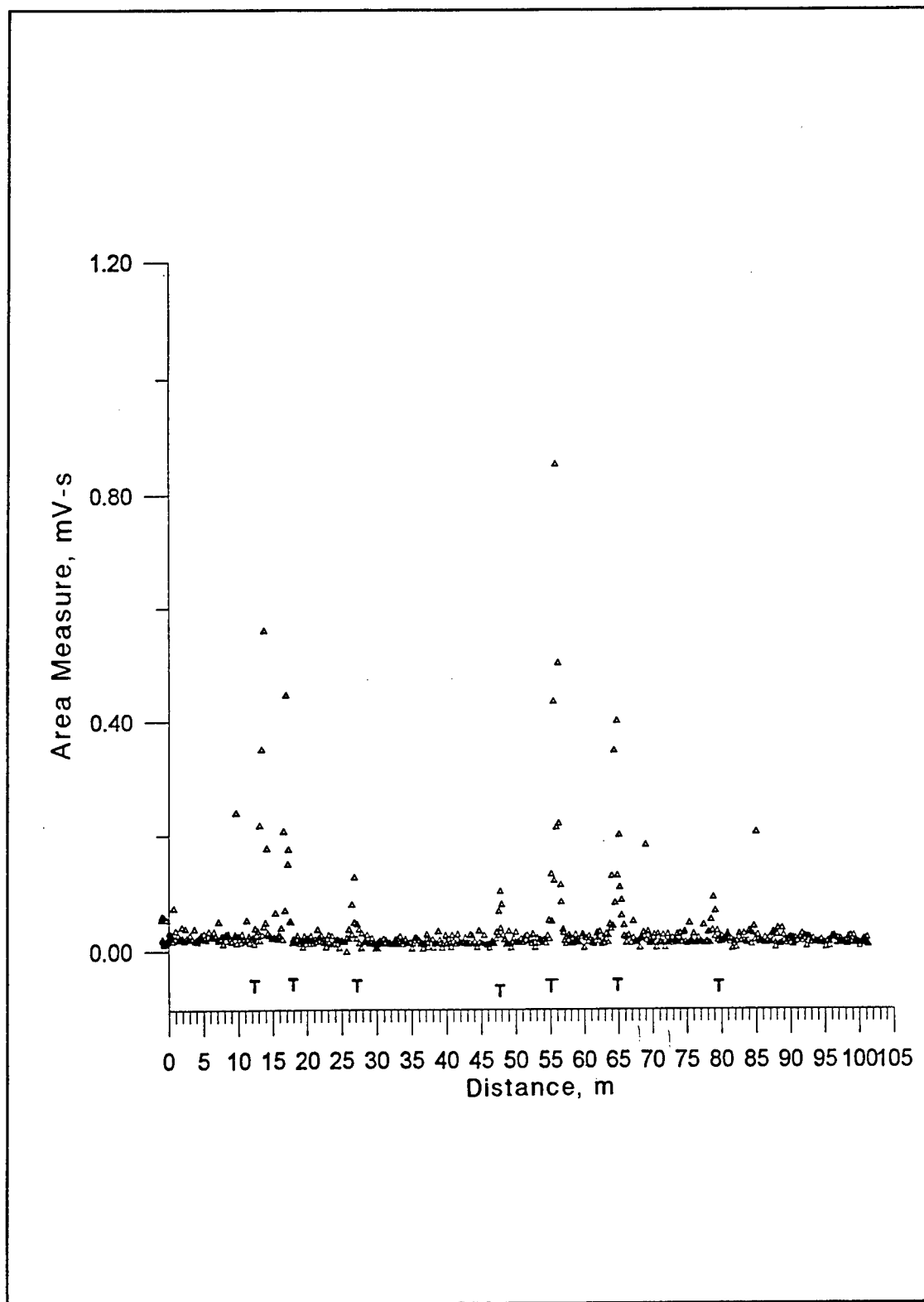


Figure 44. Areas of TDEM decay curves (vertical component) along same profile as Figure 42, Seabee Site, Fort Carson. Targets (T) are at same locations as the targets in Figure 42

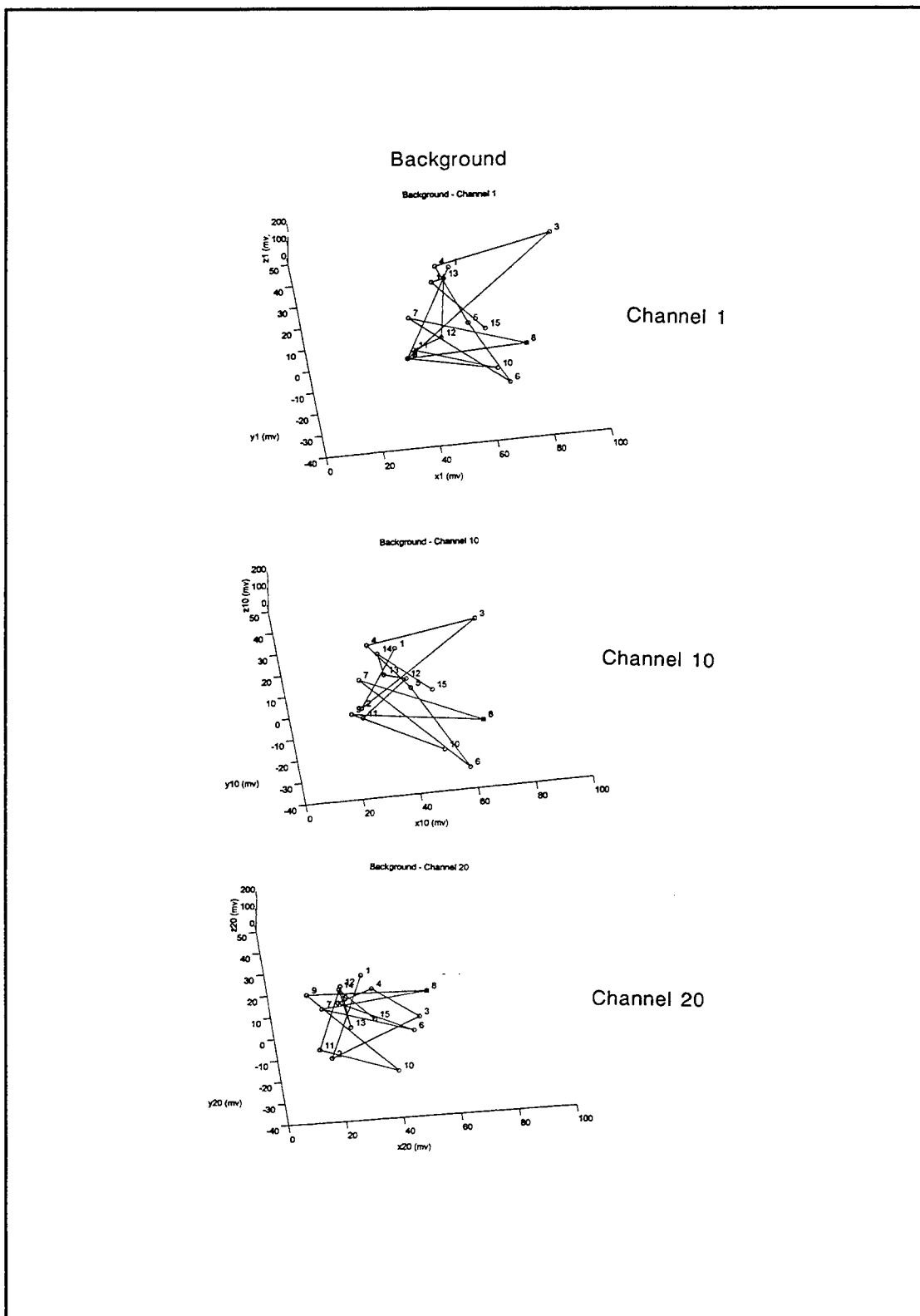


Figure 45. Three-component parameter space plot for a background location, Seabee Site, Fort Carson, for EM61-3D Channels 1, 10, and 20

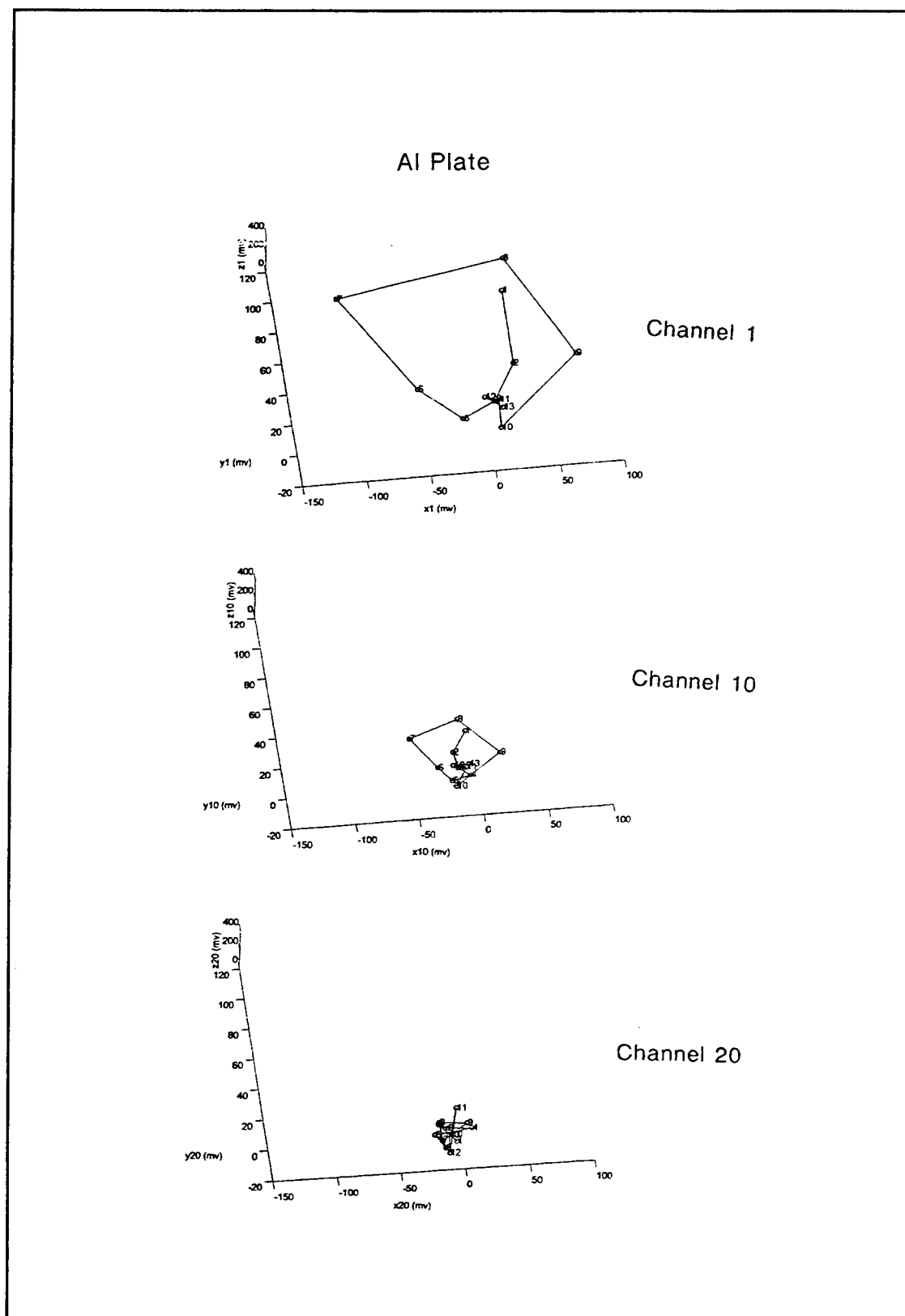


Figure 46. Three-component parameter space plot for an aluminum plate (see text for details), Seabee Site, Fort Carson, for EM61-3D Channels 1, 10, and 20

three plots for Channels 1, 10, and 20, corresponding to early, intermediate, and late times (see Figure 40 for the actual times of the channels). Figure 45 is for a “background” location, i.e., a location with no known buried objects, and hence represents the response of the soil at the site. The axes are component magnitudes in mV, with the z-component the vertical axis. The 15 points defining the geometric figure in Figure 45 are sequential measurement points along a N-S profile. Geometrically the figure resembles a “scattergram” that migrates downward and to the left as a function of time in the plots. Ultimately, at very late time, the figure should shrink to a point at (0,0,0); the fact that it doesn’t appear to behave in this manner may be due to both background (geologic) variability along the profile line and system noise. Examination of a number of noisy, fixed location decay curves (Figure 31 is an example of a nearly noise-free decay curve, while Figure 41 contains some noisy decay curves) indicates that noise in the vertical component may be as large as 20 mV for some channels for the prototype system. Figure 45 indicates comparable noise levels for the two horizontal components.

Figure 46 shows a three-component, profile plot crossing a 20- × 20-cm (8- × 8-in.) aluminum plate buried at a depth of 5 cm to the top of the plate. The center of the plate is crossed near profile point 8. Note the larger axis intervals in Figure 46 than in Figure 45. Geometrically, the plot figure resembles an ellipse with a cusp at the origin, similar to that observed for some structures in gravity gradient space plots (Butler 1995). The plot figure shrinks in size, apparently maintaining the cusp, and approaches a “point” at the origin at late time (Channel 20). Actually, considering the component scale differences between Figures 45 and 46, the plot figure size at channel 20 is comparable in size to the background plot at Channel 20. It is the well-defined figure shape and cusp that apparently exists for the aluminum plate that holds promise for discrimination and identification (Butler 1995).

As a contrasting case to the conducting flat plate, consider an iron (ferrous) sphere, i.e., magnetically permeable and conducting (Figure 47). The sphere is 12.4 cm diameter, buried at a depth of 10 cm to the top, and lies approximately beneath profile position 7 (indicated by an asterisk). An important consideration for analyses of Figure 46 and 47 is that both objects are buried at depths smaller than the Tx dimensions. This consideration means that, except possibly for the vertical component, symmetry in the components should not be expected, as it would for a deeply buried object, where the Tx approximates a dipole source. The three-component spatial profile plots for Channels 1, 10, and 20 for this case (Figure 47) indicate a much different geometrical structure and time response than the conducting flat plate case. *From the perspective view of Figure 47* (identical to Figure 46), the plot figure appears to have a well-defined geometry at early time but then collapses apparently to a “line” at late time. The point directly above the sphere has a positive cross-track (x) component at early time that becomes negative by intermediate times. The cross-track component is a precise indicator of the location of the object. Noise is clearly contaminating the plot figures and prevents the easy recognition of diagnostic features, particularly from the one perspective view.

Decay times in three-component space. For surface positions approximately directly over selected objects, plate, and spheres, time-decay curves in

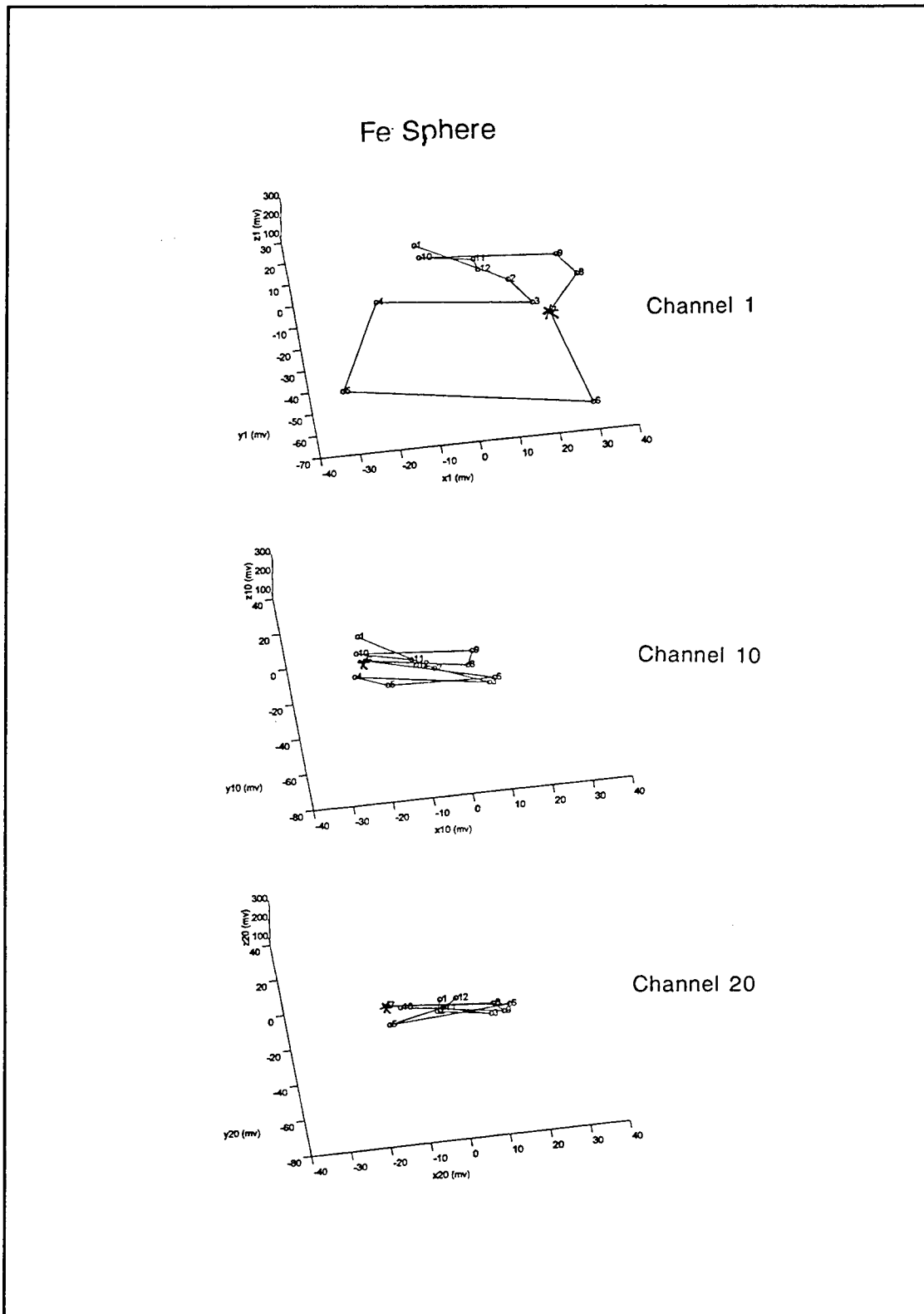


Figure 47. Three-component parameter space plot for an iron sphere (profile location of sphere indicated by '*'; see text for details), Seabee Site, Fort Carson, for EM61-3D Channels 1, 10, and 20

three-component space are plotted in Figure 48. A background decay curve is also shown in Figure 48 for comparison. The aluminum plate and iron sphere are the same targets referenced in the two preceding paragraphs. The aluminum sphere (spherical shell) is 25.4 cm in diameter and is buried 60 cm to top. There is a dramatic difference in the character of the plate and sphere responses. The two spheres show an approximately monotonic decrease (through intermediate times), in the vertical (z) and cross-track (x) components, and then a transition back to increasing values of the cross-track component. Differences in the slopes of the decay curves and the character of the response after the transition at intermediate times are caused by the added permeability response for the iron sphere. Three-component decay plots for three ordnance items (one mortar and two artillery projectiles) and one metallic AT mine are shown in Figure 49. The decay responses of the projectiles are totally different in character from the decay plots in Figure 48. The decay response of the metallic (steel) AT mine is totally different than the projectiles responses but resembles the aluminum plate response. For the steel mine, there is also a transition at intermediate to late times that resembles the transition of the iron sphere.

Multifrequency FDEM System

The second emerging technology considered as part of this effort is a multifrequency FDEM system designated the GEM-3 (Geophex 1997). The system is monostatic, consisting of three concentric coils, with the outer coil (nominally 0.5-m diam) the primary Tx, the middle coil used to cancel the primary field over a region at the center, creating a magnetic cavity, and a Rx coil within the magnetic cavity. The primary field is generated by a composite waveform, that can generate one frequency or multiple frequencies simultaneously. The system is broadband, measuring both quadrature and in-phase components over the frequency range 90 Hz to 24 kHz. Data acquisition rates up to 10 Hz are possible with multiple frequencies, and the system can also operate in time domain.

The potential of the multifrequency FDEM concept is illustrated in Figures 50 and 51, from a survey of the Center Square area of the Seabee Site. The ellipses in the figures surround the registration targets (an aluminum plate to the north and an iron sphere to the south at each location). EMI anomalies appear in the plots, for 4,050 Hz and 12,270 Hz, as small, tightly grouped, closed contours. With the plotting threshold selected for the anomaly plots, most background noise is suppressed. The key features of the two figures are summarized:

- a. For the anomaly plot of the quadrature component at 4,050 Hz (Figure 50), only the southern iron sphere targets are detected.
- b. For the anomaly plot of the in-phase component at 12,270 Hz (Figure 51), only the northern aluminum plates are detected.

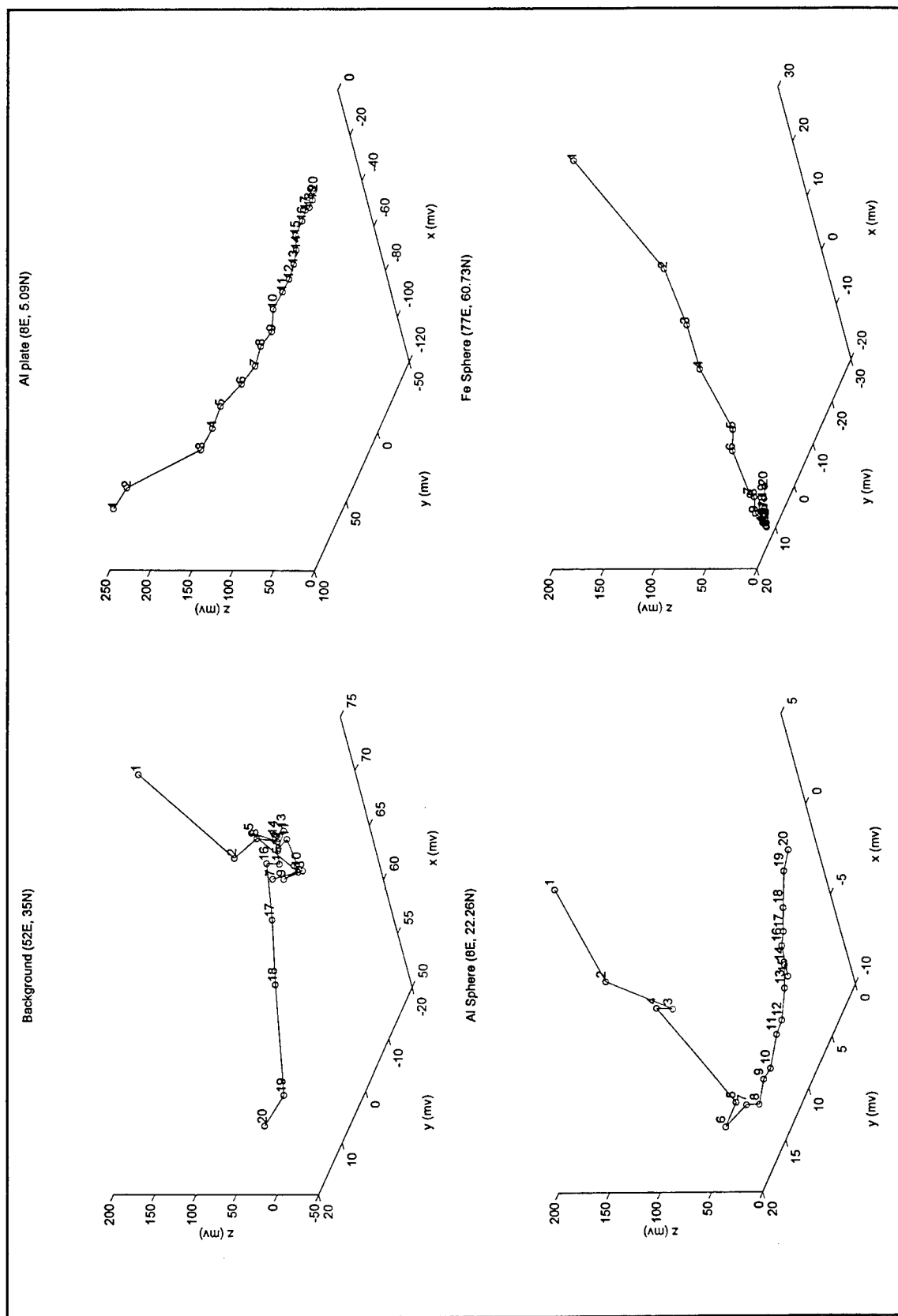


Figure 48. Three-component time-decay plots for background (top left), aluminum plate (top right), iron sphere (bottom right), and aluminum sphere (bottom left). Points are component values at the time for the 20 measurement channels

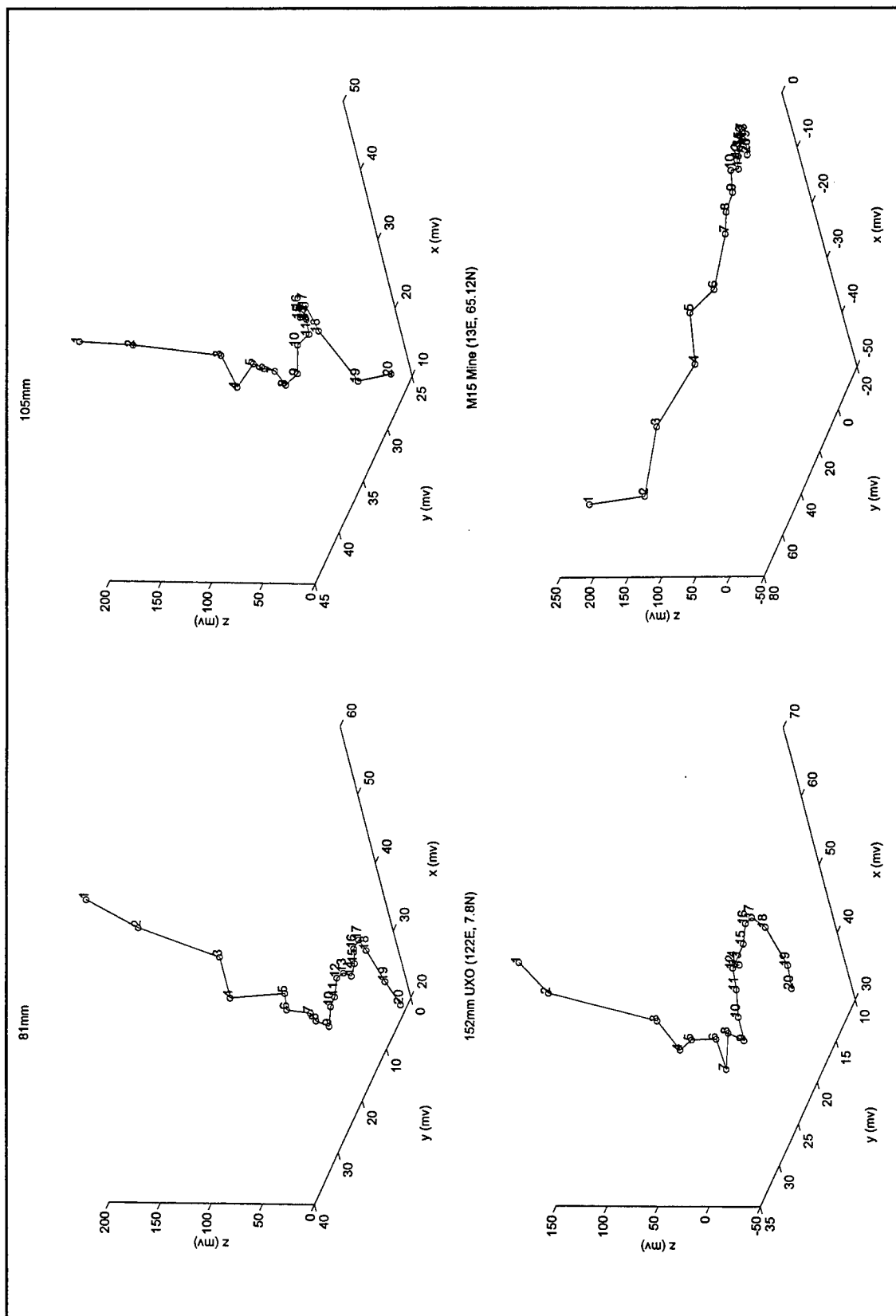


Figure 49. Three-component time-decay plots for 81-mm mortar (top left; inclination 90, depth to top 20 cm), 105-mm projectile (top right; inclination 0, azimuth 90, depth to top 55 cm), 152-mm projectile (bottom left; inclination 0, azimuth 0, depth to top 105 cm), and M15 metallic (steel) AT mine (33.7 cm diameter, depth to top 15 cm). [Points are component values at the time for the 20 measurement channels.]

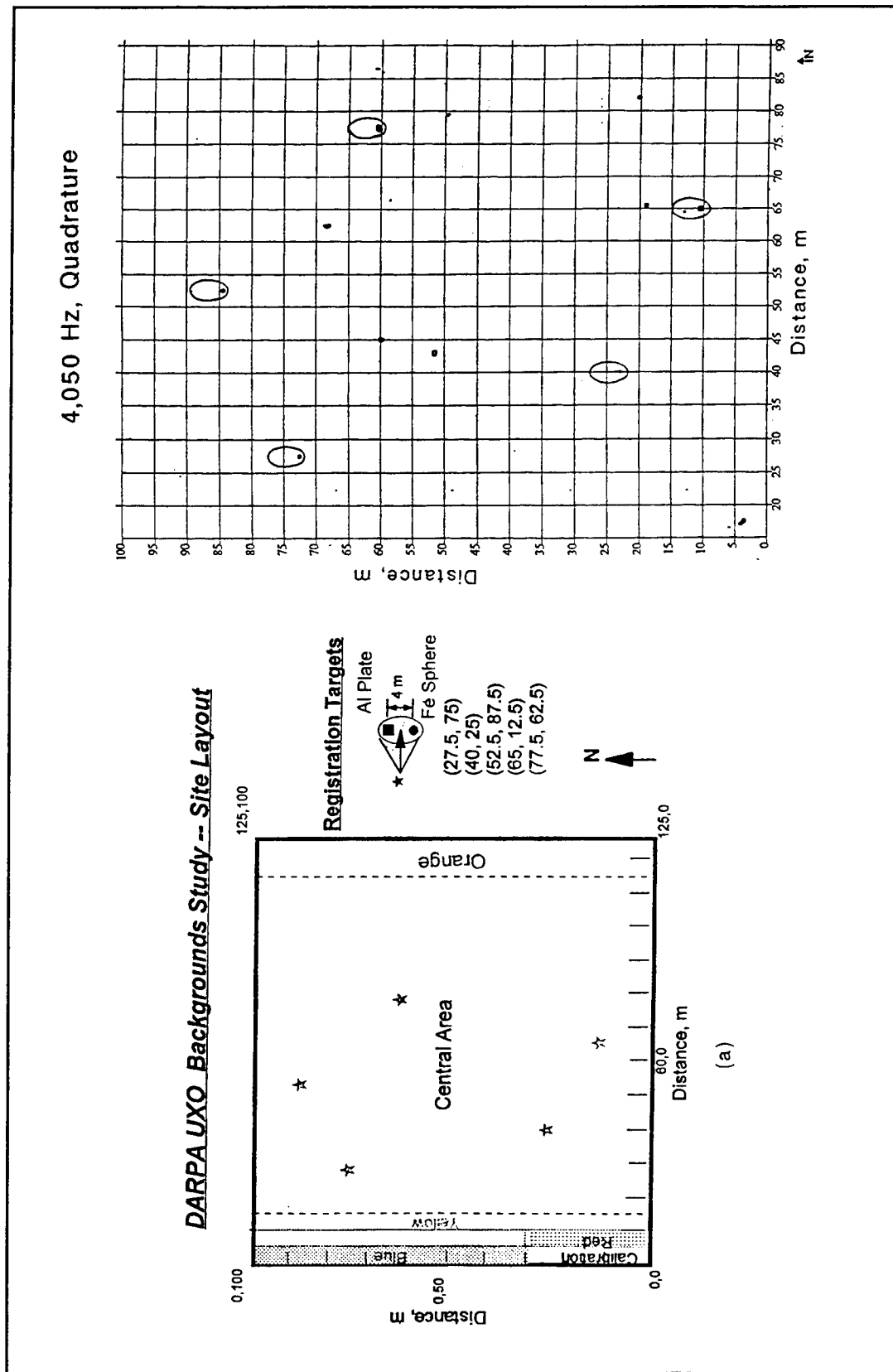


Figure 50. Multifrequency FDEM survey results at Seabee site. Basic site layout for reference (left) and an EMI response map (right) at 4,050 Hz (quadrature component) for a portion of the Center Square area are shown

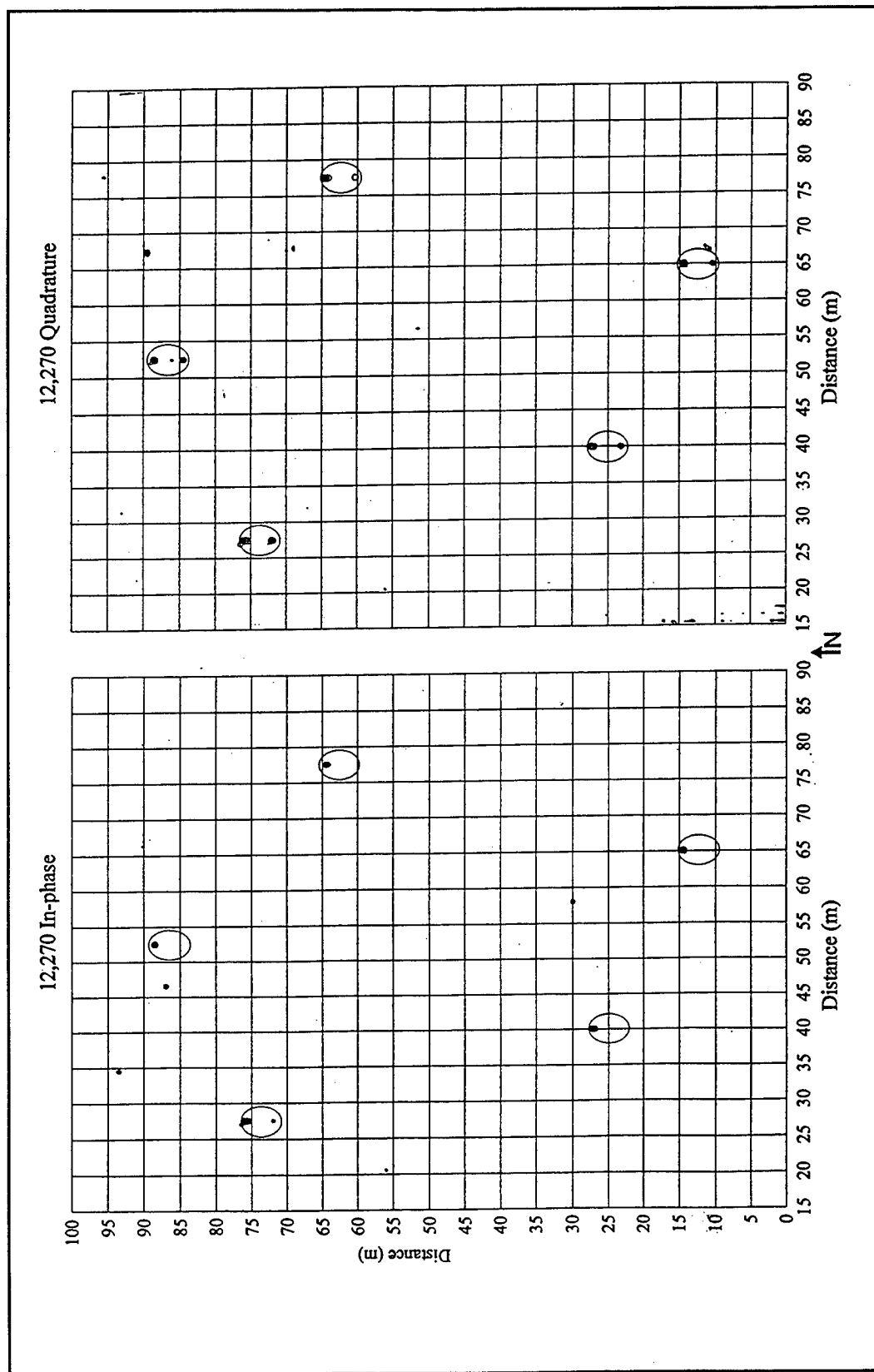


Figure 51. Multi-frequency FDEM survey results at Seabee site. EMI response maps at 12,270 Hz, in-phase component (left) and quadrature component (right). These responses, along with the 4,050-Hz response in Figure 50, illustrate material type, geometry and frequency dependence

- c. While for the quadrature component at 12,270 Hz, both the aluminum plate and the iron sphere are detected.

These features indicate that the EMI response is both frequency, material type, and geometry dependent.

The above observations suggest the possibility of electromagnetic induction spectroscopy (Private communication, I. J. Won, Geophex, Ltd.),¹ where the in phase and quadrature components as a function of frequency for an object define a EMI spectra, diagnostic of the size, geometry, and material type of a buried object. Figure 52 illustrates the EMI spectra of an ordnance item (30 mm projectile) and various metallic objects which are possible clutter sources at sites. Each spectra is obtained by measuring in phase and quadrature components at a single location above the objects as a function of frequency, and is observed to be distinctive for each indicated object. Figure 53 carries the spectra observations further, by indicating spectra dependence on orientation for a given ordnance item (37 mm projectile). There is early indication that the spectra of an ordnance item with inclination I ($0 \leq I \leq 90$ deg) can be deduced from in-plane measurements of spectra of the object at $I = 0$ deg and $I = 90$ deg. For example, the spectra for the case $I = 45$ deg in Figure 53 can be replicated by simple averaging of the spectra for the horizontal and vertical spectra cases. To carry this concept to general 3-D orientations will require three-component measurements and development of data transformations from analytical and/or numerical modeling that are validated by measurements.

Closure for Two Emerging EMI Technologies

The two EMI systems briefly examined here were prototype systems at the time of the field data acquisition. Both systems were used at JPG Phase III UXO Technology Demonstrations either just prior to or just after their use at the DARPA sites, and both systems are currently in varying stages of advanced development and commercialization. There are still active investigations utilizing data acquired by the prototype systems at the DARPA sites and at JPG Phase III. The work presented here and also the work of other investigators demonstrates considerable potential for UXO discrimination and identification with these emerging technology systems. The full potential of the concepts will likely be realized only if the systems undergo advanced development as multicomponent *and* multichannel or multifrequency systems. Also, full phenomenological modeling capability is required for the TDEM and FDEM cases. In spite of the large amounts of data acquired by the systems compared to standard systems, such as total field magnetometers, the standard EM61, and single-frequency EMI systems and metal detectors, both systems are capable of efficiently surveying large areas.

¹ Geophex, Ltd., Raleigh, North Carolina.

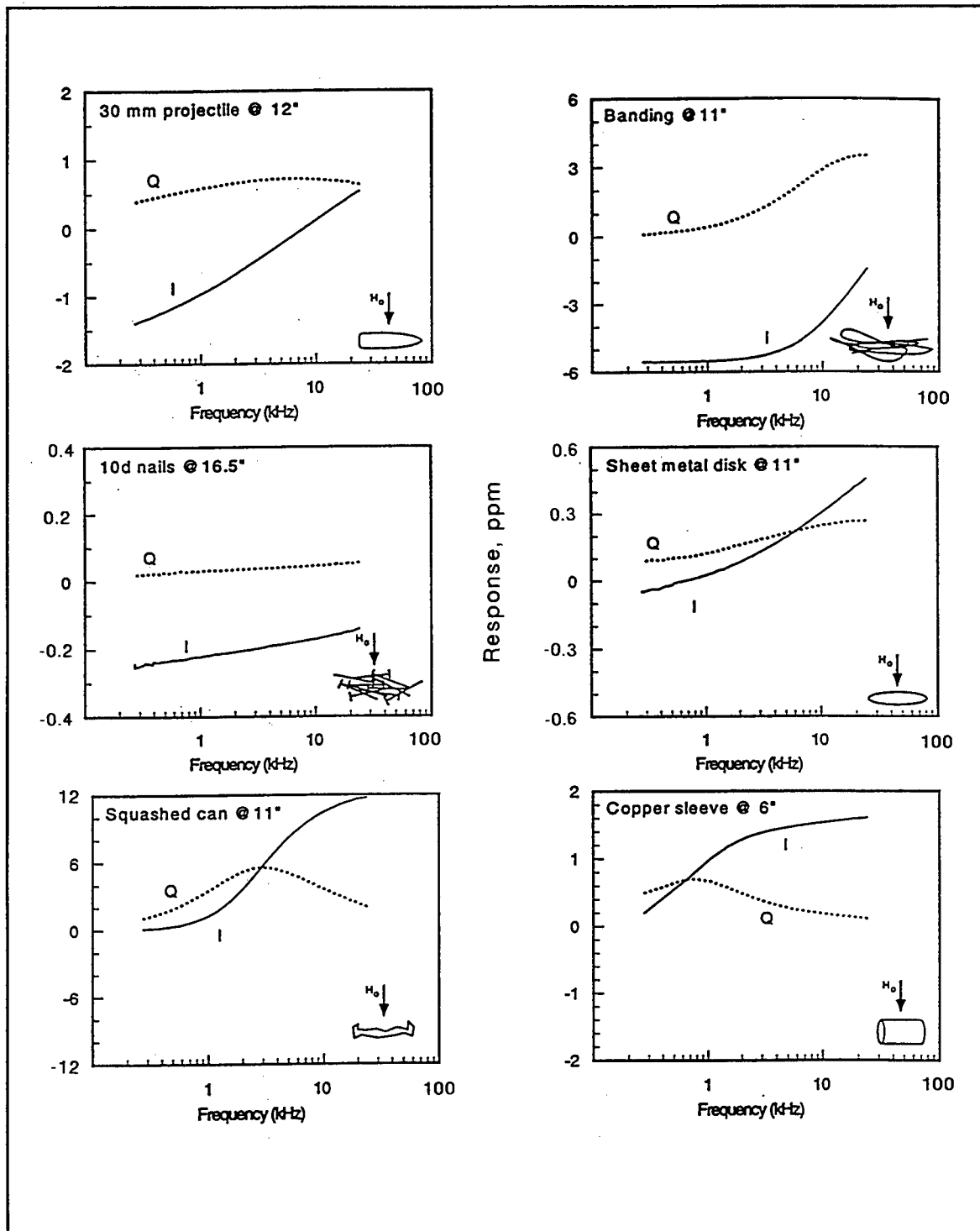


Figure 52. Comparison of EMI response spectra for an ordnance item (upper left) and various clutter items; illustrates discrimination potential. (Private Communication, I.J. Won, Geophex, Ltd.)

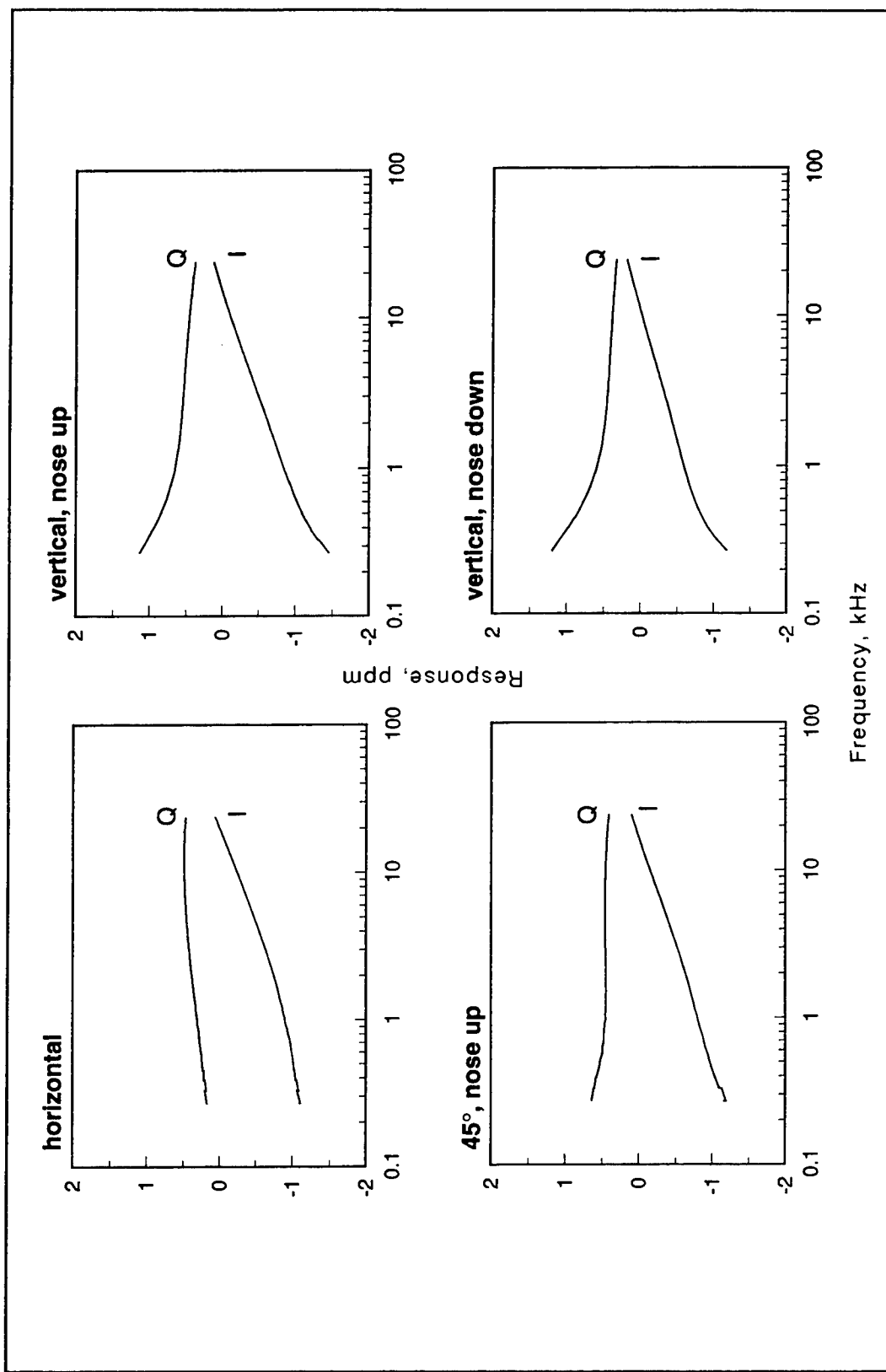


Figure 53. EMI response spectra (multifrequency FDEM) for a 37-mm projectile at various orientations

8 Summary, Conclusions, and Recommendations

Summary and Conclusions

This report presents a broad view of the UXO detection, discrimination, and identification requirements and of problems associated with achieving those requirements. Concluding that UXO detection, except for problematic cases, is presently possible with single- or multisensor geophysical datasets, the report concentrates on defining the current status of detection capability and then addresses the discrimination and identification problems. There are two problematic cases for which detection capability does not currently exist: (1) very small, widely spaced, single-ordnance items, such as 20-mm projectiles; (2) ordnance items buried too deeply, relative to their size, for detection with present technology. Very small ordnance items such as the frequently present 20-mm projectiles are generally buried at very shallow depths. *The anomaly magnitudes and spatial wavelengths of such small ordnance items prohibit a general detection capability on large, live sites with current technology, although closely spaced groups or clusters of small ordnance items may be detectable.* For any size ordnance and site-specific conditions, there are burial depth limits below which the object cannot be detected for each current technology (e.g., TFM, EMI, GPR), and hence there is a burial depth for a given object below which it cannot be detected by any current technology. The maximum burial depths for detection by current technology are fundamental physical limitations, not to be improved or solved by improved sensors for current technology (e.g., a buried object at a “real world” live site that is not detected with a TFM sensor with 0.01 nT sensitivity will *not* be detected by an improved TFM sensor with 0.001 nT sensitivity).

The report concludes that there is not sufficient information content in currently deployed single-sensor survey data to allow UXO discrimination, except in very special cases. General discrimination capability requires multisensor datasets and integrated or joint interpretation. The Naval Research Laboratory MTADS system, for example, can acquire high quality multisensor (TFM, TFG, and TDEM) datasets at high data densities over large areas at reasonable production rates (current production rate estimates are 15 acres (6 hectares or 0.06 km²) per day for TFM/TFG and 7 to 8 acres per day for TDEM). Currently, multisensor integration (“data fusion”) generally occurs at the data processing and interpretation stage, not the data acquisition stage. Also,

multisensor integration by most practitioners consists of side-by-side comparison and correlation of processed data maps or images. Model-based interpretation procedures for discrimination are rapidly advancing, but are limited to analyses of each type of sensor data separately, followed by the side-by-side comparison procedure and empirical correlation between the model interpretations. There are also efforts to achieve multisensor integration using neural network, "fuzzy logic," and expert system type approaches. These are generally nonphysics-based approaches, and they rely on large sensor signature databases; successful application of these approaches for UXO discrimination are reported. This report assesses procedures for model-based interpretation and presents a proposed multisensor data integration algorithm.

The report also concludes that UXO identification or classification is not feasible with currently deployed technology. Limited, reported successes in UXO identification using *empirical correlation* of physical properties such as interpreted magnetic moment from test site surveys to measured magnetic moments for actual ordnance items cannot be extended to general surveys of real world UXO contaminated sites. A key component of the ultimate solution of the UXO discrimination and identification requirement is the development of physics-based models for forward and inverse modeling of geophysical signatures. A distinct possibility exists that the data required for UXO identification cannot be obtained during large area surveys that are designed to detect and map UXO-like targets. The logical procedure, following detection, is to conduct localized area surveys over the identified targets (or selected targets) for final discrimination and identification.

A versatile magnetic modeling program for UXO is documented that is successfully validated by comparison to measured TFM data. The program models the UXO as prolate spheroids; a geometry which closely approximates the geometry of many UXO and has the elongated symmetry axis of UXO. The problem of TDEM modeling of realistic UXO geometries (cylinders and prolate spheroids) is considered and some success illustrated for the full time-domain solution. However, it is concluded that the complete time-domain EMI solution for UXO geometries requires an extensive and dedicated effort.

Finally, two emerging EMI technologies, a multicomponent, multichannel TDEM system and a multifrequency FDEM system, are evaluated. Both of these systems were prototype systems at the time of acquisition of the datasets used for this study. Various analysis techniques for the data from these prototype systems is considered. The potential for discrimination and identification with these systems is identified and is considered convincing enough to recommend continued study of analysis techniques and continued, advanced development of the systems.

Recommendations

The following specific recommendations for future research, development, and technology investments are the mainly the result of the work documented in this report. Some of the recommendations, however, are intuitive and already recognized by many investigators.

Current technology multisensor platforms. For cost- and time-efficient UXO detection surveys of large areas, a self-propelled, towed, or autonomous multisensor platform is required. The platform must have integrated positioning capability. The platform should have closely spaced arrays of sensors. The recommended sensors for the platform are total field magnetometer (TFM) and time-domain electromagnetic induction (TDEM) systems. The TFM arrays can be arranged to acquire both TFM and total field vertical gradient (TFG) data. Current technology may require separate surveys of areas with the magnetometer arrays and the TDEM arrays. The Navy's MTADS system is an example of this type recommended system using current deployable technology. Hand-carried versions of the current technology sensors must be available for use in densely wooded areas.

Enhancements for current technology multisensor platforms. Readily identifiable technology enhancements for current technology multisensor platforms include: (a) greater numbers of closer-spaced sensors in the arrays, particularly to address the very small-size ordnance problem; (b) sensor systems with greater sampling rates along track; (c) capability to acquire TFM and TDEM data simultaneously; (d) "real-time" UXO detection decision aids. The development and utilization of UXO test sites is a necessary adjunct to the recommended enhancements.

Multisensor data integration for UXO discrimination. Except for positioning data, all integration should be accomplished at the data processing and interpretation stage and not at the data acquisition stage. While there may be some potential in the approach of using neural networks and other nonphysics-based approaches for multisensor integration for discrimination, the recommendation from the present work is that data integration and interpretation be achieved by fundamental physics-based modeling approaches. The recommendation does not preclude the utilization or fundamental value of large, measured UXO signature libraries for validation of modeling capability, or the use of large libraries of model computed UXO signatures for signature matching approaches to discrimination and identification.

Emerging technology for UXO discrimination and identification. This report identifies several emerging technologies in Chapter 7 and discusses two of the technologies in detail. Emerging technologies offer the greatest hope and potential for capability for remote discrimination of UXO anomalies from false alarm anomalies and for identification or classification of buried UXO. Research and development of these emerging technologies must be aggressive, with the goal of integrating the new capabilities into deployable systems and platforms.

Integration of new technology into deployable systems and multisensor platforms. Integration of new technological capability into deployable hand-held systems and multisensor platforms must be encouraged and supported, but only after needed research and development and field validation at well-controlled UXO test sites. Accompanying the emerging technology sensor development must be data processing and interpretation procedures to complete the technology. Some of the emerging technologies may prove to have general applicability, while some will be limited to localized investigation for UXO identification. Also, some may prove to have very limited applicability and not justify any type advanced development. Some of the identified emerging

technology may be available for integration into deployable systems in the near-term, say 2 to 3 years: e.g., (a) three-axis vector magnetometers, (b) multiple axis magnetic gradiometers; (c) single-component (vertical) multichannel TDEM systems; (d) single-component multifrequency FDEM systems; (e) near real-time, high-resolution microgravimetry. Other emerging technologies may require a longer term investment, say 3 to 5 years, such as multicomponent TDEM and FDEM systems and full tensor magnetic gradiometers. The final identified emerging technology, acoustic wavefield imaging, may not prove feasible or applicable to real world UXO problems and certainly represents a longer term investment.

References

- AETC-Geometrics. (1996). "MagAID, magnetic anomaly identification and detection: quick instruction guide," Geometrics, Inc., Sunnyvale, CA.
- Altshuler, Thomas W. (1996). "Shape and orientation effects on magnetic signature prediction for unexploded ordnance." *Proceedings of the UXO Forum '96*. Williamsburg, VA, 282-291.
- Altshuler, Thomas W., Andrews, Anne M., Dugan, Regina E., George, Vivian, Mulqueen, Michael P., and Sparrow, David A. (1995). "Demonstrator performance at the unexploded ordnance advanced technology demonstration at Jefferson Proving Ground (Phase I) and implications for UXO clearance," IDA Paper F-3114, Institute for Defense Analyses, Alexandria, VA.
- Arfken, George. (1985). *Mathematical methods for physicists*. Academic Press, Orlando, FL.
- Barrow, Bruce, Khadr, Nagi, DiMarco, Robert, and Nelson, Herbert H. (1996). "The combined use of magnetic and electromagnetic sensors for detection and characterization of UXO." *Proceedings of the Symposium on Applications of Geophysics to Environmental and Engineering Problems, SAGEEP 96*. Keystone, CO, 469-477.
- Barrow, Bruce, DiMarco, Robert, Khadr, Nagi, and Nelson, Herbert. (1997). "Processing and analysis of UXO signatures measured with MTADS." *Proceedings of the UXO Forum '97*. Nashville, TN, 8-18.
- Baum, Carl E. (1996). "The SEM representation of acoustic and elastodynamic scattering," *AMEREM '96 Abstracts*. Albuquerque, NM, 286.
- Bell, Thomas. (1997). "Buried UXO detection, location and discrimination," Material for Defense Science Board Review, VA-072-086-B, AETC, Inc., Arlington, VA.
- Bell, Thomas, and Barrow, Bruce. (1997). "Model-based processing helps new UXO sensors separate ordnance from scrap," *Ordnance and Explosive Environment* 4(3), 3.

- Bennett, Hollis H. (1995). "Remote sensing of surface unexploded ordnance at Black Hills Army Depot, Edgemont, South Dakota," Technical Report EL-95-28, U.S. Army Engineer Waterways Experiment Station, Vicksburg, MS.
- Bhattacharyya, B. K. (1969). "Bicubic spline interpolation as a method for treatment of potential field data," *Geophysics* 31(2), 402-423.
- Burger, H. Robert. (1992). *Exploration geophysics of the shallow subsurface*. Prentice Hall, Englewood Cliffs, NJ.
- Burrough, P. A. (1986). *Principles of geographical information systems for land resources assessment*. Oxford University Press, New York.
- Butler, Dwain K. (1983). "Cavity detection and delineation research, Report 1--Microgravimetric and magnetic surveys: Medford Cave Site, Florida," Technical Report GL-83-1, U.S. Army Engineer Waterways Experiment Station, Vicksburg, MS.
- Butler, Dwain K. (1986). "Military Hydrology, Report 10: Assessment and field examples of continuous wave electromagnetic surveying for ground water," Miscellaneous Paper EL-79-6, U. S. Army Engineer Waterways Experiment Station, Vicksburg, MS.
- Butler, Dwain K. (1994). "Detection and delineation of subsurface cavities, tunnels, and mines." *Proceedings of the 1994 Chicago Geotechnical Lecture Series: Current Topics in Geotechnical/ Geoenvironmental Engineering*. Illinois Section, American Society of Civil Engineers.
- Butler, Dwain K. (1995). "Generalized gravity gradient analysis for 2-D inversion," *Geophysics* 60(4), 1018-1028.
- Butler, Dwain K., and Fitterman, David V. (1986). "Transient electromagnetic methods for ground-water assessment," Miscellaneous Paper GL-86-27, U. S. Army Engineer Waterways Experiment Station, Vicksburg, MS.
- Butler, Dwain K., Gangi, Anthony F., Wahl, Ronald E., Yule, Donald E., and Barnes, Donald E. (1982). "Analytical and data processing techniques for interpretation of geophysical survey data with special application to cavity detection," Miscellaneous Paper GL-82-16, U.S. Army Engineer Waterways Experiment Station, Vicksburg, MS.
- Butler, Dwain K., Sharp, Michael K., Sjostrom, Keith J., Simms, Janet E., Llopis, Jose L., and Fitterman, David V. (1996). "Assessment of geophysical methods for subsurface geologic mapping, Cluster 13, Edgewood Area, Aberdeen Proving Ground, Maryland," Technical Report GL-96-17, U.S. Army Engineer Waterways Experiment Station, Vicksburg, MS.
- Carmichael, Robert S. (1989). *Practical handbook of physical properties of rocks and minerals*. CRC Press Inc., Boca Raton, FL.

- Das, Yogadhis, McFee, John E., Toews, Jack, and Stuart, Gregory C. (1990). "Analysis of an electromagnetic induction detector for real-time location of buried objects," *IEEE Transactions on Geoscience and Remote Sensing* 28(3), 278-288.
- DeProspo, Douglas, and DiMarco, Robert L. (1996). "Automatic detection and characterization of magnetic anomalies in total field magnetometer data." *Proceedings of the UXO Forum '96*, Williamsburg, VA, 301-307.
- Dobroka, M., Gyulai, A., Ormos, T., Csokas, J., and Dresen, L. (1991). "Joint Inversion of seismic and geoelectric data recorded in an underground coal mine," *Geophysical Prospecting* 39(5), 643-666.
- ESRI. (1997). "ArcView® GIS: The geographic information system for everyone," Version 3.0a, Environmental Systems Research Institute, Inc., Redlands, CA.
- Franklin, A.G., Patrick, D.M., Butler, D.K., and Hynes-Griffin, M.E. (1981). "Foundation considerations in siting of nuclear facilities in karst terrains and other areas susceptible to ground collapse," NUREG/CR-2062, U.S. Nuclear Regulatory Commission, Washington, DC.
- Gallagher, Robyn. (1989). "Gridding experiments in an image-processing environment." *Expanded Abstracts of the Fifty-Ninth Annual International Meeting of the Society of Exploration Geophysicists*. Dallas, TX, 332-335.
- Geophex. 1997. "Geophysical characterization of two UXO test sites," Prepared for U.S. Army Engineer Waterways Experiment Station, Job No. 677, Geophex, Ltd, Raleigh, NC.
- George, Vivian, and Altshuler, Thomas W. (1997). "Design of the DARPA background clutter data collection experiment." *Proceedings of the UXO Forum '97*. Nashville, TN, 115-126.
- Geosoft. (1996). *OASIS montaj v4.0*. Geosoft, Inc., Toronto, Ontario, Canada.
- Golden Software. (1995). *SURFER for Windows: User's Guide, Version 6*. Golden Software, Inc., Golden, CO.
- Hohmann, Gerald W. (1987). "Numerical modeling for electromagnetic methods of geophysics." *Electromagnetic Methods in Applied Geophysics, Volume I, Theory*. Society of Exploration Geophysicists, Tulsa, OK, 313-363.
- Hollyer, Greg, Racic, Louis, and Butler, Dwain K. (1997). "Enhancing geophysical data acquisition, processing and analysis for UXO detection, characterization and discrimination." *Proceedings of the UXO Forum '97*. Nashville, TN, 183-194.
- Johnson, B., Moore, T. G., Blejer, B. J., Lee, C. F., Opar, T. P., Ayasli, S., and Primmerman, C.A. (1996). "A research and development strategy for unexploded ordnance sensing," Project Report EMP-1, Lincoln Laboratory, Massachusetts Institute of Technology, Lexington, MA.

- Lavelly, Eugene M. (1996). "Model based approach to UXO imaging using the time domain electromagnetic method." *Proceedings of the UXO Forum 1996*. Williamsburg, VA, 315-324.
- Lavelly, Eugene M., and Grimm, Robert. (1997). "Toward joint inversion of magnetic and electromagnetic data for improved discrimination of UXO," *Proceedings of the UXO Forum '97*. Nashville, TN, 394-403.
- MacLeod, Ian N., and Dobush, Tim M. (1990). "Geophysics—more than numbers, processing and presentation of geophysical data." *Proceedings of the Fourth National Outdoor Action Conference on Aquifer Restoration, Ground Water Monitoring and Geophysical Methods*. Las Vegas, NV, 1081-1095.
- Marquardt, D. W. (1963). "An algorithm for least-squares estimation of non-linear parameters." *Journal of the Society of Industrial and Applied Mathematics* 11, 431-441.
- McDonald, J. R., and Robertson, R. (1996). "Multisensor Towed Array Detection System (MTADS), an automated high-efficiency survey system for characterization of ordnance and explosive waste (OE) sites." *Proceedings of the UXO Forum 1996*. Williamsburg, VA, 53-59,.
- McDonald, J. R., Nelson, H. H., Robertson Richard, Altshuler, Thomas W., and Andrews, Anne M. (1997). "Field demonstration of the multisensor towed array detection system (MTADS)." *Proceedings of the UXO Forum '97*. Nashville, TN, 243-254.
- McFee, John E., and Das, Yogadhis. (1990). "A multipole expansion model for compact ferrous object detection." *Proceedings of the ANTEM Symposium on Antenna Technology and Applied Electromagnetics*. Manitoba, Canada, 633-638.
- McNeill, J. D., and Bosnar, Miro. (1996). "Application of time domain electromagnetic techniques to UXO detection." *Proceedings of the UXO Forum 1996*. Williamsburg, VA, 34-42.
- Meju, Max A. (1994). *Geophysical data analysis: understanding inverse problem theory and practice*. Course Notes Series, Volume 6, Society of Exploration Geophysicists, Tulsa, OK.
- Millhouse, S., Helms, L., Foley, J., Gifford, M. (1996). "Ordnance and explosives (OE) program geographic information system (GIS) and knowledge base (KB)." *Proceedings of the UXO Forum 1996*. Williamsburg, VA, 469-478, .
- McDonald, J. R., Nelson, H. H., Neece, J., Robertson, R., and Jeffries, R. A. (1997). "MTADS unexploded ordnance operations at the Badlands Bombing Range, Pine Ridge Reservation, Cunny Table, South Dakota," NRL/PU/6110-98-353, Naval Research Laboratory, Washington, DC.

- Nelson, H.H., McDonald, J.R., and Robertson, R. (1997). "Multisensor ordnance signatures for algorithm development and model training." *Proceedings of the Symposium on the Application of Geophysics to Engineering and Environmental Problems*. Reno, NV, 863-869.
- Office of Secretary of Defense. (1997). "Unexploded ordnance clearance: annual report to congress," UXO Clearance Steering Group, Washington, DC.
- Parker, Robert L. (1994). *Geophysical Inverse Theory*. Princeton University Press, Princeton, NJ.
- Parsons Engineering Science, Inc. (1997). "Background characterization of the response of geophysical sensors for subsurface UXO detection," Prepared for U.S. Army Engineer Waterways Experiment Station, Vicksburg, MS, Parsons Engineering Science, Inc., Fairfax, VA.
- Pennella, John J. (1982). "Magnetometer techniques in the detection of projectiles," NAVEODTECHCEN Technical Report TR-239, Naval Explosive Ordnance Disposal Technology Center, Indian Head, MD.
- Roest, Walter R., Verhoef, Jacob, and Pilkington, Mark. (1992). "Magnetic interpretation using the 3-D analytic signal," *Geophysics* 57(1), 116-125.
- Sandberg, Stewart K. (1990). "Microcomputer software for individual or simultaneous inverse modeling of transient electromagnetic, resistivity, and induced polarization soundings," Open-File Report OFR 90-1, New Jersey Geological Survey.
- Scollar, I., Tabbagh, A., Hesse, A., and Herzog, I. (1990). *Archaeological Prospecting and Remote Sensing*. Cambridge University Press, New York.
- Sheriff, Robert E. (1991). *Encyclopedic dictionary of exploration geophysics*. Geophysical Reference Series, Society of Exploration Geophysicists, Tulsa, OK.
- Simms, Janet E., and Butler, Dwain K. (1992). "Assessment and selection of an automated electrical resistivity interpretation procedure," Technical Report GL-92-12, U.S. Army Engineer Waterways Experiment Station, Vicksburg, MS.
- Simms, Janet E., Butler, Dwain K., and Powers, Michael H. (1995). "Full waveform inverse modeling of ground penetrating radar data: An initial approach," Miscellaneous Paper GL-95-4, U.S. Army Engineer Waterways Experiment Station, Vicksburg, MS.
- Stratton, J. (1941). *Electromagnetic Theory*. McGraw-Hill, New York, NY.
- Telford, W. M., Geldart, L. P., and Sheriff, R. E. (1990). *Applied Geophysics*. Cambridge University Press, New York.
- Headquarters U. S. Army Corps of Engineers. (1995). "Geophysical exploration for engineering and environmental investigations," Engineer Manual EM 1110-1-1802, Washington, DC.

- U. S. Army Environmental Center (USAEC). (1994). "Unexploded ordnance advanced technology demonstration program at Jefferson Proving Ground (Phase I)," Report No. SFIM-AEC-ET-CR-94120, Aberdeen Proving Ground, MD.
- USAEC. (1995). "Evaluation of individual demonstrator performance at the unexploded ordnance advanced technology demonstration program at Jefferson Proving Ground (Phase I)," Report No. SFIM-AEC-ET-CR-95033, Aberdeen Proving Ground, MD.
- USAEC. (1996). "Unexploded ordnance advanced technology demonstration program at Jefferson Proving Ground (Phase II)," Report No., SFIM-AEC-ET-CR-96170, Aberdeen Proving Ground, MD.
- USAEC. (1997). "UXO technology demonstration program at Jefferson Proving Ground, Phase III," Report No. SFIM-AEC-ET-CR-97011, Aberdeen Proving Ground, MD.
- Wait, James R. (1982). *Geoelectromagnetism*. Academic Press, New York.
- Ward, Stanley H., and Hohmann, Gerald W. (1987). "Electromagnetic theory for geophysical applications," *Electromagnetic Methods in Applied Geophysics, Volume I, Theory*. Society of Exploration Geophysics, Tulsa, OK, 131-311.

Appendix A WES Ordnance Signature Datasets, Magnetic Profile Measurements

Chart1

Data cor to 1 B.S.:60mm, 60 cm offset, all orientations

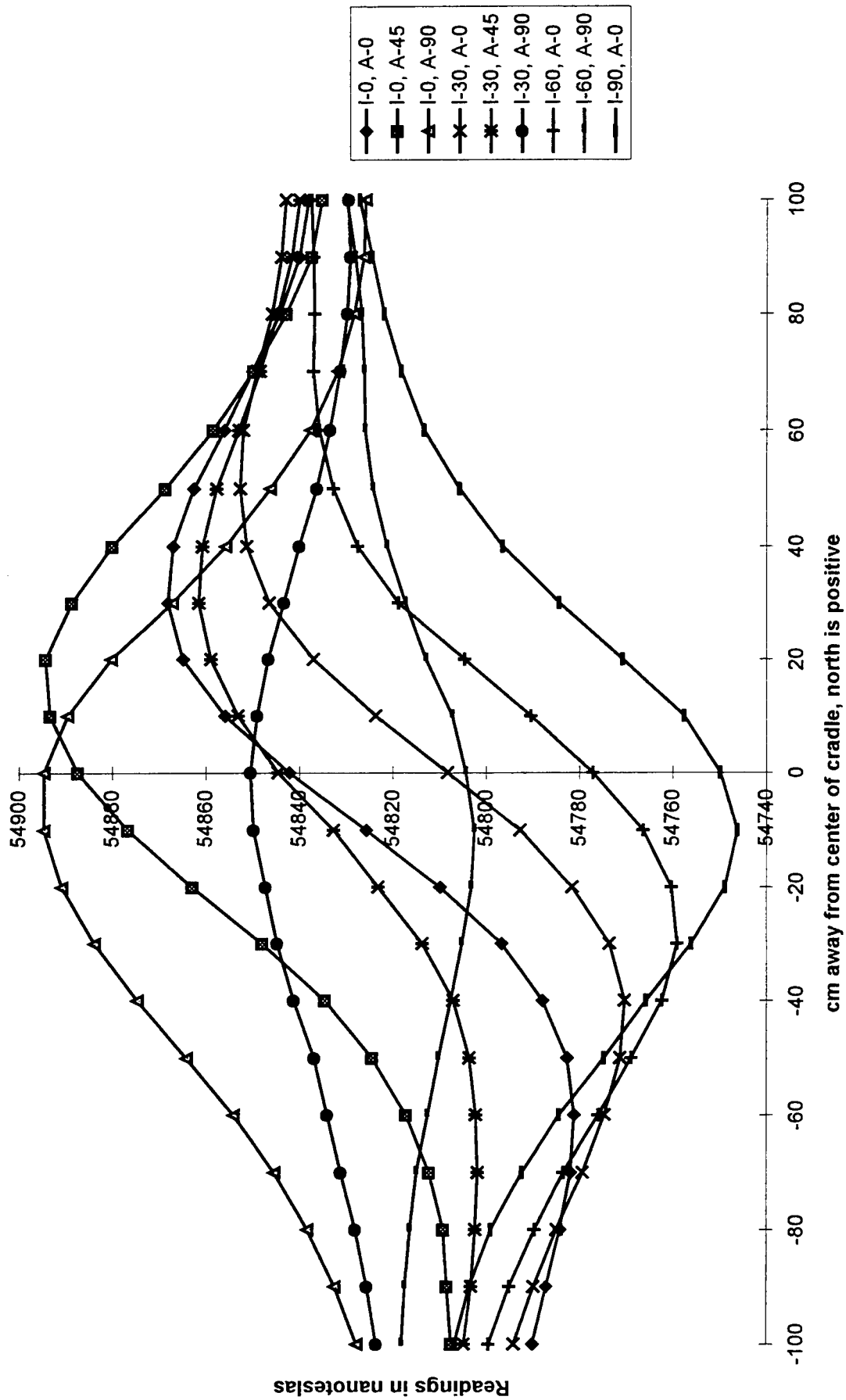


Chart6

Data cor to 1 B.S.:81 mm,0 cm offset, all orientations except for 90 deg incl, 0 deg azi

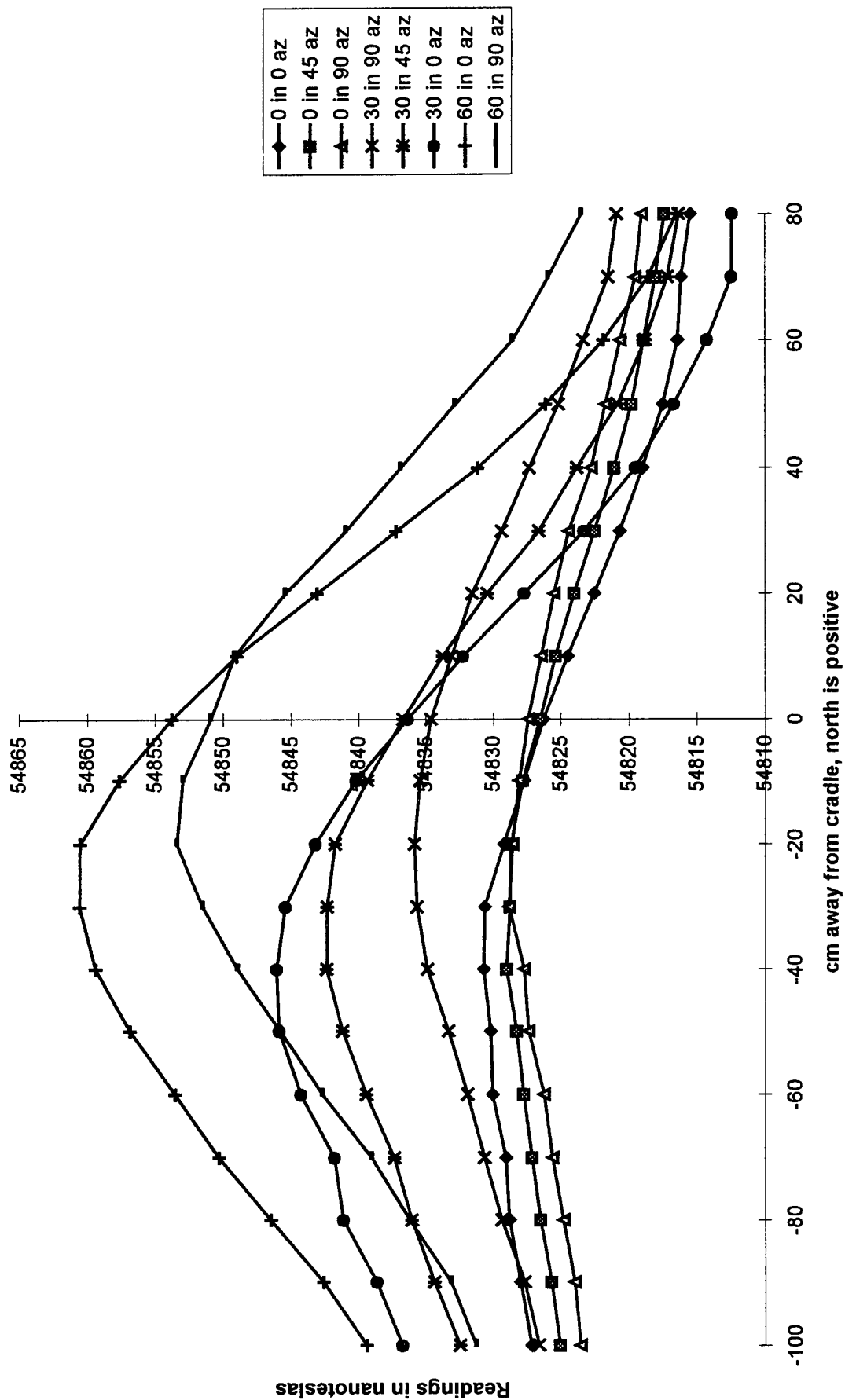


Chart7

Data cor to 1 B.S.:105 mm shell, 0 cm offset, all orientations, background readings subtr

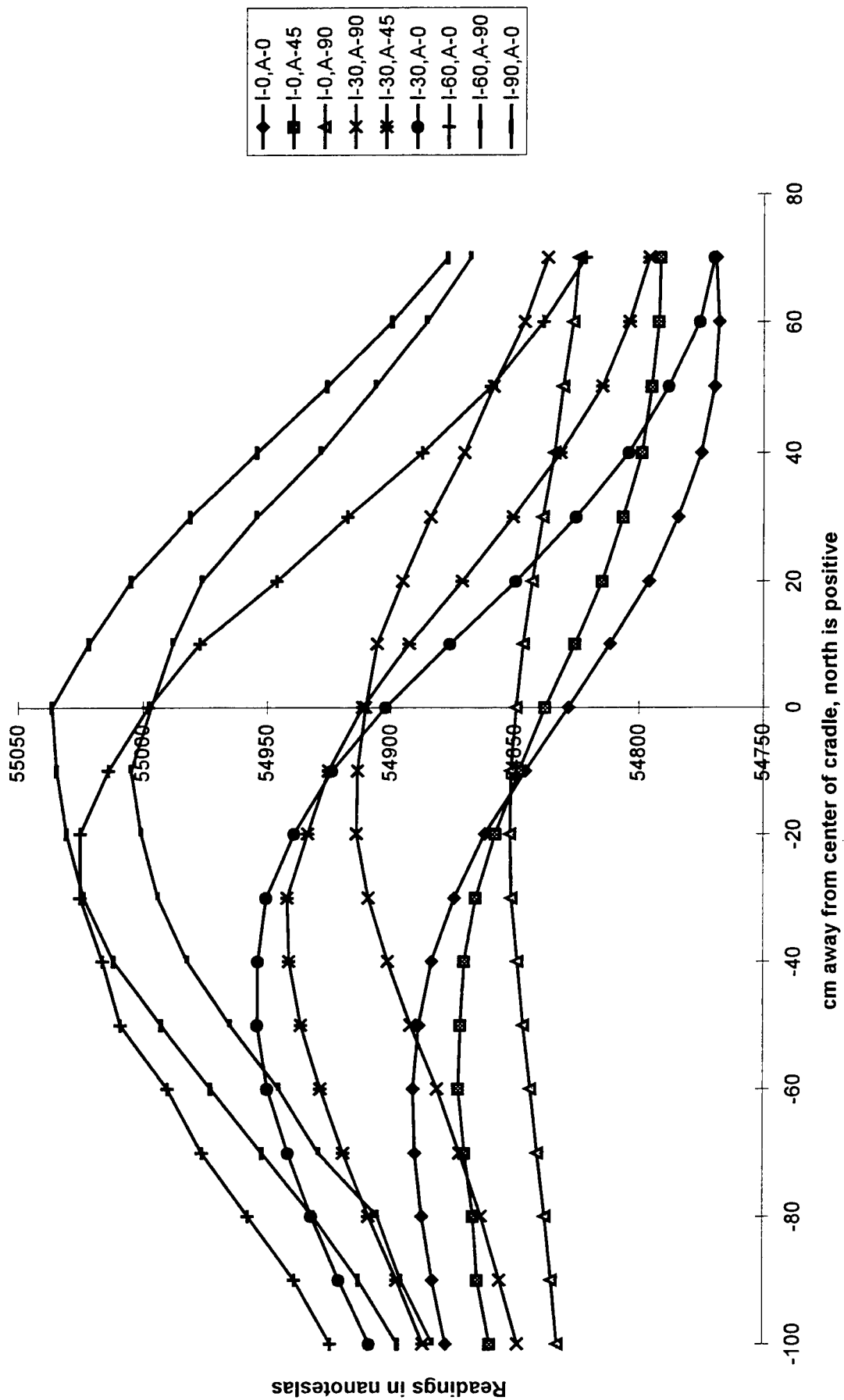
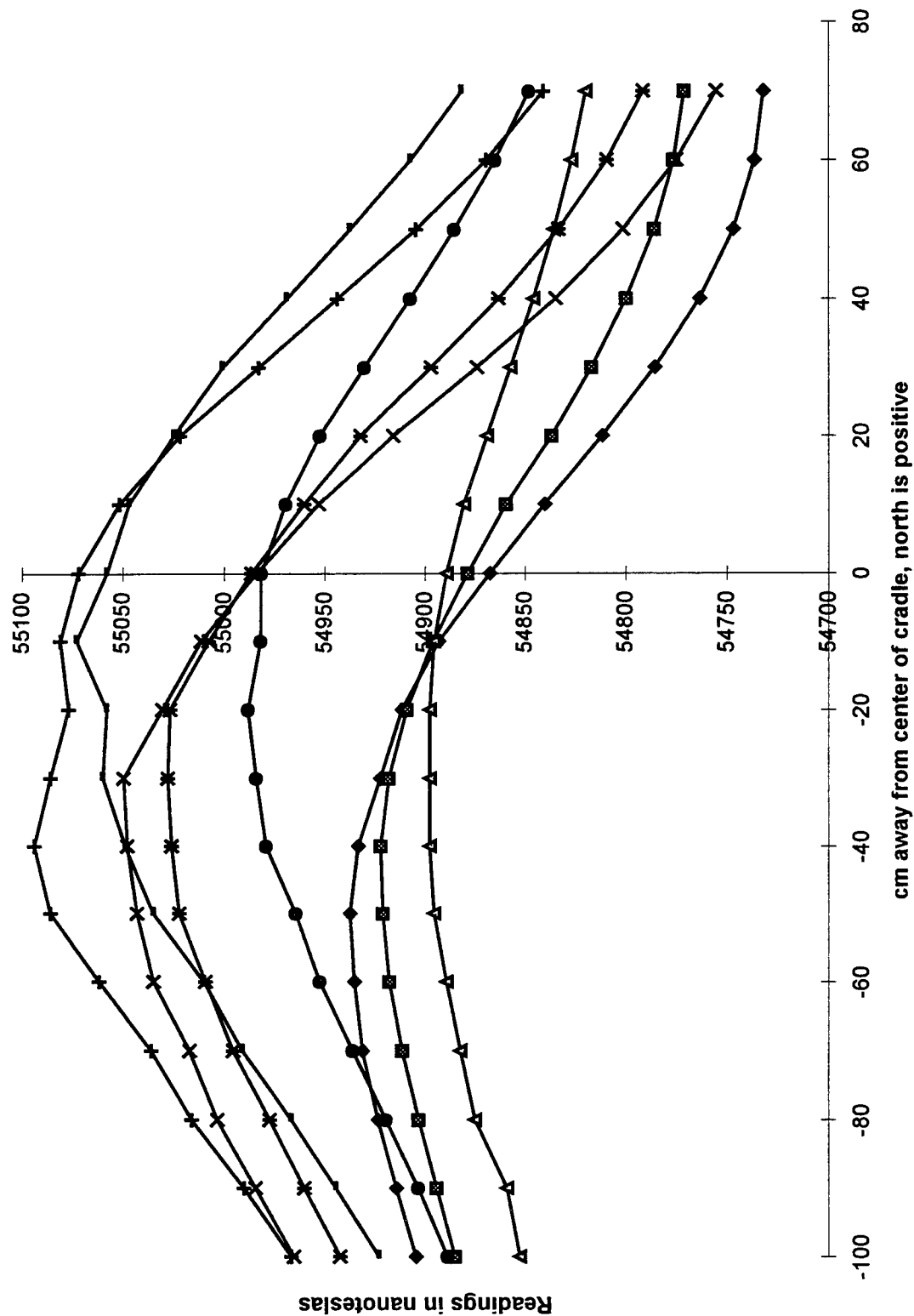


Chart2

Data cor to 1 B.S.:155 mm, 0 cm offset, all orientations except 90 deg incl, 0 deg azi



Data cor to 1 B.S.:90 mm, 0 cm offset, 0 deg incl, 0 deg azi, values avg

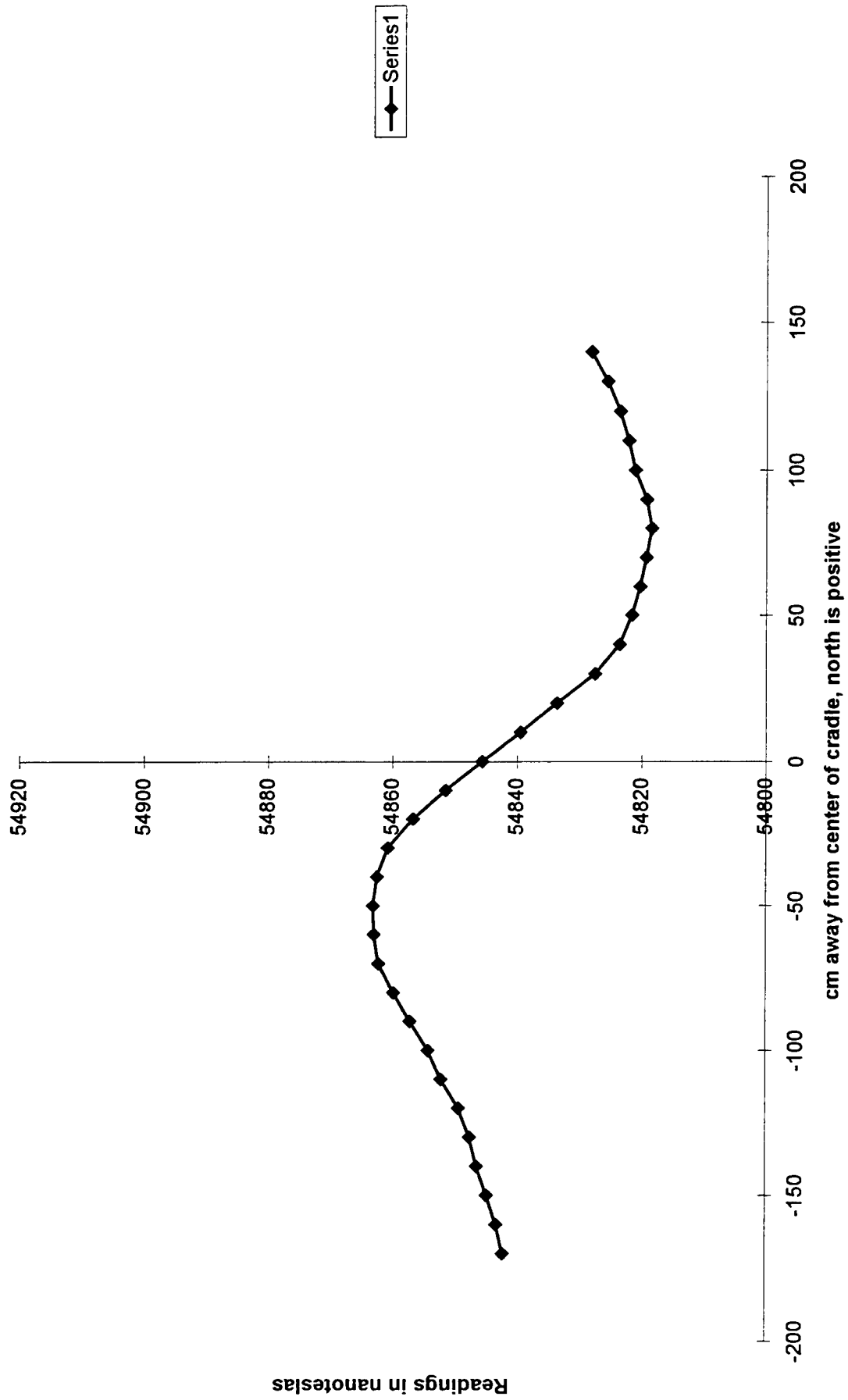


Chart20

Data cor to 1 B.S.:90 mm, 40cm, 0 deg incl, 0 deg azi, values avg

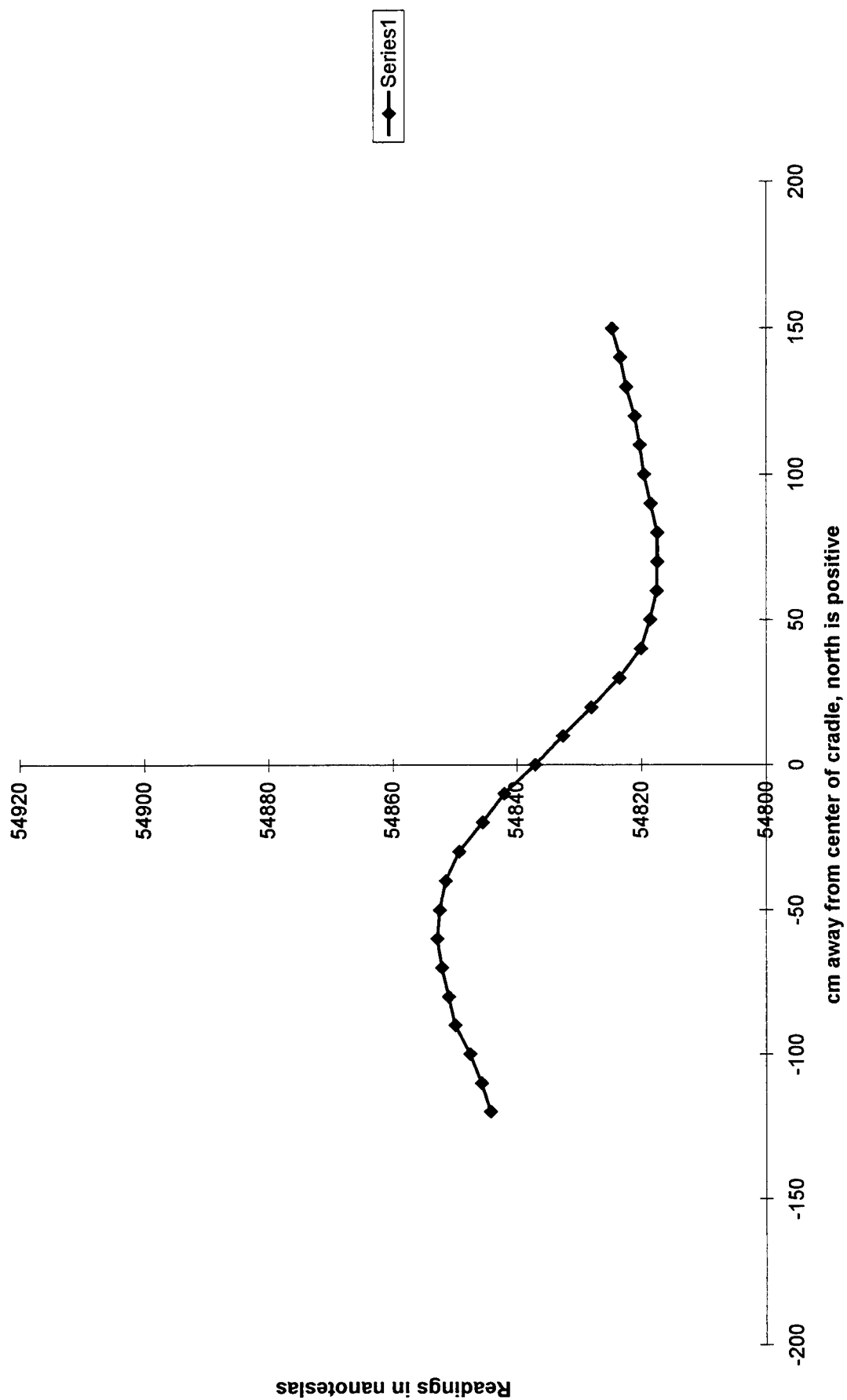
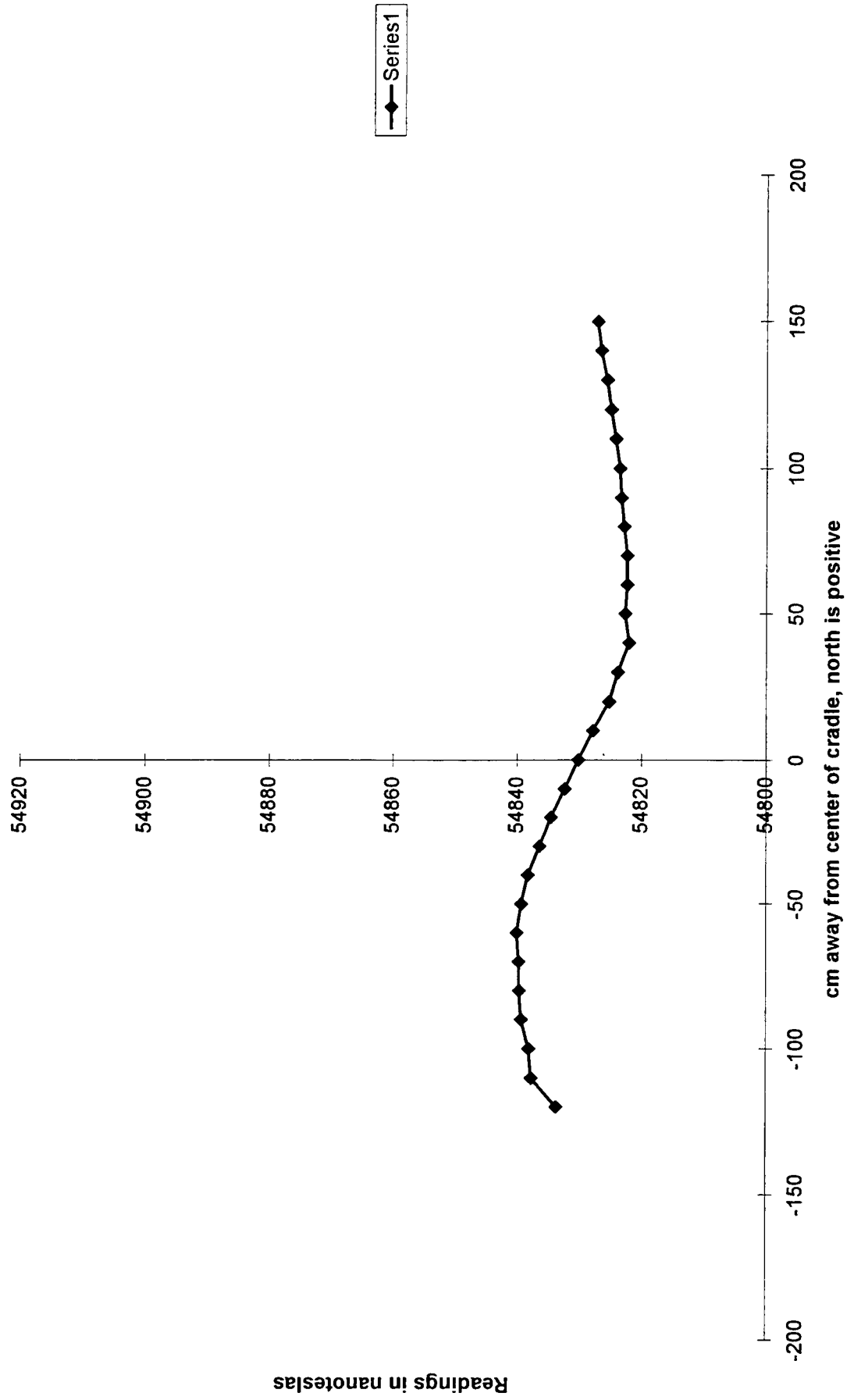


Chart34

Data cor to 1 B.S.:90 mm, 80 cm offset, 0 deg incl, 0 deg azi, values avg



Data cor to 1 B.S.:90 mm, 0 cm offset, 0 deg incl, 45 deg azi, values avg

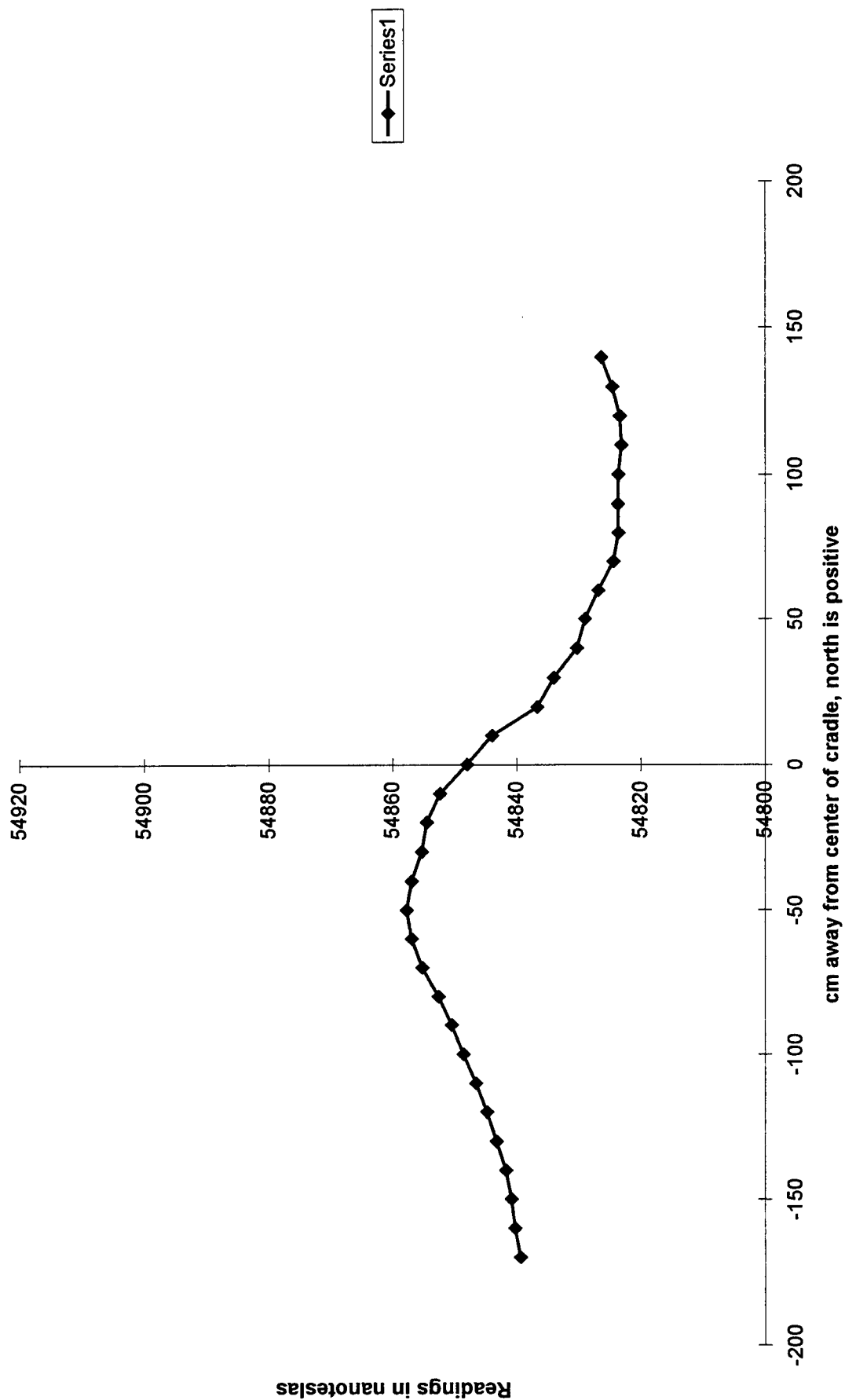


Chart31

Data cor to 1 B.S.:90 mm, 40 cm offset, 0 deg incl, 45 deg azi

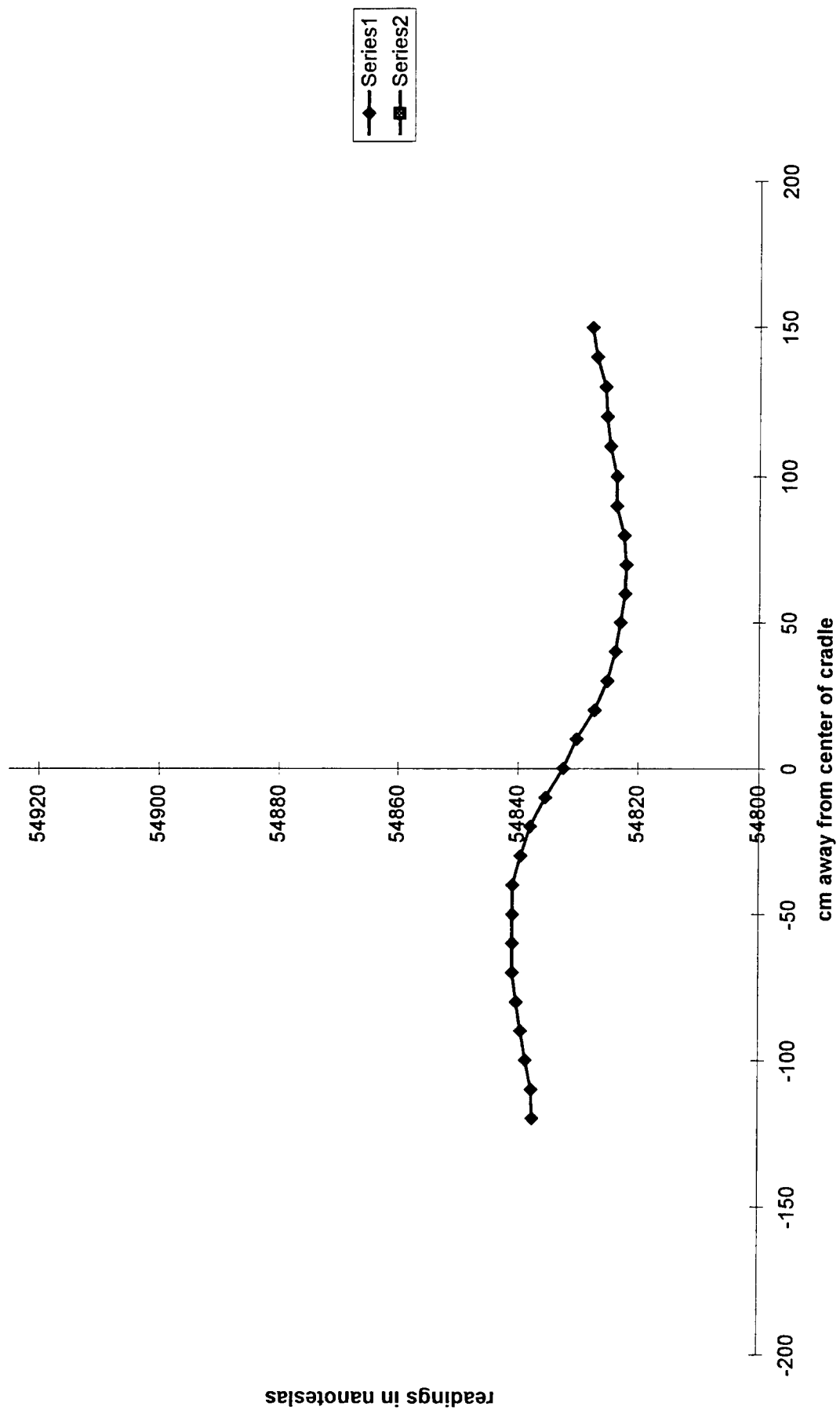
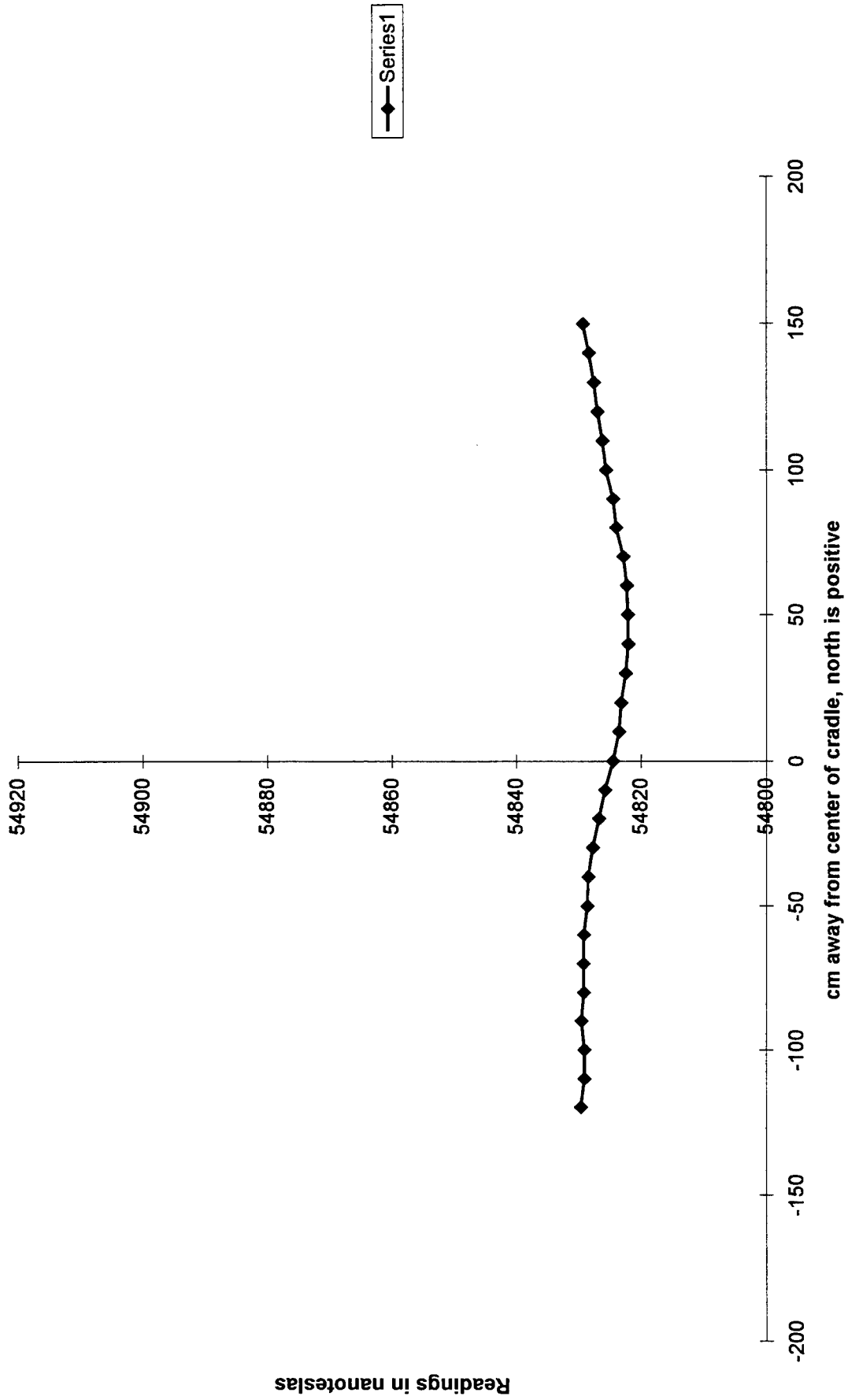


Chart4

Data cor to 1 B.S.:90 mm, 80 cm offset, 0 deg incl, 45 deg azi, values avg



Data cor to 1 B.S.:90 mm, 0 cm offset, 0 deg incl, 90 deg azi, values avg

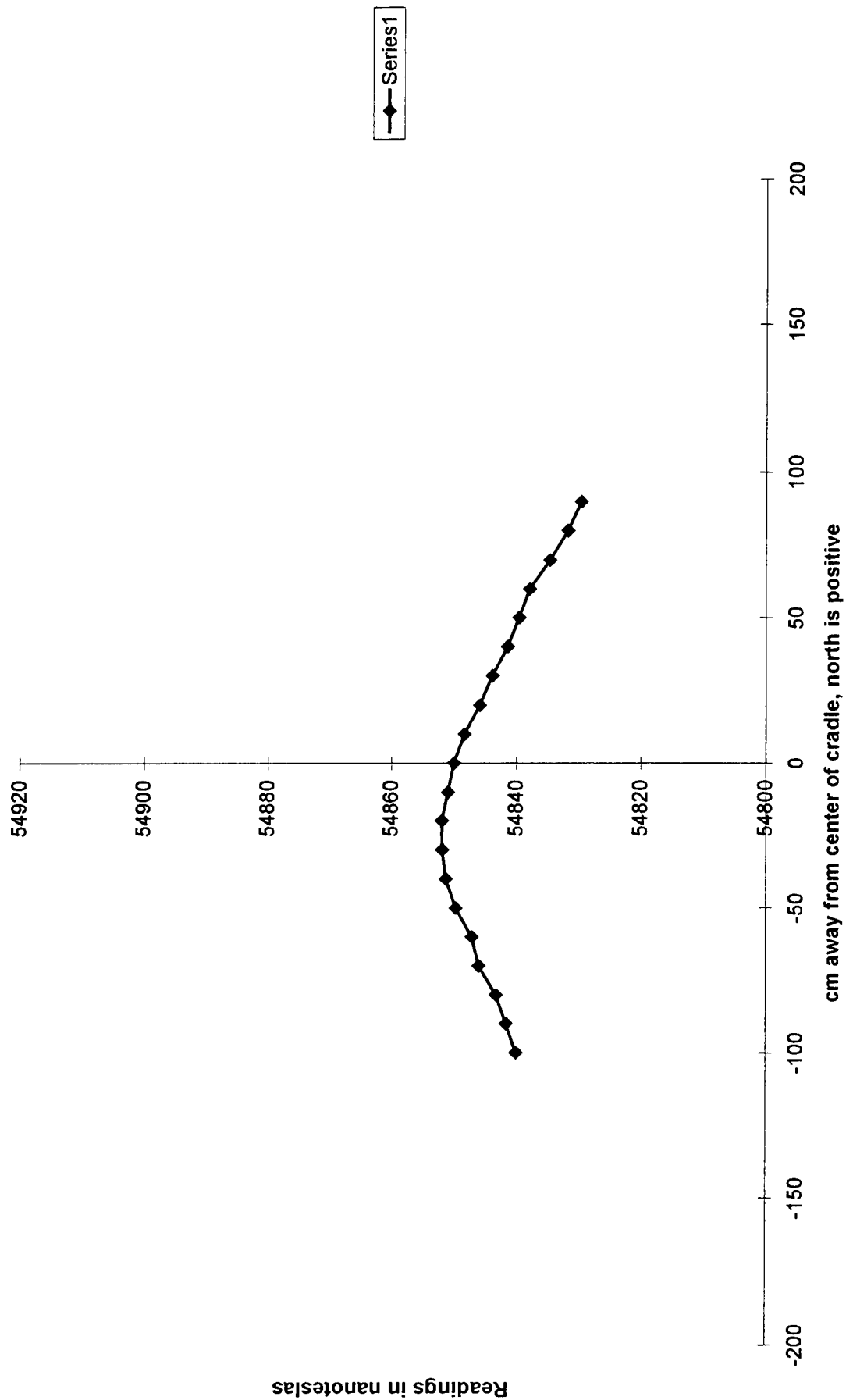


Chart45

Data cor to 1 B.S.:90 mm, 40 cm offset, 0 deg incl, 90 deg azi, values avg

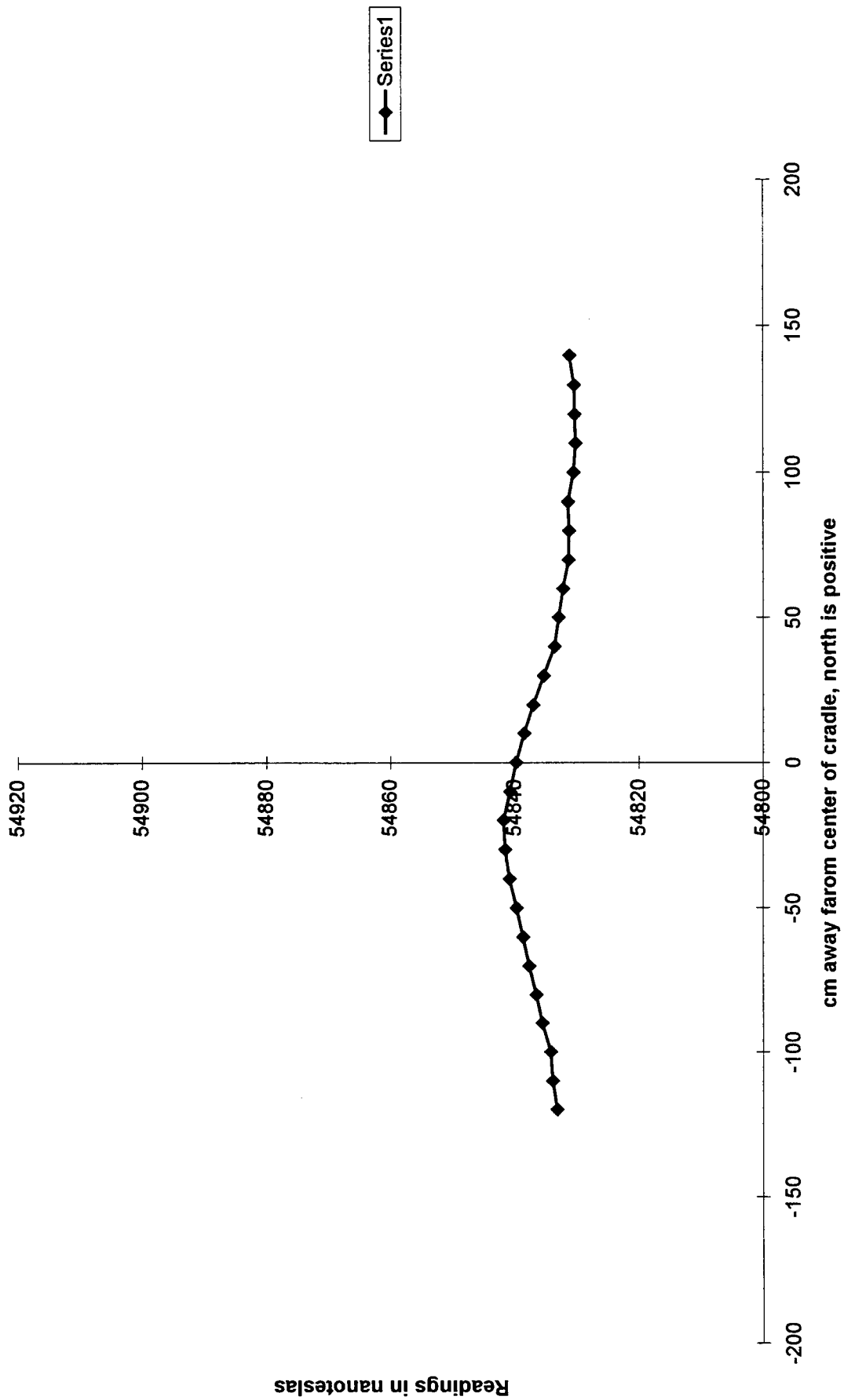
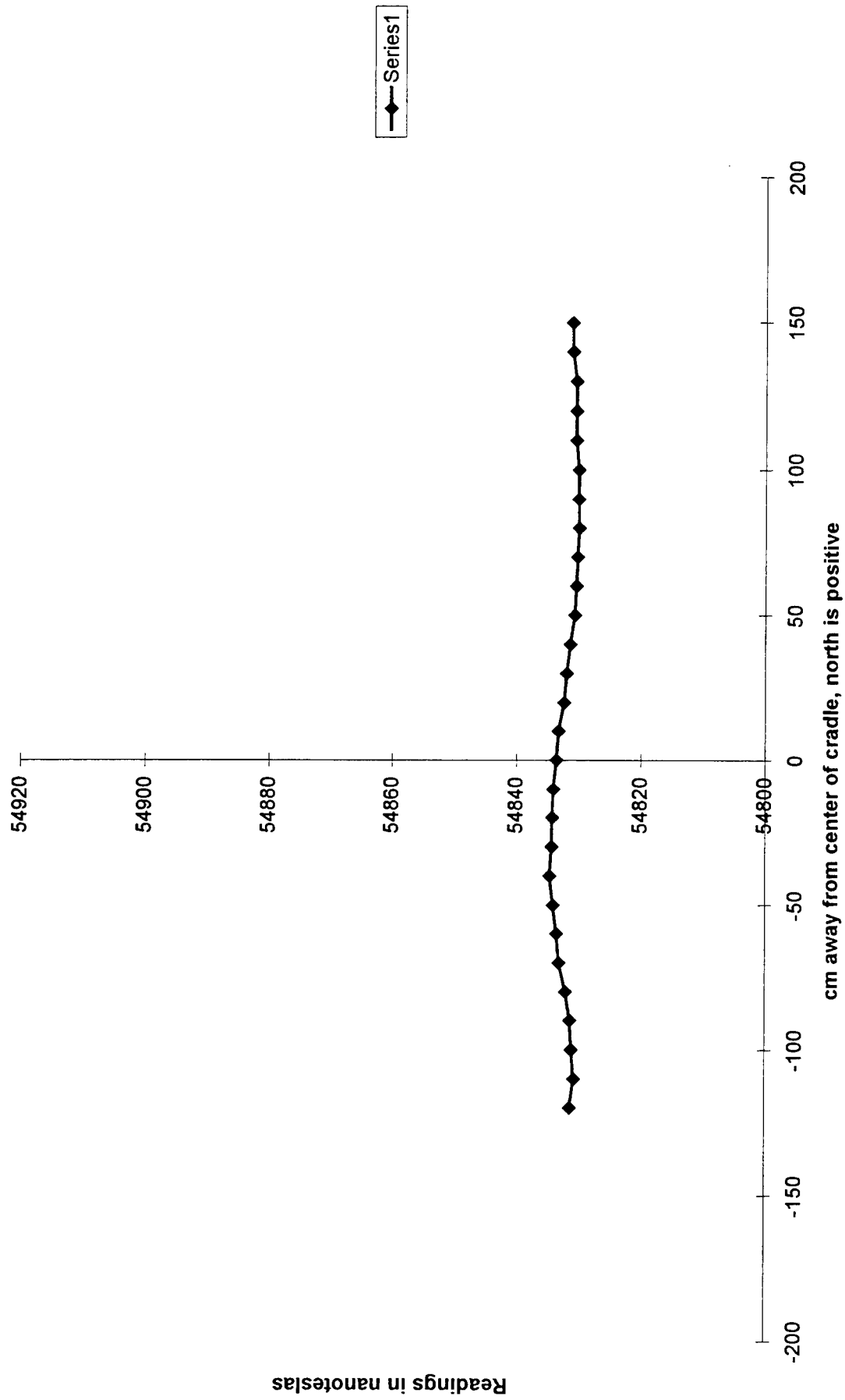
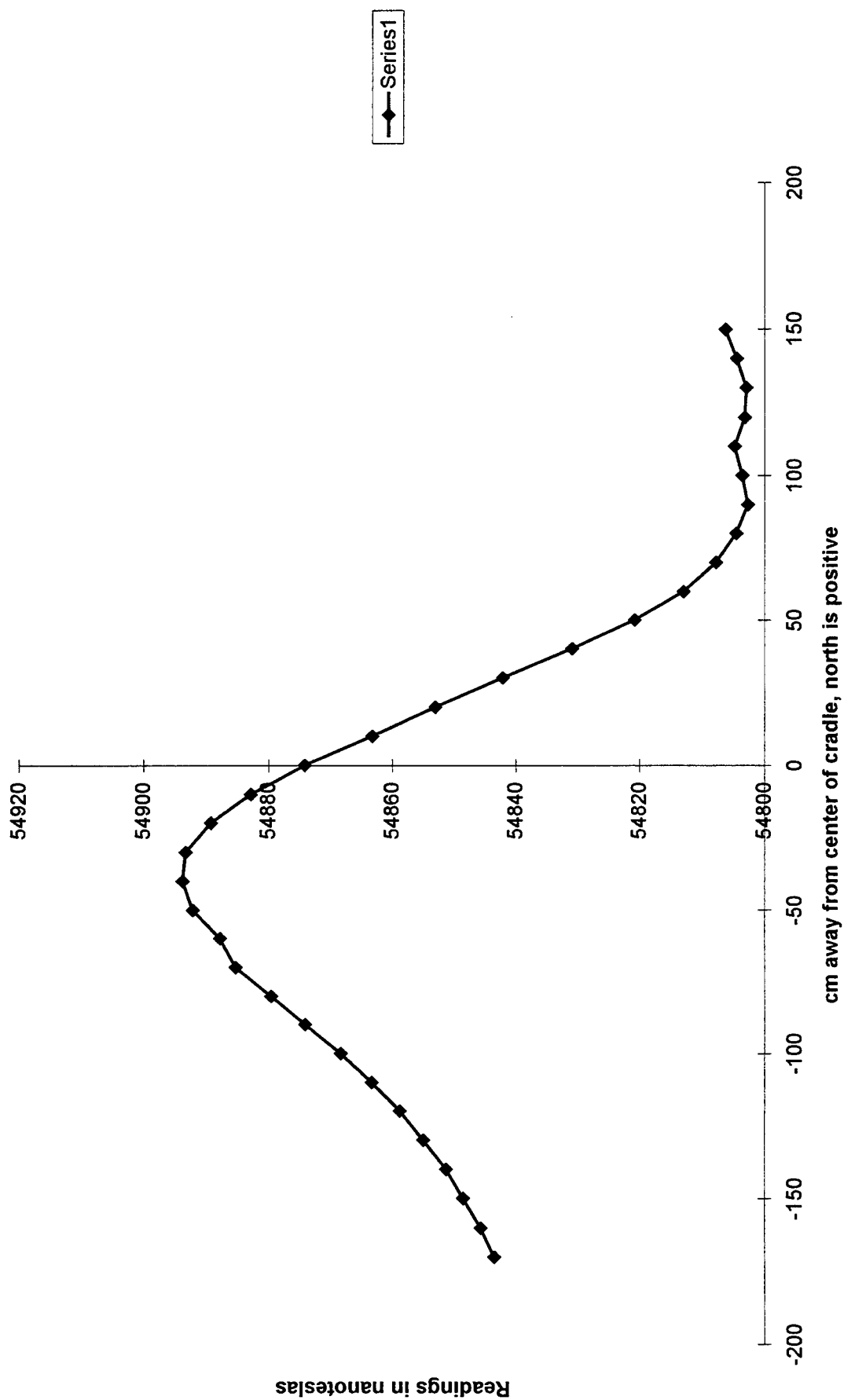


Chart46

Data cor to 1 B.S.:90 mm, 80 cm offset, 0 deg incl, 90 deg azi, values avg



Data cor to 1 B.S.:90 mm, 0 cm offset, 30 deg incl, 0 deg azi, values avg



Data cor to 1 B.S.:90 mm, 40 cm offset, 30 deg incl, 0 deg azi, values avg

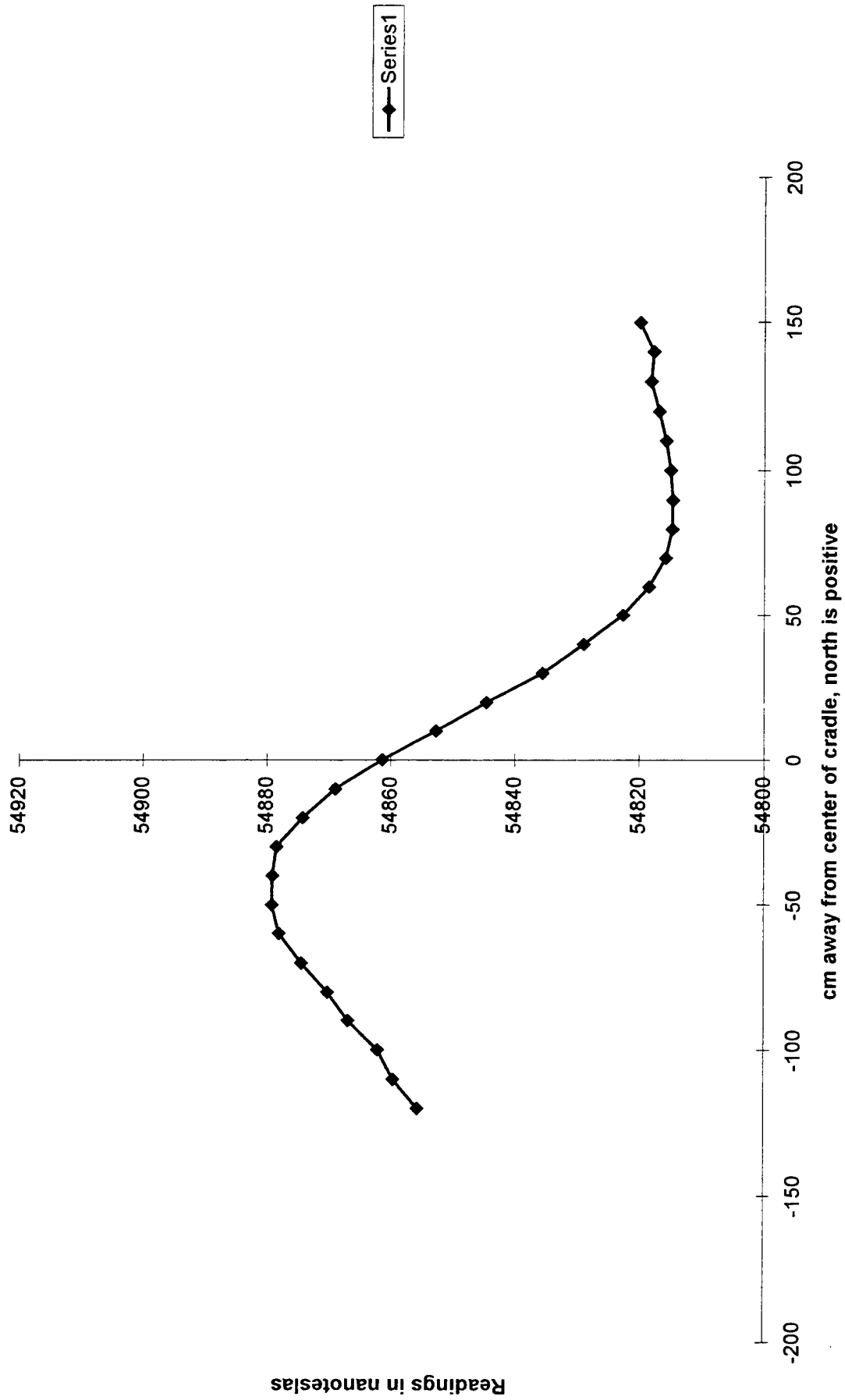


Chart50

Data cor to 1 B.S.:90 mm, 80 cm offset, 30 deg incl, 0 deg azi, values avg

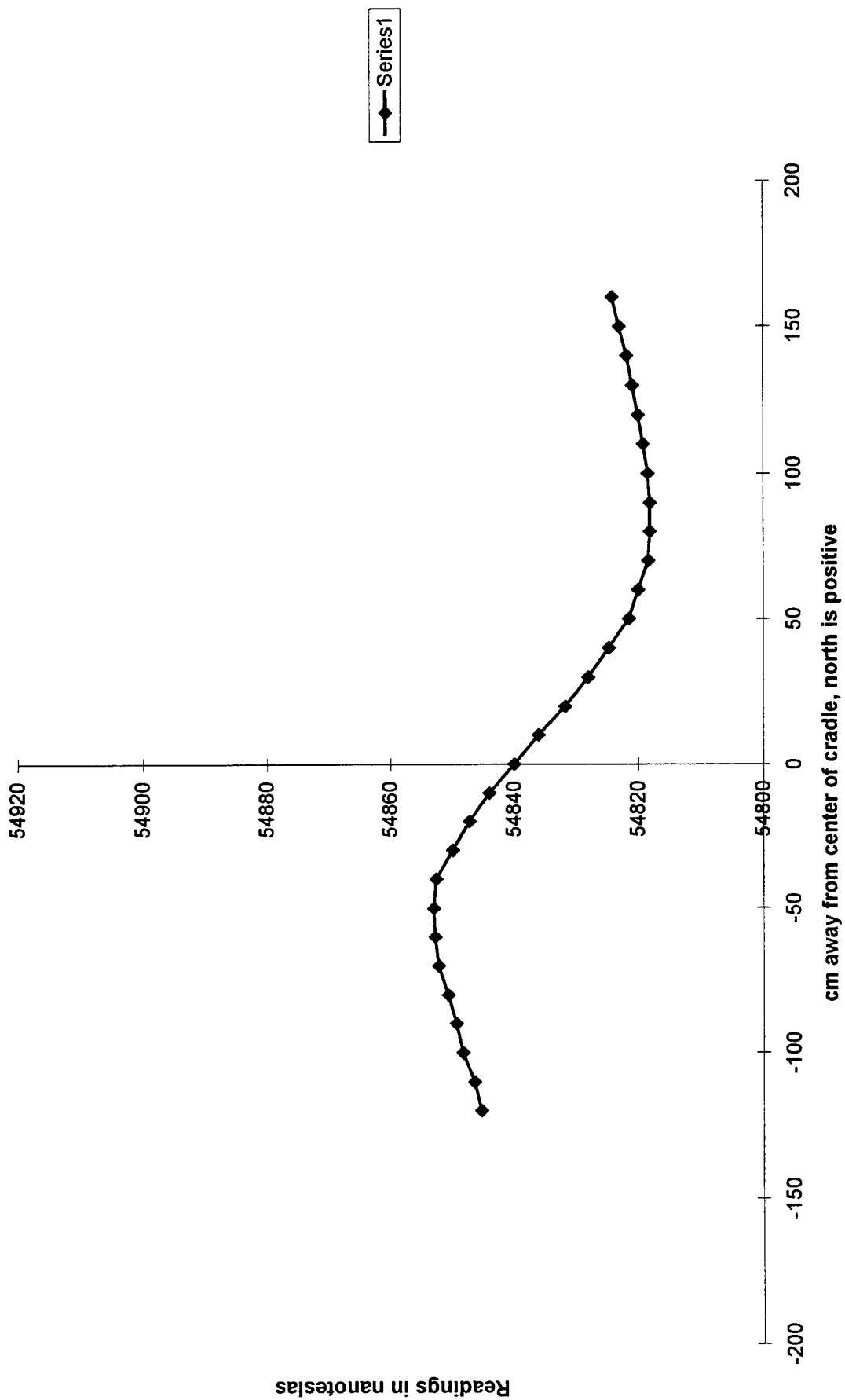


Chart51

Data cor to 1 B.S.:90 mm, 0 cm offset, 30 deg incl, 45 deg azi, values avg

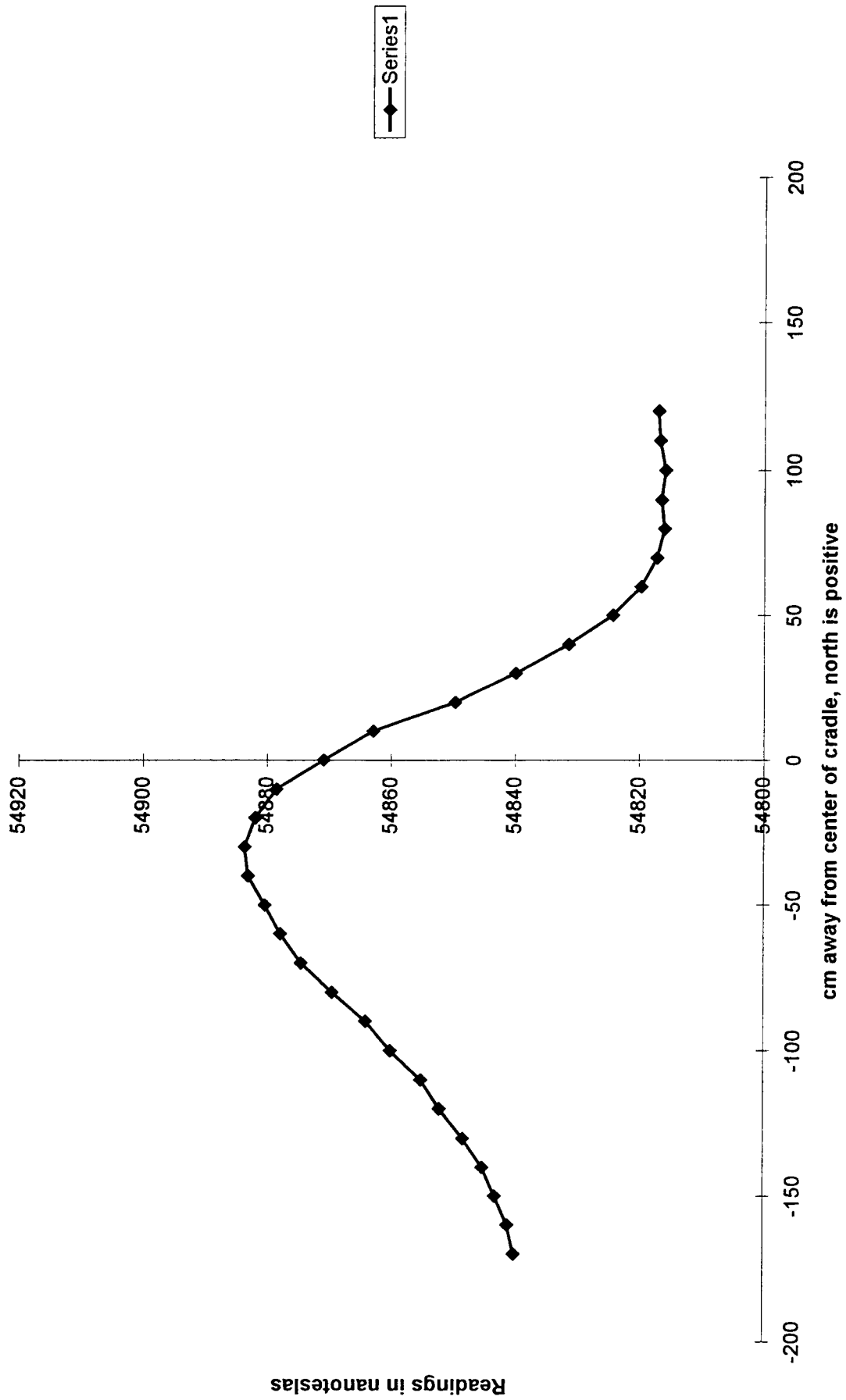
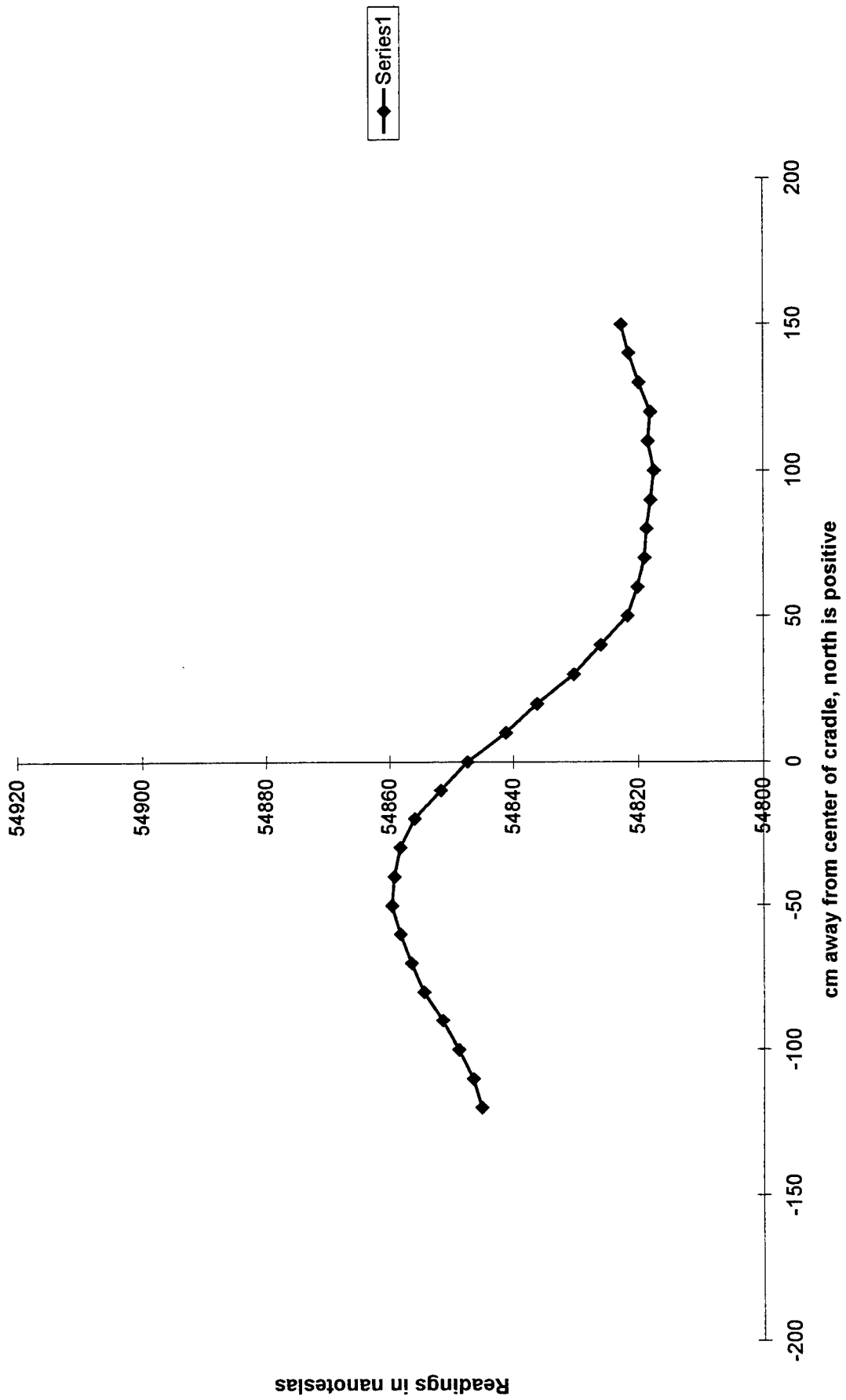


Chart52

Data cor to 1 B.S.:90mm, 40 cm offset, 30 deg incl, 45 deg azi, values avg



Data cor to 1 B.S.:90 mm, 80 cm offset, 30 deg incl, 45 deg azi, values avg

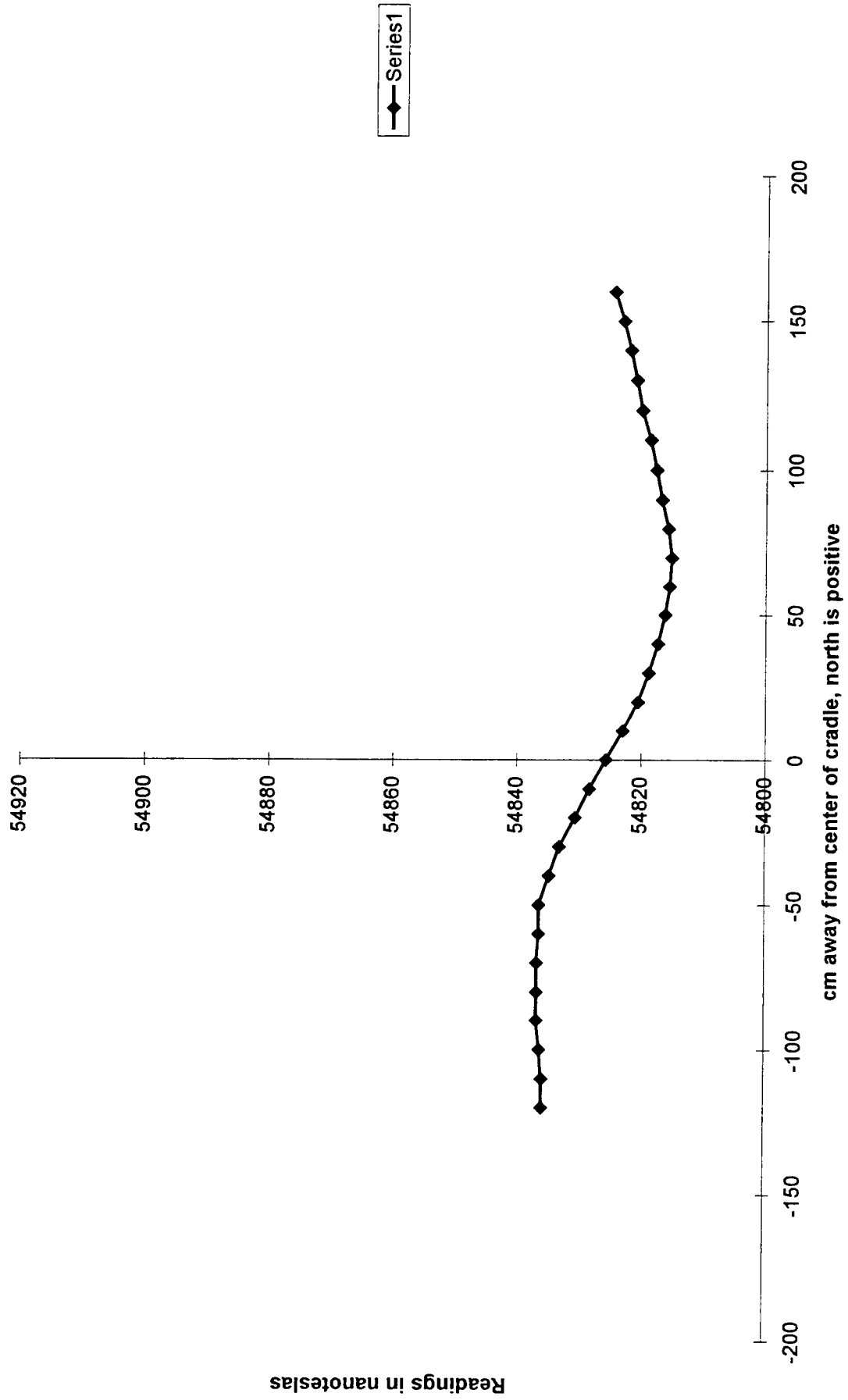


Chart54

Data cor to 1 B.S.: 90 mm, 0 cm offset, 30 deg incl, 90 deg azi, values avg

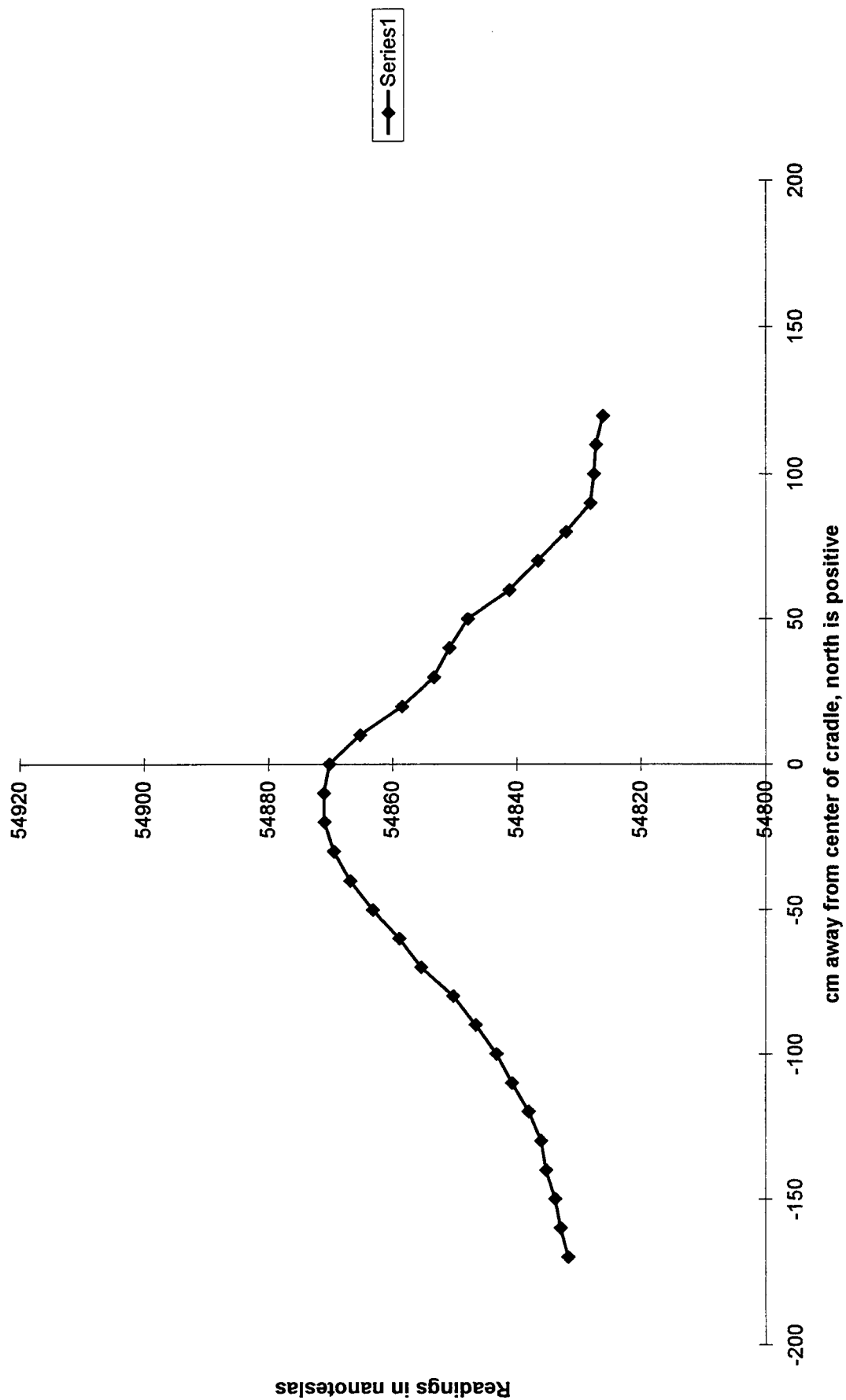


Chart55

Data cor to 1 B.S.:90 mm, 40 cm offset, 30 deg incl, 90 deg azi, values avg

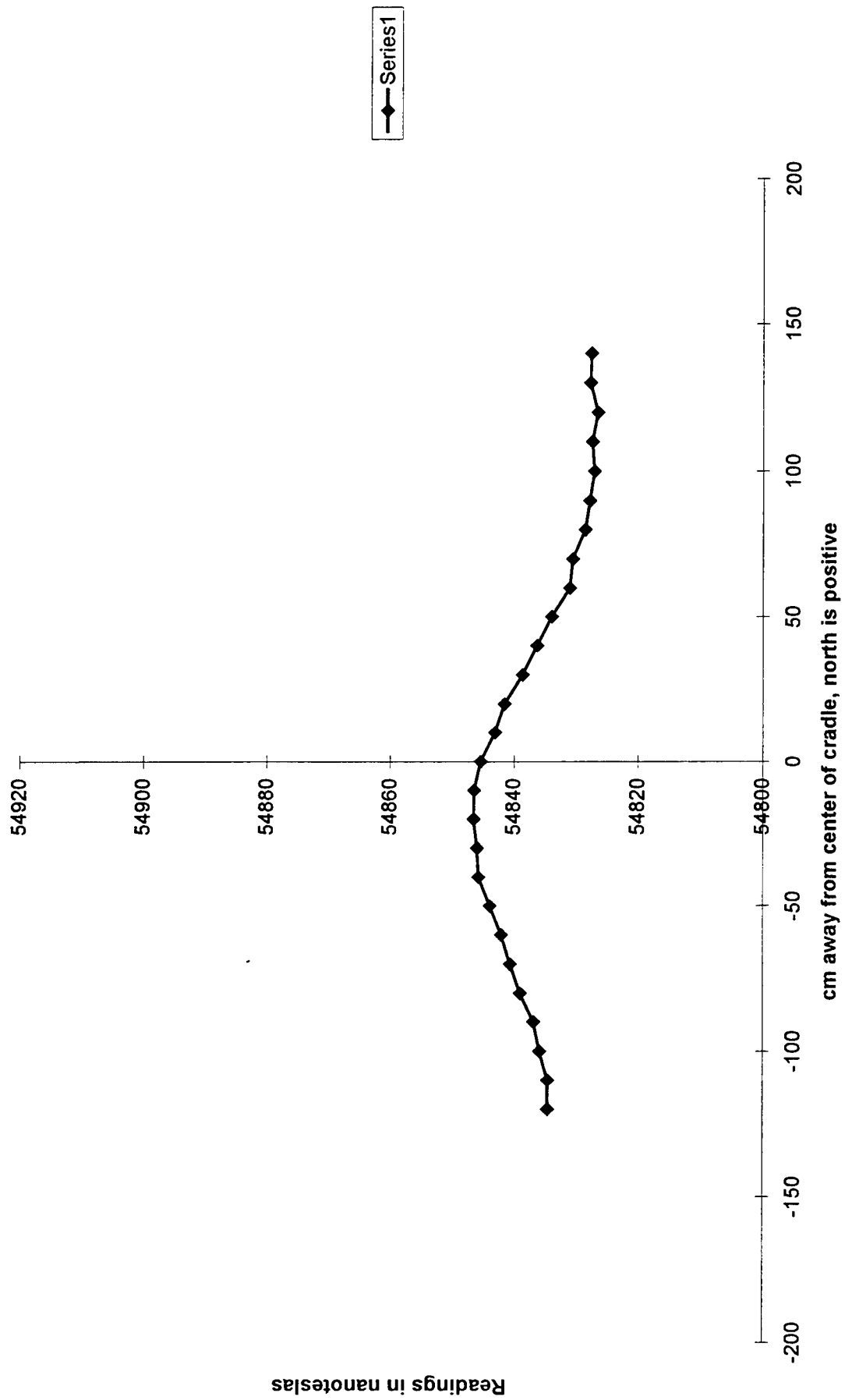


Chart56

Data cor to 1 B.S.:90 mm, 80 cm offset, 30 deg incl, 90 deg azi, values avg

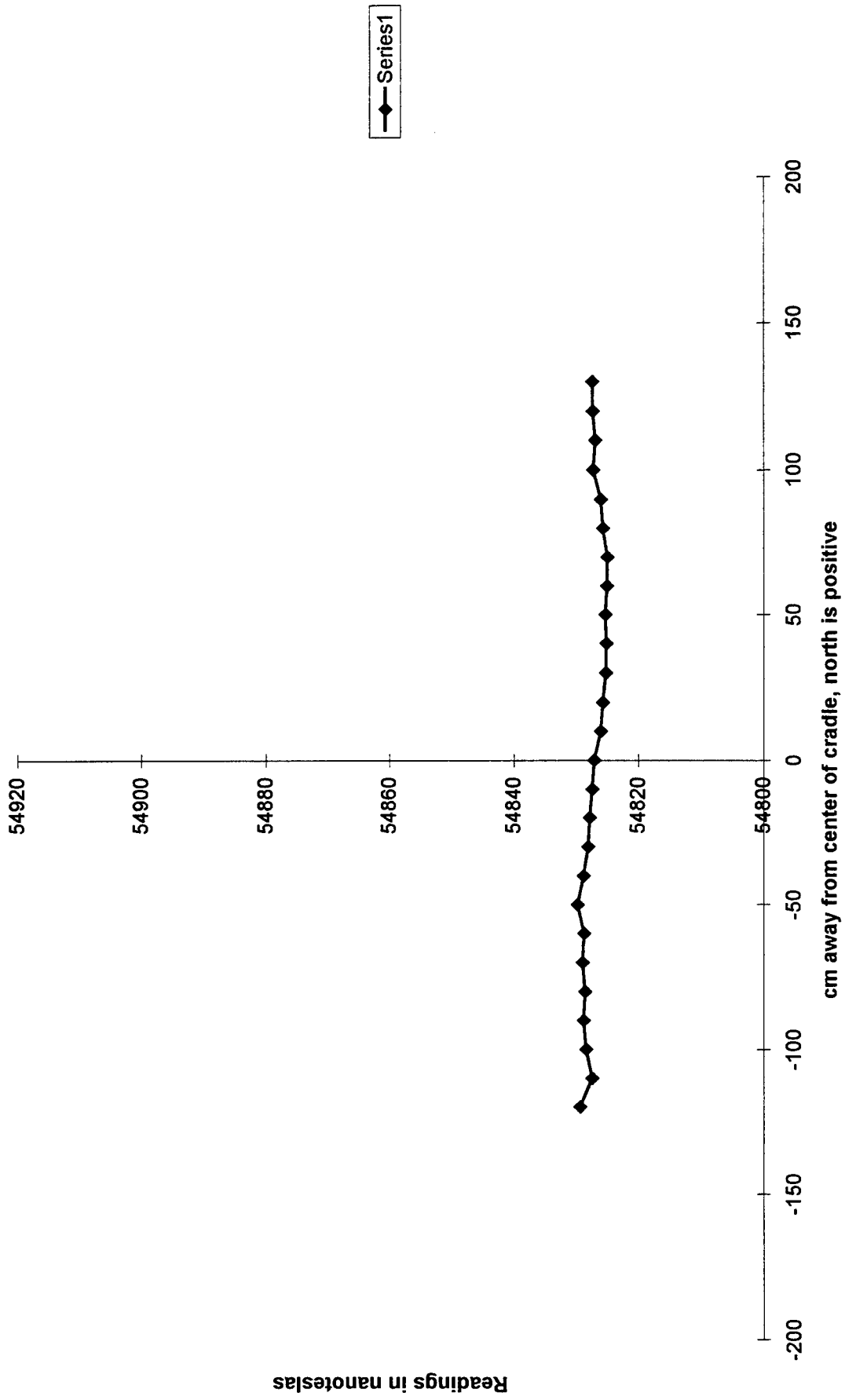


Chart57

Data cor to 1 B.S.:90mm, 0 cm offset, 60 deg incl, 0 deg azi, values avg

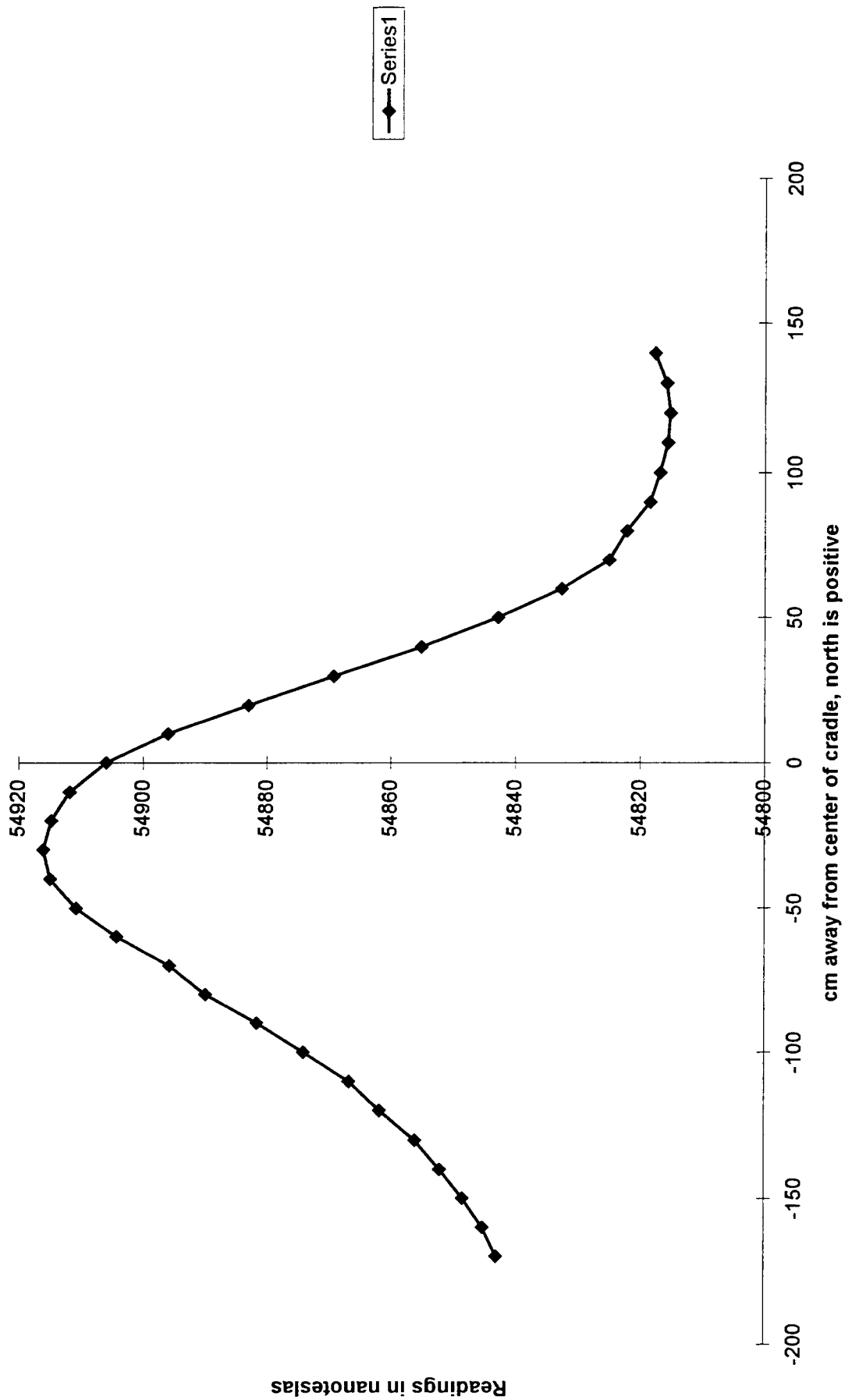
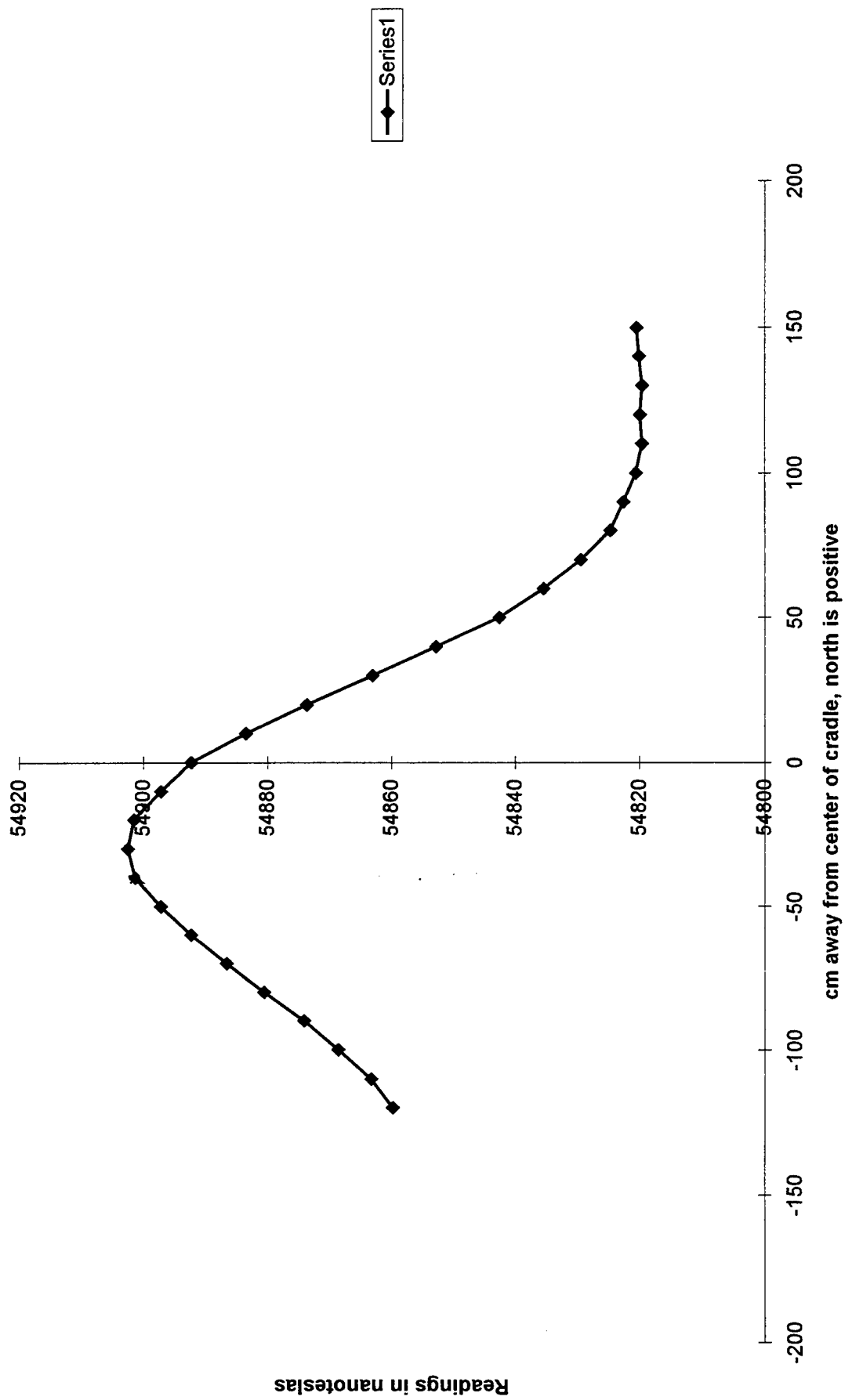
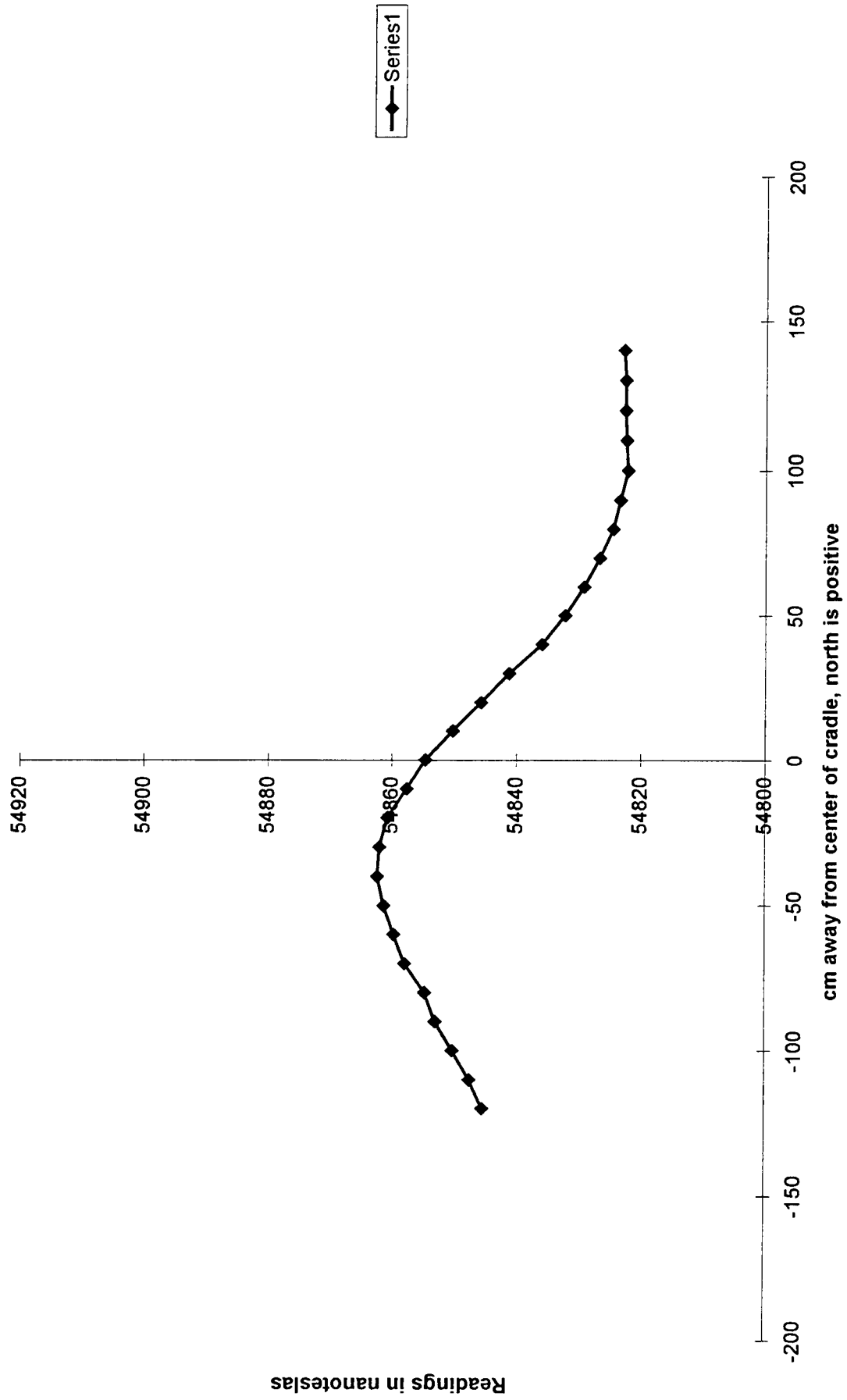


Chart58

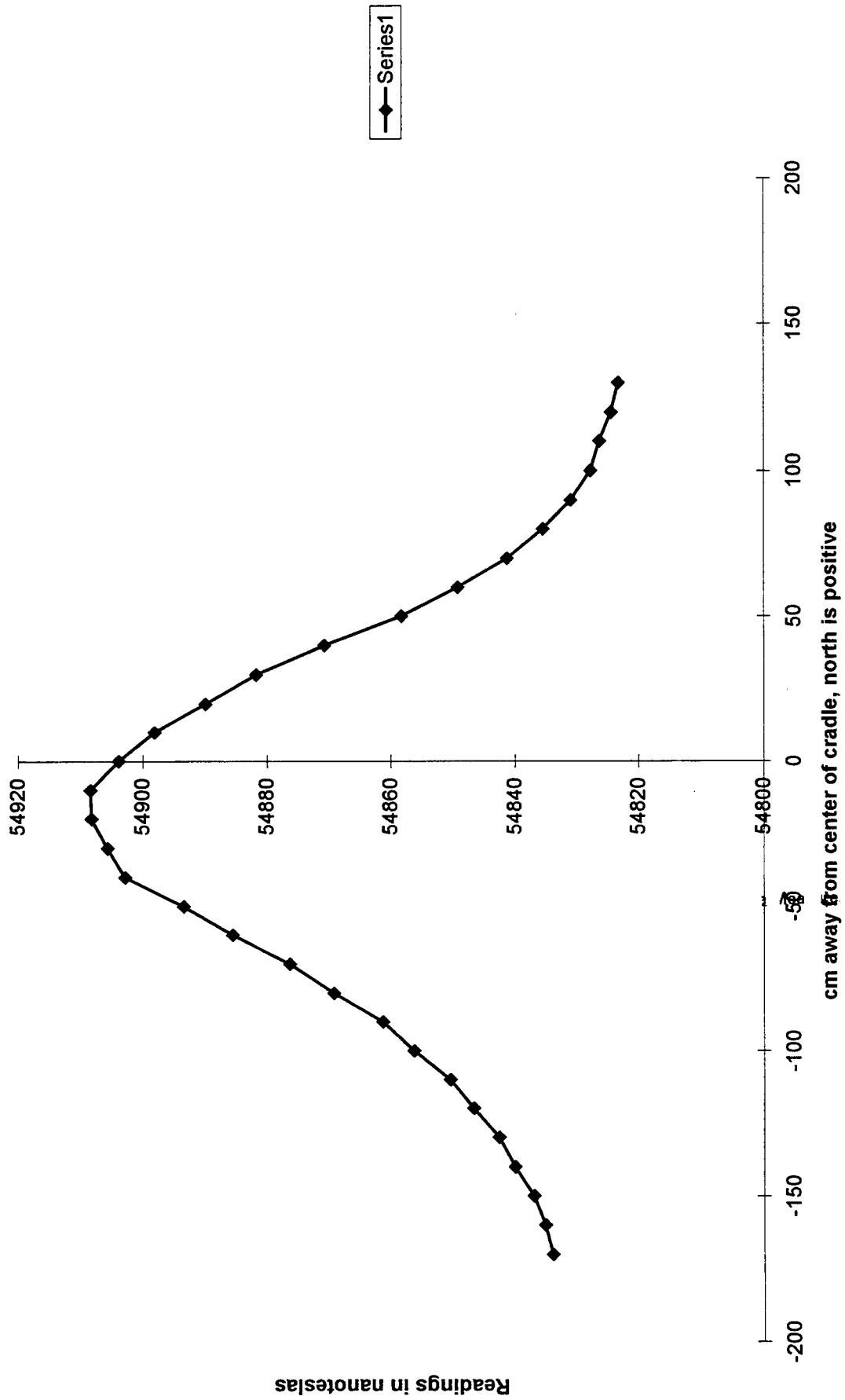
Data cor to 1 B.S.:90 mm, 40 cm offset, 60 deg incl, 0 deg azi, values avg



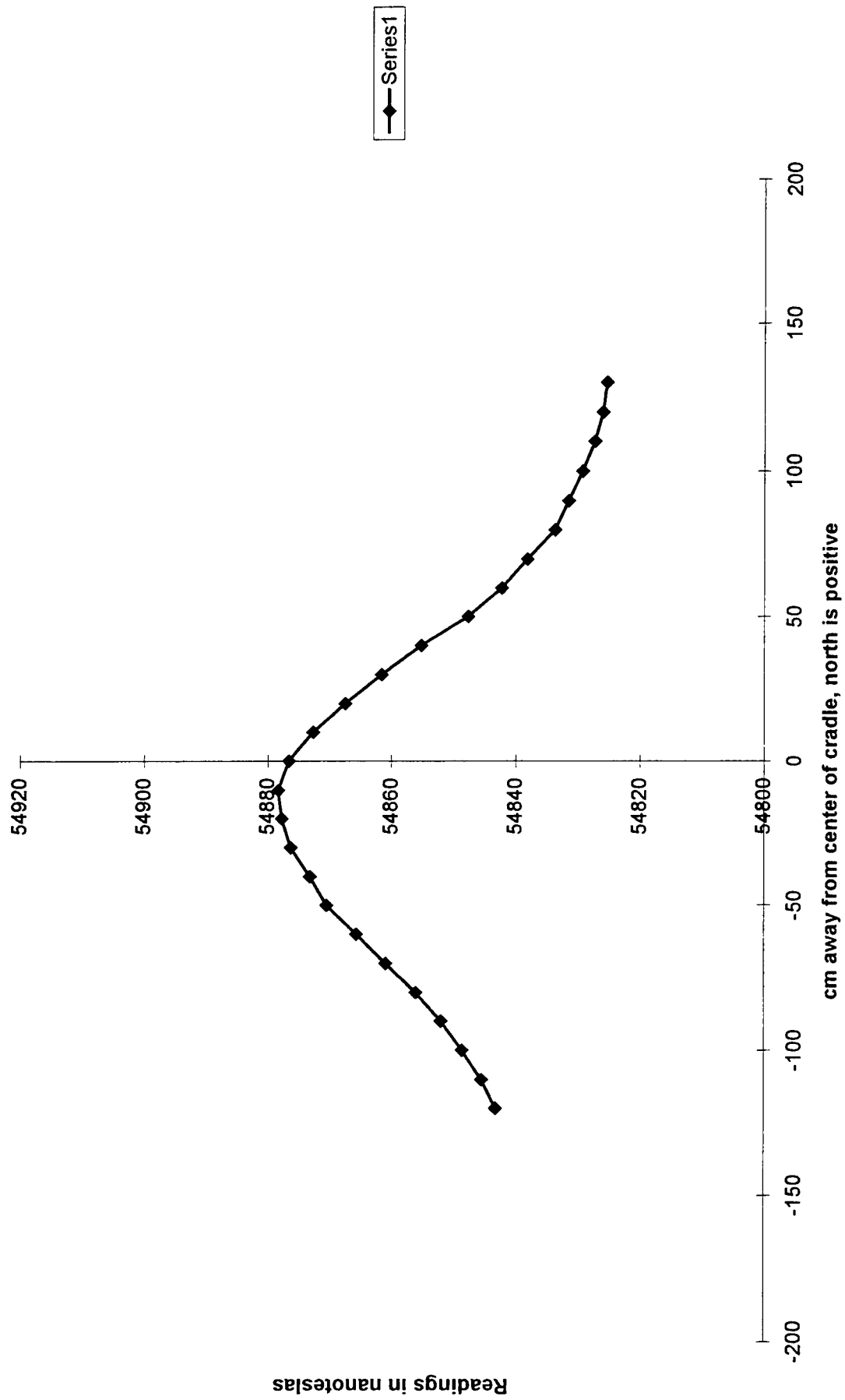
Data cor to 1 B.S.:90 mm, 80 cm offset, 60 deg incl, 0 deg azi, values avg



Data cor to 1 B.S.:90 mm, 0 cm offset, 60 deg incl, 90 deg azi, values avg



Data cor to 1 B.S.:90 mm, 40 cm offset, 60 deg incl, 90 deg azi, values avg



Data cor to 1 B.S.:90 mm, 80 cm offset, 60 deg incl, 90 deg azi, values avg

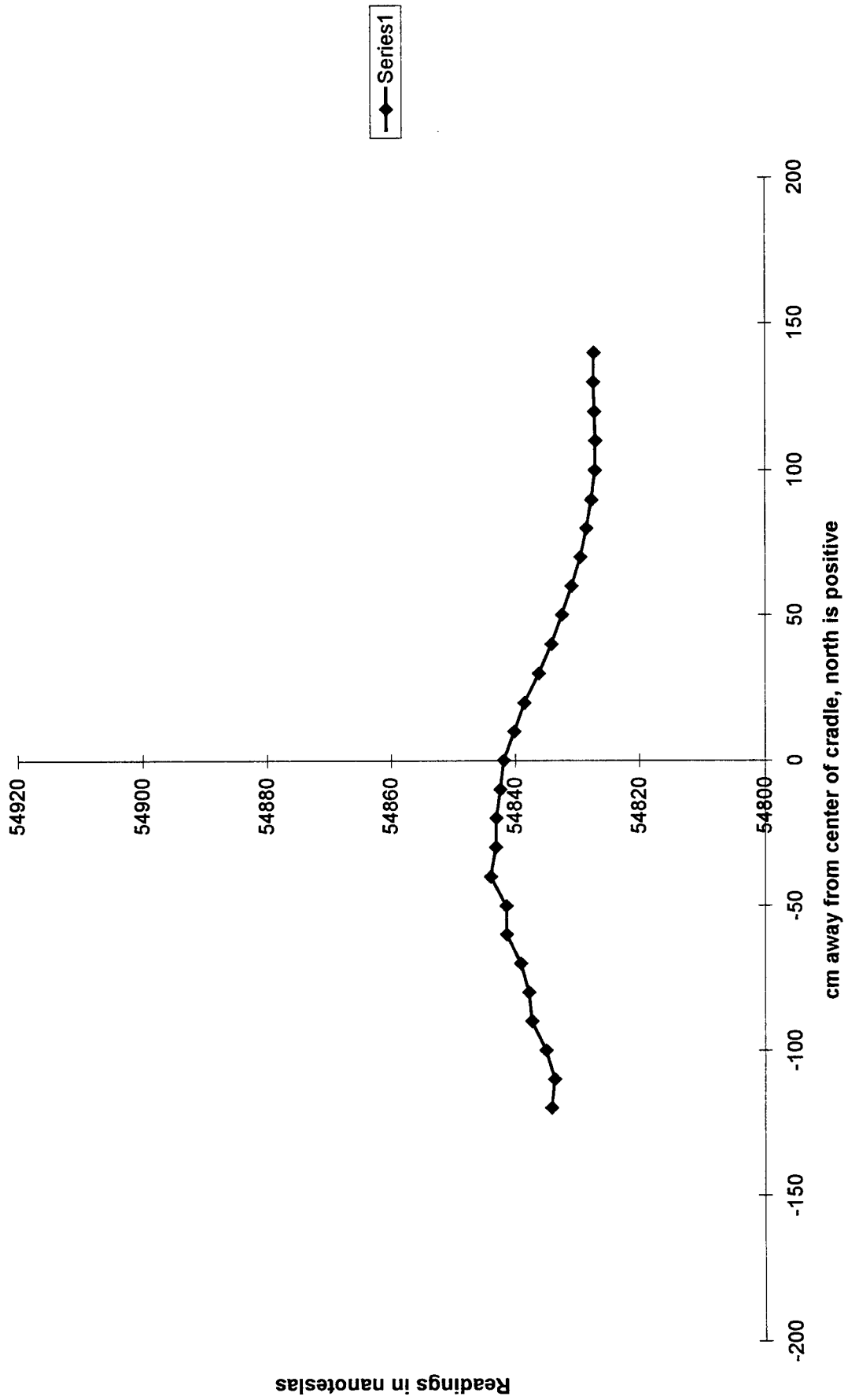
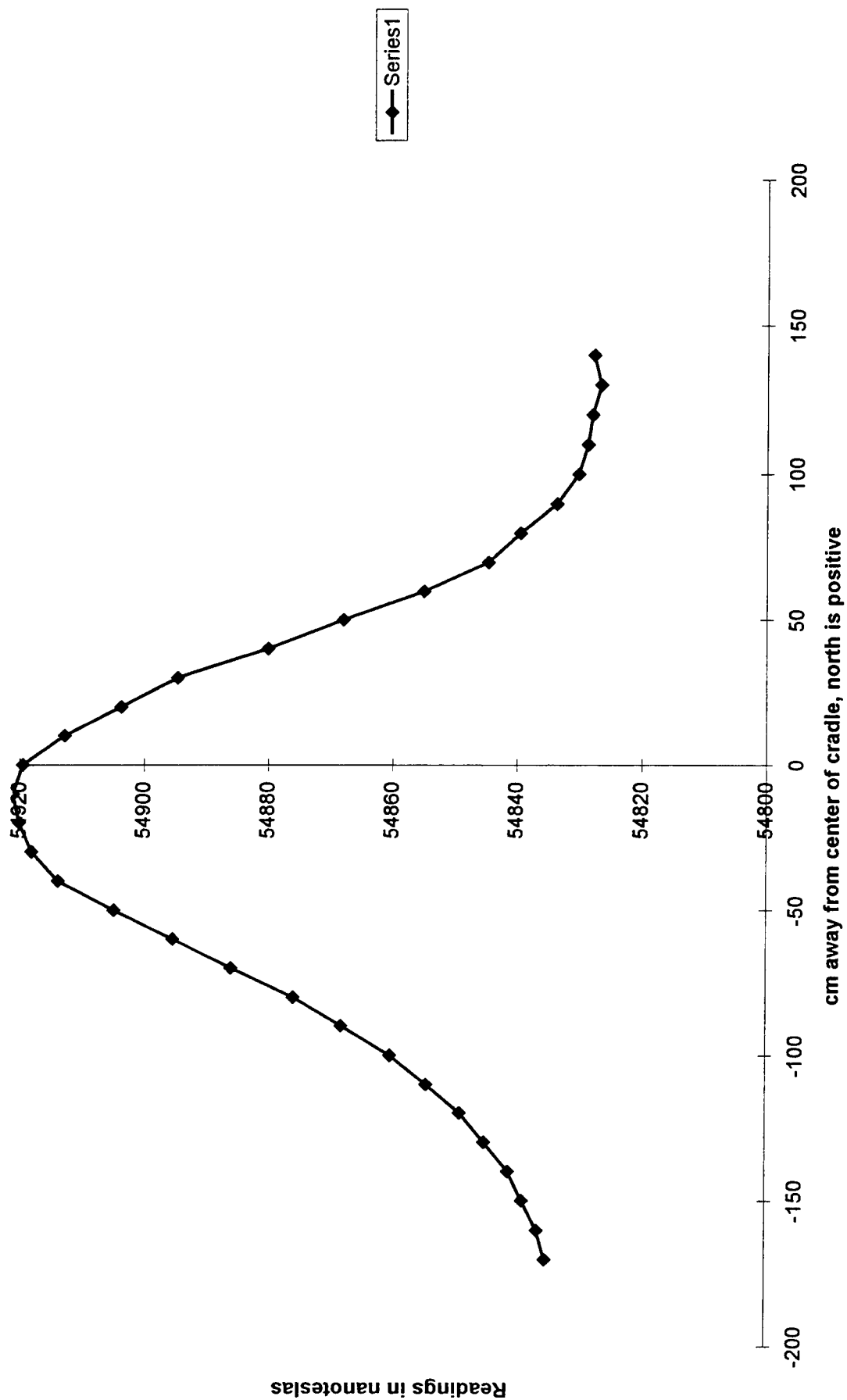


Chart63

Data cor to 1 B.S.:90 mm, 0 cm offset, 90 deg incl, 0 deg azi, values avg



Data cor to 1 B.S.:90 mm, 40 cm offset, 90 deg incl, 0 deg azi, values avg

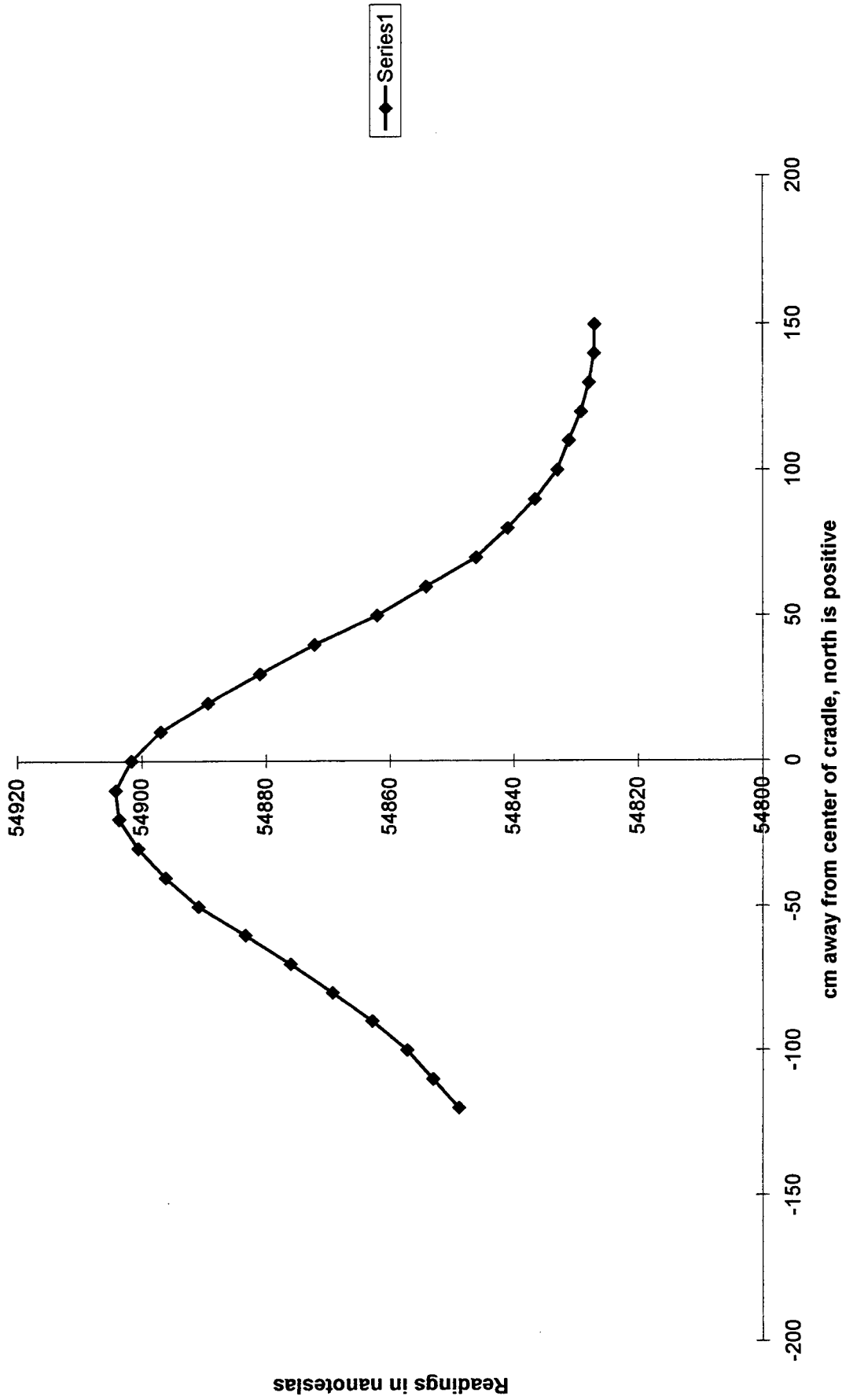
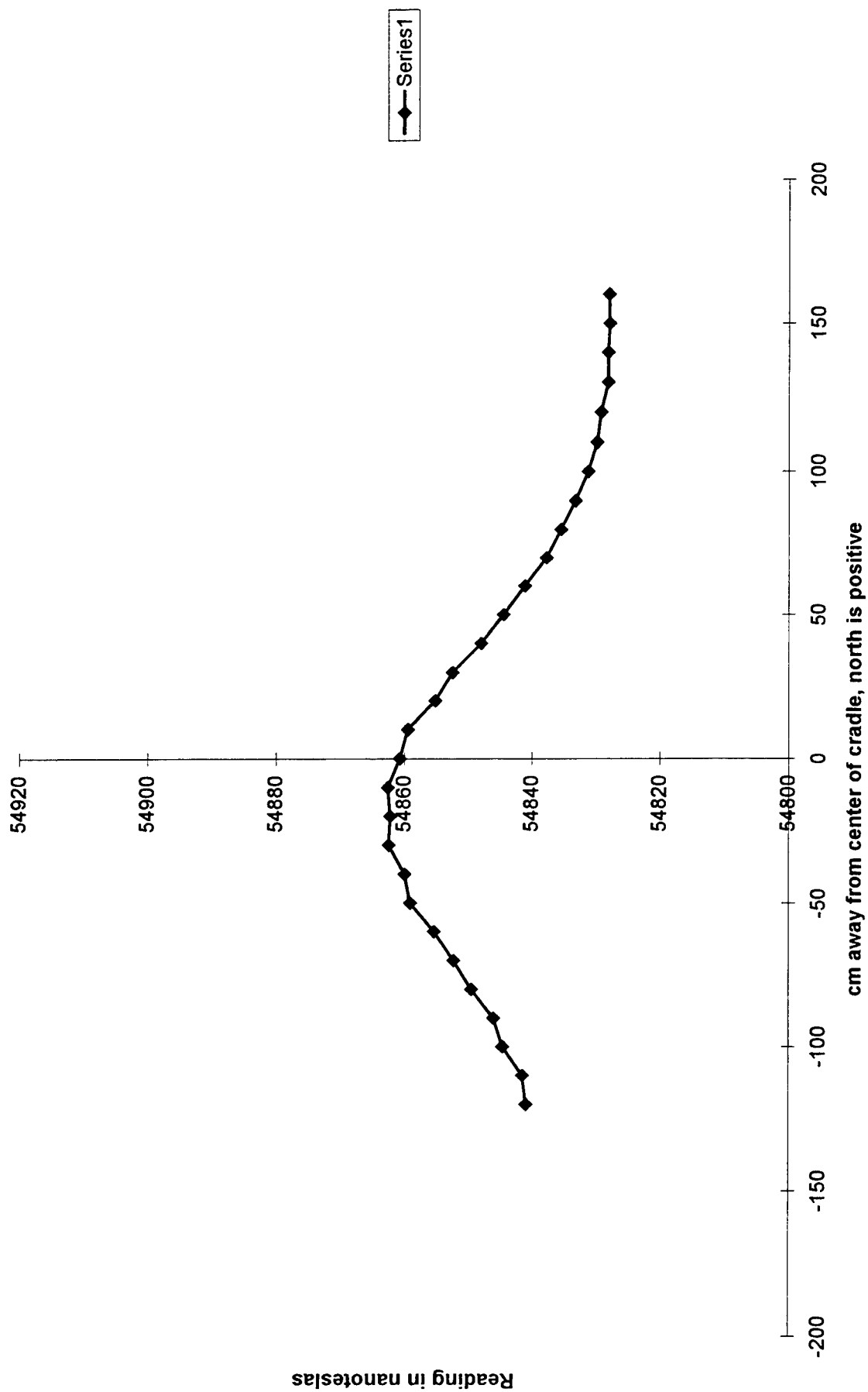


Chart65

Data cor to 1 B.S.:90 mm, 80 cm offset, 90 deg incl, 0 deg azi, values avg



Appendix B

***MAGMOD* Program Listing**

```

%ccco+++magmod
%ccc+++main
%%%% Prolate Spheroid Magnetic Modeling Program  %%%
%
%%%% Main program and GUI control for MAGMOD
% Original program developed by Dr. Paul J. Wolfe while at the U.S. Army
% Engineer Waterways Experiment Station (WES), Vicksburg, MS. The
% GUI and other program modifications were developed by
% Dr. Cary B. Cox, WES. The overall effort was directed by
% Dr. Dwain K. Butler, WES.
clear;
;
screen=get(0,'ScreenSize');
set(0,'defaultfigureposition',screen);
sss=screen(3)/800;
h=figure;
main=figure;
infig=figure;
outfig=figure;
figure(h);
;
screenx(1)=screen(1)+5;
screenx(2)=screen(2)+5;
screenx(3)=screen(3)-5;
screenx(4)=screen(4)-5;
;
screeny(1)=screenx(1)+5;
screeny(2)=screenx(2)+5;
screeny(3)=screenx(3)-5;
screeny(4)=screenx(4)-5;
;
;
fr_1=uicontrol(main,'Style','frame',...
'Position',screenx,...
'BackgroundColor','c');
;
;

div=1.;
namef='magmodel.mat'
load lastp.mat;
load last.mat;
namep=namef;
;
;
pb6=uicontrol(main,'Style','push',...
'Position',[40,110,245,40]*sss,...
'String','EXIT',...
'Callback','close(h);close(outfig);close(infig);close(main);clear;']);
;
;
pb5=uicontrol(main,'Style','push',...
'Position',[40,210,245,40]*sss,...
'String','HARD COPY',...
'Callback','figure(h);plotter,eval(["print ","plotter"]);figure(main);']);
;
;
ee5=uicontrol(main,'Style','text',...
'Position',[300,230,245,20]*sss,...
'String','Plotter Code','Units','pixels');
;
;
pb5x=uicontrol(main,'Style','push',...
'Position',[300,160,220,40]*sss,...
'String','PLAY MOVIE',...
'Callback','plamov;figure(main);']);
;
;
plotter='-ddesket';
qq5=uicontrol(main,'Style','edit',...
'Position',[300,210,245,20]*sss,...
'BackgroundColor','r',...
'String',plotter,...
'Callback',plotter=get(qq5,'String'));
;
;

```



```

themenul=['3d Mesh',...
'3d Mesh & Contour',...
'3d Filled surface',...
'3d Filled surface & Contour',...
'3d illuminated surface',...
'Contour map with body projection',...
'Contour map without body projection',...
'1 Projection parallel to X (grid Legend body)',...
'2 Projection parallel to X (grid Legend body)',...
'3 Projection parallel to X (grid Legend body)',...
'4 Projection parallel to X (grid Legend body)',...
'1 Projection parallel to Y (grid Legend body)',...
'2 Projection parallel to Y (grid Legend body)',...
'3 Projection parallel to Y (grid Legend body)',...
'4 Projection parallel to Y (grid Legend body)',...
'1 Projection parallel to X (Simple Plot)',...
'2 Projection parallel to X (Simple Plot)',...
'3 Projection parallel to X (Simple Plot)',...
'4 Projection parallel to X (Simple Plot)',...
'1 Projection parallel to Y (Simple Plot)',...
'2 Projection parallel to Y (Simple Plot)',...
'3 Projection parallel to Y (Simple Plot)',...
'4 Projection parallel to Y (Simple Plot)'];

off='DATA NOT SELECTED';

thedata=['NONE|X-Component of the Field',...
'Y-Component of the Field',...
'Z-Component of the Field',...
'Magnitude of the field',...
'Total Field Anomaly',...
'Vector Representation of Horiz Component',...
'Representation of Spheroidal Body',...
'Surface of Spheroidal Body',...
'Listing of Major Parameters'];

```

```

fr_2=icontrol(outfig,'Style','frame',...
'Position',screeny,...
'BackgroundColor','b');
;
;
tx1=icontrol(outfig,'Style','text','Units','pixels',...
'Position',[20,490,275,25]*sss,...
'BackgroundColor','y',...
'String','DATA TYPE');
;
tx2=icontrol(outfig,'Style','text','Units','pixels',...
'Position',[320,490,275,25]*sss,...
'BackgroundColor','y',...
'String','PLOT TYPE');
;
tx3=icontrol(outfig,'Style','text','Units','pixels',...
'Position',[620,490,110,25]*sss,...
'BackgroundColor','y',...
'String','CROSS VALUES');
;
;
ndogs=1;
str1a=num2str(cval(1,ndogs));str2a=num2str(cval(2,ndogs));
str3a=num2str(cval(3,ndogs));str4a=num2str(cval(4,ndogs));
yy=465;dostuff;
ndogs=2;
str1a=num2str(cval(1,ndogs));str2a=num2str(cval(2,ndogs));
str3a=num2str(cval(3,ndogs));str4a=num2str(cval(4,ndogs));
yy=yy-80;dostuff;
ndogs=3;
str1a=num2str(cval(1,ndogs));str2a=num2str(cval(2,ndogs));
str3a=num2str(cval(3,ndogs));str4a=num2str(cval(4,ndogs));
yy=yy-80;dostuff;
ndogs=4;
str1a=num2str(cval(1,ndogs));str2a=num2str(cval(2,ndogs));
str3a=num2str(cval(3,ndogs));str4a=num2str(cval(4,ndogs));

```

```

yy=yy-80,dostuff;
ndogs=5;
str1a=num2str(cval(1,ndogs));str2a=num2str(cval(2,ndogs));
str3a=num2str(cval(3,ndogs));str4a=num2str(cval(4,ndogs));
yy=yy-80,dostuff;
ndogs=6;
str1a=num2str(cval(1,ndogs));str2a=num2str(cval(2,ndogs));
str3a=num2str(cval(3,ndogs));str4a=num2str(cval(4,ndogs));
yy=yy-80,dostuff;
;
;
;
pbo1=icontrol(outfig,'Style','push',...
'Position',[620,520,110,30]*sss,'BackgroundColor','c',...
'String','RETURN',...
'CallBack',...
[save lastp.mat dipole octopole dattyp plttyp namep cval',...
'figure(main)']);
;
;
;
txz=icontrol(outfig,'Style','text','Units','pixels',...
'Position',[320,540,130,20]*sss,...
'BackgroundColor','y',...
'String','PLOT FORMAT');
;
;
mode=1;
typmen=icontrol(outfig,'Style','Popup',...
'Position',[320,520,130,30]*sss,'BackgroundColor','c',...
'Value',1,...
'String',...
['Tall|Landscape|Portrait|Tall-Report|Landscape-Report|*Landscape-Report
'],...
'CallBack','[mode=get(typmen,"Value");]');
;
txq=icontrol(outfig,'Style','text','Units','pixels',...
'Position',[460,540,130,20]*sss,...
'BackgroundColor','y',...
'String','FILE NAME');
;
edxx=icontrol(outfig,'Style','edit',...
'Position',[460,520,130,19]*sss,'BackgroundColor','c',...
'String',namep,...
'CallBack','[namep=get(edxx,"String");]');
;
cba=icontrol(outfig,'Style','Checkbox',...
'Position',[20,520,130,30]*sss,'Value',dipole,'BackgroundColor','c',...
'String','Include Dipole',...
'CallBack','[dipole=get(cba,"Value");]');
;
cbao=icontrol(outfig,'Style','Checkbox',...
'Position',[160,520,130,30]*sss,'Value',octopole,'BackgroundColor','c',...
'String','Include Octopole',...
'CallBack','[octopole=get(cbao,"Value");]');
;
figure(main);
*****
*****
%cccc++mostuff
;
;
;
;
if ncat~=17,
ed(ncat)=icontrol(infig,'Style','edit','Units','pixels',...
'Position',[20,y1,150,25]*sss,...
'String',vvv,...
'UserData',ncat,...
'BackgroundColor','w',...
'CallBack','[for kcat=1:16,
vvv=get(ed(kcat),"String");
vvv=(["f",vvv,""])]');
;

```

```

'if kcat==1,v1=str2num(vvvv);end;',...
'if kcat==2,v2=str2num(vvvv);end;',...
'if kcat==3,v3=str2num(vvvv);end;',...
'if kcat==4,v4=str2num(vvvv);end;',...
'if kcat==5,v5=str2num(vvvv);end;',...
'if kcat==6,v6=str2num(vvvv);end;',...
'if kcat==7,v7=str2num(vvvv);end;',...
'if kcat==8,v8=str2num(vvvv);end;',...
'if kcat==9,v9=str2num(vvvv);end;',...
'if kcat==10,v10=str2num(vvvv);end;',...
'if kcat==11,v11=str2num(vvvv);end;',...
'if kcat==12,v12=str2num(vvvv);end;',...
'if kcat==13,v13=str2num(vvvv);end;',...
'if kcat==14,v14=str2num(vvvv);end;',...
'if kcat==15,v15=str2num(vvvv);end;',...
'if kcat==16,v16=str2num(vvvv);end;end;]],
end,
,
et(ncat)=uicontrol('infig','Style','text','Units','pixels',...
'Position',[200,y1,400,25]*sss,...
'BackgroundColor','c',...
'String',name(ncat,1:55));

*****
*
;
;
%ccc++tplotfig
function izzz=plotfig(modex,dipole,octopole,...
    dattyp,plttyp,MorF,name,ccval,compfile,nframe);
global saveax vcontour;
;
gridon=1;
if modex < 4, mode=modex;else,mode=10+(modex-3);end;
;
eval(['load ',name,'],');
name,Phideg,
measfile=compfile;
readmeas=0;
if exist(measfile)==2,readmeas=1;end;
;
OUTX=zeros(nx,ny);OUTY=zeros(nx,ny);OUTZ=zeros(nx,ny);
OUTmag=zeros(nx,ny);OUTanom=zeros(nx,ny);
;
if dipole == 1,
    OUTX=OUTX+DIPx;OUTY=OUTY+DIPy;OUTZ=OUTZ+DIPz;
    OUTmag=OUTmag+DIPmag; OUTanom=OUTanom+DIPanom;
end;
if octopole == 1,
    OUTX=OUTX+OCTx;OUTY=OUTY+OCTy;OUTZ=OUTZ+OCTz;
    OUTmag=OUTmag+OCTmag; OUTanom=OUTanom+OCTanom;
end;
;
dood(1)='m';
dood(2)='M';
dood(3)='s';
dood(4)='S';
dood(5)='i';
dood(6)='c';
dood(7)='C';
dood(8)='1';
dood(9)='2';
dood(10)='3';
dood(11)='4';
dood(12)='5';
dood(13)='6';
dood(14)='7';
dood(15)='8';
dood(16)='i';
dood(17)='@';
dood(18)='#';
dood(19)='$';
dood(20)='%';

```

```

dcod(21)='^';
dcod(22)='&';
dcod(23)='*';
;
dcod2(1)='^';
dcod2(2)='x';
dcod2(3)='y';
dcod2(4)='z';
dcod2(5)='m';
dcod2(6)='a';
dcod2(7)='v';
dcod2(8)='b';
dcod2(9)='B';
dcod2(10)='p';
;
nplots=0;datatype='';plottype='';
;
clear crossval;crossval=[];
;
mm=0;ll=0;
for ii=1:6,
    if dattyp(ii) >= 2, ll=ll+1;
    datatype(ll:ll)=dcod2(fix(dattyp(ii)));
    plottype(ll:ll)=dcod(fix(pltyp(ii)));
    if pltyp(ii) > 7 & dattyp(ii) <
        7, mm=mm+1; crossval(mm, 1:4)=ccval(1:4, ii); end;
    end;
end;
nplots=ll;
;
is=size(crossval);
if is(1) ~= 0,
    cvx=round((crossval-Xmin)*(nx-1)/(Xmax-Xmin))+1;
    cvy=round((crossval-Ymin)*(ny-1)/(Ymax-Ymin))+1;
end;
;
;

%
%
% PLOTFIG
%
% This script runs from within magplot.m which provides
% the user parameter and plots magnetic field results
% calculated by magfield.m running within magplot.m
%
% Used by: MAGPLOT
% Uses: BODYPROJ.M, CALCBODY.M, PARAMLST.M
%
% Written by Paul Wolfe(Wright State University) for
% US Army Corps of Engineers, Geotechnical Laboratory,
% July 1996.
%
clg;lx0=length(X0); %clear the Figure window.
%clf %set up constant vector to show
Yconst=zeros(49,1); % the body projection on profiles.
;
;
if nplots>6, nplots=6;end;
grow=1;
qcol=1;
if nplots > 1,qcol=2;end;
if nplots > 2,qrow=2;end;
if nplots > 4,qrow=3;end;
;
Northlb=['North 'MorF']; %Define axis labels for unit
Westlb=['West 'MorF']; % system, i.e., meters or ft.
Depthlb=['Depth 'MorF'];
if readmeas==1,
    fid=fopen(measfile);
    [measured,mcount]=fscanf(fid,'%f%f',[2,inf]);
    measured=measured';
    npoints=mcount/2;
    fclose(fid);
end;
;

```

```

ip=1;
bodyproj;
for mp=1:nplots,
    %index for profile plot matrix.
    %Step through the subwindows.
    if datatype(mp)=='b' | datatype(mp)=='B',
        colormap('default');
        lxo=length(X0);
        for bbb1=1:lxo,
            calcbody; % a script to calculate spheroid
            if datatype(mp)=='B' %surface plot selected
                subplotx(mode,grow,qcol,mp),surf(XSPH, YSPH, ZSPH);
            if bbb1==1, hold on; end;
            if bbb1==lxo,
                vv=axis,dx=vv(2)-vv(1);dy=vv(4)-vv(3);dz=vv(6)-vv(5);
                mxd=max([dx dy dz]);
                axis([vv(1),vv(1)+mxd,vv(3),vv(3)+mxd,vv(5),vv(5)+mxd]);
                axis('equal');
                xlabel(Northlb);ylabel(Westlb);zlabel(Depthlb);
                title('Spheroid');
            else,
                %
                axis([vv(1),vv(1)+mxd,vv(3),vv(3)+mxd,vv(5),vv(5)+mxd]);
                %
                axis('equal');
            end;
            else
                %default to mesh
                subplotx(mode,grow,qcol,mp),mesh(XSPH, YSPH, ZSPH);
            if bbb1==1,
                xlabel(Northlb);ylabel(Westlb);zlabel(Depthlb);
                title('Spheroid');
                hold on;
            end;
            end;
            colormap('default');%axis('normal');
            end;hold off;
            elseif datatype(mp)=='v';
                subplotx(mode,grow,qcol,mp),bodyproj;
                mmz=rem(nframe,3)+1;
                quiver(X(mmz:3:nx),Y(mmz:3:ny),OUTX(mmz:3:nx,mmz:3:ny),OUTY(m
mmz:3:nx,mmz:3:ny)),
hold on;contour(X,Y,OUTAnom);for bbb1=1:lx0,
plot(Xrot(bbb1,:),Yrot(bbb1,:), 'W-');end;hold off;
title('Horizontal Vectors');axis('square');axis('equal');
xlabel(Northlb);ylabel(Westlb);
elseif datatype(mp)=='p'
subplotx(mode,grow,qcol,mp),paramlst;
else
    if datatype(mp)=='x'
        dfile=OUTX; plabel='x component';
        elseif datatype(mp)=='y'
            dfile=OUTY; plabel='y component';
        elseif datatype(mp)=='z'
            dfile=OUTZ; plabel='z component';
        elseif datatype(mp)=='m'
            dfile=OUTmag; plabel='Magnitude';
        elseif datatype(mp)=='a'
            dfile=OUTAnom; plabel='Total Field Anomaly';
        else
            dfile=OUTAnom; plabel='Total Field Anomaly';
        end;
        if plottype(mp)=='m'
            subplotx(mode,grow,qcol,mp),mesh(X,Y,dfile),
            ;
            axax=axis;
            maxx=max(max(dfile));minmin=min(min(dfile));
            text(Xmax,Ymin,axax(6),[' Max ',num2str(maxmax),' Min
',num2str(minmin)]);
            ;
            if nframe==0, saveax=axis;end;
            if nframe > 0, axis(saveax);end;
            title(plabel);
            xlabel(Northlb);ylabel(Westlb);zlabel('nanoteslas');
            elseif plottype(mp)=='M'
                subplotx(mode,grow,qcol,mp),meshc(X,Y,dfile),
                ;

```

```

axax=axis;
maxmax=max(max(df1le));minmin=min(min(df1le));
text(Xmax,Ymin,axax(6),' Max ',num2str(maxmax),' Min
',num2str(minmin));
;
    if nframe ==0, saveax=axis;end;
    if nframe > 0, axis(saveax);end;
    title(plabel);
    xlabel(Northlb);ylabel(Westlb);zlabel('nanoteslas');
    elseif plottype(mp)=='s'
        subplotx(mode,grow,qcol,mp),surf(X,Y,df1le),
        if nframe ==0, saveax=axis;end;
        if nframe > 0, axis(saveax);end;
        title(plabel);
        xlabel(Northlb);ylabel(Westlb);zlabel('nanoteslas');
        elseif plottype(mp)=='S'
            subplotx(mode,grow,qcol,mp),surfc(X,Y,df1le),
            if nframe ==0, saveax=axis;end;
            if nframe > 0, axis(saveax);end;
            title(plabel);
            xlabel(Northlb);ylabel(Westlb);zlabel('nanoteslas');
            elseif plottype(mp)=='i'
                subplotx(mode,grow,qcol,mp),surf(X,Y,df1le),shading interp;
                if nframe ==0, saveax=axis;end;
                if nframe > 0, axis(saveax);end;
                title(plabel);colormap(gray);
                xlabel(Northlb);ylabel(Westlb);zlabel('nanoteslas');
                elseif plottype(mp)=='C'
                    subplotx(mode,grow,qcol,mp),
                    conlabl=contour3(X,Y,df1le);axis('square');axis('equal');%clabel(conlabl);
                    if nframe ==0, saveax=axis;end;
                    if nframe > 0, axis(saveax);end;
                    title(plabel);xlabel(Northlb);ylabel(Westlb);
                    elseif plottype(mp)=='c'
                        bodyproj;
                        subplotx(mode,grow,qcol,mp),

```

```

    if nframe==0,mx=max(max(df1le));mn=min(min(df1le));
    vcontour=[mn:(mx-mn)/20:mx];

    conlabl=contour(X,Y,df1le,vcontour);axis('square');axis('equal');%clabel(con
    labl);
    end;
    if nframe >0,

    conlabl=contour(X,Y,df1le,vcontour);axis('square');axis('equal');%clabel(con
    labl);
    end;
    if nframe <0,
        conlabl=contour(X,Y,df1le);axis('square');axis('equal');clabel(conlabl);
        end;
    if nframe ==0, saveax=axis;end;
    if nframe > 0, axis(saveax);end;
    title(plabel);xlabel(Northlb);ylabel(Westlb);
    hold on;for bbb1=1:lx0,plot(Xrot(bbb1,:),Yrot(bbb1,:), 'w');end;
    hold off;
    elseif plottype(mp)=='l'
        subplotx(mode,grow,qcol,mp),
        plot(X,df1le(cvx(ip,1,:), 'w',Xrot(1,:), Yconst,'go');
        title(plabel);xlabel(Northlb);ylabel('nanoteslas');
        ax=axis;range=ax(4)-ax(3);axis([ax(1),ax(2),ax(4)-2*range,ax(4)]);
        hold on;
        if readmeas==1
            plot(measured(:,1),measured(:,2),'w+');
            end;
            hold off;fixleg(1,gridon,df1le,X,'X',cvx,crossval,ip);
            ip=ip+1;
            elseif plottype(mp)=='2';
                subplotx(mode,grow,qcol,mp);
                plot(X,df1le(cvx(ip,1,:), 'w',X,df1le(cvx(ip,2,:), 'b',Xrot(1,:), Yconst,'go');
                title(plabel);xlabel(Northlb);ylabel('nanoteslas');
                ax=axis;range=ax(4)-ax(3);axis([ax(1),ax(2),ax(4)-2*range,ax(4)]);
                hold on;

```



```

end;
hold off; fixleg(4,gridon,dfile,Y,'Y',cyy,crossval,ip);
ip=ip+1;
elseif plottype(mp)=='l';
subplotx(mode,grow,qcol,mp);
plot(X,dfile(cvx(ip,1),:),'w',X,dfile(cvx(ip,2),:),'b',...
title(plabel);xlabel(Northlb);ylabel('nanoteslas');
hold on;
if readmeas==1
plot(measured(:,1),measured(:,2),'w+');
end;
hold off;
elseif plottype(mp)=='%';
subplotx(mode,grow,qcol,mp);
plot(Y,dfile(:,cyy(ip,1)),'w');
title(plabel);xlabel(Westlb);ylabel('nanoteslas');
hold on;
if readmeas==1
plot(measured(:,1),measured(:,2),'w+');
end;
hold off;
ip=ip+1;
elseif plottype(mp)=='^';
subplotx(mode,grow,qcol,mp);
plot(Y,dfile(:,cyy(ip,1)),'w',Y,dfile(:,cyy(ip,2)),'b');
title(plabel);xlabel(Westlb);ylabel('nanoteslas');
hold on;
if readmeas==1
plot(measured(:,1),measured(:,2),'w+');
end;
hold off;
ip=ip+1
elseif plottype(mp)=='&';
subplotx(mode,grow,qcol,mp);
plot(Y,dfile(:,cyy(ip,1)),'w',Y,dfile(:,cyy(ip,2)),'b',...
Y,dfile(:,cyy(ip,3)),'r');
title(plabel);xlabel(Westlb);ylabel('nanoteslas');
hold on;
if readmeas==1
plot(measured(:,1),measured(:,2),'w+');
end;
hold off;
fixleg(4,gridon,dfile,Y,'Y',cyy,crossval,ip);
ip=ip+1;
elseif plottype(mp)=='l';
subplotx(mode,grow,qcol,mp);
plot(X,dfile(cvx(ip,1),:),'w',X,dfile(cvx(ip,2),:),'b',...
title(plabel);xlabel(Northlb);ylabel('nanoteslas');
hold on;
if readmeas==1
plot(measured(:,1),measured(:,2),'w+');
end;
hold off;
ip=ip+1;
elseif plottype(mp)=='@';
subplotx(mode,grow,qcol,mp);
plot(X,dfile(cvx(ip,1),:),'w',X,dfile(cvx(ip,2),:),'b');
title(plabel);xlabel(Northlb);ylabel('nanoteslas');
hold on;
if readmeas==1
plot(measured(:,1),measured(:,2),'w+');
end;
hold off;
ip=ip+1;
elseif plottype(mp)=='#';
subplotx(mode,grow,qcol,mp);
plot(X,dfile(cvx(ip,1),:),'w',X,dfile(cvx(ip,2),:),'b',...
X,dfile(cvx(ip,3),:),'r');
title(plabel);xlabel(Northlb);ylabel('nanoteslas');
hold on;
if readmeas==1
plot(measured(:,1),measured(:,2),'w+');
end;
hold off;
ip=ip+1;
elseif plottype(mp)=='$';
subplotx(mode,grow,qcol,mp);

```



```

end;
hold off;
ip=ip+1;
elseif plottype(mp)=='*',
subplotx(mode,grow,qcol,mp);
plot(Y,dfile(:,cyy(ip,1)), 'w', Y,dfile(:,cyy(ip,2)), 'b', ...
      Y,dfile(:,cyy(ip,3)), 'r', Y,dfile(:,cyy(ip,4)), 'm');
title(plabel);xlabel(Westlb);ylabel('nanoteslas');
hold on;
if readmeas==1
plot(measured(:,1),measured(:,2),'w+');
end;
hold off;
ip=ip+1;
else
bodyproj;
subplotx(mode,grow,qcol,mp);
conlabl=contour(X,Y,dfile);axis('square');axis('equal');%clabel(conlabl);
title(plabel);xlabel(Northlb);ylabel(Westlb);
hold on;for bbb1=1:xx0,plot(Xrot(bbb1,:),Yrot(bbb1,:), 'w:'),end;
hold off;
end;
end;
end;
end;

*****
***
%ccc+++bodyproj
% BODYPROJ
% This script, which is a subprogram to plotfig,
% calculates the elliptical projection of
% the body on a horizontal plane such as the ground surface
% to help identify where the magnetic signature is
% located relative to the body.
%
*****

```

```

% Used by : PLOTFIG.M and also by FPLOTFIG.M
% Uses: none
%
% Written by Paul Wolfe(Wright State University) for
% US Army Corps of Engineers, Geotechnical Laboratory,
% August 1996.
%
% Construct an ellipse which is the vertical cross section
% of the spheroid with length L and diameter 2a.
for bbb1=1:length(X0);
Theta=Thetadeg(bbb1)*pi/180.;
Phi=(Phideg(bbb1)+90.)*pi/180.;
psi=linspace(0,2*pi,49);
rhoFull=1./(sqrt((cos(psi)/D(bbb1/2)).^2+(sin(psi)/(L(bbb1/2)).^2)));
% Rotate the ellipse symmetry axis by Theta from Z axis
psi1=psi-Theta;
% Convert to cartesian coords and find the maximum x value
% which is the semi-major axis of the projection on the surface.
[XXrot,YYrot]=pol2cart(psi1,rhoFull);
be=max(XXrot);
% Calculate the projected ellipse.
rhoProj=1./(sqrt((cos(psi)/(D(bbb1/2)).^2+(sin(psi)/be).^2)));
% Rotate the ellipse axis so that it is oriented
% at angle Phi relative to the surface X axis.
%psi2=psi+Phi-pi/2;
psi2=psi+Phi;
% Find the corresponding cartesian coordinates.
[XXrot,YYrot]=pol2cart(psi2,rhoProj);
% Shift to the proper body center location.
XXrot=XXrot+X0(bbb1);
YYrot=YYrot+Y0(bbb1);
Xrot(bbb1,:)=XXrot;
Yrot(bbb1,:)=YYrot;
end;
*****

```

%Make a

```

%ccc+++calcbody
%          CALCBODY
% This script uses the paramters passed from magplot to
% generate a figure of the body spheroid.
% It will use plot routine mesh unless surf is specifically
% selected.
%
% Used by: PLOTFIG.M (and MAGPLOT.M)
% also by: FPLOTFIG.M (and FMAGPLOT.M)
% Uses: none
%
% Written by Paul J. Wolfe (Physics, Wright State Univ.) for
% US Army Corps of Engineers, Geotechnical Laboratory, July 1996.
%
% .....
% I=lddeg*pi/180;          %Convert angles to radians.
Theta=Thetadeg(bbb1)*pi/180;
Phi=(Phideg(bbb1)+90)*pi/180;
angle
COSI=cos(I);
SINI=sin(I);
COSTh=cos(Theta);
SINTh=sin(Theta);
COSPhi=cos(Phi);
SINPhi=sin(Phi);
B0=[B0mag*COSI; 0; -B0mag*SINI]; %Earth's field vector
Rot=[COSPhi, SINPhi, 0; %Rotation matrix from surface
-COSTh*SINPhi, COSTh*COSPhi, SINTh; % to body coordinates.
SINTh*SINPhi, -SINTh*COSPhi, COSTh];
%.....
R0=[X0(bbb1); Y0(bbb1); Z0(bbb1)];
vector of the body
% center location.
% Create a default sphere.
[xsph,ysph,zsph]=sphere; %Scale the x axis of spheroid.
xsph=D(bbb1)*xsph/2; %Scale the y axis of spheroid.
ysph=D(bbb1)*ysph/2;

zsph=(L(bbb1)/2)*zsph; %Scale the long axis of spheroid.
ns=21; %Default rows
ms=21; %Default columns
for n=1:ns; %Step through rows
for m=1:ms; %Step through columns
%Calculate the location vector for a data point in body coords.
rs=[xsph(n,m),ysph(n,m),zsph(n,m)];
RS=Rot'*rs+R0; %Rotate and translate the point
% into surface coordinate system.
XSPH(n,m)=RS(1); %Write the point in a new set of
YSPH(n,m)=RS(2); % matrices.
ZSPH(n,m)=RS(3); %
end;
end;
%***** END OF PROGRAM *****

*****
*****

function
izzz=magfield(name,Xmin,Xmax,Ymin,Ymax,Z,B0mag,lddeg,L,D,div,perm,.
.. Thetadeg,Phideg,X0,Y0,Z0,MorF);
;
L=L/div;D=D/div;
head=name;
izzz=0;
;
; MAGFIELD
;
; This MATLAB script calculates the dipole and octopole
% contributions to the magnetic field at each grid
% point for the body and field data specified in SPHEROID.M
%
```

```

% Used by; UXOMODEL.M
% Uses: none
%
% Written by Paul J. Wolfe(Physics, Wright State Univ.) for US
% Army Corps of Engineers, Geotechnical Laboratory; July 1996
%
l=lddeg*pi/180;           %Convert angles to radians.
Theta=Thetadeg*pi/180;
Phi=(Phideg+90)*pi/180;  %Add 90 degrees to make Euler angle
COSI=cos(I);
SINI=sin(I);
COSTh=cos(Theta);
SINTh=sin(Theta);
COSPhi=cos(Phi);
SINPhi=sin(Phi);
B0=[B0mag*COSI; 0; -B0mag*SINI]; %Earth's field vector
Rot=[COSPhi, SINPhi, 0; %Rotation matrix from surface
-COSTh*SINPhi, COSTh*COSPhi, SINTh; % to body coordinates.
SINTh*SINPhi, -SINTh*COSPhi, COSTh];
a=D/2; %Body cross section radius.
if MorF=='f'
    a=0.3048*a; %Convert feet to meters.
end;
;
e=L/D; %Body elongation parameter.
if e==1,
    E=-1;
    A1=2/3; A3=A1;
end;
if e > 1,
    E=log(e-sqrt(e^2-1))/sqrt(e^2-1); %E-parameter.
end;
if e < 1,
    E=atan(e*(1.-e^2)^(-.5)-pi/2)*(1.-e^2)^(-.5);
end;
if e==1,
    DIPx=zeros(nx,ny);
    X=linspace(Xmin,Xmax,nx);
    Y=linspace(Ymin,Ymax,ny);
    % Set up output matrices.
    DIPx=zeros(nx,ny);
    %
    % Set up loops to go through each grid point and
    % calculate the field.
    %
    nx=41;
    ny=41;
    %32 points in each direction.
    %This can be increased in the
    % Professional Version.
    %Vector of X grid values.
    %Vector of Y grid values.
    M1=e*(e+E)/(e^2-1);
    A3=-2*e*(1/e+E)/(e^2-1);
end;
;
%F-parameters.
F1=(perm-1)/(1+A1*(perm-1)/2);
F3=(perm-1)/(1+A3*(perm-1)/2);
b0=Rot*B0;
mu0=400*pi;
M=[F1*b0(1); F1*b0(2); F3*b0(3)];
M=M/mu0;
Vol=4*pi*e*a^3/3;
I11=Vol*a^2/5;
I33=I11*e^2;
m1=M*Vol;
m31=[3*M(1)*I11, M(2)*I11, M(3)*I11;
M(2)*I11, M(1)*I11, 0;
M(3)*I11, 0, M(1)*I33];
m32=[ M(2)*I11, M(1)*I11, 0;
M(1)*I11, 3*M(2)*I11, M(3)*I11;
0, M(3)*I11, M(2)*I33];
m33=[ M(3)*I11, 0, M(1)*I33;
0, M(3)*I11, M(2)*I33;
M(1)*I33, M(2)*I33, 3*M(3)*I33];
%
% Find earth's field in body
% coordinates.
% magnetic permeability of
% space in nanotesla*m/Amp
%Magnetization vector.
%Volume of the body.
%Minor axis "inertia".
%Major axis "inertia".
%Magnetic dipole moment vector
m31=[3*M(1)*I11, M(2)*I11, M(3)*I11;
M(2)*I11, M(1)*I11, 0;
M(3)*I11, 0, M(1)*I33];
m32=[ M(2)*I11, M(1)*I11, 0;
M(1)*I11, 3*M(2)*I11, M(3)*I11;
0, M(3)*I11, M(2)*I33];
m33=[ M(3)*I11, 0, M(1)*I33;
0, M(3)*I11, M(2)*I33;
M(1)*I33, M(2)*I33, 3*M(3)*I33];
%
% Set up loops to go through each grid point and
% calculate the field.
%
    nx=41;
    ny=41;
    %32 points in each direction.
    %This can be increased in the
    % Professional Version.
    %Vector of X grid values.
    %Vector of Y grid values.
    X=linspace(Xmin,Xmax,nx);
    Y=linspace(Ymin,Ymax,ny);
    % Set up output matrices.
    DIPx=zeros(nx,ny);

```

```

DIPy=zeros(nx,ny);
DIPz=zeros(nx,ny);
DIPmag=zeros(nx,ny);
DIPanom=zeros(nx,ny);
OCTx=zeros(nx,ny);
OCTy=zeros(nx,ny);
OCTz=zeros(nx,ny);
OCTmag=zeros(nx,ny);
OCTanom=zeros(nx,ny);
bd=zeros(3,1);
boct=zeros(3,1);
for n=1:nx;
    for m=1:ny;
        R=[X(n)-X0; Y(m)-Y0; Z-Z0];
        if MorF=='f'
            R=0.3048*R;
            end;
            r=Rot*R;
            rmag=sqrt(r'*r)+eps;
            bd=mu0*(-m1+3*(m1'*r)*(r/rmag^2)/(4*pi*rmag^3);
            %end dipole calculation
            %octopole field section
            termA=r(1)*trace(m31)+r(2)*trace(m32)+r(3)*trace(m33); %subterms
            termB=r(1)*(r*(m31*r))+r(2)*(r*(m32*r))+r(3)*(r*(m33*r));
            boct(1)=mu0*(3*trace(m31)-15*(r(1)*termA+r*(m31*r))/rmag^2+35*r(1)
            )*(termB/rmag^4)/(4*pi*rmag^5);
            boct(2)=mu0*(3*trace(m32)-15*(r(2)*termA+r*(m32*r))/rmag^2+35*r(2)
            )*(termB/rmag^4)/(4*pi*rmag^5);
            boct(3)=mu0*(3*trace(m33)-15*(r(3)*termA+r*(m33*r))/rmag^2+35*r(3)
            )*(termB/rmag^4)/(4*pi*rmag^5);
            %end octopole calculation
        %
        % Transform magnetic dipole field bd from body coordinates
        % back to surface coordinates as Bd.
        Bd=Rot'*bd;
        DIPx(n,m)=Bd(1); %fill in X component of dipole field.
        DIPy(n,m)=Bd(2); %fill in Y component of dipole field.
        DIPz(n,m)=Bd(3); %fill in Z component of dipole field.
        Bdsqrd=Bd'*Bd;
        DIPmag(n,m)=sqrt(Bdsqrd); %fill in magnitude of dipole field.
        DIPanom(n,m)=sqrt(B0mag^2+Bdsqrd+2*B0'*Bd)-B0mag; %fill in dipole
        % total field anomaly.
        % Transform magnetic octopole field bo from body coordinates
        % back to surface coordinates as Bo.
        Boct=Rot'*boct;
        OCTx(n,m)=Boct(1); %fill in X component of octopole field.
        OCTy(n,m)=Boct(2); %fill in Y component of octopole field.
        OCTz(n,m)=Boct(3); %fill in Z component of octopole field.
        Boctsqrd=Boct'*Boct;
        OCTmag(n,m)=sqrt(Boctsqrd); %fill in magnitude of octopole field.
        OCTanom(n,m)=sqrt(B0mag^2+Boctsqrd+2*B0'*Boct)-B0mag; %fill in
        octopole total field anomaly.
        % There may be a small error for very large anomalies because this
        % calculation treats the octopole term independently from the dipole
        % term when calculating the contribution to the total field anomaly.
        %
        end;
        %End X loop*****
        %End Y loop$$$
        %transpose matrices to get
        % x and y axes in the usual
        % orientation for plots.
        %transpose matrices to get
        % x and y axes in the usual
        % orientation for plots.
        OCTx=OCTx';
        OCTy=OCTy';
        OCTz=OCTz';
        OCTmag=OCTmag';
        OCTanom=OCTanom';
        eval(['save ',name,' MorF B0mag Ideg Theta Thetadeg Phi Phideg L D perm

```

```

X0 Y0 Z0 X'...
' Xmin Xmax nx Y Ymin Ymax ny Z Rot DIPx DIPy DIPz DIPmag
DIPanom'...
' OCTx OCTy OCTz OCTmag OCTanom nx ny head:[]);
%***** END OF PROGRAM
%*****

*****
;
; % program to combine files
;
; clear;
nameoo=input('Output File Name: ','s');
;
kntccc=0;
namein(1)='z';
while namein ~= [],
;
namein=input('Input File Name: ','s');
if namein ~= [],
eval(['load ',namein]);
kntccc=kntccc+1,
;
; % set constant values from first file
;
; if kntccc==1,
B0magl=B0mag;
MorF1=MorF;
Idegl=Ideg;
X1=X;
Y1=Y;
Z1=Z;
;
; % Zero the values to be summed
;

DIPanom=zeros(size(DIPanom));
DIPmags=zeros(size(DIPmag));
DIPxs=zeros(size(DIPx));
DIPys=zeros(size(DIPy));
DIPzs=zeros(size(DIPz));
OCTanom=zeros(size(OCTanom));
OCTmags=zeros(size(OCTmag));
OCTxs=zeros(size(OCTx));
OCTys=zeros(size(OCTy));
OCTzs=zeros(size(OCTz));
;
; % Clear values to be appended
;
; X0s=[];
; Y0s=[];
; Z0s=[];
; Ds=[];
; Ls=[];
; Phidegs=[];
; Thetadegs=[];
; perms=[];
;
; end;
;
; % check and see if the current file has the same constant values
;
; if (B0magl==B0mag) & (MorF1==MorF) & (Idegl==Ideg)...
;     & (X1==X) & (Y1==Y) & (Z1==Z),
;
; % its good, so append new parameters to old list;
;
; X0s=[X0s X0];
; Y0s=[Y0s Y0];
; Z0s=[Z0s Z0];
; Ds=[Ds D];
; Ls=[Ls L];

```

```

Phidegs=[Phidegs Phidegl];
Thetadegs=[Thetadegs Thetadegl];
perms=[perms perm];
;
DIPanoms=DIPanoms+DIPanom;
DIPmags=DIPmags+DIPmag;
DIPxs=DIPxs+DIPx;
DIPys=DIPys+DIPy;
DIPzs=DIPzs+DIPz;
OCTanoms=OCTanoms+OCTanom;
OCTmags=OCTmags+OCTmag;
OCTxs=OCTxs+OCTx;
OCTys=OCTys+OCTy;
OCTzs=OCTzs+OCTz;
;
result='GOOD';
;
else,
result='BAD';
end;
end;
end;
;
% rename for new file
;
X0=X0s;
Y0=Y0s;
Z0=Z0s;
D=Ds;
L=Ls;
Phideg=Phidegs;
Thetadeg=Thetadegs;
perm=perms;
;
DIPanom=DIPanoms;
DIPmag=DIPmags;
DIPx=DIPxs;
DIPy=DIPys;
DIPz=DIPzs;
OCTanom=OCTanoms;
OCTmag=OCTmags;
OCTx=OCTxs;
OCTy=OCTys;
OCTz=OCTzs;
;
% clear old storage values
;
clear X0s Y0s Z0s Ds Ls Phidegs Thetadegs perms;
clear DIPanoms DIPanoms DIPxs DIPys DIPzs OCTanoms OCTmags
OCTxs OCTys OCTzs;
clear B0mag1 MorF1 ldeg1 X1 Y1 Z1;
;
% save data
;
nameo=nameoo;
clear nameoo namein;
eval(['save ',nameo,']);

*****
%cccc++paramlst
% PARAMLST
% This script makes a figure subplot which is a list
% of key paramters in the model.
%
% Used by PLOTFIG.M
% Uses: none
%
% Written by Paul Wolfe(Wright State University) for
% US Army Corps of Engineers, Geotechnical Laboratory,
% August 1996.
%
q=7./6.;

```

```

yup=inspace(0,1,10);
xover=inspace(0,1,10);
xorig=0*xover;
yorig=0*yup;
xright=inspace(10,10,10);
ytop=inspace(10,10,10);
plot(xover,yorig,xorig,yup,xright,yup,xover,ytop);
axis('off');
text(0.4,10.8*q,head);
text(0.4,10.2*q,['The data file name is ',name]);
if dipole==1
    if octopole==0
        text(0.4,9.6*q,'This is only the dipole contribution');
    end;
    if octopole==1
        text(0.4,9.6*q,'Combined dipole & octopole contribution');
    end;
elseif dipole==0
    if octopole==1
        text(0.4,9.6*q,'This is only the octopole contribution');
    end
else
    text(0.4,9.6*q,'Something is wrong with the multipolarity. ');
end;
text(0.4,9.0*q,['Earth Field= ',sprintf('%8.1f',B0mag),' nT']);
text(0.4,8.4*q,['Inclination= ',sprintf('%5.1f',Ideg),' degrees']);
text(0.4,7.8*q,['Instrument height= ',sprintf('%5.2f',Z),' m',MorF]);
if MorF=='f'
    text(0.4,7.2*q,['Body Length= ',sprintf('%5.2f',L*12),' inches']);
    text(0.4,6.6*q,['Body Diameter= ',sprintf('%5.2f',D*12),' inches']);
elseif MorF=='m'
    text(0.4,7.2*q,['Body Length= ',sprintf('%5.2f',L),' meters']);
    text(0.4,6.6*q,['Body Diameter= ',sprintf('%5.2f',D),' meters']);
end;
text(0.4,6.0*q,['Body center location X= ',sprintf('%5.2f',X0),MorF]);
text(0.4,5.4*q,['Body center location Y= ',sprintf('%5.2f',Y0),MorF]);
text(0.4,4.8*q,['Body center location Z= ',sprintf('%5.2f',Z0),MorF]);
text(0.4,4.2*q,['Relative permeability = ',sprintf('%5.2f',perm)]);
text(0.4,3.6*q,['Angle of body symmetry axis relative');
text(0.4,3.0*q,[' to the space Z axis = ',sprintf('%5.2f',Thetadeg),' deg']);
text(0.4,2.4*q,['Angle of body symmetry axis relative');
text(0.4,1.8*q,[' to the space X axis = ',sprintf('%5.2f',Phideg),' deg']);

*****
;
nameex=input('Output file name: ','s');
ihand=fopen(nameex,'w');
yn=input('Log all Batch Files (y/n): ','s');
if yn == 'y' | yn == 'Y',
    ex=2,knt=1;
    while ex==2,
        name=sprintf('bat%3.3i.mat',knt);
        ex=exist(name);
        if ex==2,names(knt,1:10)=name;knt=knt+1;end;
    end;
    knt=knt-1;
else;
    knt=1;
    namein=input('File name to Log: ','s');
end;
for ii=1:knt,
    if yn == 'y' | yn == 'Y', namein=[names(ii,1:10)];end;
    eval(['load ',namein,']);
    clear t;
    if MorF=='m',
        t=sprintf(' %2.2i: %2.2i: %2.2i \n\r Metric Units
        ',fix(tim(4)),fix(tim(5)),fix(tim(6)));
    else,
        t=sprintf(' %2.2i: %2.2i: %2.2i \n\r English
        Units',fix(tim(4)),fix(tim(5)),fix(tim(6)));
    end;
    fprintf(ihand,'\n');

```



```

maxoct,X(lmxx8),Y(lmxy8),minoct,X(lmnx8),Y(lmny8),distance8);
fprintf(ihand,' DIP %10.2f%%6.2f%10.2f%%6.2f%10.2f%%6.2f%10.2f%%6.2f
%9.2f\n',...
maxdip,X(lmxx2),Y(lmxy2),mindip,X(lmnx2),Y(lmny2),distance2);
fprintf(ihand,' D&O %10.2f%%6.2f%10.2f%%6.2f%10.2f%%6.2f%10.2f%%6.2f
%9.2f\n',...);

maxoctdip,X(lmxx82),Y(lmxy82),minoctdip,X(lmnx82),Y(lmny82),distance
e82);
;
[maxoct,lmxx8]=max(max(OCtx));
[minoct,lmnx8]=min(min(OCtx));
[maxoct,lmxy8]=max(max(OCy));
[minoct,lmny8]=min(min(OCy));
[maxdip,lmxx2]=max(max(DIPx));
[mindip,lmnx2]=min(min(DIPx));
[maxdip,lmxy2]=max(max(DIPy));
[mindip,lmny2]=min(min(DIPy));
[maxoctdip,lmxx82]=max(max(OCtDIPx));
[minoctdip,lmnx82]=min(min(OCtDIPx));
[maxoctdip,lmxy82]=max(max(OCtDIPy));
[minoctdip,lmny82]=min(min(OCtDIPy));
distance8=sqrt((X(lmxx8)-X(lmnx8))^2+(Y(lmxy8)-Y(lmny8))^2);
distance2=sqrt((X(lmxx2)-X(lmnx2))^2+(Y(lmxy2)-Y(lmny2))^2);
distance82=sqrt((X(lmxx82)-X(lmnx82))^2+(Y(lmxy82)-Y(lmny82))^2);
;
fprintf(ihand,' RESULTS Y Component\n');
fprintf(ihand,' Max X Y Min X Y Dist \n');
fprintf(ihand,' OCT %10.2f%%6.2f%10.2f%%6.2f%10.2f%%6.2f%10.2f%%6.2f
%9.2f\n',...
maxoct,X(lmxx8),Y(lmxy8),minoct,X(lmnx8),Y(lmny8),distance8);
fprintf(ihand,' DIP %10.2f%%6.2f%10.2f%%6.2f%10.2f%%6.2f%10.2f%%6.2f
%9.2f\n',...);
maxdip,X(lmxx2),Y(lmxy2),mindip,X(lmnx2),Y(lmny2),distance2);
fprintf(ihand,' D&O %10.2f%%6.2f%10.2f%%6.2f%10.2f%%6.2f%10.2f%%6.2f
%9.2f\n',...);

maxoctdip,X(lmxx82),Y(lmxy82),minoctdip,X(lmnx82),Y(lmny82),distance
e82);
;
[maxoct,lmxx8]=max(max(OCtz));
[minoct,lmnx8]=min(min(OCtz));

```

```

[maxoct,lmxy8]=max(max(OCTz));
[minoct,lmy8]=min(min(OCTz));
[maxdip,lmx8]=max(max(DIPz));
[mindip,lmx2]=min(min(DIPz));
[maxdip,lmy2]=max(max(DIPz));
[mindip,lmy2]=min(min(DIPz));
[maxoctdip,lmx82]=max(max(OCTDIPz));
[minoctdip,lmx82]=min(min(OCTDIPz));
[maxoctdip,lmy82]=max(max(OCTDIPz));
[minoctdip,lmy82]=min(min(OCTDIPz));
distance8=sqrt((X(lmx8)-X(lmx8))^2+(Y(lmx8)-Y(lmy8))^2);
distance2=sqrt((X(lmx2)-X(lmx2))^2+(Y(lmx2)-Y(lmy2))^2);
distance82=sqrt((X(lmx82)-X(lmx82))^2+(Y(lmx82)-Y(lmy82))^2);
;
fprintf(ihand,' RESULTS Z Component\n');
fprintf(ihand,' Max X Y Min X Y Dist\n');
fprintf(ihand,' OCT %10.2f%6.2f%6.2f%10.2f%6.2f%6.2f\n',...
%9.2f\n',...
maxoct,X(lmx8),Y(lmy8),minoct,X(lmx8),Y(lmy8),distance8);
fprintf(ihand,' DIP %10.2f%6.2f%6.2f%10.2f%6.2f%6.2f\n',...
%9.2f\n',...
maxdip,X(lmx2),Y(lmy2),mindip,X(lmx2),Y(lmy2),distance2);
fprintf(ihand,' D&O %10.2f%6.2f%6.2f%10.2f%6.2f%6.2f\n',...
%9.2f\n',...
maxoctdip,X(lmx82),Y(lmy82),minoctdip,X(lmx82),Y(lmy82),distance82);
;
end;
fclose(ihand);

*****
;
namein=input('File name to Log: ','s');

eval(['load ',namein, '.j']);
namex=input('Output file name: ','s');
ihand=fopen(namex, 'w');
clear t;
if MorF=='m',
t=sprintf('%2.2i:%2.2i:%2.2i\nr Metric Units
',fix(tim(4)),fix(tim(5)),fix(tim(6)));
else,
t=sprintf('%2.2i:%2.2i:%2.2i\nr English
Units',fix(tim(4)),fix(tim(5)),fix(tim(6)));
end;
fprintf(ihand, '\nr');
fprintf(ihand, [' File ',namein, '\nr Date ',day, '\nr Time',t, '\nr\nr']);
fprintf(ihand, [' UXO Location(x,y,z) %10.4f%10.4f
%10.4f\nr'],X0,Y0,Z0);
fprintf(ihand, [' UXO Size(length,diameter) %10.4f%10.4f\nr'],L,D);
fprintf(ihand, [' UXO Rotation(about Z,about X) %10.4f
%10.4f\nr'],Thetadeg,Phideg);
fprintf(ihand, [' UXO Perm %10.4f\nr\nr'],perm);
fprintf(ihand, [' Earth Field (Mag, Dir) %12.4f%10.4f\nr\nr'],B0mag,lddeg);
fprintf(ihand, [' Instruments height %10.4f\nr\nr'],Z);
fprintf(ihand, [' Model X Size (Max, Min, num) %10.4f%10.4f
%10\nr\nr'],Xmax,Xmin,nx);
fprintf(ihand, [' Model Y Size (Max, Min, num) %10.4f%10.4f%10i\nr\nr'],Ymax,Ymin,ny);
OCTDIPanom=OCTanom+DIPanom;
OCTDIPmag=OCTmag+DIPmag;
OCTDIPx=OCTx+DIPx;
OCTDIPy=OCTy+DIPy;
OCTDIPz=OCTz+DIPz;
;
[maxoct,lmx8]=max(max(OCTanom));
[minoct,lmx8]=min(min(OCTanom));
[maxoct,lmy8]=max(max(OCTanom));
[minoct,lmy8]=min(min(OCTanom));

```

```

[imaxoctdip,lmaxx82]=max(max(OCTDIPmag));
[minoctdip,lminx82]=min(min(OCTDIPmag));
[imaxoctdip,lmaxy82]=max(max(OCTDIPmag));
[minoctdip,lminy82]=min(min(OCTDIPmag));
distance8=sqrt((X(lmaxx8)-X(lminx8))^2+(Y(lmaxx8)-Y(lminy8))^2);
distance2=sqrt((X(lmaxx2)-X(lminx2))^2+(Y(lmaxx2)-Y(lminy2))^2);
distance82=sqrt((X(lmaxx82)-X(lminx82))^2+(Y(lmaxx82)-Y(lminy82))^2);
;
fprintf(ihand,' Magnitude      Max      Min      Xloc      Yloc      Dist
        \n');
fprintf(ihand,[' OCT          %10.4f          %10.4f%10.4f%10.4f%10.4f\n'],...
        maxoct,X(lmaxx8),Y(lminy8));
fprintf(ihand,[' OCT          %10.4f          %10.4f%10.4f%10.4f%10.4f\n'],...
        minoct,X(lminx8),Y(lminy8),distance8);
fprintf(ihand,[' DIP          %10.4f          %10.4f%10.4f%10.4f%10.4f\n'],...
        maxdip,X(lmaxx2),Y(lminy2));
fprintf(ihand,[' DIP          %10.4f          %10.4f%10.4f%10.4f%10.4f\n'],...
        mindip,X(lminx2),Y(lminy2),distance2);
fprintf(ihand,[' D&O          %10.4f          %10.4f%10.4f%10.4f%10.4f\n'],...
        maxoctdip,X(lmaxx82),Y(lminy82));
fprintf(ihand,[' D&O          %10.4f          %10.4f%10.4f%10.4f%10.4f\n'],...
        minoctdip,X(lminx82),Y(lminy82),distance82);
;
[maxoct,lmaxx8]=max(max(OCTx));
[minoct,lminx8]=min(min(OCTx));
[maxoct,lmaxy8]=max(max(OCTx));
[minoct,lminy8]=min(min(OCTx));
[maxdip,lmaxx2]=max(max(DIPx));
[mindip,lminx2]=min(min(DIPx));
[maxdip,lmaxy2]=max(max(DIPx));
[mindip,lminy2]=min(min(DIPx));
[maxoctdip,lmaxx82]=max(max(OCTDIPx));
[minoctdip,lminx82]=min(min(OCTDIPx));
[maxoctdip,lmaxy82]=max(max(OCTDIPx));
[minoctdip,lminy82]=min(min(OCTDIPx));
;
[imaxdip,lmaxx2]=max(max(DIPanom));
[mindip,lminx2]=min(min(DIPanom));
[imaxdip,lmaxy2]=max(max(DIPanom));
[mindip,lminy2]=min(min(DIPanom));
[imaxoctdip,lmaxx82]=max(max(OCTDIPanom));
[minoctdip,lminx82]=min(min(OCTDIPanom));
[imaxoctdip,lmaxy82]=max(max(OCTDIPanom));
[minoctdip,lminy82]=min(min(OCTDIPanom));
distance8=sqrt((X(lmaxx8)-X(lminx8))^2+(Y(lmaxx8)-Y(lminy8))^2);
distance2=sqrt((X(lmaxx2)-X(lminx2))^2+(Y(lmaxx2)-Y(lminy2))^2);
distance82=sqrt((X(lmaxx82)-X(lminx82))^2+(Y(lmaxx82)-Y(lminy82))^2);
;
fprintf(ihand,' Total Field Anomaly      Max      Min      Xloc      Yloc
        Dist \n');
fprintf(ihand,[' OCT          %10.4f          %10.4f%10.4f%10.4f%10.4f\n'],...
        maxoct,X(lmaxx8),Y(lminy8));
fprintf(ihand,[' OCT          %10.4f          %10.4f%10.4f%10.4f%10.4f\n'],...
        minoct,X(lminx8),Y(lminy8),distance8);
fprintf(ihand,[' DIP          %10.4f          %10.4f%10.4f%10.4f%10.4f\n'],...
        maxdip,X(lmaxx2),Y(lminy2));
fprintf(ihand,[' DIP          %10.4f          %10.4f%10.4f%10.4f%10.4f\n'],...
        mindip,X(lminx2),Y(lminy2),distance2);
fprintf(ihand,[' D&O          %10.4f          %10.4f%10.4f%10.4f%10.4f\n'],...
        maxoctdip,X(lmaxx82),Y(lminy82));
fprintf(ihand,[' D&O          %10.4f          %10.4f%10.4f%10.4f%10.4f\n'],...
        minoctdip,X(lminx82),Y(lminy82),distance82);
;
[maxoct,lmaxx8]=max(max(OCTmag));
[minoct,lminx8]=min(min(OCTmag));
[maxoct,lmaxy8]=max(max(OCTmag));
[minoct,lminy8]=min(min(OCTmag));
[maxdip,lmaxx2]=max(max(DIPmag));
[mindip,lminx2]=min(min(DIPmag));
[maxdip,lmaxy2]=max(max(DIPmag));
[mindip,lminy2]=min(min(DIPmag));
;

```

```

distance8=sqrt((X(lmxx8)-X(lmny8))^2+(Y(lmxx8)-Y(lmny8))^2);
distance2=sqrt((X(lmxx2)-X(lmny2))^2+(Y(lmxx2)-Y(lmny2))^2);
distance82=sqrt((X(lmxx82)-X(lmny82))^2+(Y(lmxx82)-Y(lmny82))^2);
;
fprintf(ihand,' X Component      Max      Min      Xloc      Yloc      Dist
\nr');
fprintf(ihand,' OCT          %10.4f      %10.4f %10.4f %10.4f\nr'],...
maxoct,X(lmxx8),Y(lmny8));
fprintf(ihand,' OCT          %10.4f %10.4f %10.4f %10.4f\nr'],...
minoct,X(lmxx8),Y(lmny8),distance8);
fprintf(ihand,' DIP          %10.4f      %10.4f %10.4f %10.4f\nr'],...
maxdip,X(lmxx2),Y(lmny2));
fprintf(ihand,' DIP          %10.4f %10.4f %10.4f %10.4f\nr'],...
mindip,X(lmxx2),Y(lmny2),distance2);
fprintf(ihand,' D&O          %10.4f      %10.4f %10.4f %10.4f\nr'],...
maxoctdip,X(lmxx82),Y(lmny82));
fprintf(ihand,' D&O          %10.4f %10.4f %10.4f %10.4f\nr
\nr'],...
minoctdip,X(lmxx82),Y(lmny82),distance82);
;
[maxoct,lmxx8]=max(max(OCTz));
[minoct,lmnx8]=min(min(OCTz));
[maxoct,lmxy8]=max(max(OCTz));
[minoct,lmny8]=min(min(OCTz));
[maxdip,lmxx2]=max(max(DIPz));
[mindip,lmnx2]=min(min(DIPz));
[maxdip,lmxy2]=max(max(DIPz));
[mindip,lmny2]=min(min(DIPz));
[maxoctdip,lmxx82]=max(max(OCTDIPz));
[minoctdip,lmnx82]=min(min(OCTDIPz));
[maxoctdip,lmxy82]=max(max(OCTDIPz));
[minoctdip,lmny82]=min(min(OCTDIPz));
distance8=sqrt((X(lmxx8)-X(lmny8))^2+(Y(lmxx8)-Y(lmny8))^2);
distance2=sqrt((X(lmxx2)-X(lmny2))^2+(Y(lmxx2)-Y(lmny2))^2);
distance82=sqrt((X(lmxx82)-X(lmny82))^2+(Y(lmxx82)-Y(lmny82))^2);
;
fprintf(ihand,' Z Component      Max      Min      Xloc      Yloc      Dist
\nr');
fprintf(ihand,' OCT          %10.4f      %10.4f %10.4f %10.4f\nr'],...
maxoct,X(lmxx8),Y(lmny8));

```

```

for i3=1:ii3;
    %10.4f%10.4f%10.4f%10.4f%10.4f\nr',...
    minoct,X(lmxx8),Y(lmny8),distance8);
for i4=1:ii4;
    %10.4f%10.4f%10.4f%10.4f\nr',...
    fprintf(ihand,[' DIP %10.4f
maxdip,X(lmxx2),Y(lmxy2));
for i6=1:ii6;
    %10.4f%10.4f%10.4f%10.4f%10.4f\nr',...
    fprintf(ihand,[' DIP
mindip,X(lmxx2),Y(lmny2),distance2);
for i7=1:ii7;
    %10.4f%10.4f%10.4f%10.4f\nr',...
    fprintf(ihand,[' D&O
maxoctdip,X(lmxx82),Y(lmxy82));
for i8=1:ii8;
    %10.4f%10.4f%10.4f%10.4f%10.4f\nr
    fprintf(ihand,[' D&O
minoctdip,X(lmxx82),Y(lmny82),distance82);
for i9=1:ii9;
    %10.4f%10.4f%10.4f%10.4f%10.4f\nr
    fclose(ihand);
;
fclose(ihand);
*****
%ccc+++dobatch.m
load last.mat;
kntknt=0;
ii1=length(Xmax);
ii2=length(Xmin);
ii3=length(Ymax);
ii4=length(Ymin);
ii5=length(Z);
ii6=length(B0mag);
ii7=length(1deg);
ii8=length(L);
ii9=length(D);
ii10=length(perm);
ii11=length(Thetadeg);
ii12=length(Phideg);
ii13=length(X0);
ii14=length(Y0);
ii15=length(Z0);
;
for il=1:il1;
for i2=1:ii2;

```



```

'set(ev1(kdogs),"Visible","off");...
'set(ev2(kdogs),"Visible","off");...
'set(ev3(kdogs),"Visible","off");...
'set(ev4(kdogs),"Visible","off");...
'else,...
'set(pm(kdogs),"Visible","on");...
'tval=-1;if plttyp(kdogs) > 7,tval=rem(plttyp(kdogs),4);end;...
'if tval >= 0,set(ev1(kdogs),"Visible","on");end;...
'if tval >= 1,set(ev2(kdogs),"Visible","on");end;...
'if tval >= 2,set(ev3(kdogs),"Visible","on");end;...
'if tval >= 3,set(ev4(kdogs),"Visible","on");end;...
'end;end;]);
;
set(cb(ndogs),'Value',dattyp(ndogs));
;
pm(ndogs)=uicontrol(outfig,'Style','Popup','Position',[xxx,yy,275,75]*sss,...
'String',themenue,...
'Value',plttyp(ndogs),'BackgroundColor','c',...
'Callback','for kdogs=1:6,plttyp(kdogs)=get(pm(kdogs),'Value');',...
'tval=-1;if dattyp(kdogs)~=1 & dattyp(kdogs) < 7 & plttyp(kdogs) > 7,
'tval=rem(plttyp(kdogs),4);end;...
'if tval >= 0, set(ev1(kdogs),"Visible","on");else,...
'set(ev1(kdogs),"Visible","off");end;...
'if tval >= 1, set(ev2(kdogs),"Visible","on");else,...
'set(ev2(kdogs),"Visible","off");end;...
'if tval >= 2, set(ev3(kdogs),"Visible","on");else,...
'set(ev3(kdogs),"Visible","off");end;...
'if tval >= 3, set(ev4(kdogs),"Visible","on");else,...
'set(ev4(kdogs),"Visible","off");end;end;]);
;
;
ev1(ndogs)=uicontrol(outfig,'Style','edit',...
'Position',[xxx,yy,110,15]*sss,...
'String',str1a,'BackgroundColor','c',...
'Visible','off',...
'Callback','for kdogs=1:4,str1a=get(ev1(kdogs),'String');',...
'tval=-1;if dattyp(kdogs) > 7,tval=rem(plttyp(kdogs),4);end;...
'if tval >= 0, set(ev1(ndogs),'Visible','on');
else,set(ev1(ndogs),'Visible','off');end;
'if tval >= 1, set(ev2(ndogs),'Visible','on');
else,set(ev2(ndogs),'Visible','off');end;
'if tval >= 2, set(ev3(ndogs),'Visible','on');
else,set(ev3(ndogs),'Visible','off');end;
'if tval >= 3, set(ev4(ndogs),'Visible','on');
else,set(ev4(ndogs),'Visible','off');end;
end;
'if dattyp(ndogs)~=1 & dattyp(ndogs) < 7 & plttyp(ndogs) > 7,
tval=rem(plttyp(ndogs),4);
end;
set(pm(ndogs),'Visible','off');
if dattyp(ndogs) ~= 1 & dattyp(ndogs) < 7,
set(pm(ndogs),'Visible','on');
set(pm(ndogs),'Value',plttyp(ndogs));
tval=-1;
if dattyp(ndogs)~=1 & dattyp(ndogs) < 7 & plttyp(ndogs) > 7,
tval=rem(plttyp(ndogs),4);
end;
if tval >= 0, set(ev1(ndogs),'Visible','on');
else,set(ev1(ndogs),'Visible','off');end;
if tval >= 1, set(ev2(ndogs),'Visible','on');
else,set(ev2(ndogs),'Visible','off');end;
if tval >= 2, set(ev3(ndogs),'Visible','on');
else,set(ev3(ndogs),'Visible','off');end;
if tval >= 3, set(ev4(ndogs),'Visible','on');
else,set(ev4(ndogs),'Visible','off');end;
end;
'CallBack','for kdogs=1:4,str2a=get(ev2(kdogs),'String');',...
'cval(1,kdogs)=str2num(str1a);end;]);
ev2(ndogs)=uicontrol(outfig,'Style','edit',...
'Position',[xxx,yy-15,110,15]*sss,...
'String',str2a,'BackgroundColor','c',...
'Visible','off',...
'Callback','for kdogs=1:4,str2a=get(ev2(kdogs),'String');',...
'cval(2,kdogs)=str2num(str2a);end;]);
ev3(ndogs)=uicontrol(outfig,'Style','edit',...
'Position',[xxx,yy-30,110,15]*sss,...
'String',str3a,'BackgroundColor','c',...
'Visible','off',...
'Callback','for kdogs=1:4,str3a=get(ev3(kdogs),'String');',...
'cval(3,kdogs)=str2num(str3a);end;]);
ev4(ndogs)=uicontrol(outfig,'Style','edit',...
'Position',[xxx,yy-45,110,15]*sss,...
'String',str4a,'BackgroundColor','c',...
'Visible','off',...
'Callback','for kdogs=1:4,str4a=get(ev4(kdogs),'String');',...
'cval(4,kdogs)=str2num(str4a);end;]);
;
set(pm(ndogs),'Visible','off');
if dattyp(ndogs) ~= 1 & dattyp(ndogs) < 7,
set(pm(ndogs),'Visible','on');
set(pm(ndogs),'Value',plttyp(ndogs));
tval=-1;
if dattyp(ndogs)~=1 & dattyp(ndogs) < 7 & plttyp(ndogs) > 7,
tval=rem(plttyp(ndogs),4);
end;
if tval >= 0, set(ev1(ndogs),'Visible','on');
else,set(ev1(ndogs),'Visible','off');end;
if tval >= 1, set(ev2(ndogs),'Visible','on');
else,set(ev2(ndogs),'Visible','off');end;
if tval >= 2, set(ev3(ndogs),'Visible','on');
else,set(ev3(ndogs),'Visible','off');end;
if tval >= 3, set(ev4(ndogs),'Visible','on');
else,set(ev4(ndogs),'Visible','off');end;
end;
'CallBack','for kdogs=1:4,str1a=get(ev1(kdogs),'String');',...

```



```

end;
;
*****
%ccc++subplotx
function subplotx(modx,qrow,qcol,mp);
;
mode=rem(modx,10);modr=fix(modx/10);
;
if mode==1,orient tall;end;
if mode==2,orient landscape;end;
if mode==3 & modr==0,orient portrait;end;
if mode==3 & modr==1,orient landscape;end;
;
if modr==0,
subplot(qrow,qcol,mp);
else,
kind=qcol*qrow;
;
if mode==1,
xlen1=6;
ylen1=7;
xlen2=60;
ylen2=25;
xlen3=25;
ylen3=25;
xlen5=25;
ylen5=2;
xst1=25;
yst1=2;
xst2=[.25,.25];
yst2=[.2,.60];
xst3=[.25,6,.25,6];
yst3=[.2,.2,.60,.60];
xst5=[.25,6,.26,6,.26,6];
;
if mode==2,
xlen1=70;
ylen1=60;
xlen2=30;
ylen2=50;
xlen3=25;
ylen3=25;
xlen5=15;
ylen5=25;
xst1=15;
yst1=25;
xst2=[.15,.50];
yst2=[.25,.25];
xst3=[.15,6,.15,6];
;
if mode==3,
xlen1=70;
ylen1=60;
xlen2=30;
ylen2=50;
xlen3=25;
ylen3=25;
xlen5=15;
ylen5=25;
xst1=15;
yst1=25;
xst2=[.15,.50];
yst2=[.25,.25];
xst3=[.15,6,.15,6];
;
yst5=[.15,.15,425,425,70,70];
end;
;

```

```

yst3=[.25,.25,.60,60];
xst5=[.15,.15,.40,.40,.65,65];
yst5=[.25,.6,.25,.6,.25,.6];
end;
;
if kind==1,xlen=xlen1,ylen=ylen1,xst=xst1,yst=yst1,end;
if kind==2,xlen=xlen2,ylen=ylen2,xst=xst2(mp),yst=yst2(mp),end;
if kind==3 |
kind==4,xlen=xlen3,ylen=ylen3,xst=xst3(mp),yst=yst3(mp),end;
if kind==5 |
kind==6,xlen=xlen5,ylen=ylen5,xst=xst5(mp),yst=yst5(mp),end;
;
axes('position',[xst,yst,xlen,ylen]);
;
end;

*****

global rectzz;
load last.mat;
;
;
ii1=length(Xmax);
ii2=length(Xmin);
ii3=length(Ymax);
ii4=length(Ymin);
ii5=length(Z);
ii6=length(B0mag);
ii7=length(ldeg);
ii8=length(L);
ii9=length(D);
ii10=length(perm);
ii11=length(Thetadeg);

magfield(namef,Xmax(ii1),Xmin(ii2),Ymax(ii3),Ymin(ii4),Z(ii5),...
B0mag(ii6),ldeg(ii7),L(ii8),D(ii9),div,perm(ii10),Thetadeg(ii11),...
Phideg(ii12),X0(ii13),Y0(ii14),Z0(ii15),MorF);
;
load lastp.mat;figure(h);

plotfig(mode,dipole,octopole,dattyp,plttyp,MorF,namep,cval,compfile,iframe
);
figure(h);
eval(['print -dgif8 F',num2str(iframe),'.GIF']);
rectzz=get(gcf,'Position');
rectzz(1:2)=[0 0];

```



```

xright=linspace(10,10,10);
ytop=linspace(10,10,10);
plot(xover,yorig,yup,xright,yup,xover,ytop);
axis('off');
text(0.4,9.6*q,head);
text(0.4,9.0*q,['Earth Field= ',sprintf('%8.1f,B0mag), ' nT']);
text(0.4,8.4*q,['Inclination= ',num2str(1deg), ' degrees']);
if MorF=='f'
    text(0.4,7.8*q,['Body Length= ',num2str(L*12), ' inches']);
    text(0.4,7.2*q,['Body Diameter= ',num2str(D*12), ' inches']);
elseif MorF=='m'
    text(0.4,7.8*q,['Body Length= ',num2str(L), ' meters']);
    text(0.4,7.2*q,['Body Diameter= ',num2str(D), ' meters']);
end,
text(0.4,6.6*q,['Relative permeability= ',num2str(perm)]);
text(0.4,6.0*q,['Angle of body symmetry axis relative= ',
num2str(Thetadeg), ' deg']);
text(0.4,5.4*q,[' to the space Z axis= ',num2str(Thetadeg), ' deg']);
text(0.4,4.8*q,['Angle of body symmetry axis relative= ',
num2str(Phideg), ' deg']);
text(0.4,4.2*q,[' to the space X axis= ',num2str(Phideg), ' deg']);
text(0.4,3.6*q,['Body center location= ',num2str(X0),', ',num2str(Y0),', ...
', ',num2str(Z0),', ',MorF]);
text(0.4,3.0*q,['Instrument height= ',num2str(Z),', ',MorF]);
text(0.4,2.4*q,['The data file name is ',name]);
if dipole==1
    if octopole==0
        text(0.4,1.8*q,'This is only the dipole contribution');
    end;
    if octopole==1
        text(0.4,1.8*q,'This is the combined dipole and octopole
contribution');
    end;
elseif dipole==0
    if octopole==1
        text(0.4,1.8*q,'This is only the octopole contribution');
    end
else

```

```

text(0.4,1.8*q,'Something is wrong with the multipolarity. ');
end;

```

REPORT DOCUMENTATION PAGE

Form Approved
OMB No. 0704-0188

Public reporting burden for this collection of information is estimated to average 1 hour per response, including the time for reviewing instructions, searching existing data sources, gathering and maintaining the data needed, and completing and reviewing the collection of information. Send comments regarding this burden estimate or any other aspect of this collection of information, including suggestions for reducing this burden, to Washington Headquarters Services, Directorate for Information Operations and Reports, 1215 Jefferson Davis Highway, Suite 1204, Arlington, VA 22202-4302, and to the Office of Management and Budget, Paperwork Reduction Project (0704-0188), Washington, DC 20503.

1. AGENCY USE ONLY (Leave blank)		2. REPORT DATE September 1998	3. REPORT TYPE AND DATES COVERED Final report
4. TITLE AND SUBTITLE Multisensor Methods for Buried Unexploded Ordnance Detection, Discrimination, and Identification			5. FUNDING NUMBERS
6. AUTHOR(S) Dwain K. Butler, Ernesto R. Cespedes, Cary B. Cox, Paul J. Wolfe			
7. PERFORMING ORGANIZATION NAME(S) AND ADDRESS(ES) U.S. Army Engineer Waterways Experiment Station, 3909 Halls Ferry Road, Vicksburg, MS 39180-6199; Wright State University, Dayton, OH 45435-0001			8. PERFORMING ORGANIZATION REPORT NUMBER Technical Report SERDP-98-10
9. SPONSORING/MONITORING AGENCY NAME(S) AND ADDRESS(ES) U.S. Army Corps of Engineers Washington, Dc 20314-1000			10. SPONSORING/MONITORING AGENCY REPORT NUMBER
11. SUPPLEMENTARY NOTES Available from National Technical Information Service, 5285 Port Royal Road, Springfield, VA 22161.			
12a. DISTRIBUTION/AVAILABILITY STATEMENT Approved for public release; distribution is unlimited.			12b. DISTRIBUTION CODE
13. ABSTRACT (Maximum 200 words) <p>Unexploded ordnance (UXO) cleanup is the number one priority Army installation remediation/restoration requirement. The problem is enormous in scope, with millions of acres and hundreds of sites potentially contaminated. Before the UXO can be recovered and destroyed, it must be located. UXO location requires surface geophysical surveys. The geophysical anomalies caused by the UXO must be detected, discriminated from geophysical anomalies caused by other sources, and ideally identified or classified. Recent UXO technology demonstrations, live site demonstrations, and practical UXO surveys for site cleanup confirm that most UXO anomalies can be detected (with probabilities of detection of 90 percent or better), however there is little evidence of discrimination capability (i.e., the false alarm rates are high), and there is no identification capability. Approaches to simultaneously increase probability of detection and decrease false alarm rate and ultimately to give identification/classification capability involve rational multisensor data integration for discrimination and advanced development of new and emerging technology for enhanced discrimination and identification. The goal of multisensor data integration is to achieve true joint inversion of data to a best-fitting model using realistic physics-based models that replicate UXO geometries and physical properties of the UXO and surrounding geologic materials. Data management, analysis, and display procedures for multisensor data are investigated. The role of empirical, quasi-empirical, and analytical modeling for</p> <p style="text-align: right;">(Continued)</p>			
14. SUBJECT TERMS Detection Discrimination Geophysics Unexploded ordnance (UXO)			15. NUMBER OF PAGES 181
			16. PRICE CODE
17. SECURITY CLASSIFICATION OF REPORT UNCLASSIFIED	18. SECURITY CLASSIFICATION OF THIS PAGE UNCLASSIFIED	19. SECURITY CLASSIFICATION OF ABSTRACT	20. LIMITATION OF ABSTRACT

13. (Concluded).

UXO geophysical signature prediction are reviewed and contrasted with approaches that require large signature databases (e.g., expert systems, neural nets, signature database comparison) for training or best-fit comparison. A magnetic modeling capability is developed, validated, and documented that uses a prolate spheroid model of UXO. The electromagnetic modeling of UXO signatures is more problematic, and an intermediate quasi-empirical modeling capability (a simple analytical model modified to reflect measured signature observations) is explored. Approaches using parameter space analysis techniques for multisensor data integration are emphasized, with examples from UXO test site and demonstration program datasets. A multichannel, multicomponent, time-domain electromagnetic system and a multifrequency, frequency-domain electromagnetic system are highlighted as emerging technologies with potential to advance capabilities for UXO discrimination and identification.